Graphene: Synthesis, Characterization, Properties and Chemical Modification

A THESIS SUBMITTED FOR

Doctor of Philosophy

By

K. S. Subrahmanyam

Chemistry and Physics of Materials Unit

Jawaharlal Nehru Centre for Advanced Scientific Research

(A Deemed University)

Bangalore – 560064

November 2011

Dedicated

To

AMMA, NANNA

DECLARATION

I hereby declare that the matter embodied in this thesis entitled **"*Graphene: Synthesis, Characterization, Properties and Chemical Modification*"** is the result of investigations carried out by me under the supervision of Prof. C. N. R. Rao, FRS at the Chemistry and Physics of Materials Unit, Jawaharlal Nehru Centre for Advanced Scientific Research, Bangalore, India and that it has not been submitted elsewhere for the award of any degree or diploma.

In keeping with the general practice in reporting scientific observations, due acknowledgement has been made whenever the work described is based on the findings of other investigators.

K. S. Subrahmanyam

CERTIFICATE

I hereby certify that the matter embodied in this thesis entitled ***"Graphene: Synthesis, Characterization, Properties and Chemical Modification"*** has been carried out by Mr. K. S. Subrahmanyam, at the Chemistry and Physics of Materials Unit, Jawaharlal Nehru Centre for Advanced Scientific Research, Bangalore, India under my supervision and that it has not been submitted elsewhere for the award of any degree or diploma.

_____

Prof. C. N. R. Rao, FRS

(Research Supervisor)

Acknowledgements

I am extremely grateful to my research supervisor Prof. C. N. R. Rao, FRS without whom none of this would have been possible. I am indebted to him for giving me an opportunity to work with him, and teaching me how to appreciate science, to perform research and to communicate ideas. Not only has he been an excellent teacher and mentor, but also a valuable moral support on the personal front. The strong scientific foundation that he has given me will continue to guide and inspire me in my future career.

My deepest thanks to Mrs. Indumati Rao and Mr. Sanjay for their affection and hospitality.

I would like to express my sincere thanks to Dr. A. Govindaraj who has helped me a great deal in carrying out the various experiments. It has been a good learning experience working with him in the lab.

I would like to thank Prof. Swapan K. Pati (TSU) and Prof. U. V. Waghmare (TSU) for collaborative work.

I am thankful to the past and present chairmen of CPMU Prof. C. N. R. Rao, Prof. G. U. Kulkarni and Prof. S. Balasubramanian, chairman of NCU Prof. C. N. R. Rao, allowing me to utilize the various facilities in the centre.

I thank Prof. A. Sundaresan for magnetic measurements facility.

I am thankful to Usha Madam, Anil, Vasu, Selvi, Dr. Kunal Dr. Basavaraj (VEECO) and Mahesh for their help with the various characterization techniques. I thank Srinath and Srinivas for their technical help.

I would like to thank Dr. Vivek, Dr. Gomathi, Anupama, Dr. Rakesh, Dr. Leela, Ramakrishna, Bello, Dr. Prashant, Gopalakrishnan, Urmi, Piyush, Mohan, Nidhi, Rana and Ram Kumar for working with me on various problems.

I thank Mrs. Shashi, Mrs. Sudha, Mrs. Aruna (ICMS), Mr. Gowda and Mr. Victor for their help.

I would like to thank Venkat and Prakash for their help with CHN analysis, Dr. Bhat, Dr. Neenu, Dr. Vivek, Dr. Rakesh, and Dr. Gomathi for their help with the Raman measurements, Mr. Pranab and Mr. Nitesh for magnetic measurements, Dr. Saikrishna for BET surface area measurements, Mrs. Josena and Dr. Kalyan for gas chromatography measurements, Dr. Neena, Dr. Vijay, and Naren for their help with the AFM measurements. Radha for EBL, Dr. Karthik and Ms. Sireesha for TEM imaging, Mr. Malli, Mr. Jitesh and Mr. Kishore for XPS measurements, Mr. Prakash, Mr. Sudip, Mr. Arpan and Mr. Ritesh for gas adsorption measurements.

I am thankful to all academic staff members (Mrs. Sukanya, Dr. Princy) and administrative staff for their support, in particular senior administrative officer A.N. Jayachandra.

I am thankful to all computer lab staff members for their help.

I am thankful to all work shop members (Arogyanathan, Moorthy and Sunil).

I would like to thank Dr. Prashant, Barun, Dr. Sashi, Gopalakrishnan, Govind and Dr. A. Govindaraj for their help in writing thesis.

I would like to thank all my past and present lab mates, Dr. Vivek, Dr Chandu, Dr. Bhat, Dr. Leela, Dr. Rakesh, Dr. Biswas, Dr. Neenu, Anupama, Dr. Prashant, Dr. Latte, Manjunatha, Bello, Dr. Kalyani, Dr. Gomathi, Dr. Sandeep, Basant, Barun,

Dr. Prabhakar Rao, Dr. Thiru, Dr. Claudy, Dr. Jyoti, Dr. Kalyan, Ramakrishna, Dr. Angshuman, Urmi, Ajmala, Dr. Sundarayya, Dr. Nagaraju, Rajasekharyya, Dr. Nusrat, Dr. Joshi, Dr. Sashi, Moses, Anirban, Nitesh, Rana, Pramoda, Sunita, Srinu and Govind for their constant cheerful company and help in various occasions.

I would like to thank Mr. M. Srinivasa Rao, my teacher, who has been giving constant encouragement and suggestions in my life.

I would like to thank all university of Hyderabad, school of chemistry faculty, classmates and friends.

Special thanks to my friends Chary, Saraiah, Subbareddy, Raja, Sinu, Madhu, Balu, Shiva, Ganesh, Koti, Guru, Nagarjuna, Hari, Bochkar, Vijji, Venki, Rag, Mohan, Naidu, Vasu, Leela, Rakesh, Krishna, KKR, Kalyani, Sonia, Neenu, Anupama, Barun, Basanath, Kalyan, Rasheed, Subbareddy, Krishna, Venkat, Naren, Sridhar, Jayaram, RK, Mukthi, Mahesh, Nag babu, Anand, Satthi, Srinu and Kiran.

I would like thank all my teachers, friends and relatives at my native place.

Finally, I wish to express my gratitude to my family members without their support and encouragement, this study would not have been possible.

The short, yet long endeavour of Ph.D. has been made possible because of the help, advice, suggestions and support provided by multiple hands. I have taken this opportunity to mention a few of them. However, my sincere thanks extend to everyone who has played a role in making this dream a reality.

Preface

The thesis consists of seven chapters of which the first chapter provides a brief overview of graphene. Chapter 2 deals with the synthesis and characterization of graphene. When graphene research was initiated in our laboratory, there was little information available on synthesis and characterization methods. This necessitated exploration of various methods of synthesis. Different synthetic routes namely, exfoliation of graphite oxide, conversion of nanodiamond, chemical vapor deposition and reduction of graphene oxide, including newly discovered arc discharge route and radiation induced reduction of graphene oxide have been described. The samples so obtained have been characterized by utilizing different techniques such as electron microscopy, Raman spectroscopy and atomic force microscopy.

Chapter 3 describes different ways of functionalizing graphene. Amidation and reaction with organo silane or tin solubilize graphene in organic solvents whereas wrapping with surfactants gives water soluble graphene. Noncovalent π-π interaction with a pyrene derivative solubilizes graphene in dimethylformamide.

Chapter 4 presents some properties of few-layer graphenes and comprises six parts. Part 1 deals with the surface properties and uptake of H_2, CO_2 and CH_4 by graphene. Part 2 and 3 presents magnetic and electrochemical properties of graphene respectively. Magnetic properties of different graphene samples have been investigated and magnetism in graphene could be tuned by adsorption of certain specific molecules. Electron transfer kinetics of different graphenes and their use as electrode material in supercapacitors have been investigated. Part 4 deals with emission properties of graphene based materials and part 5 gives patterning and lithography based on graphene.

In Chapter 5, investigations on interaction of graphene with electron donor and acceptor molecules and different metal nanoparticles have been presented. The G, D and 2D bands in the Raman spectra of graphene have been employed to examine the interaction of electron donor and acceptor molecules as well as of different metal nanoparticles with graphene.

Band gap engineering of graphene can effectively be achieved by doping it suitably. Chapter 6 describes different routes of doping graphene with boron and nitrogen. The arc discharge technique to prepare graphene has been effectively employed to chemically dope graphene.

Chapter 7 presents chemical storage of H_2 by graphene. To chemically store hydrogen in graphene, Birch-reduction and H_2 plasma treatment have been employed.

Contents

CHAPTER 1

GRAPHENE: AN OVERVIEW

1.1 Nature of graphene and related aspects

1.1.1 Allotropes of carbon

Carbon is one of the most interesting elements in the periodic table and it plays a unique role in nature. The formation of carbon (Figure 1) in stars as a result of the merging of three helium nuclei, known as triple alpha process, is the initial step in the formation of many heavy elements.[1] Carbon has the ability to form very long chains of interconnecting C-C bonds which is known as catenation. Due to catenation, carbon forms the highest number of

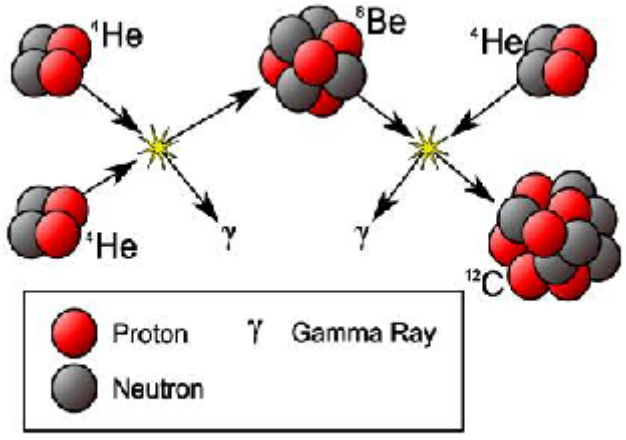

Figure 1. Overview of the triple-alpha process.

$$2He^{4} + 2He^{4} \rightarrow 4Be^{8}$$

$$4Be^{8} + 2He^{4} \rightarrow 6C^{12} + \gamma + 7.367\ MeV$$

compounds compared to any other element. The capability of carbon atoms to form complicated networks[2] is fundamental to organic chemistry and forms the basis for the existence of life. Elemental carbon forms many allotropes (Figure 2) such as diamond, graphite, fullerenes[3-5] and nanotubes.[6]

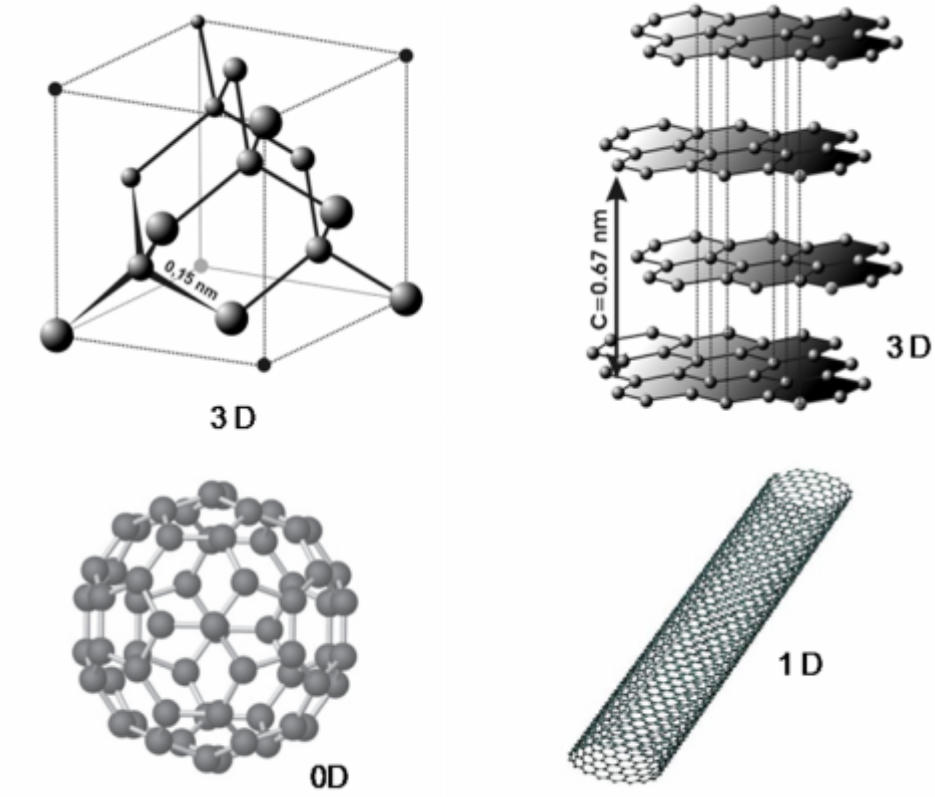

Figure 2. 3D, 1D and 0D allotropes of carbon.

1.1.2 Brief history of graphene

The two-dimensional form of carbon called graphene (or '2D graphite') is the mother of all graphitic forms. It is a single-layer of carbon atoms tightly packed into a honeycomb lattice which can be either wrapped up into 0D fullerenes, rolled into 1D nanotubes or stacked into 3D graphite (Figure 3). Although there has been a great surge in

graphene research recently, graphene-related materials produced from graphite oxide (GO) were already reported in 1962, and the chemical modifications of graphite were performed as early as 1840. In the 1940s[7] a number of theoretical studies suggested that the graphitic

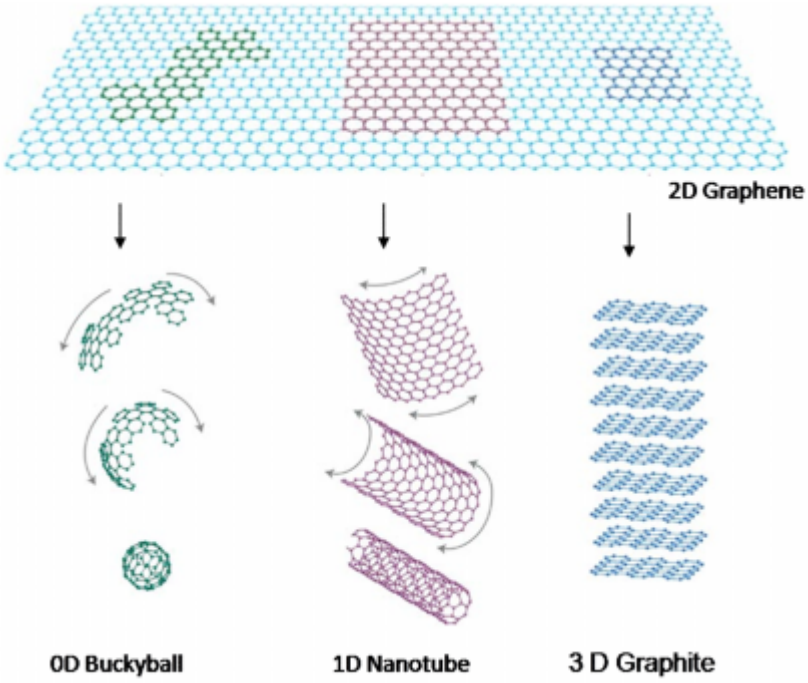

Figure 3. Mother of all graphitic forms. (From ref. [15]).

layers in their isolated form might exhibit extraordinary characteristics. Following the theoretical studies, later, several researchers made attempts to prepare graphene by employing different procedures like thermal deflagration of GO, mechanical exfoliation of GO followed by reduction,[8] sublimation of silicon from single crystals of silicon carbide (0001),[9] and by micromechanical approach.[10, 11] Most of these procedures resulted in multi-layered graphene and the products were not characterized properly. In 2004 Geim and co-workers employed the same "micro-mechanical approach" reported by Roscoe *et al*.[11] and found that the approach enables the generation of extremely thin graphene films with a

single layer or few layers.[12, 13] Also, by applying the same technique they could obtain two-dimensional crystals of other materials, including boron nitride, high-temperature superconductor Bi-Sr-Ca-Cu-O and some dichalcogenides.[14] The graphene samples have been characterized by a variety of microscopic and other physical techniques like atomic force microscopy (AFM), transmission electron microscopy (TEM), scanning tunneling microscopy (STM) and Raman spectroscopy.[15] It has been showed that graphene is a two-dimensional semi-metal with a tiny overlap between valence and conductance bands. Graphene exhibits a strong ambipolar electric field effect with very high concentrations of electrons and holes, up to $10^{13}/cm^2$ and room-temperature mobilities of ~10,000 $cm^2/V.s$ (Figure 4).[12] It is interesting that single-layer graphene placed on a silicon wafer with a 300 nm thick layer of SiO_2, becomes visible in an optical microscope.[16]

Types of graphene: Graphene can be classified as three types: single-, double- and few- (3 to <10) layer graphenes. Films containing more than 10 layers can be considered as thin films of graphite. It was shown that the electronic structure of graphene rapidly evolves with the number of layers, approaching the 3D limit of graphite at 10 layers.[17] Moreover, only single- and bi- layer graphenes have simple electronic spectra: they are both zero-gap semiconductors (they can also be referred to as zero-overlap semimetals) with a single type of electrons and holes. After more than two layers, the spectra become increasingly complicated by the overlapping of the conduction and valence bands[17] and thus by the appearance of several types of charge carriers.

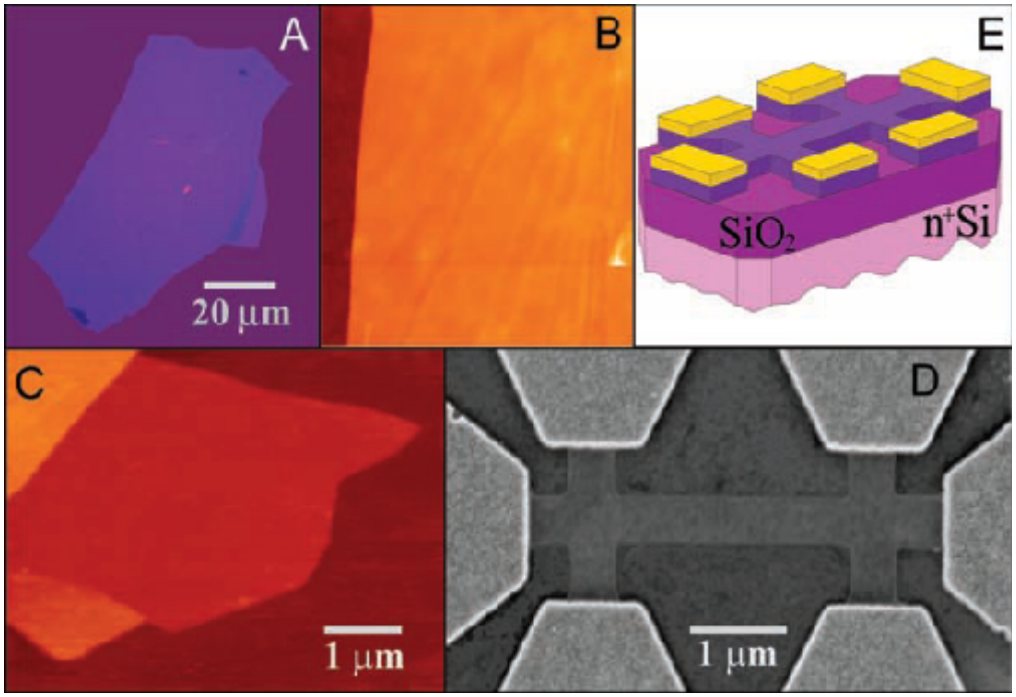

Figure 4. Graphene films. (A) Photograph (in normal white light) of a relatively large multilayer graphene flake with thickness ~3 nm on top of an oxidized Si wafer. (B) Atomic force microscope (AFM) image of 2 μm by 2 μm area of this flake near its edge. Colors: dark brown, SiO_2 surface; orange, 3 nm height above the SiO_2 surface. (C) AFM image of single-layer graphene. Colors: dark brown, SiO_2 surface; brown-red (central area), 0.8 nm height; yellow-brown (bottom left), 1.2 nm; orange (top left), 2.5 nm. Notice the folded part of the film near the bottom, which exhibits a differential height of ~0.4 nm. (D) Scanning electron microscope image of an experimental device prepared from FLG. (E) Schematic view of the device in (D). (From ref. [12]).

1.1.3 Stability of graphene

Graphene is the two-dimensional counterpart of three dimensional graphite, exhibiting high crystal quality and ballistic conduction. But according to some earlier reports, perfect two-dimensional crystals cannot exist in free state.[18-22] This discrepancy can be resolved by considering the graphene structures studied so far to be an integral part of a

larger, three-dimensional structure, either supported by a substrate or embedded in a three-dimensional matrix.[23-25] But surprisingly, individual graphene sheets (Figure 5) freely suspended on a micro fabricated scaffold in vacuum or in air have also been reported.[26] At first more than 70 years ago, Peierls[19, 20] and Landau[27, 28] raised questions about the existence of a strictly two-dimensional (2D) crystal. They showed that, in the standard harmonic approximation,[29] thermal fluctuations destroy the long-range order which leads to the melting of 2D lattice at any finite temperature. Later, Mermin and Wagner proved that a magnetic long-range order could not exist in one and two dimensions[27] and later extended the proof to crystalline order in 2D.[22] Importantly, number of experiments on thin films were in agree with the theory, showing that below a certain thickness, typically of dozens of

Figure 5. TEM image of a suspended graphene membrane.

(Scale bar, 500 nm) (From ref. [26]).

atomic layers, the films segregate into islands or decompose unless they constitute an inherent part of a three-dimensional (3D) system.[30-32] However, although the theory does not allow perfect crystals in 2D space, it does not forbid nearly perfect 2D crystals in 3D space. Indeed, a detailed analysis of the 2D crystal problem beyond the harmonic

approximation has led to the conclusion[33-35] that the interaction between bending and stretching long-wavelength phonons could in principle stabilize atomically thin membranes through their deformation in the third dimension.[35]

1.1.4 Electronic structure

Graphene honeycomb lattice is composed of two equivalent carbon sublattices A and B, as shown in Figure 6a. Figure 6b shows the first Brillouin zone of graphene, with the high-symmetry points M, K, K' and Γ marked. Note that K and K' are two inequivalent points in the Brillouin zone. The s, p_x and p_y orbitals of carbon atoms form σ bonds with neighboring carbon atoms. The π electrons in the p_z orbital, one from each carbon, form the bonding π and the anti-bonding π* bands of graphene. Dispersion relation of these π-electrons is described by the tight binding model, incorporating only the first nearest neighbor interactions [Eq.(1)]:[36, 37]

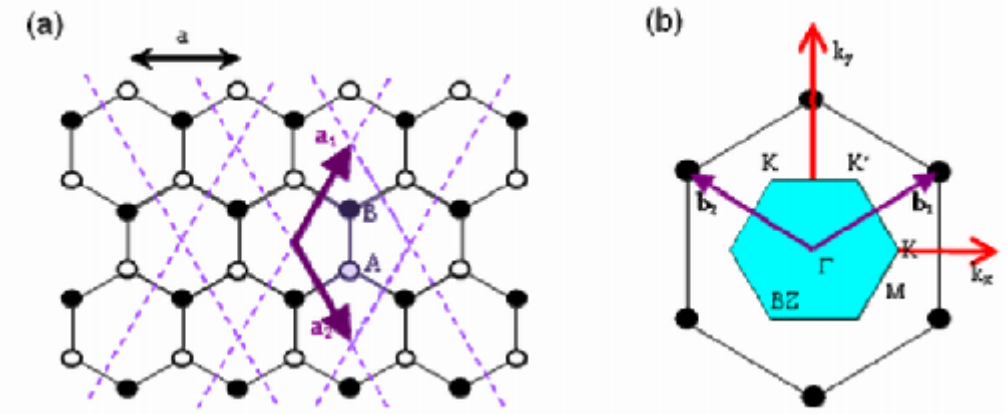

Figure 6. (a) Graphene lattice. $\vec{a}_1$ and $\vec{a}_2$ are the unit vectors. (b) Reciprocal lattice of graphene. Shaded hexagon is the first Brillouin zone. $\vec{b}_1$ and $\vec{b}_2$ are the reciprocal lattice vectors.

$$E^{\pm}(k_x, k_y) = \pm\gamma_0\sqrt{1+4\cos\frac{\sqrt{3}k_x a}{2}\cos\frac{k_y a}{2}+4\cos^2\frac{k_y a}{2}} \qquad (1)$$

where $a = \sqrt{3}a_{CC}$, a_{CC} is the carbon – carbon distance (1.42 A□) and γ_o, the transfer integral, is the matrix element between the π-orbitals of neighboring carbon atoms and its magnitude is ~ 3eV. The – sign in Eq.1 refers to the π-band which is fully occupied in graphene and the + sign corresponds to the totally empty anti-bonding π* band. The π and π* bands touch at the K and K' points. A Taylor expansion of Eq.1 around K or K' points yield linear dispersion bands [Eq. (2)].

$$E^{\pm}(k) = \pm\gamma\left|\vec{k}\right| \qquad (2)$$

Here, $\vec{k}$ is measured with respect to the K-point, $\gamma = \hbar v_F = \sqrt{3}a\gamma_0 / 2$ and v_F is the Fermi group velocity. The linear bands, a result of graphene's crystal symmetry, are a hallmark of graphene, giving rise to many of the interesting physical properties such as half-integer quantum Hall effect, Berry's phase and Klein–paradox.[38, 39] Within the linear–band approximation, the constant energy contours are circles around the K and K' points. The effective Hamiltonian near the K-point can be expressed by the Dirac equation with zero mass [Eq. (3)].

$$H = \begin{pmatrix} 0 & \gamma k \\ \gamma k & 0 \end{pmatrix} = \hbar v_F \, \vec{\sigma}.\vec{k} \qquad (3)$$

Here $\vec{\sigma}$ is the 2d pseudospin Pauli matrix. Physically, this implies that the electronic states near the K- point are composed of states belonging to different sublattices A and B and their relative contributions is taken into account using two component wave functions (spinors). The eigen functions near K are given by Eq. (4).

$$\psi^{o}_{s,k}(\vec{r}) = \frac{1}{\sqrt{2}}\begin{pmatrix} 1 \\ se^{i\theta_k} \end{pmatrix} e^{i\vec{k}.\vec{r}} \qquad (4)$$

where s = ± 1 is the band index and $\theta_{\vec{k}}$ is the polar angle of the wavevector $\vec{k}$. Eq.4 reflects that the pseudospin vector is parallel to the wavevector $\vec{k}$ in the upper band (s = 1) and is anti-parallel in the lower band (s = -1). The wavefunctions at K and K' are related by time-reversal symmetry. The pseudospin and Berry phase may be manipulated by application of an inhomogeneous lattice distortion. Interestingly, a non-constant lattice distortion can lead to a valley-Hall effect, analogous to the spin-Hall effect in semiconductors.[40]

The electronic dispersion of bilayer graphene is different from that of single-layer graphene. The lattice structure of a bilayer graphene is shown in Figure 7a and b, where the top and bottom layers are represented by solid and dashed lines, and indexes 1 and 2 label the sublattices of the bottom and top layers, respectively. The A_2 sublattice of the top layer is exactly on top of the sublattice B_1 of the bottom layer. In addition to the in-plane nearest neighbor hopping energy γ_0 (A_1-B_1 or A_2-B_2), there is interlayer hopping energy γ_1 (A_2-B_1). Taking only these two energy scales and neglecting all other hopping energies (B_2-A_1, A_2-A_1 or B_2-B_1), the Hamiltonian of a bilayer graphene near the K-point can be written as Eq. (5).

$$H = \begin{pmatrix} 0 & \gamma k & 0 & 0 \\ \gamma k & 0 & \gamma_1 & 0 \\ 0 & \gamma_1 & 0 & \gamma k \\ 0 & 0 & \gamma k & 0 \end{pmatrix} \tag{5}$$

The eigen values of this Hamiltonian are given by Eq. (6)

$$E_{sj}(k) = s\left[\left(\sqrt{\left(\frac{\gamma_1}{2}\right)^2 + (\gamma_0 k)^2}\right)(-1)^j \frac{\gamma_1}{2}\right] \tag{6}$$

where s = ± 1 is a band index j is a subband index (j = 1,2). Figure 7c shows the electronic dispersion of the bilayer, where γ_1 is the energy separation between the two subbands in

conduction or valence bands. There is no gap between the valence band and the conduction band. However, a gap can open on application of an electric field perpendicular to the bi-layer.[41, 42] A band gap has been observed by angle-resolved photo-emission experiments on a chemically doped bilayer graphene,[24] where the electric field arises due to charge transfer from the dopants to the carbon atoms. A direct application of top-gate electric field to the

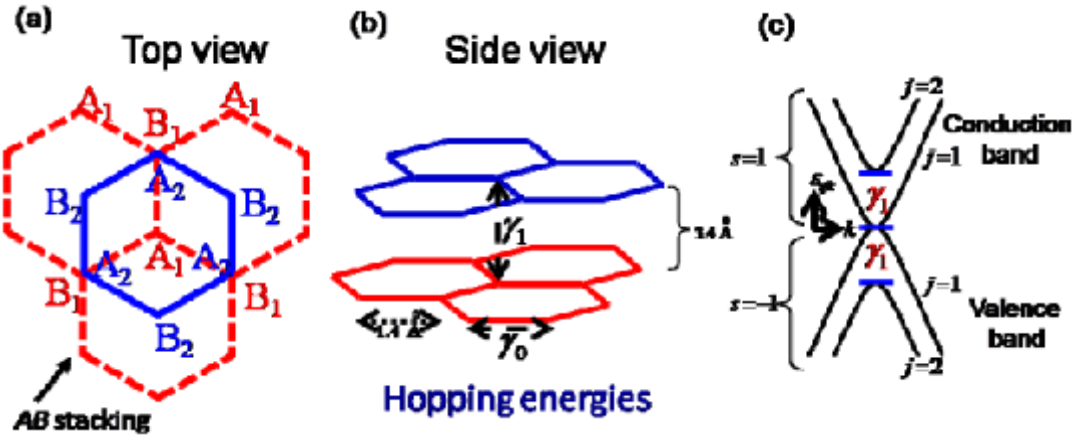

Figure 7. (a) Top and (b) side view of a bilayer graphene. A_1, B_1 are the sub lattices of the bottom layer and A_2, B_2 are sublattices of the top layer. (c) Energy dispersion of a bilayer graphene. Here γ_1 is the energy separation between the two sub bands.

back gated bilayer field effect transistor gives a controlled way to manipulate the band gap, presenting a possibility of electrostatically controlled graphene-based devices.[43]

Quantum Hall Effect: The massless Dirac Fermion nature of carriers in single-layer graphene has interesting consequences on the energy spectrum of the Landau levels (LL) produced in the presence of a magnetic field perpendicular to the graphene layer.[44-46] The energies of the Landau levels, indexed by integer j, are given by $E_j = \pm v_F \sqrt{2|j|e\hbar B}$. Notice

that E_j is proportional to $\sqrt{B}$, in contrast to conventional 2-dimensional electron-gas with parabolic bands where $E_j = \left(j + \frac{1}{2}\right)\hbar eB/m^*$. Furthermore, since the bands touch at the K and K' points, the j=0 Landau level is shared equally between electrons and holes, whereas in parabolic bands, the first LL is shifted by $\hbar eB/2m^*$. These peculiarities of the Dirac Fermions lead to anomalous quantum hall effect (QHE) with half–integer quantization of the Hall conductivity, instead of an integer QHE. The Hall conductivity, σ_{xy}, in single-layer graphene shows a plateau quantized at $\frac{4e^2}{h}\left(j + \frac{1}{2}\right)$ as a function of carrier density, n_s, at a fixed magnetic field or as a function of B at a fixed n_s. Another interesting feature is that the splitting between the LLs (j=0 and j=1) is 240 meV at 45 T which makes the observation of QHE possible at room temperature.[47]

For bilayer graphene, the quasi-particles are chiral but with a finite mass. The Landau levels in this case are given by $E_j = \pm\frac{\hbar eB}{m^*}\sqrt{j(j-1)}$, leading to two degenerate levels j=0 and j=1 at zero energy. This results in the absence of the zero energy plateau, $\sigma_{xy} = j.4e^2/h$, where j is an integer except j=0.[48] The opening of a gap in bilayer graphene by the electric field is also reflected in the quantum hall plateaus.[49]

1.5 Phonons and Raman Spectroscopy

Single-layer graphene belongs to the D_{6h} point group which reduces to D_{3d} for the AB bilayer and ABC trilayer and D_{3h} for the ABA trilayer. The zero-wavevector (q=0) optical phonons in single-layer graphene belong to the irreducible representations E_{2g} (R) and B_{2g}, where R and IR refer to Raman and infrared active modes. The eigen vectors of these optical

modes (Figure 8a) show that the E_{2g} mode (degenerate transverse optic (TO) and longitudinal optic (LO)) is an in-plane optical vibration with the frequency ~ 1582 cm^{-1}.[50, 51] The two neighboring atoms vibrate opposite to one another, resulting in large bond distortions. In the B_{2g} mode, the carbon atoms move perpendicular to the graphene plane. For bilayer graphene with AB stacking with 4 atoms per unit cell, the optical modes are $2E_g$ (R) + $2E_{1u}$ (IR) + A_{2u} (IR) + 2 B_{1g}. The eigen-vectors of E_g and E_{1u} are shown in Figure 8b. The IR active E_{1u} mode is slightly higher in frequency (~7cm^{-1}) as compared to the Raman E_g mode.

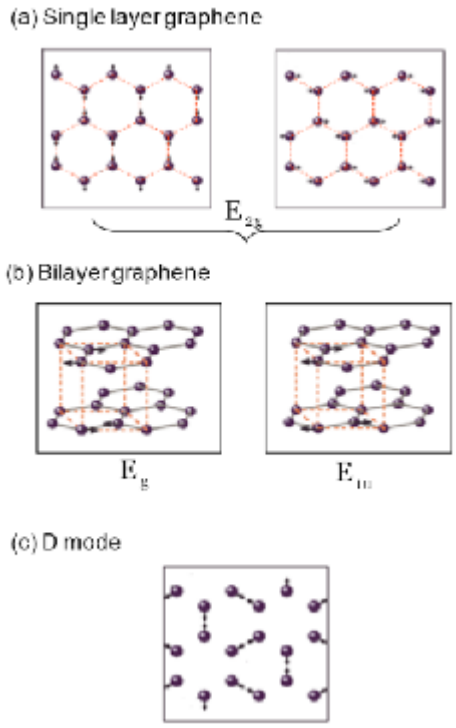

Figure 8. (a) Atomic displacements for the E_{2g} (TO/LO) modes at Γ in monolayer graphene. (b) For bilayer, atomic displacements of E_g (R) and E_{1u} (IR) modes at Γ. Here one mode for each degenerate pair is shown. (c) Atomic displacements for the highest TO mode at K. (Ref. [51]).

Vibrational properties of ultra thin n-layer graphene (n=1-7) have been studied using first-principles density functional theory.[52] It is found that a low frequency optical phonon (~110 cm^{-1}) with out-of-plane displacements exhibits a large sensitivity to the number of layers, although the interlayer spacing does not change appreciably as n varies. This low-frequency mode is yet to be observed experimentally and can prove to be a marker for the number of layers.

Figure 9 shows the phonon dispersion of single-layer graphene using density functional theory.[51] The branch indexed as ZA refers to the out-of-plane acoustic mode which has a q^2-dispersion, in contrast to the linear q dispersion of the longitudinal and

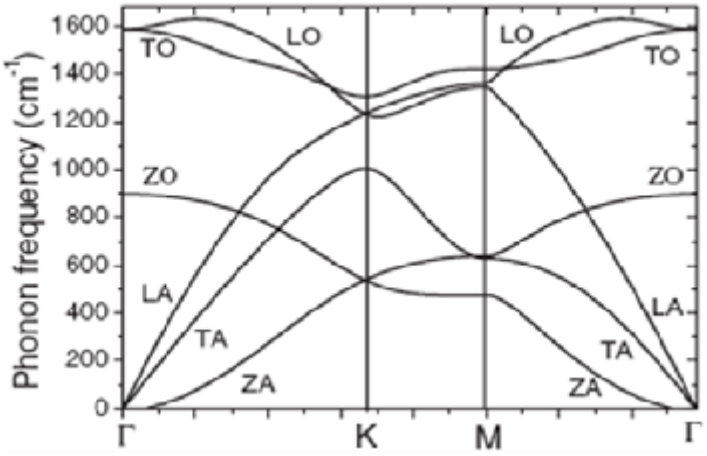

Figure 9. Phonon dispersion for monolayer graphene. (From ref. [51]).

transverse acoustic modes. Many recent calculations have discussed the important issue of electron-phonon coupling in graphene.[53-56] The degenerate E_{2g} phonon at Γ and the highest TO phonon at K have strong electron-phonon interactions, resulting in Kohn anomalies in the phonon dispersion. The Kohn anomaly refers to the anomalous screening of phonons of wavevector **q** which can connect two points $\mathbf{k_1}$ and $\mathbf{k_2}$ on the Fermi surface such that

$\mathbf{k_2} = \mathbf{k_1} + \mathbf{q}$.[57] For graphene and metallic nanotubes, the Kohn anomalies occur at **q= 0** and **q = K.** The eigen vectors of the phonon modes responsible for the Raman D-band transform according to the A_1 and B_1 representations of C_{6v} are shown in Figure 8c.[51] The two sublattice atoms move circularly in opposite directions.

Raman spectroscopy is a powerful probe for characterizing sp^2 and sp^3 carbon materials – be it graphite, diamond-like carbon, diamond, poly-aromatic compounds, fullerenes and carbon nanotubes. Raman fingerprints of single, bi- and few layer graphenes are different and have been investigated by several groups.[58-64] A typical Raman spectrum of single-layer graphene is shown in Figure 10. The symmetry allowed E_{2g} mode at the Γ-point, usually termed as the G-mode, appears at ~1583 cm^{-1}. The other Raman modes seen

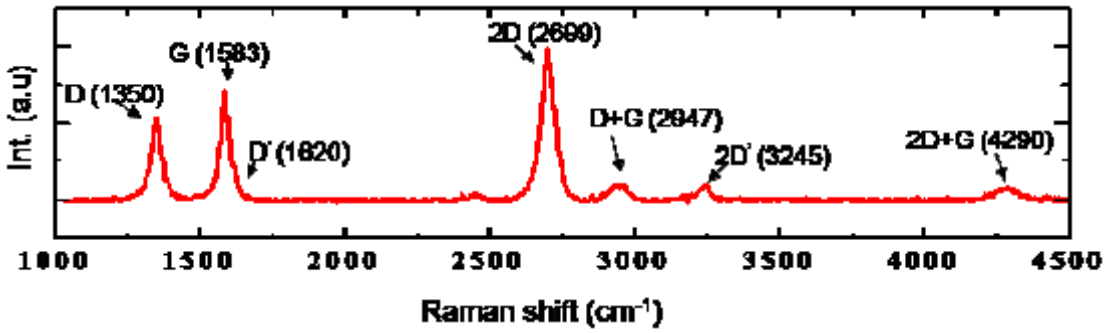

Figure 10. Typical Raman spectrum of single-layer graphene prepared by mechanical exfoliation method. The excitation laser wavelength was 514.5 nm.

are at ~1350 cm^{-1}(D-mode), 1620 cm^{-1}(D'-mode), 2680 (2D or D^*mode), 2950 (D+G), 3245(2D') and 4290 cm^{-1}(2D+G). The mode at ~ 1350 cm^{-1}, termed as the D-mode, is a disorder – activated Raman mode and is associated with the TO – branch near the K-point. Its frequency depends on the incident laser energy (~50 cm^{-1}/eV) and has been

understood[65-68] based on the double resonance Raman process shown in Figure 11. The Raman tensor can be written in fourth order perturbation theory as Eq. (7)

$$R = \sum_{a,b,c} \frac{M_{er} M_{e-def} M_{ep} M_{er}}{(E - E_a - i\gamma)(E - h\omega_p^q - E_b - i\gamma)(E - h\omega_p^q - E_c - i\gamma)} \qquad (7)$$

Here, E_L is the energy of the incident laser photon, M's are the matrix elements and γ is the life-time broadening of the intermediate electronic states a, b and c. Figure 11a shows the four steps involved in defect –assisted Raman process: step one is the electron – radiation interaction with matrix element M_{er}, the second step is the electron-phonon interaction (M_{ep}) making a phonon assisted inter-valley transition, the third step is defect-assisted transition

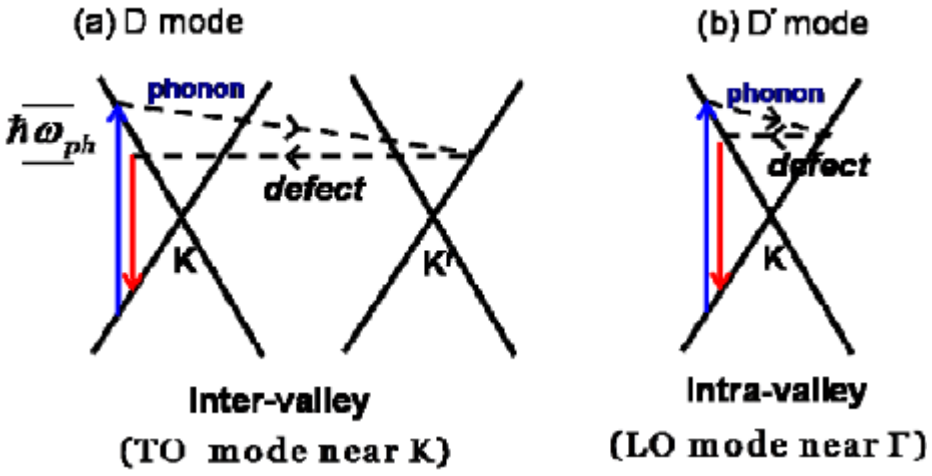

Figure 11. Double resonance Raman scheme for the (a) D and (b) D' modes. Vertical solid lines represent interband electronic transitions accompanied by photon absorption or emission. Dashed arrow represents phonon emission and horizontal dotted line represents the defect scattering.

$M_{e\text{-}def}$ to take care of the momentum conservation and the fourth step is the electron-radiation interaction. In the double resonance Raman process, the phonon with wavevector **q** is so

chosen that the energy denominator is minimum. A change in the incident photon energy results in choosing a phonon of different wavevector on the TO-branch and hence the shift in the D-mode frequency arises due to the dispersion of the phonon branch near the K-point of the Brillouin zone. The mode at ~1620 cm^{-1}, termed as D', also arises due to the double resonance process, involving intra-valley scattering involving LO phonon near the Γ – point (Figure 11b).

The mode at ~ 2680 cm^{-1} is the second – order Raman scattering involving TO phonons near the K-point. It is labeled as the D* or 2D mode. Unlike the D-band, disorder is not required for the wavevector conservation because two-phonons of equal and opposite momentum can satisfy the Raman requirement of q~0. Hence, one can observe the 2D band in the Raman spectra, even though the D-mode is absent (See Figure 13). Like the D-band, this Raman band is highly dispersive with incident photon energy (~100 cm^{-1}/eV), almost twice of the dispersion of the D-band. Double resonance Raman scattering shown in Figure 12a can quantitatively explain the dependence of the 2D Raman band frequency on the laser

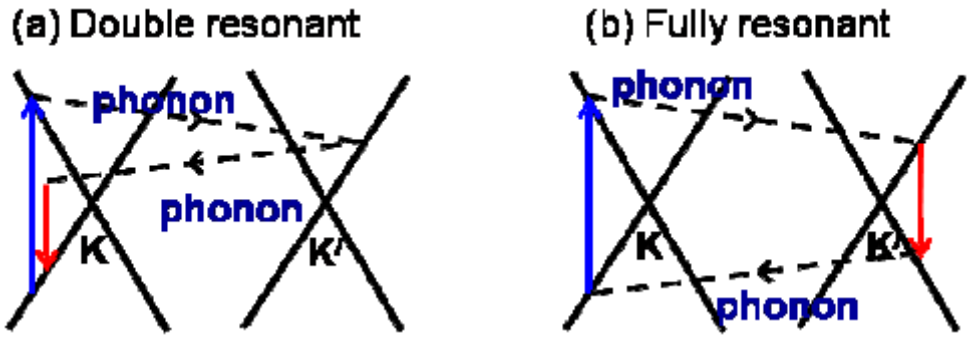

Figure 12. Double resonance Raman process for the two-phonon Raman scattering. Notation same as in Figure 11.

photon energy. It has been pointed out[65, 66] that the Raman process shown in Figure 12b, labeled fully resonant, is more dominant than the double resonance process. In bilayer

graphene, the electronic dispersion is different from that in single-layer graphene (See Figure 7c) and hence the shape of 2D band is different from that in single-layer graphene.[60, 61] Figure 13 shows the comparative Raman spectra of mono- and bi-layer graphenes along with

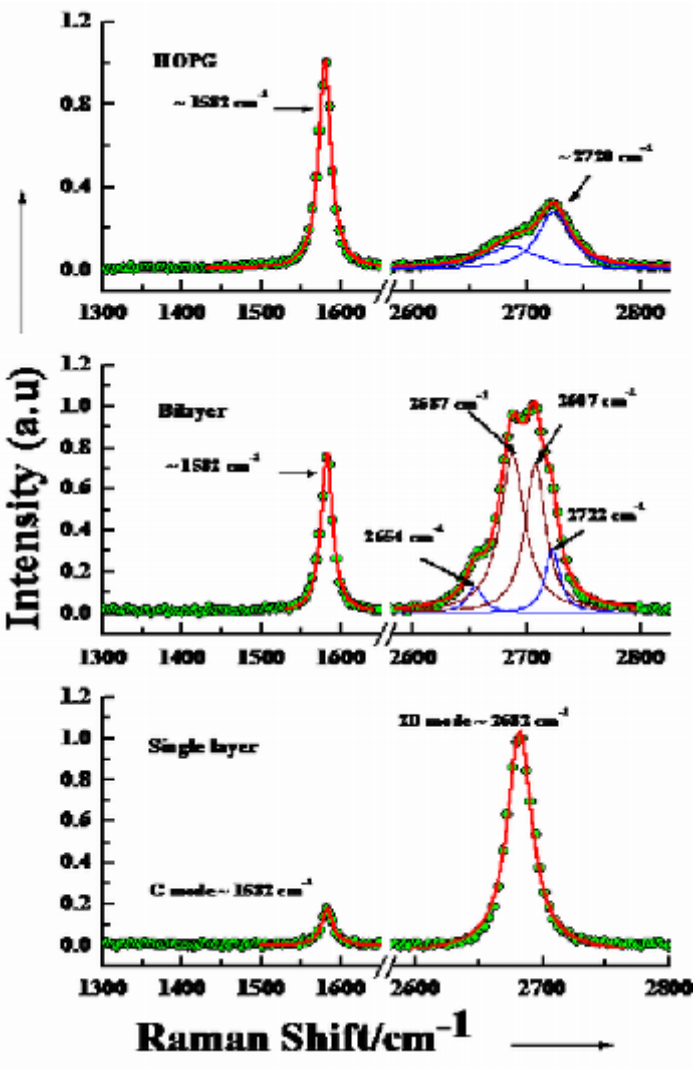

Figure 13. Raman spectra of single-layer graphene and bilayer graphene prepared by mechanical exfoliation of HOPG. Note that even though the D-mode is absent in graphene samples, the 2D mode is strong. The 2D band in bilayer graphene is deconvoluted into 4 bands arising due to double resonance processes. (From ref. [63]).

the spectrum of HOPG. Ferrari *et al*.[60] have shown that the 2D band in bilayer graphene can be decomposed into 4 bands arising from the different phonon assisted inter-valley transitions shown in Figure 14. It is found[63] that the position of the Raman G-band in mechanically exfoliated single-layer graphene varies from 1582 cm^{-1} to ~ 1594 cm^{-1}. The line-width also varies from ~20 cm^{-1} to 14 cm^{-1}. Figure 15 shows the variation of the G-mode frequency ω_G and its full width at half-maximum (FWHM) as a function of the intensity ratio of the D and G modes, I_D/ I_G. The latter is a measure of the disorder in the sample, which can be edges, charge puddles, ripples or any other defects. The data in Figure 15 reflects the unintentional charge doping of the graphene by defects. The intensity of D-band is related to the edge chirality.[67] It is weak at the zigzag edge and strong at the arm-chair edge.

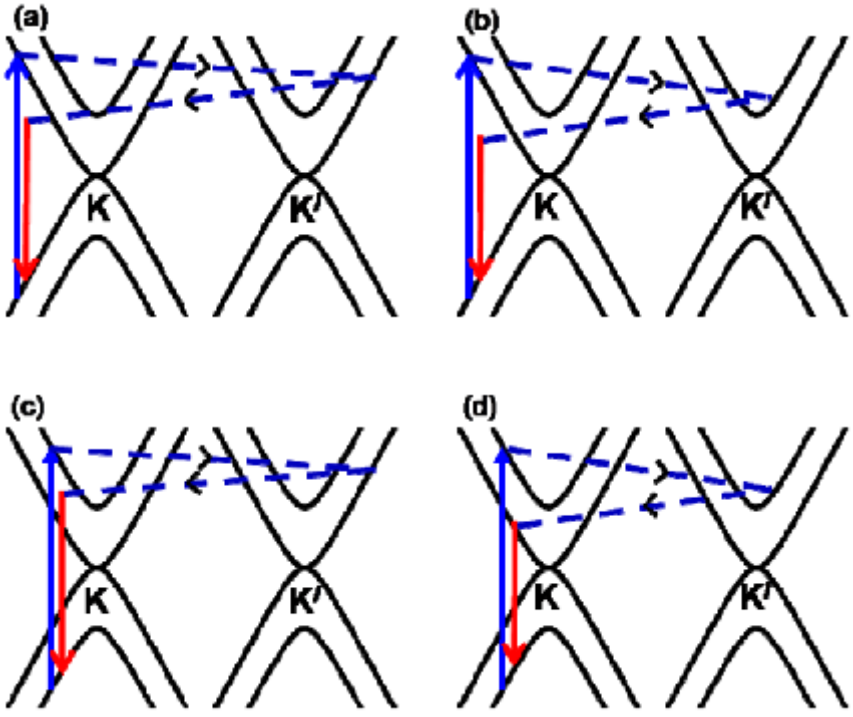

Figure 14. Schematic representation of all the four possibilities in a double resonance Raman process. The solid vertical lines are electronic transitions and dotted lines represent emission of phonons.

Raman spectra are routinely used to characterize graphene samples. The shift and splitting of Raman modes can be used to determine the strain in graphene layers. Raman spectra of epitaxial graphene layers grown on SiC show a significant blue shift of the G-band (~20cm^{-1}) and 2D bands (~60cm^{-1}) as compared to graphene prepared by micromechanical clevage.[68, 69] This mainly arises due to compressive strain that builds up when sample is cooled down after annealing.

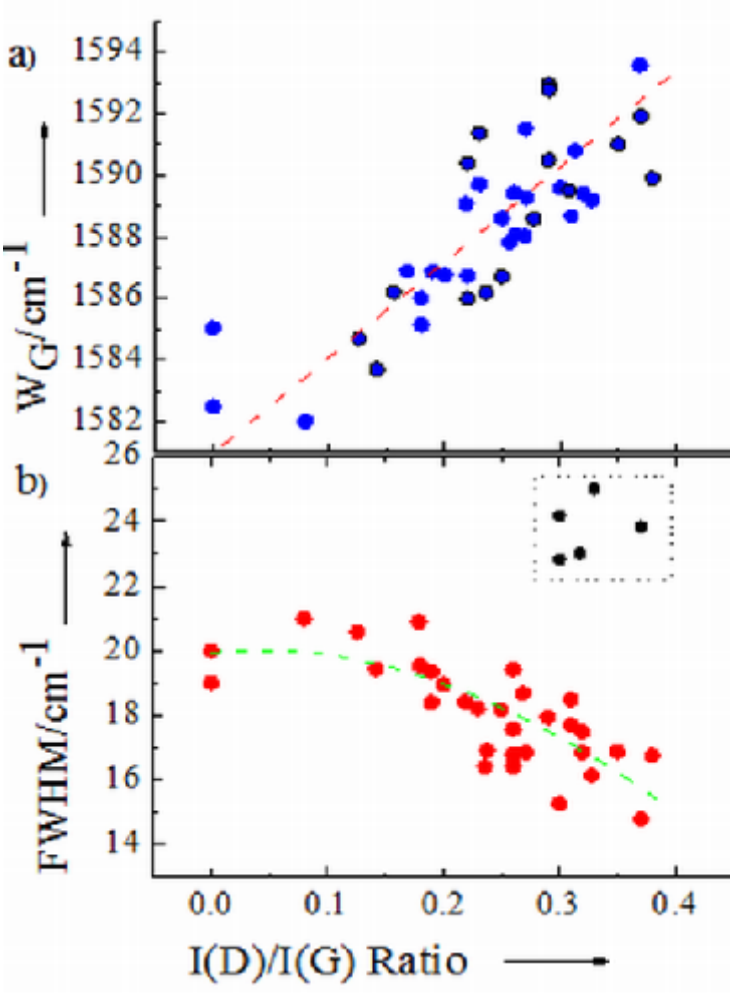

Figure 15. Peak position of G-mode, ω_G, and its FWHM of different samples of single-layer graphene as a function of the I_D/I_G ratio. The dashed lines are guide to the eye. (From ref. [63]).

In graphene monolayer under uniaxial strain, the doubly degenerate E_{2g} mode splits into two components – one polarized along the strain and the other perpendicular to it.[70, 71] This results in splitting of the G-band into two bands G^+ and G^- which are red shifted for the uniaxial tensile strain. The red shifts for 1% strain are ~11cm^{-1} for G^+ band, ~32cm^{-1} for G^- band.[72] For the 2D band, the corresponding shift is ~64 cm^{-1}, which can also have contributions from the changes in the phonon wavevector arising from relative movement of the Dirac cones.[72] This can contribute to the asymmetric broadening of the 2D band.

1.1.6 Graphene nanoribbons

Depending on the width and edge configuration, graphene nanoribbons (GNRs) can be either metallic or semiconducting. GNRs narrower than 10 nm can be semiconductors regardless of the edges and excellent candidates for use in electronic devices, such as field-effect transistors.[73] Whereas for larger widths, the properties of the GNRs are mainly dependent on the edge configurations. Graphene nanoribbons with controlled widths were prepared by unzipping carbon nanotubes (Figure 16). In this process, multiwalled carbon nanotubes comprising 15–20 concentric cylinders were intercalated with concentrated sulfuric acid and potassium permanganate at room temperature and heated at 55–70 °C. This process yielded nanoribbons up to 4 micrometres long, with widths of 100–500 nanometres and thicknesses of 1–30 graphene layers. GNRs were also prepared by employing different procedures such as lithography, chemical and sonochemical synthetic methods, chemical vapor deposition and micromechanical cleavage.[74]

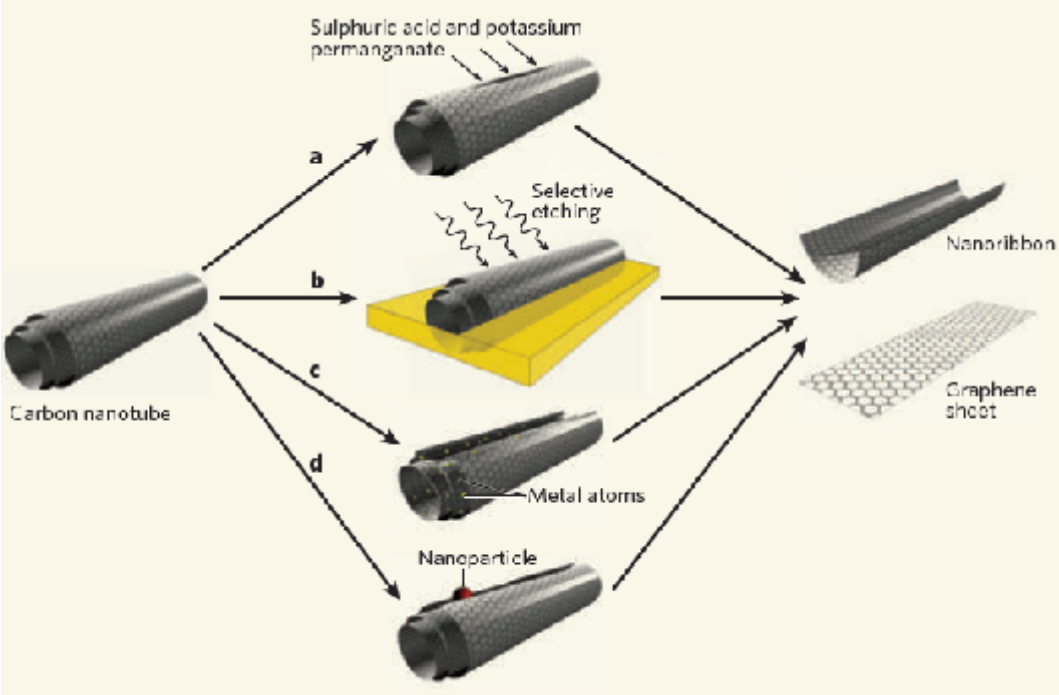

Figure 16. Methods for unzipping carbon nanotubes. (a) Unzipping of multiwalled carbon nanotubes by treating with sulfuric acid and potassium permanganate (an oxidizing agent) to form nanoribbons or graphene sheets. (b) Argon plasma etching of nanotubes embedded polymer film. (c) Insertion of alkali-metal atoms between the concentric cylinders of a multiwalled carbon nanotube, causes graphene sheets to peel off. (d) A method still to be explored would use catalytic metal nanoparticles to cut along the length of a nanotube like a pair of scissors. (From ref. [73]).

1.1.7 Graphane

Graphane is a "hypothetical" two-dimensional polymer of carbon and hydrogen with a hexagonal network. All the carbon atoms in graphane are sp^3 hybridized and the hydrogen atoms are bonded to carbon on both sides of the plane in an alternating manner. First-

principles calculations predicted that graphane is stable and that its binding energy is comparable to benzene, cyclohexane, and polyethylene.

Hydrocarbons are the simplest organic compounds containing only carbon and hydrogen.[75] Some of them naturally occur in the form of crude oil and natural gas and others are synthesized. Hydrocarbons are usually good fuels. They are readily oxidized to produce carbon dioxide and water, with a considerable release of energy. All known hydrocarbons, until now, are molecules with a linear or cyclic carbon backbone. In contrast to existing hydrocarbons, graphane is an extended two-dimensional system, containing covalent C-H bonds. It is predicted to be a semiconductor, because of its novel structure and low dimensionality. Fully fluorinated analog of graphane, poly-(carbon monofluoride) with formula CF, has been synthesized earlier.[76] Since fluorine is known to replace hydrogen in many hydrocarbons, the existence of this fully fluorinated form extends further support to the prediction of this new material.

Graphane has two favorable conformations, one is a chair-like conformer and the other is a boat-like conformer. In chair-like conformer, hydrogen atoms are bonded on both sides of the plane in an alternating manner whereas in boat-like conformer, hydrogen atoms are bonded in an alternating manner as pairs (Figure 17). In the chair conformer, the calculated C-C bond length is 1.52 Å which is similar to the sp^3 bond length of 1.53 Å in diamond and is much greater than 1.42 Å, characteristic of sp^2 carbon in graphene. The boat conformer has two different types of C-C bonds: C-C bonds connected to hydrogen atoms on opposite sides of the plane with a bond length of 1.52 Å and C-C bonds connected to hydrogen atoms on the same side of the plane with a slightly longer bond length of 1.56 Å, due to H-H repulsion.[77] The C-H bond length in both conformers is ~ 1.1 Å which is

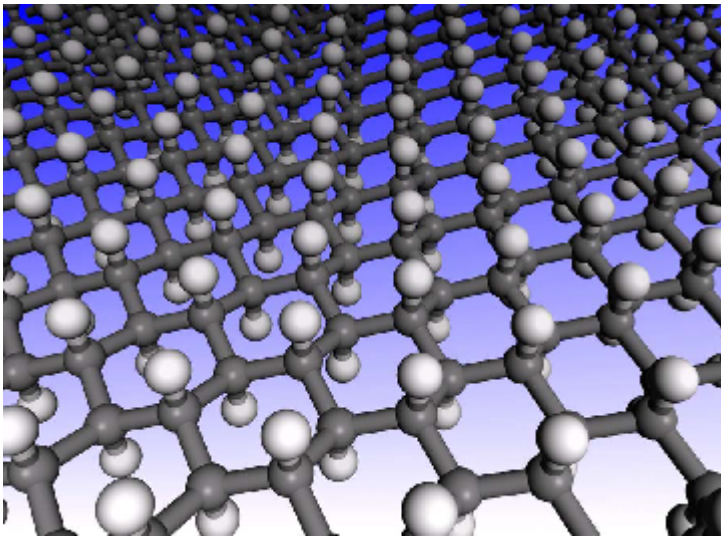

Figure 17. Structure of graphane in the chair conformation. The carbon atoms are shown in gray and the hydrogen atoms in white. The figure shows the hexagonal network with carbon in the sp^3 hybridization. (From ref. [77]).

typical for C-H bonds in hydrocarbons. Graphane bonds are fully saturated and there is no opportunity for hydrogen bonding between the sheets.

Ryu *et al*. have experimentally shown that the reaction of single-layer graphene with hydrogen atoms generates sp^3 C-H bonds on the basal plane and the reduced material gets dehydrogenated on photothermal heating.[78] In their experiments graphene samples coated with hydrogen silsesquioxane (HSQ) (30 nm thick) were irradiated with 30 keV electrons at various doses (0.5~8 mC/cm^2). In another approach, Elias *et. al*.[79] have employed hydrogen plasma to produce hydrogenated graphene samples. In this process, graphene samples deposited on silicon substrate were exposed to hydrogen plasma ignited between two aluminum electrodes. It has been also shown that the reaction with hydrogen is reversible, the original metallic state, the lattice spacing, and even the quantum Hall effect could be restored after annealing.

1.2 Applications

1.2.1Batteries

Owing to its reversibility and reasonable specific capacity graphite is generally employed as an anode material in Li-ion batteries (Figure 18). However, new electrode materials with higher capacity and stability need to be developed for Li-ion batteries to achieve higher energy density and durability. Graphene has been considered as one of the promising anodic materials in Li-ion batteries, as it has good electrical conductivity, high

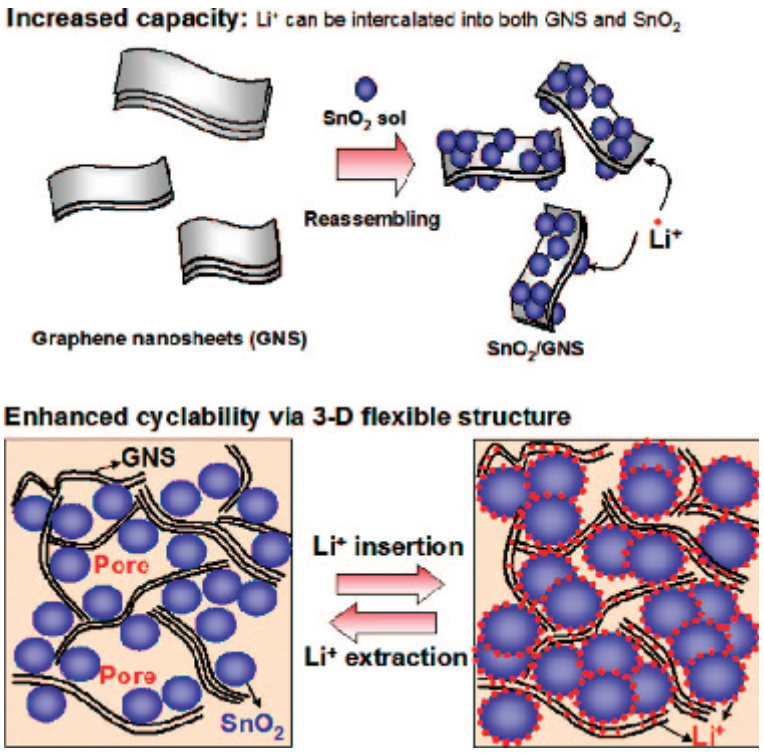

Figure 18. Schematic illustration of synthesis and structure of SnO_2/graphene for battery application. (From ref. [74]).

surface area and chemical tolerance.[80, 81] Song *et al*.[82] have reported that graphene exhibits a relatively high reversible capacity of 672 $mAhg^{-1}$, having much enhanced cycling performance relative to graphite. The capacity and cycle performance of Li-ion battery has

been further improved using graphene based hybrid nanostructures as electrodes.[74, 83] Typical examples of those nanostructures employed are TiO_2, SnO_2, CNTs, Co_3O_4 and $Co(OH)_2$ (Figure 18). It was suggested that the synergetic effect between two components in hybrid nanostructures might be responsible for their improved performance due to the maximum utilization of electrochemically active area of graphene.

1.2.2 Transparent conducting electrodes

Transparent conducting films are an essential part of many electronic gadgets. Generally, thin metal or metal oxide films (ITO, In_2O_3: Sn) are used for these purposes.[84] However, high cost, limited supply and brittleness of these materials hamper their use in flexible substrates, resulting in a search for new types of materials.[85] Recently carbon nanotube films have been used as an alternative transparent conductor in various photonic devices including electric-field-activated optical modulators,[86] organic solar cells[87] and liquid crystal displays.[88] After its discovery, graphene has drawn attention as a possible potential transparent electrode material due to its extraordinary thermal, chemical and mechanical stability combined with its high transparency and atomic layer thickness. The high hole transport mobility, large surface area and inertness against oxygen and water poses graphene as a promising candidate for photovoltaic applications. Monolayer graphene is highly conductive and highly transparent (absorbs only 2.3% of white light), making it useful as transparent electrodes for dye-sensitized solar cells (DSSC).[81] Composites of graphene and poly (3,4-ethylenedioxythiophene) (PEDOT-PSS) as a counter electrode have shown high transmittance (>80%) and high electro catalytic activity, resulting in 4.5% overall energy conversion efficiency. Transparent graphene film was also reported to be used for organic solar cells.[89] It acts as an excellent acceptor material for favoring more efficient

electron–hole separation. Initially, Chen *et al*.[90] fabricated photovoltaic devices employing an organic solution-processed graphene as a new electron-accepter material and poly- (3-hexylthiophene) (P3HT) and poly (3-octylthiophene) (P3OT) as donor materials (Figure 19). Later on, inorganic–organic hybrid solar cells were fabricated using ZnO and graphene nano composite. Li *et al*.[91] have fabricated a photovoltaic device using graphene/QDs nanofilm in which graphene as acceptor exhibited the best performance of all the reported carbon/QD solar cells. Foldability of graphene films deposited on a polyethylene terephthalate (PET) substrate (thickness, 100 μm) coated with a thin polydimethylsiloxane (PDMS) layer (thickness, 200 μm) was evaluated by measuring resistance as a function of bending radii.[92]

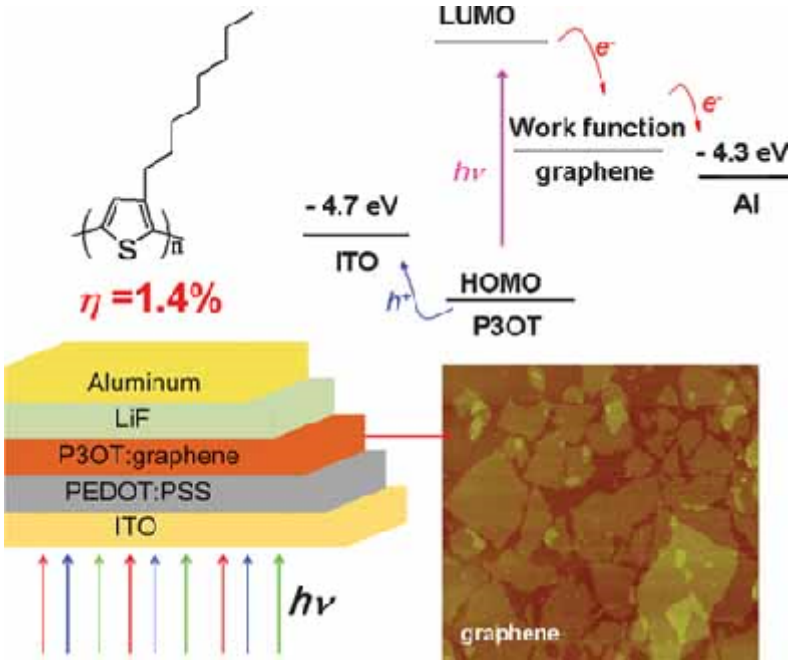

Figure 19. Schematic of the device with P3OT/graphene thin film as the active layer and the structure ITO (ca. 17Ω sq^{-1})/PEDOT:PSS (40 nm)/P3OT:graphene (100 nm)/LiF (1 nm)/Al (70 nm) and energy level diagram of P3OT and graphene. (From ref. [91]).

The resistance show little variation up to the bending radius of 2.3 mm (approximate tensile strain of 6.5%) and are perfectly recovered after unbending. Jang and coworkers[93] employed inkjet printing and vapour deposition to deposit graphene oxide onto poly (vinylidene fluoride) (PVDF), which is then reduced to create a graphene film. This new method of making controlled graphene films has been employed to fabricate thin transparent loudspeakers (Figure 20). The speaker system consists of a PVDF thin film sandwiched between two graphene electrodes. A converse piezoelectric effect arising from the application of an electrical current from the sound source distorts the PVDF film, and thus creates sound waves. Although similar speakers using PEDOT:PSS electrodes are already available in market, the new system has advantages over the existing technology in terms of

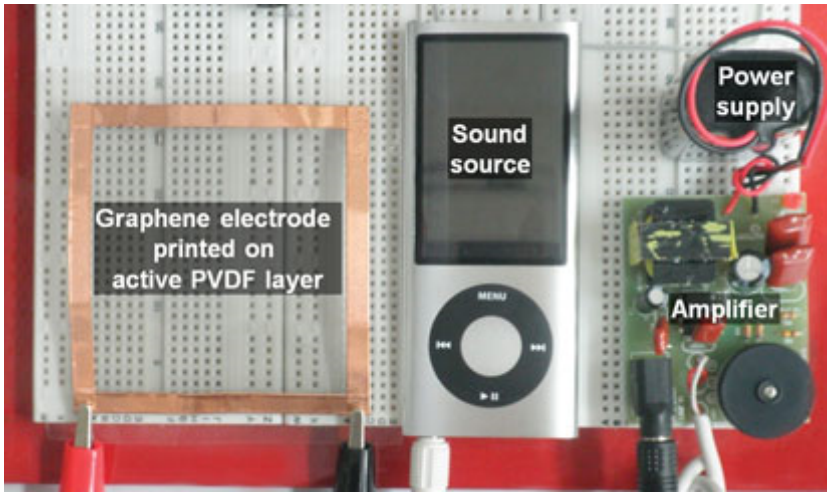

Figure 20. Photograph of a poly (vinylidene fluoride)-based thin film acoustic actuator using flexible and transparent graphene electrodes. (From ref. [94]).

cost and power consumption. Graphene is cheaper than other electrodes such as metals and conducting polymers, besides, the graphene-based acoustic actuator does not need expensive high power voltage amplifiers due to low power consumption.

1.2.3 Composites

Graphite is soft and flaky, and cannot be used in load-bearing structures. This problem could be solved by making a composite material of graphene sheets and polymers. The manufacturing of such composites requires not only that graphene sheets be produced on a sufficient scale but that they also be incorporated, and homogeneously distributed, into various matrices. Unfortunately, owing to their hydrophilic nature, graphene oxide sheets can only be dispersed in aqueous media that are incompatible with the most organic polymers. In addition, graphite oxide is electrically insulating, unlike graphite, which limits its usefulness for the synthesis of conductive nanocomposites. It has been demonstrated,[94, 95] however, that the electrical conductivity of graphite oxide can be significantly increased by chemical reduction, presumably owing to the restoration of a graphitic network of sp^2 bonds. Processing of nanographene platelets to produce composites has been briefly reviewed by Jang *et al*.[96] Polyacrylonitrile nanofibers reinforced by graphite nanoplatelets have been prepared and have improved mechanical properties.[97] Hansma *et al*.[98] indicated how a combination of adhesives and high-strength structures such as graphene and carbon nanotubes can yield strong, lightweight, and damage-resistant materials. Ramanathan *et al*.[99] reported that 1 wt% of functionalized graphene sheets in poly(acrylonitrile) increases the glass transition temperature (T_g) of the polymer by over 40 ºC and an increase of nearly 30 ºC is observed with only 0.05 wt% of graphene in poly(methyl methacrylate) (PMMA). An addition of approximately 1 wt% of graphene to PMMA leads to an increase in the elastic modulus by 80% and in the ultimate tensile strength by 20%. A comparative study by these workers shows that among all the nano-filler materials considered, single-layer functionalized graphene gives the best results. Das *et al*.[100]

have studied the mechanical properties of polyvinyl alcohol (PVA) and PMMA composites reinforced by functionalized few-layer graphene by employing the nanoindentation technique. The addition of 0.6 wt% of the graphene results in a significant increase in both the elastic modulus and hardness. The crystallinity of PVA also increases with the addition of few-layer graphene. An observed improvement in the mechanical properties of the polymers is suggested to have arisen from the good mechanical interaction between the polymer and the few-layer graphene, which in turn, provides better load-transfer between the matrix and the fiber. Epoxy composites of few-layer graphene show very interesting properties which are useful for the development of thermal interface materials for electronic packaging and advanced composites.[101] A loading of nearly 25 vol% of graphene into epoxy matrix enhances the thermal conductivity by more than 3000%. This surpasses the performance of conventional fillers that require a loading of nearly 70 vol% to achieve the same thermal conductivity.

Booth *et al.*[102] have prepared graphene membranes having diameter of 100 mm. They exhibit high stiffness and support large loads. Atomic simulation has been employed to investigate the elastic properties of single-layer graphene.[103] Metal nanoparticles have been mechanically entrapped between graphene sheets to facilitate better contact between the particles and the polymer matrix.[104] Transparent and electrically conductive graphene–silica composite films have been fabricated by incorporating graphene oxide sheets into silica sols followed by spin-coating, chemical reduction, and thermal curing.[105] Polystyrene–graphene composites with a conductivity of 0.1 Sm^{-1} at only 1 vol% have been reported to exhibit a percolation threshold of 0.1 vol% for room temperature electrical conductivity.[106] An another interesting composite of graphene is the electrically conducting graphene paper. It is

not only biocompatible but also mechanically strong (Figure 21).[107] The paper has been prepared by directional flow induced assembly of graphene sheets dispersed in solution. The graphene composites could be very useful: for example, in the manufacture of fuselages for aircraft, which must combine low weight, high strength and electrical conductivity. This last property is necessary for protection against lightning strikes while in flight. The potential

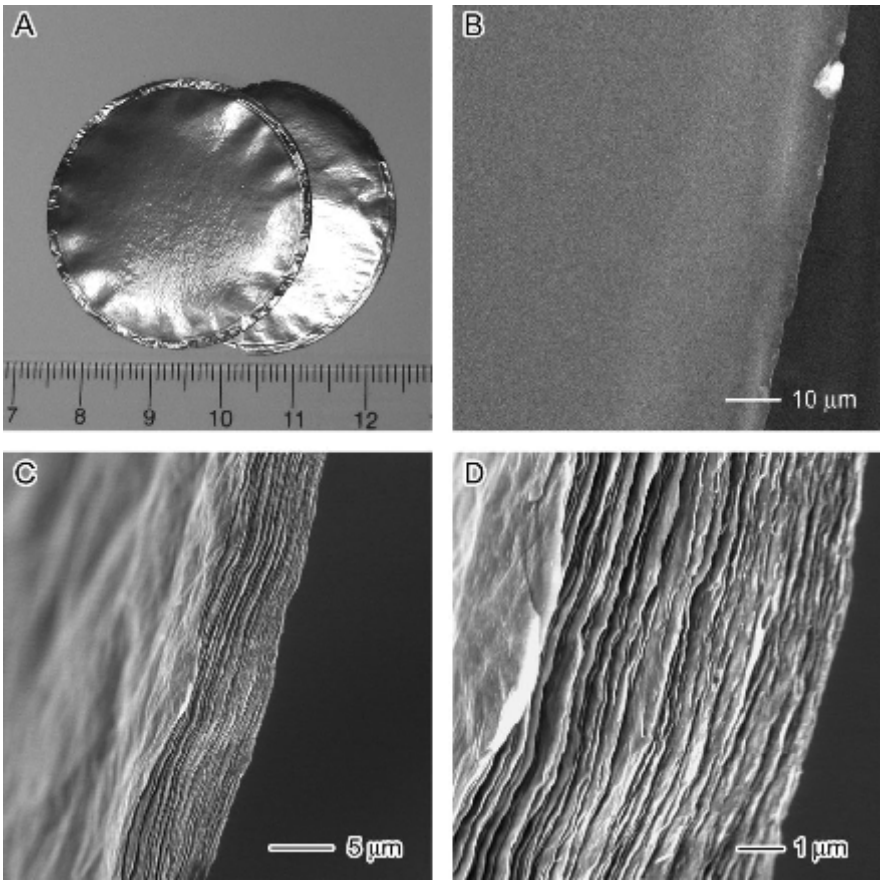

Figure 21. (A) Photograph of two pieces of free-standing graphene paper fabricated by vacuum filtration of chemically prepared graphene dispersions, followed by air drying and peeling off the membrane. Front and back surfaces shown. (B) Top-view scanning electron microscope (SEM) image of a graphene paper sample showing the smooth surface. (C,D) Side-view SEM images of a ca. 6mm thick sample at increasing magnification. (From ref. [108]).

properties of these graphene sheet-based composites thus appear promising due to the extremely high aspect ratios (the average lateral dimension of ~ 1 mm) of the graphene sheets. The intrinsic mechanics of the sheets: their crumpling, wrinkling and folding, and whether they can be processed to be non-crumpled sheets (so that layering could be more effectively achieved) are important issues for further study.

1.2.4 Sensors

In many applications, solid-state gas sensors have been widely employed due to their high sensitivity, low production costs and miniature sizes.[108, 109] Recently, gas sensors using carbon nanotubes and semiconductor nanowires have also been demonstrated.[110, 111] The ultimate goal of any detection method is to attain the level of sensing even single atom or molecule. Such resolution has so far been beyond the reach of any detection technique, including solid-state gas sensors known for their exceptional sensitivity. The main reason for the limitation is fluctuations due to thermal motion of charges and defects,[112] which leads to intrinsic noise exceeding the sought-after signal from individual molecules, usually by many orders of magnitude. But the micrometer-size sensors made from graphene are capable of detecting even individual molecules. Such gas sensors rely on the change in their electrical conductivity.[113] The observed change in conductivity arises due to a change in the carrier concentration of graphene, caused by adsorbed gaseous molecules acting as donors or acceptors. Some interesting properties of graphene render its sensitivity up to single atom or molecule level detection. First, as graphene is a two-dimensional (2D) material all carbon atoms in the plane are exposed to the analyte of interest.[114] Second, graphene is highly conductive with low Johnson noise (electronic noise generated by the thermal agitation of the charge carriers inside an electrical conductor at equilibrium, which happens irrespective of

any applied voltage), therefore, a little change in carrier concentration can cause a marked variation in electrical conductivity.[114] Third, graphene has very few crystal defects,[15, 44, 115] ensuring a low level of noise caused by thermal switching. Finally, four-probe measurements can be made on a single-crystal graphene device with ohmic electrical contacts having low resistance.[114] All these features contribute to maximize the signal-to-noise ratio to a level sufficient for detecting changes in a local concentration by less than one electron charge, e, at room temperature. Since the first report on graphene sensing by Schedin *et al*.[114] in 2007, sensing properties of graphene have been examined by several groups. Graphene showed good sensing properties towards NO_2, NH_3, H_2O and CO (Figure 22) and sensing properties were fully recoverable. In addition to NO_2 and NH_3, dinitrotoulene (DNT), a volatile compound found in explosives, was also detected.[116] The sensing mechanism in case of NO_2 and NH_3 was attributed to hole induced conduction and electron induced conduction respectively. The sensing mechanism was primarily attributed to charge-transfer at the graphene surface.[116] Dinitrotoulene sensing mechanism was similar to that of NO_2 and the limit of detection of dinitrotoulene was reported to be 28 ppb.

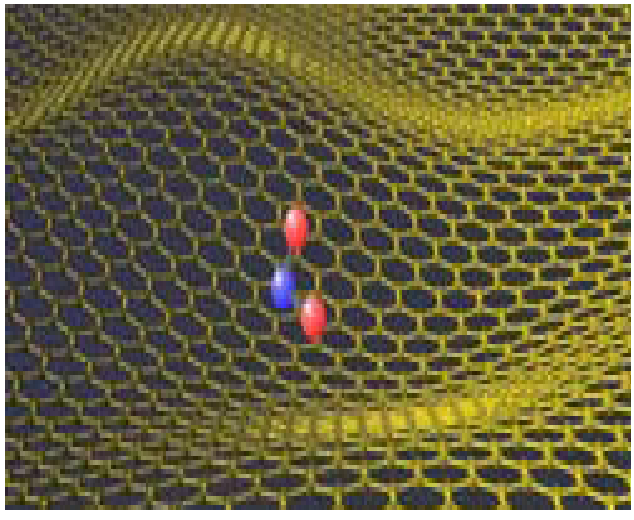

Figure 22. Graphene sheets could detect just a single molecule of nitrogen dioxide.

Ghosh *et al*.[117] have studied the sensor characteristics of thick films made of few-layer graphenes for NO_2, H_2O and aliphatic alcohols. Good sensitivities were observed for NO_2 and H_2O, and the sensitivity was mainly found to be affected by boron or nitrogen doping. Gas-sensing properties of graphene sheets deposited on $LiTaO_3$ substrates have been reported.[118] Glucose sensors based on graphene have been reported.[119, 120] With glucose oxidase (GOD) as an enzyme model, Shan *et al*. constructed a novel polyvinylpyrrolidone protected graphene/polyethylenimine-functionalized ionic liquid/GOD electrochemical biosensor. Through the sensor, they reported direct electron transfer of GOD, demonstrating graphene's potential application for fabrication of glucose sensors. A linear response up to 14 mM of glucose was observed by them. [120] The possibilities of single-layer graphene to act as a mass sensor and an atomic dust detector have also been indicated.[121]

Graphene chemically modified by electrodeposition of Pd nanoparticles[122] has been reported to show good response for H_2 sensing, as Pd has good affinity towards H_2. DFT calculations show that aluminum-doped graphene strongly chemisorbs CO molecules, forming Al-CO bonds. Thus, aluminum-doped graphene is expected to be a potential candidate for the detection of CO.[123] Chemically modified graphene has been used in bioelectronics as a sensor at both the microbial and the molecular level.[124] It acts as an interface to recognize single bacteria, a label-free, reversible DNA detector, and a polarity-specific molecular transistor for protein/DNA adsorption.

1.2.5 Field emission properties

Field emission (FE) is an electron emission process in which electrons are emitted from a material under the application of high electric field. Such a high field is created by field enhancement at the tip of a sharp object. Recently, a graphene/polymer composite thin

film has been fabricated for achieving a field enhancing structure, required for FE applications.[125] The FE cathodes were prepared by dissolution of graphene in polystyrene, followed by spin coating on to silicon substrates.[125] The orientation of the graphene sheets in the composite thin films was varied by controlling the spin coating speeds. Relatively better FE was observed from films prepared at a spin coating speed of 600 rpm; the turn-on electric field (E_{to}) in such sample was ~4 V/μm and the field enhancement factor (β) was ~1200. Wu *et al*.[126] have prepared graphene films by electrophoretic deposition (EPD) method. In this process, graphene films, generated by exfoliation of graphite, were dispersed in isoprophyl alcohol and the resulting solution was deposited onto indium tin oxide (ITO) coated glass substrates by EPD. Graphene cathodes prepared by this method demonstrated an E_{to} of 2.3 V/μm and a β of ~3700. Malesevic *et al*.[127] demonstrated microwave plasma enhanced chemical vapor deposition (MW-PECVD) to fabricate vertically aligned few-layer graphene (FLG) FE cathodes on titanium and silicon. Few-layer graphene was synthesized by MW-PECVD with H_2 and CH_4 precursor gases, at 700 °C. The quality of few-layer graphene films was observed to be dependent on the ratio of H_2/CH_4 gases; best quality was achieved when the ratio was 8:1. Graphene cathodes prepared by this method demonstrated an E_{to} of 1 V/μm, β of ~7500 and a current density of 14 mA/cm^2 (Figure 23). The advantage of this method is direct synthesis of graphene on metallic substrates, thus creating ohmic contacts, which are essential for FE applications. Moreover, no further processing is required. The drawback of this method is the limited scope to control the few-layer graphene (FLG) density, which can cause field-screening effect. However, it might take a while to demonstrate a real FE device, which can reach the market.

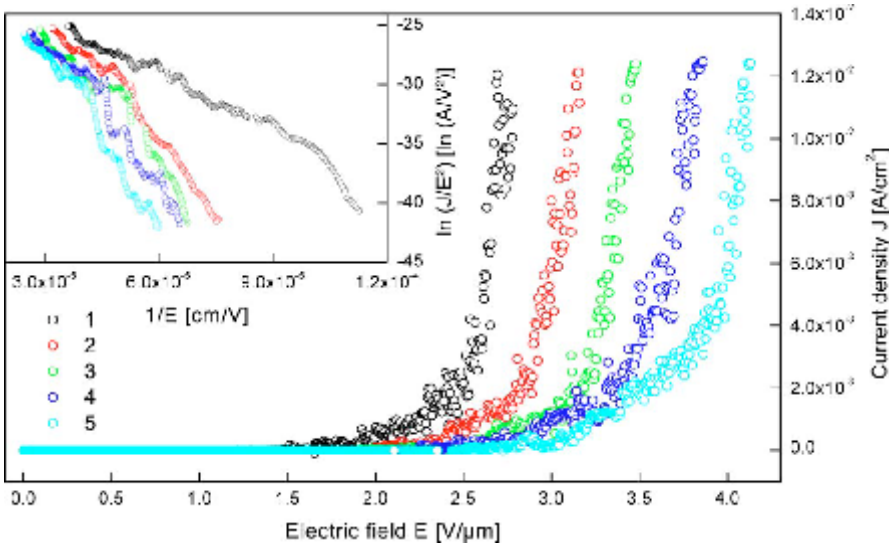

Figure 23. Current density as a function of applied electric field for few-layer graphene (FLG) grown on silicon with gas ratio H_2 /CH_4=8/1. The results are shown for five voltage cycles without exposure to air in between each cycle and maintaining a constant vacuum. The inset visualizes the same data, plotted according to the Fowler-Nordheim relation (FN) relation. (From ref. [128]).

1.2.6 Support membrane for transmission electron microscopy

Graphene is effectively the thinnest material that we can make out of atoms. Surprisingly, it is also very strong, thanks to a lack of crystal boundaries to break along and very strong bonds between carbon atoms (carbon nanotubes are made from rolled up graphene, and it has been suggested that cabling made from nanotubes would be strong enough to create an elevator into space). As a result, we can use it to hold micro- and nanoscopic objects to look at in an electron microscope (e.g. DNA, nanoparticles) in a similar way we use glass slides in an optical microscope. Graphene is the perfect material for this, as it is made of only carbon. It is very thin, thus, it will not interfere as much as other

materials, with the TEM images taken. Also, it has a very simple crystal structure so can easily be eliminated from diffraction patterns.

1.2.7 Molecular sieves

The open honeycomb structure of graphene means it might be possible to use it as a net or sieve for atoms and small molecules, since only objects of this size will be able to fit through the lattice. So it could be used in a way analogous to a filter paper, trapping large molecules and allowing smaller ones to pass through.

1.3 Graphene may be the new silicon

Interestingly, graphene is fast replacing silicon (the material at the heart of all computer chips) in electronics. It could allow electronics to process information and produce radio transmissions 10 times better than silicon-based devices. Usage of graphene could produce faster and more powerful cell phones, computers as well as other electronics.

1.4 References

[1] W. A. Fowler, *Rev. Mod. Phys.* **1984**, *56*, 149.

[2] L. Pauling, *The Nature of the Chemical Bond*, Cornell University Press, Ithaca, NY, **1960**.

[3] R. F. Curl, *Rev. Mod. Phys.* **1997**, *69*, 691.

[4] H. Kroto, *Rev. Mod. Phys.* **1997**, *69*, 703.

[5] R. E. Smalley, *Rev. Mod. Phys.* **1997**, *69*, 723.

[6] S. Iijima, *Nature* **1991**, *354*, 56.

[7] P. R. Wallace, *Phys. Rev.* **1947**, *71*, 622.

[8] H.P. Boehm, *Angew. Chem. Int. Ed.* **2010**, *49*, 9332.

[9] A. J. van Bommel, J. E. Crombeen, A. van Tooren, *Surf. Sci.* **1975**, *48*, 463.

[10] X. Lu, M. Yu, H. Huang, R. S. Ruoff, *Nanotechnology* **1999**, *10*, 269.

[11] C. Roscoe, J. M. Thomas, *Proc. R. Soc. London Ser. A* **1967**, *297*, 397.

[12] K. S. Novoselov, A. K. Geim, S. V. Morozov, D. Jiang, Y. Zhang, S. V. Dubonos, I. V. Grigorieva, A. A. Firsov, *Science* **2004**, *306*, 666.

[13] K. S. Novoselov, A. K. Geim, S. V. Morozov, D. Jiang, M. I. Katsnelson, I. V. Grigorieva, S. V. Dubonos, A. A. Firsov, *Nature* **2005**, *438*, 197.

[14] K. S. Novoselov, D. Jiang, F. Schedin, T. J. Booth, V. V. Khotkevich, S. V. Morozov, A. K. Geim, *Proc. Natl Acad. Sci. USA* **2005**, *102*, 10451.

[15] A. K. Geim, K. S. Novoselov, *Nat. Mater.* **2007**, *6*, 183.

[16] P. Blake, E. W. Hill, A. H. Casrto Neto, K. S. Novoselov, D. Jiang, R. Yang, T. J. Booth, A. K. Geim, *Appl. Phys. Lett.* **2007**, *91*, 063124.

[17] B. Partoens, F. M. Peeters, *Phys. Rev. B* **2006**, *74*, 075404.

[18] K. S. Novoselov, D. Jiang, F. Schedin, T. J. Booth, V. V. Khotkevich, S. V. Morozov, A. K. Geim, *Proc. Natl Acad. Sci. USA* **2005**, *102*, 10451.

[19] R. E. Peierls, *Helv. Phys. Acta* **1934**, *7*, 81.

[20] R. E. Peierls, *Ann. Inst. Henri Poincare* **1935**, *5*, 177.

[21] L. D. Landau, *Phys. Z. Sowjetunion* **1937**, *11*, 26.

[22] N. D. Mermin, *Phys. Rev.* **1968**, *176*, 250.

[23] C. Berger, Z. Song, X. Li, X. Wu, N. Brown, C. Naud, D. Mayou, T. Li, J. Hass, A. N. Marchenkov, E. H. Conrad, P. N. First, W. A. de Heer, *Science* **2006**, *312*, 1191.

[24] T. Ohta, A. Bostwick, T. Seyller, K. Horn, E. Rotenberg, *Science* **2006**, *313*, 951.

[25] S. Stankovich, D. A. Dikin, G. H. B. Dommett, K. M. Kohlhaas, E. J. Zimney, E. A. Stach, R. D. Piner, S. T. Nguyen, R. S. Ruoff, *Nature* **2006**, *442*, 282.

[26] J. C. Meyer, A. K. Geim, M. I. Katsnelson, K. S. Novoselov, T. J. Booth, S. Roth, *Nature* **2007**, *446*, 60.

[27] L. D. Landau, E. M. Lifshitz, *Statistical Physics Part I*, Pergamon, Oxford, **1980**.

[28] L. D. Landau, *Zur Theorie der Phasenumwandlungen II. Phys. Z., Vol. 11*, Sowjetunion **1937**.

[29] M. Born, K. Huang, *Dynamical Theory of Crystal Lattices*, Clarendon, Oxford, **1954**.

[30] J. A. Venables, G. D. T. Spiller, M. Hanbucken, *Rep. Prog. Phys.* **1984**, *47*, 399.

[31] M. Zinke-Allmang, L. C. Feldman, M. H. Grabow, *Surf. Sci. Rep.* **1992**, *16*, 377.

[32] J. W. Evans, P. A. Thiel, M. C. Bartelt, *Surf. Sci. Rep.* **2006**, *1*, 61.

[33] D. R. Nelson, L. Peliti, *J. Physique* **1987**, *48*, 1085.

[34] P. Le Doussal, L. Radzihovsky, *Phys. Rev. Lett.* **1992**, *69*, 1209.

[35] D. R. Nelson, T. Piran, S. Weinberg, *Statistical Mechanics of Membranes and Surfaces*, World Scientific, Singapore, **2004**.

[36] R. Saito, G. Dresselhaus, M. S. Dresselhaus, *Physical Properties of Carbon Nanotubes*, Imperial College Press, London, **1998**.

[37] A. H. Castro Neto, F. Guinea, N. M. R. Peres, K. S. Novoselov, A. K. Geim, *Rev. Mod. Phys.* **2009**, *81*, 109.

[38] M. I. Katsnelson, K. S. Novoselov, A. K. Geim, *Nat. Phys.* **2006**, *2*, 620.

[39] M. I. Katsnelson, *Mater. Today* **2007**, *10*, 20.

[40] P. Gosselin, A. Bérard, H. Mohrbach, S. Ghosh, *Eur. Phys. J. C* **2009**, *59*, 883.

[41] E. McCann, V. I. Fal'ko, *Phys. Rev. Lett.* **2006**, *96*, 086805.

[42] H. Min, B. Sahu, S. K. Banerjee, A. H. MacDonald, *Phys. Rev. B* **2007**, *75*, 155115.

[43] J. B. Oostinga, H. B. Heersche, X. Liu, A. F. Morpurgo, L. M. K. Vandersypen, *Nat. Mater.* **2008**, *7*, 151.

[44] K. S. Novoselov, A. K. Geim, S. V. Morozov, D. Jiang, M. I. Katsnelson, I. V. Grigorieva, S. V. Dubonos, A. A. Firsov, *Nature* **2005**, *438*, 197.

[45] Y. Zhang, J. W. Tan, H. L. Stormer, P. Kim, *Nature* **2005**, *438*, 201.

[46] Z. Jiang, Y. Zhang, Y. W. Tan, H. L. Stormer, P. Kim, *Solid State Commun.* **2007**, *143*, 14.

[47] K. S. Novoselov, Z. Jiang, Y. Zhang, S. V. Morozov, H. L. Stormer, U. Zeitler, J. C. Maan, G. S. Boebinger, P. Kim, A. K. Geim, *Science* **2007**, *315*, 1379.

[48] K. S. Novoselov, E. McCann, S. V. Morozov, V. I. Fal'ko, M. I. Katsnelson, U. Zeitler, D. Jiang, F. Schedin, A. K. Geim, *Nat. Phys.* **2006**, *2*, 177.

[49] E. V. Castro, K. S. Novoselov, S. V. Morozov, N. M. R. Peres, J. M. B. Lopes dos Santos, J. Nilsson, F. Guinea, A. K. Geim, A. H. Castro Neto, *Phys. Rev. Lett.* **2007**, *99*, 216802.

[50] S. Reich, C. Thomsen, *Philosophical Transactions of the Royal Society a-Mathematical Physical and Engineering Sciences* **2004**, *362*, 2271.

[51] J.-A. Yan, W. Y. Ruan, M. Y. Chou, *Phys. Rev. B* **2008**, *77*, 125401.

[52] S. K. Saha, U. V. Waghmare, H. R. Krishnamurthy, A. K. Sood, *Phys. Rev. B* **2008**, *78*, 165421.

[53] S. Piscanec, M. Lazzeri, J. Robertson, A. C. Ferrari, F. Mauri, *Phys. Rev. B* **2007**, *75*, 035427.

[54] O. Dubay, G. Kresse, *Phys. Rev. B* **2003**, *67*, 035401.

[55] M. Lazzeri, F. Mauri, *Phys. Rev. Lett.* **2006**, *97*, 266407.

[56] C. H. Park, F. Giustino, M. L. Cohen, S. G. Louie, *Nano Lett.* **2008**, *8*, 4229.

[57] W. Kohn, *Phys. Rev. Lett.* **1959**, *2*, 393.

[58] A. Gupta, G. Chen, P. Joshi, S. Tadigadapa, P. C. Eklund, *Nano Lett.* **2006**, *6*, 2667.

[59] A. C. Ferrari, *Solid State Commun.* **2007**, *143*, 47.

[60] A. C. Ferrari, J. C. Meyer, V. Scardaci, C. Casiraghi, M. Lazzeri, F. Mauri, S. Piscanec, D. Jiang, K. S. Novoselov, S. Roth, A. K. Geim, *Phys. Rev. Lett.* **2006**, *97*, 187401.

[61] M. A. Pimenta, G. Dresselhaus, M. S. Dresselhaus, L. G. Cancado, A. Jorio, R. Saito, *Phys. Chem. Chem. Phys.* **2007**, *9*, 1276.

[62] D. Graf, F. Molitor, K. Ensslin, C. Stampfer, A. Jungen, C. Hierold, L. Wirtz, *Nano Lett.* **2007**, *7*, 238.

[63] A. Das, B. Chakraborty, A. Sood, *Bull. Mater. Sci.* **2008**, *31*, 579.

[64] Z. Ni, Y. Wang, T. Yu, Z. Shen, *Nano Res.* **2008**, *1*, 273.

[65] D. M. Basko, *Phys. Rev. B* **2008**, *78*, 125418.

[66] D. M. Basko, *Phys. Rev. B* **2007**, *76*, 081405.

[67] Y. You, Z. Ni, T. Yu, Z. Shen, *Appl. Phy. Lett.* **2008**, *93*, 163112.

[68] J. Rohrl, M. Hundhausen, K. V. Emtsev, T. Seyller, R. Graupner, L. Ley, *Appl. Phy. Lett.* **2008**, *92*, 201918.

[69] N. Ferralis, R. Maboudian, C. Carraro, *Phys. Rev. Lett.* **2008**, *101*, 156801.

[70] Z. H. Ni, H. M. Wang, Y. Ma, J. Kasim, Y. H. Wu, Z. X. Shen, *ACS Nano* **2008**, *2*, 1033.

[71] T. Yu, Z. H. Ni, C. L. Du, Y. M. You, Y. Y. Wang, Z. X. Shen, *J. Phys. Chem. C* **2008**, *112*, 12602.

[72] T. M. G. Mohiuddin, A. Lombardo, R. R. Nair, A. Bonetti, G. Savini, R. Jalil, N. Bonini, D. M. Basko, C. Galiotis, N. Marzari, K. S. Novoselov, A. K. Geim, A. C. Ferrari, *Phys. Rev. B* **2009**, *79*, 205433.

[73] M. Terrones, *Nature* **2009**, *458*, 845.

[74] S. Guo, S. Dong, *Chem. Soc. Rev.* **2011**, *40*, 2644.

[75] G. A. Olah, Á. Molnár, *Hydrocarbon Chemistry*, Wiley-Interscience, Hoboken, NJ, USA, **2003**.

[76] N. Watanabe, T. Nakajima, H. Touhara, *Graphite fluorides* Elsevier, Amsterdam, **1988**.

[77] J. O. Sofo, A. S. Chaudhari, G. D. Barber, *Phys. Rev. B* **2007**, *75*, 153401.

[78] S. Ryu, M. Y. Han, J. Maultzsch, T. F. Heinz, P. Kim, M. L. Steigerwald, L. E. Brus, *Nano Lett.* **2008**, *8*, 4597.

[79] D. C. Elias, R. R. Nair, T. M. G. Mohiuddin, S. V. Morozov, P. Blake, M. P. Halsall, A. C. Ferrari, D. W. Boukhvalov, M. I. Katsnelson, A. K. Geim, K. S. Novoselov, *Science* **2009**, *323*, 610.

[80] X. Wang, L. J. Zhi, K. Mullen, *Nano Lett.* **2008**, *8*, 323.

[81] S. Gilje, S. Han, M. Wang, K. L. Wang, R. B. Kaner, *Nano Lett.* **2007**, *7*, 3394.

[82] P. Guo, H. Song, X. Chen, *Electrochem.Commun.* **2009**, *11*, 1320.

[83] S. M. Paek, E. Yoo, I. Honma, *Nano Lett.* **2009**, *9*, 72.

[84] C. G. Granqvist, *Sol. Energy Mater. Sol. Cells* **2007**, *91*, 1529.

[85] J. M. Phillips, J. Kwo, G. A. Thomas, S. A. Carter, R. J. Cava, S. Y. Hou, J. J. Krajewski, J. H. Marshall, W. F. Peck, D. H. Rapkine, R. B. Vandover, *Appl. Phy. Lett.* **1994**, *65*, 115.

[86] Z. Wu, Z. Chen, X. Du, J. M. Logan, J. Sippel, M. Nikolou, K. Kamaras, J. R. Reynolds, D. B. Tanner, A. F. Hebard, A. G. Rinzler, *Science* **2004**, *305*, 1273.

[87] J. van de Lagemaat, T. M. Barnes, G. Rumbles, S. E. Shaheen, T. J. Coutts, C. Weeks, I. Levitsky, J. Peltola, P. Glatkowski, *Appl. Phy. Lett.* **2006**, *88*, 3.

[88] R. C. Y. King, F. Roussel, *Applied Physics a-Materials Science & Processing* **2007**, *86*, 159.

[89] X. Wang, L. Zhi, N. Tsao, Z. Tomovic, J. Li, K. Müllen, *Angew. Chem., Int. Ed.* **2008**, *47*, 2990.

[90] Z. Liu, Q. Liu, Y. Huang, Y. Ma, S. Yin, X. Zhang, W. Sun, Y. Chen, *Adv. Mater.* **2008**, *20*, 3924.

[91] C. X. Guo, H. B. Yang, Z. M. Sheng, Z. S. Lu, Q. L. Song, C. M. Li, *Angew. Chem. Int. Ed.* **2008**, *49*, 3014.

[92] K. S. Kim, Y. Zhao, H. Jang, S. Y. Lee, J. M. Kim, K. S. Kim, J.-H. Ahn, P. Kim, J.-Y. Choi, B. H. Hong, *Nature* **2009**, *457*, 706.

[93] K.-Y. Shin, J.-Y. Hong, J. Jang, *Chem. Commun.* **2011**, *45*, 8527.

[94] S. Stankovich, R. D. Piner, X. Q. Chen, N. Q. Wu, S. T. Nguyen, R. S. Ruoff, *J. Mater. Chem.* **2006**, *16*, 155.

[95] N. A. Kotov, I. Dekany, J. H. Fendler, *Adv. Mater.* **1996**, *8*, 637.

[96] J. Lu, L. T. Drzal, R. M. Worden, I. Lee, *Chem. Mater.* **2007**, *19*, 6240.

[97] J. J. Mack, L. M. Viculis, A. Ali, R. Luoh, G. Yang, H. T. Hahn, F. K. Ko, R. B. Kaner, *Adv. Mater.* **2005**, *17*, 77.

[98] P K Hansma, P. J. Turner, R. S. Ruoff, *Nanotechnology* **2007**, *18*, 044026.

[99] T. Ramanathan, A. A. Abdala, StankovichS, D. A. Dikin, M. Herrera Alonso, R. D. Piner, D. H. Adamson, H. C. Schniepp, ChenX, R. S. Ruoff, S. T. Nguyen, I. A. Aksay, R. K. Prud'Homme, L. C. Brinson, *Nat. Nanotechnol.* **2008**, *3*, 327.

[100] B. Das, K. Eswar Prasad, U. Ramamurty, C. N. R. Rao, *Nanotechnology* **2009**, *20*, 125705.

[101] A. Yu, P. Ramesh, M. E. Itkis, E. Bekyarova, R. C. Haddon, *J. Phys. Chem. C* **2007**, *111*, 7565.

[102] T. J. Booth, P. Blake, R. R. Nair, D. Jiang, E. W. Hill, U. Bangert, A. Bleloch, M. Gass, K. S. Novoselov, M. I. Katsnelson, A. K. Geim, *Nano Lett.* **2008**, *8*, 2442.

[103] A. Sakhaee-Pour, *Solid State Commun.* **2009**, *149*, 91.

[104] N. A. Luechinger, N. Booth, G. Heness, S. Bandyopadhyay, R. N. Grass, W. J. Stark, *Adv. Mater.* **2008**, *20*, 3044.

[105] S. Watcharotone, D. A. Dikin, S. Stankovich, R. Piner, I. Jung, G. H. B. Dommett, G. Evmenenko, S. E. Wu, S. F. Chen, C. P. Liu, S. T. Nguyen, R. S. Ruoff, *Nano Lett.* **2007**, *7*, 1888.

[106] S. Stankovich, D. A. Dikin, G. H. B. Dommett, K. M. Kohlhaas, E. J. Zimney, E. A. Stach, R. D. Piner, S. T. Nguyen, R. S. Ruoff, *Nature* **2006**, *442*, 282.

[107] H. Chen, M. B. Muller, K. J. Gilmore, G. G. Wallace, D. Li, *Adv. Mater.* **2008**, *20*, 3557.

[108] P. T. Moseley, *Meas. Sci. Technol.* **1997**, *8*, 223.

[109] S. Capone, *J. Optoelect. Adv. Mater.* **2003**, *5*, 1335.

[110] C. X. Cong, T. Yu, Z. H. Ni, L. Liu, Z. X. Shen, W. Huang, *J. Phys. Chem. C* **2009**, *113*, 6529.

[111] P. G. Collins, K. Bradley, M. Ishigami, A. Zettl, *Science* **2000**, *287*, 1801.

[112] P. Dutta, P. M. Horn, *Rev. Mod. Phys.* **1981**, *53*, 497.

[113] C. Lee, X. Wei, J. W. Kysar, J. Hone, *Science* **2008**, *321*, 385.

[114] F. Schedin, A. K. Geim, S. V. Morozov, E. W. Hill, P. Blake, M. I. Katsnelson, K. S. Novoselov, *Nat. Mater.* **2007**, *6*, 652.

[115] K. S. Nonoselov, E. McCann, S. V. Morozov, V. I. Fal'ko, M. I. Katsnelson, U. Zeitler, D. Jiang, F. Schedin, A. K. Geim, *Nat. Phys.* **2006**, *2*, 177.

[116] J. D. Fowler, M. J. Allen, V. C. Tung, Y. Yang, R. B. Kaner, B. H. Weiller, *ACS Nano* **2009**, *3*, 301.

[117] A. Ghosh, D. J. Late, L. S. Panchakarla, A. Govindaraj, C. N. R. Rao, *J. Exp. Nanosci.* **2009**, *4*, 313.

[118] R. Arsat, M. Breedon, M. Shafiei, P. G. Spizziri, S. Gilje, R. B. Kaner, K. Kalantar-zadeh, W. Wlodarski, *Chem. Phys.Lett.* **2009**, *467*, 344.

[119] J. Lu, I. Do, L. T. Drzal, R. M. Worden, I. Lee, *ACS Nano* **2008**, *2*, 1825.

[120] C. Shan, H. Yang, J. Song, D. Han, A. Ivaska, L. Niu, *Anal. Chem.* **2009**, *81*, 2378.

[121] A. Sakhaee-Pour, M. T. Ahmadian, A. Vafai, *Solid State Commun.* **2008**, *145*, 168.

[122] R. S. Sundaram, C. Gómez-Navarro, K. Balasubramanian, M. Burghard, K. Kern, *Adv. Mater.* **2008**, *20*, 3050.

[123] Z. M. Ao, J. Yang, S. Li, Q. Jiang, *Chem. Phys.Lett.* **2008**, *461*, 276.

[124] N. Mohanty, V. Berry, *Nano Lett.* **2008**, *8*, 4469.

[125] G. Eda, H. E. Unalan, N. Rupesinghe, G. A. J. Amartunga, *Appl. Phy. Lett.* **2008**, *93*, 233502.

[126] Z. S. Wu, S. Pei, W. Ren, D. Tang, L. Gao, B. Liu, C. L. F. Li, H. M. Cheng, *Adv. Mater.* **2009**, *21*, 1756.

[127] A. Malesevic, R. Kemps, A. Vanhulsel, M. P. Chowdhury, A. Volodin, C. V. Haesendonck, *J. Appl. Phys.* **2008**, *104*, 084301.

CHAPTER 2

SYNTHESIS AND CHARACTERIZATION OF GRAPHENE

Summary*

This chapter deals with the synthesis and characterization of graphene. When graphene research was initiated in this laboratory, there was little information available on the synthesis and characterization. This necessitated exploration of various methods of synthesis. This chapter presents the results of all the investigations carried out by the candidate to prepare single-layer and few-layer graphenes. The various synthetic methods studied include exfoliation of graphite oxide (EG), conversion of nanodiamond (DG), chemical vapor deposition (CVD), reduction of single-layer graphene oxide (RGO) through different routes, and the new methods developed in this laboratory which include by us namely arc evaporation of graphite in hydrogen atmosphere (HG) and radiation-induced reduction of single-layer graphene oxide (RGO).

EG was prepared by giving a sudden thermal shock to dried graphite oxide (GO). DG was obtained by transformation of nanodiamond at higher temperatures. CVD of camphor and different hydrocarbons has been carried out on different metal catalysts and also on transition metal foils. Single-layer graphene oxide (SGO) was reduced using hydrazine hydrate/ethylene glycol as reducing agent under refluxing conditions or through hydrothermal and microwave routes to obtain RGO. Arc discharge between graphite electrodes under a relatively high pressure of hydrogen yields graphene flakes (HG) generally containing 2-4 layers in the inner wall region of the arc chamber. The method is eminently suited to dope graphene with boron and nitrogen by carrying out arc

discharge in the presence of diborane and pyridine respectively. Irradiation of single-layer graphene oxide (SGO) by sunlight, UV light and KrF excimer laser yielded reduced graphene oxide. Both sunlight and ultraviolet light reduce graphene oxide well after prolonged irradiation, but laser irradiation produces graphene with negligible oxygen functionalities within a short time. Laser irradiation of graphene oxide appears to be an efficient procedure for large-scale synthesis of graphene.

All the graphene samples were examined by field emission scanning electron microscopy (FESEM), transmission electron microscopy (TEM), atomic force microscopy (AFM), Raman spectroscopy and thermogravimetric analysis (TGA). Single-layer graphene has been obtained by CVD over nickel and cobalt foils. Based on TEM and AFM measurments, HG turns out be the best means of preparing few-layer graphene comprising a smaller number (2-4) of layers. EG, DG and RGO generally possess 2-6 layers.

---

*Papers based on this work have been published in *J. Mater. Chem.(2008), J. Phys. Chem.C (2009), J. Phys. Chem. Lett. (2010), Sci. Technol. Adv. Mater.(2010) and Int. J. Nanoscience (2011).*

2.1 Introduction

Since the isolation of single-layer graphene (SLG) from highly ordered pyrolytic graphite (HOPG) in 2004, it has attracted great scientific interest owing to its unique, outstanding physico-chemical properties and possible potential applications. Though, there is a great surge in graphene research after isolation of SLG in 2004, however, synthesis of graphene related materials from graphite oxide and related chemical modifications of graphite were extensively studied in the past. As early as the 1940s,[1] a series of theoretical studies suggested that these layers if isolated, might exhibit extraordinary electronic characteristics. Graphite oxide (GO) which is currently employed as a parent material to prepare graphene and related reduced graphene oxide materials was studied extensively for more than 170 years.[2-6] For the first time in 1840, the German scientist Schafhaeutl reported the intercalation and exfoliation of graphite with sulfuric and nitric acids.[2, 5, 6] Later, different intercalates like alkali metals, fluoride salts, transition metals[7-11] and various organic species have been employed.[7, 12] On intercalation, the stacked structure of graphite remains the same with widened interlayer spacing which facilitates the delamination of graphene layers.

The effort of the British chemist Brodie in 1859 to determine the molecular weight of graphite using strong acids and oxidants ($KClO_3$)[13, 14] resulted in the formation of graphite oxide. This chemical modification of graphite has proven to be a suitable method for the preparation of graphite intercalated compounds (GICs), single-layer graphene oxide (SGO) and reduced graphene oxide (RGO).[3, 15, 16] Oxidation of graphite in this manner weakens the interplanar forces facilitating its exfoliation under ultrasonic, thermal or other energetic conditions. Nearly 40 years later, Staudenmaier reported a different method of oxidation with slight modification to Brodie's process. In this process, to prepare GO, chlorate salt was added in multiple aliquots over the course of the

reaction, instead of in a single portion.[17] The obtained product was called as graphitic acid due to its acidic properties. These intercalation and oxidation experiments were the first examples of delamination of graphite into its constituent lamellaer. Later, Hoffmann *et al*. reported that the composition of anhydrous GO is approximately $C_8O_2(OH)_2$. Ruess *et al*. have shown that GO undergoes exfoliation at 200–325 ºC on rapid heating, with the formation of light weight and voluminous black flakes—the so-called graphite oxide soot.[18] Boehm *et al*. have shown that graphite oxide soot obtained through deflagration of GO contains very thin crumpled sheets. Figure 1 shows an electron microscope image

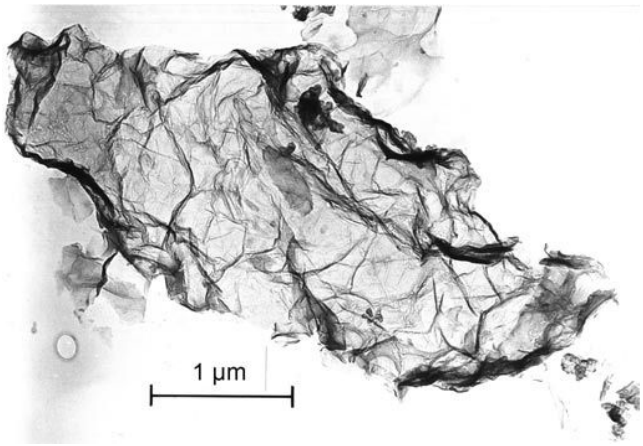

Figure 1. Electron microscope image of a particle of graphite oxide soot. Image: K. Heideklang, 1960. (From ref. [19]).

of GO soot. They have also found that GO undergoes reduction in dilute alkaline media with hydrazine, hydrogen sulfide or iron(II) salts to produce thin lamellar carbon containing small amounts of hydrogen and oxygen.[19] The number of layers present in the lamellae was determined by a set of standardized films of known thicknesses by using transmission electron microscopy (TEM). The material was found to exhibit a minimum thickness of 4.6 Å, slightly deviating from the thickness of SLG.[20-22] However, these densitometry measurements suffered from a relatively high degree of experimental error

related to variations in the thickness of the calibration standards used as well as unevenness in the photographic emulsions.[19] Regardless, Boehm concluded, "this observation confirms the assumption that the thinnest of the lamellae really consisted of single carbon layers".[19] Similar products were also obtained by the thermal deflagration (i.e., exfoliation) of GO.[23]

In 1968, Morgan and Somorjai used low-energy electron diffraction (LEED) to investigate the adsorption of various gaseous organic molecules (e.g., CO, C_2H_4, C_2H_2) onto a platinum (100) surface at high temperatures.[24] After analyzing these LEED data, May postulated in 1969 that single as well as multiple graphitic layers were present on the platinum surface.[25] Later, a number of studies on the surface segregation of single- and few-layers of carbon from different crystalline faces of transition-metal substrates, like Ni (100) and (111), Pt (111), Pd (100) and Co (0001) were reported (Figure 2).[7]

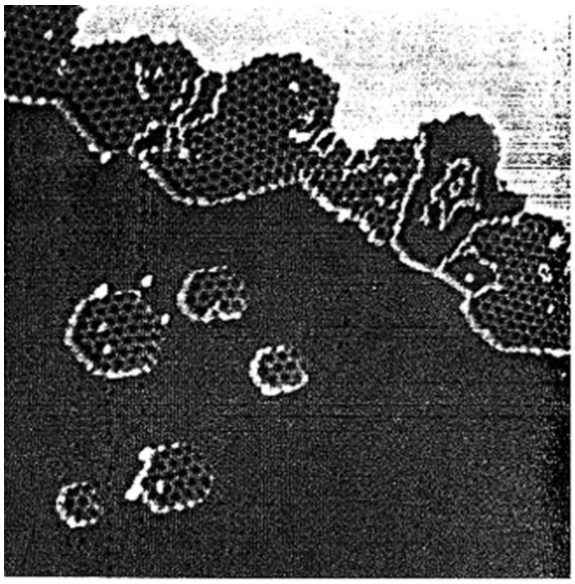

Figure 2. STM image (1000 x 1000 $Å^2$) showing the formation of a graphitic structure on a metal surface; the image was obtained at room temperature after annealing ethylene over Pt (111) at 1230 K. (From ref. [26]).

LEED and Auger electron spectroscopy studies revealed that dissolved carbon in the metal alloys undergoes phase separation at high temperature and forms single or multiple layers of carbon on the metal surface. Later these results were confirmed by scanning tunneling microscopy (Figure 2).[26]

In 1975 van Bommel *et al*. described the epitaxial sublimation of silicon from single crystals of silicon carbide (0001). At high temperatures, under ultrahigh vacuum (UHV; $<10^{-10}$ Torr) they could obtain single- and multi layered flakes of carbon consistent with the graphitic structure were obtained, as determined by LEED and Auger electron spectroscopy.[27] At temperatures below 800 °C, the SiC largely retained its native structure, whereas an increase in the temperature resulted in the appearance of "graphite rings" in the LEED pattern.[27] The authors highlighted a graphitization mechanism proposed by Badami in which three layers of residual carbon collapse onto one another upon sublimation of the silicon to effectively form graphitic sheets (Figure 3).[28] In 1999, Ruoff *et al*. employed a lithographic patterning of HOPG combined with oxygen-plasma etching to obtain thin graphene lamellae, however these

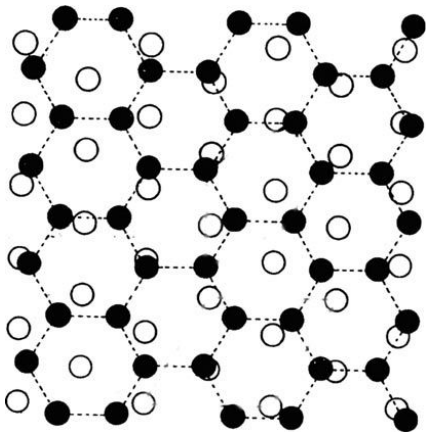

Figure 3. Model of a silicon carbide structure in which three carbon layers of SiC have collapsed upon the evaporation of Si to form a single layer; open circles represent C atoms. (From ref. [27]).

lamellae were not fully exfoliated into their respective monolayers.[29] Thin graphite layers suitable for investigation by electron microscopy have for a long time been prepared by "stripping off" highly ordered pyrographite (HOPG) or graphite crystals with cellophane-based adhesive tape.[30] Novoselov *et al*. have found that proper and patient use of this method enabled extremely thin films with only one or just a small number of graphene layers.[31, 32] This method produces defect free graphene crystals, but has the disadvantage that only small amounts can be produced. In Figure 4, we depict selected events in the history of preparation, isolation, and characterization of graphene.[7]

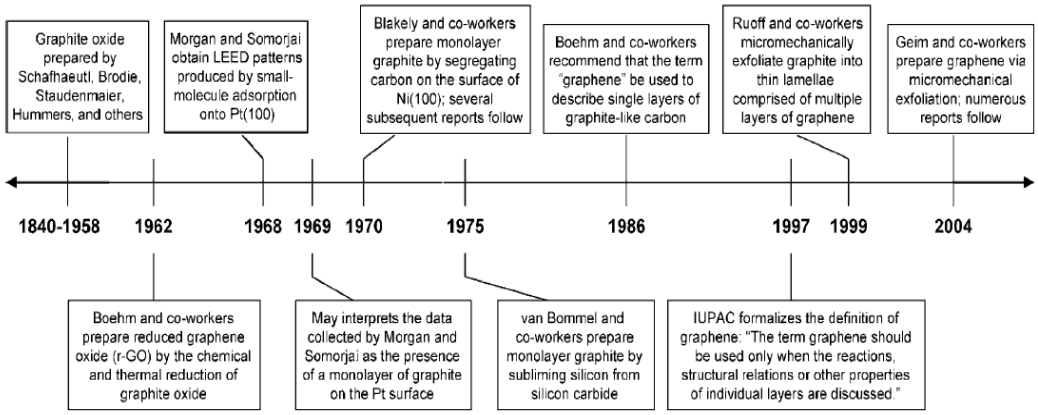

Figure 4. Timeline of selected events in the history of the preparation, isolation and characterization of graphene. (From ref. [7]).

2.2 Scope of the present investigations

As mentioned in the introduction, the approach to prepare graphene reported by Novoselov *et al*. based on the scotch tape technique allows one to deposite graphene crystallites on a silica substrate.[31] The quality of the samples produced is so good that both ballistic transport and a quantum Hall effect (QHE)[33, 34] can be observed easily. This makes graphene a promising candidate for future electronic applications, such as field-effect transistors (FETs). While this approach may suffice for certain physical measurements, however it is necessary to prepare graphene in large quantities for other

studies and applications. We have, therefore, attempted to investigate different synthetic routes, which can provide graphene in large yields.

When we started research on graphene there was little published work. In order to prepare graphene, we therefore employed different methods based on exfoliation of graphite oxide (EG),[35] conversion of nanodiamond (DG),[36] chemical vapor deposition (CG)[37, 38] and reduction of single-layer graphene oxide (RGO).[16] Two new methods were developed by us: arc evaporation of graphite (HG) and radiation induced reduction of single-layer graphene oxide (RGO).

Preparation of EG involves thermal exfoliation of graphite oxide at high temperature. In this method, graphite oxide was prepared by reacting graphite with a mixture of conc. nitric acid and sulfuric acid along with potassium chlorate at room temperature for 5 days. Thermal exfoliation of graphite oxide was then carried out in a long quartz tube at 1050°C under an Ar atmosphere. DG was obtained by thermal conversion of nanodiamond at high temperatures, employing a graphite furnace.

CVD was carried out in a two-stage furnace and camphor was slowly sublimed (170°C) by heating from the first furnace to the second furnace held at 770°C where the micron sized nickel particles were placed. Using CVD, we have also grown large area graphene films on nickel and cobalt sheets. In this process, hydrocarbons like methane, ethylene, acetylene and benzene were employed and the growth was carried out at around 800-1000 °C.

To prepare RGO, single-layer graphene oxide (SGO) obtained by ultra-sonication of graphite oxide was reduced using hydrazine hydrate/ethylene glycol as a reducing agent under refluxing conditions and through hydrothermal or microwave treatments.

In a new method formulated here, graphene was prepared by the arc evaporation of graphite rod in H_2 atmosphere without using any catalyst. This method makes use of

the knowledge that it is difficult to obtain carbon nanotubes by employing arc evaporation of graphite rod in H_2 atmosphere. It appears that H_2 plays a key role in the formation of graphene sheets by resisting them to roll into tubular form. In second method, SGO has been reduced by sunlight, UV light and KrF excimer laser. Among these, laser irradiation has proven to be an efficient procedure for large-scale synthesis of graphene within shorter time.

The graphene samples prepared by the aforementioned procedures were characterized by employing different techniques known as field emission scanning electron microscopy **(**FESEM), atomic force microscopy (AFM), transmission electron microscopy (TEM), Raman spectroscopy and thermogravimetric analysis (TGA). This is mainly due to the lack of sufficient information in literature regarding charactrerization of graphenes prepared by different methods, particularly in case of samples those have more than one layer. Both FESEM and TEM analysis showed that graphenes have wrinkled paper like structure. AFM analysis revealed the number of layers in the samples. Among all the samples, HG comes out to be the best comprising 2-4 number of layers. Raman spectra of graphene samples showed the characteristic D, G and 2D bands. Graphene films grown on nickel and cobalt sheets showed an intense sharp 2D-band, a weaker G-band and hardly any D-band. Thermogravimetric analysis inferred that graphene samples undergo oxidation in the range of 520-750 °C.

2.3 Experimental section

2.3.1 Graphene from exfoliation of graphite oxide (EG)

A first method to prepare EG involves thermal exfoliation of graphite oxide. Graphite oxide (GO) was prepared through either Staudenmaier or modified Humers method.[39, 40] In the Staudenmaier method, a 250 ml reaction flask containing a magnetic stir bar was charged with sulfuric acid (10 ml) and nitric acid (5 ml) and cooled by immersion in an ice bath. The acid mixture was stirred and allowed to cool for 15 min,

and graphite (0.5 g) was added under vigorous stirring to avoid agglomeration. After the graphite powder was well dispersed, potassium chlorate (5.5 g) was added slowly over 15 min to avoid sudden increases in temperature. The reaction flask was loosely capped to allow evolution of gas from the reaction mixture and stirred for 96 h at room temperature. On completion of the reaction, the mixture was poured into 0.5 L of deionized water and filtered. The GO was redispersed and washed in a 5% solution of HCl. The filtrate was tested with barium chloride for the presence of sulphate ions. The HCl wash was repeated until this test was negative. The GO was then washed repeatedly with deionized water until pH of the filtrate was neutral. The GO slurry was dried in vacuum at 60 °C. In modified Hummers procedure, graphite oxide (GO)[40] is prepared as follows. Graphite powder (500 mg) is added to a mixture of concentrated H_2SO_4 (12 ml) and $NaNO_3$ (250 mg) in a 500 ml flask kept in an ice bath. While stirring the mixture, 1.5 g of $KMnO_4$ is added slowly and the temperature is raised to 35 ºC. After stirring the mixture for 30 minutes, 22 ml of water is slowly added and the temperature raised to 98 ºC. After 15 minutes, the reaction mixture is diluted to 66 ml with warm water and treated with 3% of H_2O_2. Then suspension so obtained is filtered resulting in a yellow-brown powder. The resultant GO was dried under vacuum.

Graphite oxide (0.2 g), prepared as described above was placed in an alumina boat and inserted into a 1 m long quartz tube that was sealed at one end. The other end of the quartz tube was fixed to a two holed rubber stopper. An argon (Ar) inlet was inserted through one of the holes of rubber stopper, and the outlet was fixed through another hole. After purging with Ar for 10 min, the quartz tube was quickly inserted into a tube furnace preheated to 1050 ºC, and held in the furnace for 10 minutes.[35] Rapid heating (>2000 °C/min) of GO to 1050 ºC deflagrates the graphite oxide into individual sheets through evolution of CO_2 resulting the formation of black product.

2.3.2 Graphene by conversion of nanodiamond (DG)

DG was prepared by the graphitization of nanodiamond powder (particle size 4-6 nm, Tokyo Diamond Tools, Tokyo, Japan) in an inert argon atmosphere.[36] The mean size and the size distribution of the diamond particles checked by transmission electron microscopy were in good agreement with the reported. In order to avoid contamination with magnetic impurities, we treated nanodiamond particles by soaking in concentrated HCl before use. 100 mg of pristine nanodiamond powder placed in a graphite crucible was heat-treated in a locally fabricated graphite furnace (power rating 6 kW, Therelek engineers PVT LTD. Bangalore, India) in a helium atmosphere, at different temperatures 1650, 1800, 2000 and 2200 °C.

2.3.3 Graphene by CVD (CG)

To prepare graphene by CVD method, carbon sources like camphor and different hydrocarbons were employed. To prepare graphene from camphor, the reaction was carried out in a two-stage furnace under argon atmosphere. In the first furnace camphor was slowly sublimed by heating at 170 °C and sublimized vapors were passed through the second furnace held at 770 °C where the micron sized nickel particles were placed as catalyst.[37] After completion of the experiment, furnaces were allowed to cool naturally and the product was collected. The so obtained product was thoroughly washed with dilute HCl to free from the catalytic Ni particles.

We have also grown graphene on different transition metal substrates by the decomposition of hydrocarbons such as methane, ethylene, acetylene and benzene.[38] In our experiments, nickel (Ni) and cobalt (Co) foils having thickness of 0.5 mm and 2 mm respectively were used as catalysts. These foils were cut into 5x5 mm^2 pieces and polished mechanically and the CVD process was carried out by decomposing hydrocarbons around 800–1000 ºC. By employing a nickel foil as substrate, CVD was

carried out by passing methane (60-70 sccm) or ethylene (4-8 sccm) along with a high flow of hydrogen around 500 sccm at 1000 ºC for 5-10 minutes. With benzene as the hydrocarbon source, benzene vapor diluted with argon and hydrogen was decomposed at 1000 ºC for 5 minutes. On a cobalt foil, acetylene (4 sccm) and methane (65 sccm) were decomposed at 800 and 1000 ºC respectively. In all these experiments, the metal foils were cooled gradually after the decomposition.

2.3.4 Graphene by arc discharge in a H_2 atmosphere (HG)

To prepare HG, direct current (DC) arc discharge evaporation experiments were carried out in a stainless steel chamber that was filled with hydrogen and helium or methane and helium mixtures at different proportions, without using any catalyst. In a typical experiment, a graphite rod (6 mm diameter and 50 mm long) was used as an anode and a pure graphite rod (having diameter of 13 mm and 60 mm length) was used as cathode. The purity of the graphite rod was 99.998%. The discharge current was typically 100 A, and the voltage, about 38 V. The arc was maintained by continuously translating the cathode to keep a constant distance (2 mm) between it and the anode. Typical synthesis time was 10 min. Soot materials with web like appearance were formed on the inner walls of the reaction chamber and around the cathode after the evaporation. This material was characterized by employing different techniques.

2.3.5 Reduced graphene oxide (RGO)

RGO is prepared by reacting single-layer graphene oxide (SGO) in water with hydrazine hydrate at the refluxing temperature (RGO),[16] hydrothermally (RGO (HT)) or by microwave treatment (RGO (MW)). As GO readily forms a stable colloidal suspension in water, the suspension is subjected to ultrasonic treatment (300 W, 35 kHZ) for an hour to produce single-layer graphene oxide (SGO). Later, hydrazine hydrate (1 ml) is added to 100 ml of stable aqueous solution of SGO (1mg/1ml) and refluxed for 24 h. The

reduced GO turns black and precipitates at the bottom of the flask. The resulting precipitate is filtered and washed with water and methanol. Hydrothermal or micro-wave routes were also employed to reduce SGO. In this procedure, the homogeneous mixture of 25 ml of SGO solution (1mg/1ml) and 2 ml of ethylene glycol or 1 ml of hydrazine hydrate is taken in a 50 mL polytetrafluoroethylene (PTFE) lined bomb. In case of micro-wave treatment, the sealed autoclave is subjected to microwave irradiation (power 600 W, 200 °C) for 10 minutes. In hydrothermal, process the autoclave is kept in an oven at 170 °C for 24 h under autogenous pressure and allowed to cool to room temperature gradually. The so obtained black product was washed with water and ethanol.

2.3.6 Radiation-induced reduction of graphene oxide (Radiation induced RGO)

An aqueous SGO solution taken in a petri dish was exposed to sunlight for a few hours. Upon exposure, the yellow-brownish SGO undergoes reduction with time and forms black suspension. For treatment with ultraviolet radiation, the solution was irradiated with a Philips low-pressure mercury lamp (254 nm, 25 W, 90 $\mu W/cm^2$). A Lambda Physik KrF excimer laser (248 nm, 5 Hz) was employed to irradiate aqueous solutions of SGO taken in a quartz vail. The aluminum metal slit (beam shaper) which usually gives a rectangular beam was removed during laser irradiation of the solution. This makes laser energy almost uniform throughout the area where graphene oxide is present. 300 mJ beam energy at 5 Hz reprate was used for the purpose. The reduced graphene samples obtained by irradiation with sunlight, ultraviolet light and KrF excimer laser are designated as SRGO, URGO and LRGO respectively. Apart from graphene oxide reduction by various irradiation sources, graphite oxide solution in water was directly irradiated with excimer laser for an hour to see whether sonication step can be avoided.

2.4 Characterization techniques

Field emission scanning electron microscopy (FESEM): FESEM images were recorded with a FEI NOVA NANOSEM 600.

UV absorption spectroscopy: UV absorption measurements were carried out at room temperature with a Perkin-Elmer model Lambda 900 UV/Vis/NIR spectrometer.

Infrared spectroscopy: Infrared (IR) spectra were recorded on small pieces of the samples embedded in KBr pellets using Bruker FT-IR spectrometer.

Raman spectroscopy*:* Raman spectra were recorded at different locations of the sample using Jobin Yvon LabRam HR spectrometer with 632 or 514 nm Ar laser.

Transmission electron microscopy (TEM): TEM images were obtained with a JEOL JEM 3010 instrument fitted with a Gatan CCD camera operating at an accelerating voltage of 300 kV. The samples were prepared by dispersing the product in CCl_4. A drop of the suspension was then put on a holey carbon coated Cu grid and allowed to evaporate.

Thermogravimetric analysis (TGA): Thermogravimetric analysis of the samples was carried out in a flowing oxygen atmosphere with a heating rate of 10 °C per minute using a Mettler-Toledo-TG-850 apparatus.

Atomic force microscopy (AFM): AFM measurements were performed using Innova atomic force microscope. The sample preparation is as follows. 1 mg of graphene is dispersed in 3.0 ml of 1-methyl-2-pyrrolidinone (NMP) and ultrasonicated for half an hour. After allowing the suspension to settle at room temperature for 1 hr, an aliquot (0.5 mL) was taken and added to a 1.5 ml flex tube for centrifugation. The samples were centrifuged and the sedimented material was discarded after each cycle, finally yielding a light-brown suspension. The suspension was spin-coated at 5,000 RPM onto freshly cleaved, highly oriented pyrolytic graphite.

2.5 Results and discussion

We have prepared graphene by employing different independent routes including arc evaporation of graphite rod and radiation-induced reduction of graphene oxide which are newly developed by us. To know the quality of these samples, we have used different characterization techniques such as FESEM, TEM, AFM, Raman spectroscopy and TGA. Results of the synthetic aspects and conclusions from the above characterizations are summarized below.

2.5.1 Graphene from exfoliation of graphite oxide (EG)

In Figure 5, we show (a) FESEM and (b) TEM images of EG respectively. Both FESEM and TEM images of EG show wrinkled paper-like structures.

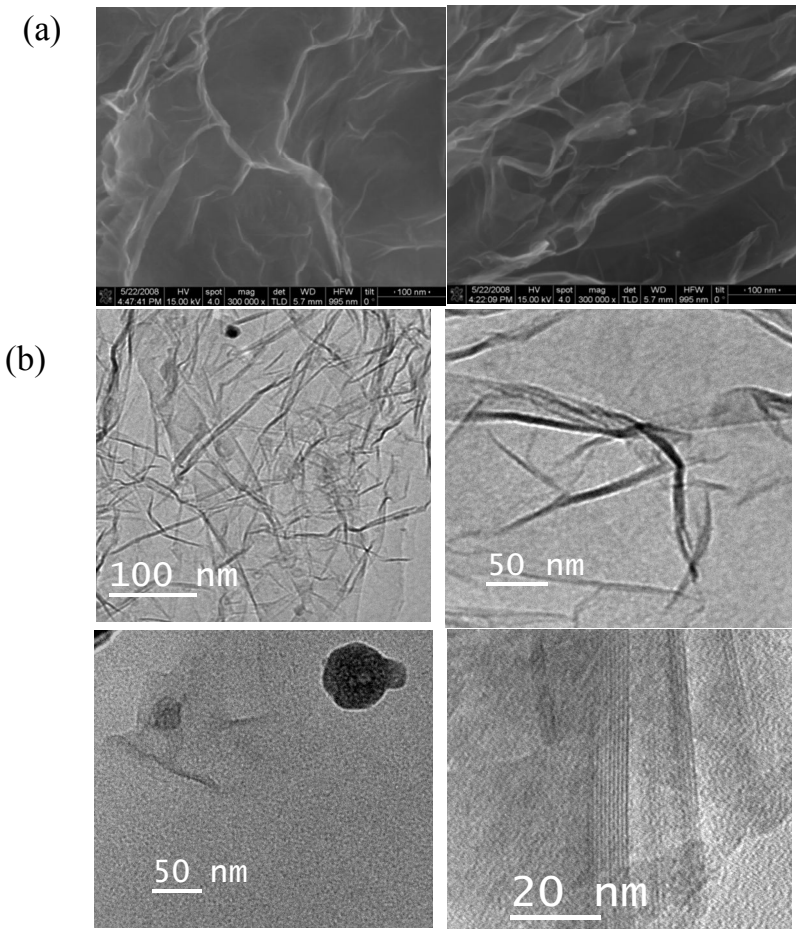

Figure 5. (a) FESEM and (b) TEM images of EG.

To determine the number of layers present in the sample, we have carried out extensive AFM study by collecting the data at different locations. In Figure 6, we show typical AFM images of EG. The cross-section height profile analysis indicates EG possesses 3 to 6 graphene layers.

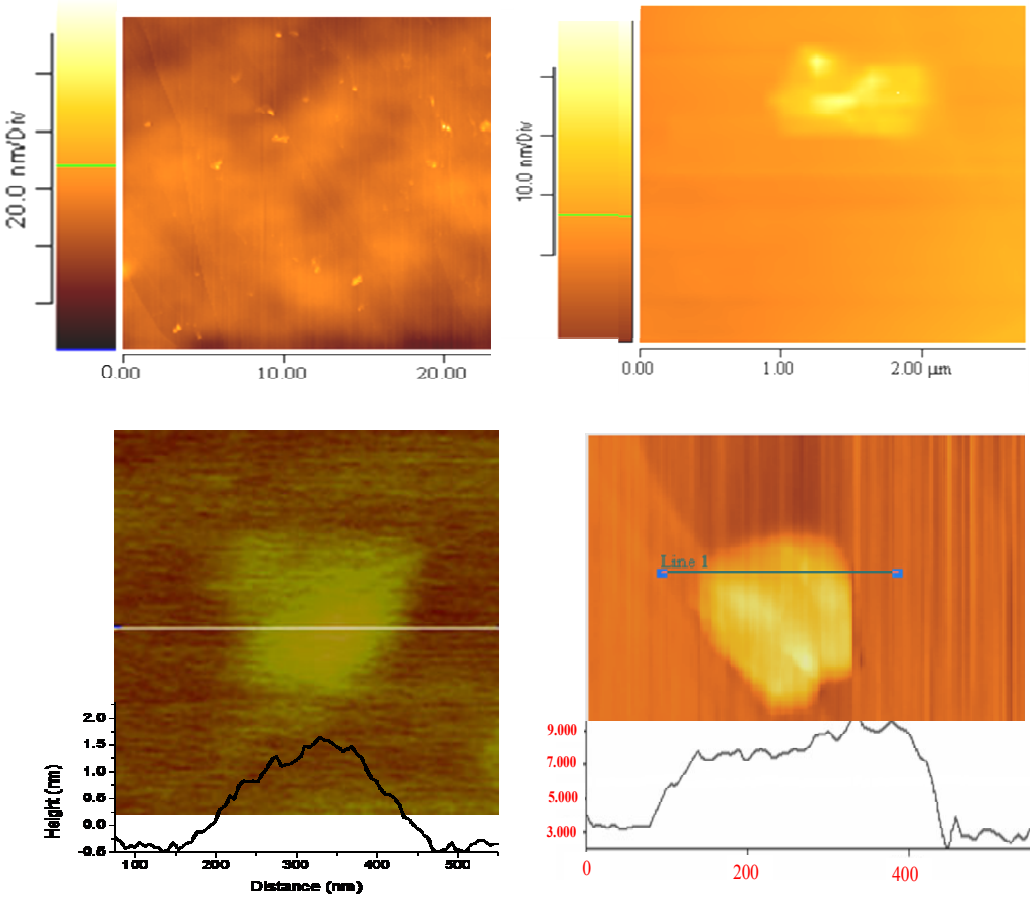

Figure 6. AFM images of EG.

Raman spectroscopy is most useful tool to characterize graphene.[41] Single-layer graphene shows the well-known G-band around 1570 cm^{-1} and a band around 1620 cm^{-1} (D′). The D′ band is defect induced and not found in graphite. The D-band around 1350 cm^{-1} arising from disorder is very weak in a single layer graphene. The 2D band (~2600 cm^{-1}) which appears in single-layer graphene is also sensitive to the number of layers and shows greater structure (often a doublet) with increase in the number of

layers. We have recorded the Raman spectra of EG sample at different locations employing 632 Ar laser. In Figure 7, we show typical Raman spectrum of EG and in Table 1 Raman band positions, I_D/I_G, and I_{2D}/I_G ratios of different EG samples are summarized.

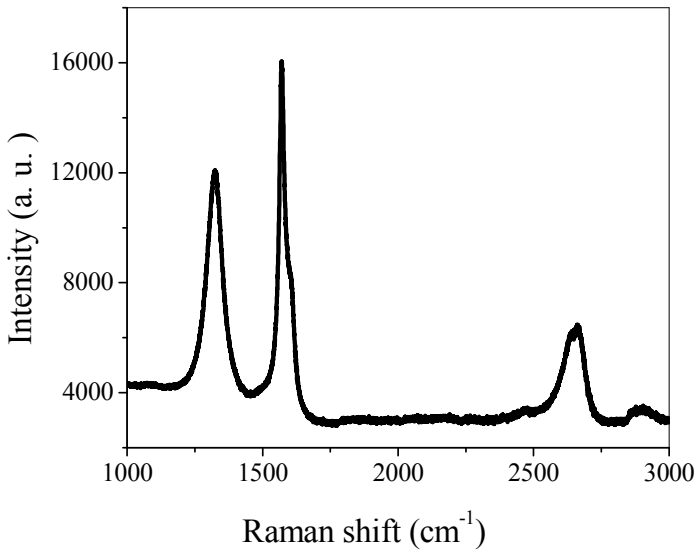

Figure 7. Raman spectrum of EG.

Table 1. Raman band positions along with $I_D/_G$, $I_{2D}/_G$ ratios.

Sample	D (cm^{-1})	G (cm^{-1})	D' (cm^{-1})	2D (cm^{-1})	I_D/I_G	I_{2D}/I_G
EG	1345 1346 1352	1580 1587 1574	1617 1608 1619	2678 2689 2705	0.6 0.7 1	0.3 0.25 0.25

Thermal exfoliation of graphite oxide at high temperatures produces graphene in bulk quantities. The so obtained graphene has wrinkled sheet structure resulting from reaction sites involved in oxidation and reduction processes. It possesses 2-6 number of layers having lateral dimensions up to 1 micron. It may find applications in catalysis, sensors and primarily in nanocomposites and storage of gases.

2.5.2 Graphene by conversion of nanodiamond (DG)

We have carried out the conversion of nanodiamond (5 nm) at high temperatures by employing a locally fabricated graphite furnace (power rating 6 kW, Therelek engineers PVT LTD. Bangalore, India). In Figure 8, we have shown a photograph of the graphite furnace employed by us. Nanodiamond samples (100-150 mg) were placed in a graphite crucible and annealed in a helium atmosphere (99.9999 %) at 1650 and 1850 ºC for 1 hr, at 2050 ºC for 1hr, 1.5hr and 2 hr and at 2200 ºC for 40 min. These samples are designated as DG-1650, DG-1850, DG-2050 (1 hr), DG-2050 (1.5 hr), DG-2050 (2 hrs) and DG-2200 respectively.

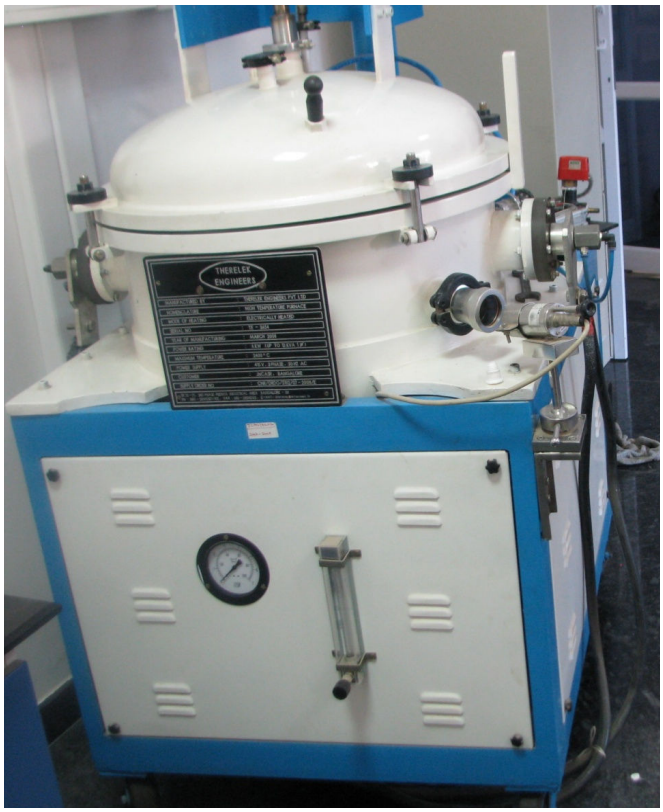

Figure 8: Photograph of the graphite furnace.

In Figure 9, we show FESEM images of DG-1650 and TEM images of nanodiamond, DG-1650, DG-1850, DG-2050 (1 hr), DG-2050 (1.5 hr), DG-2050 (2 hr) and DG-2200.

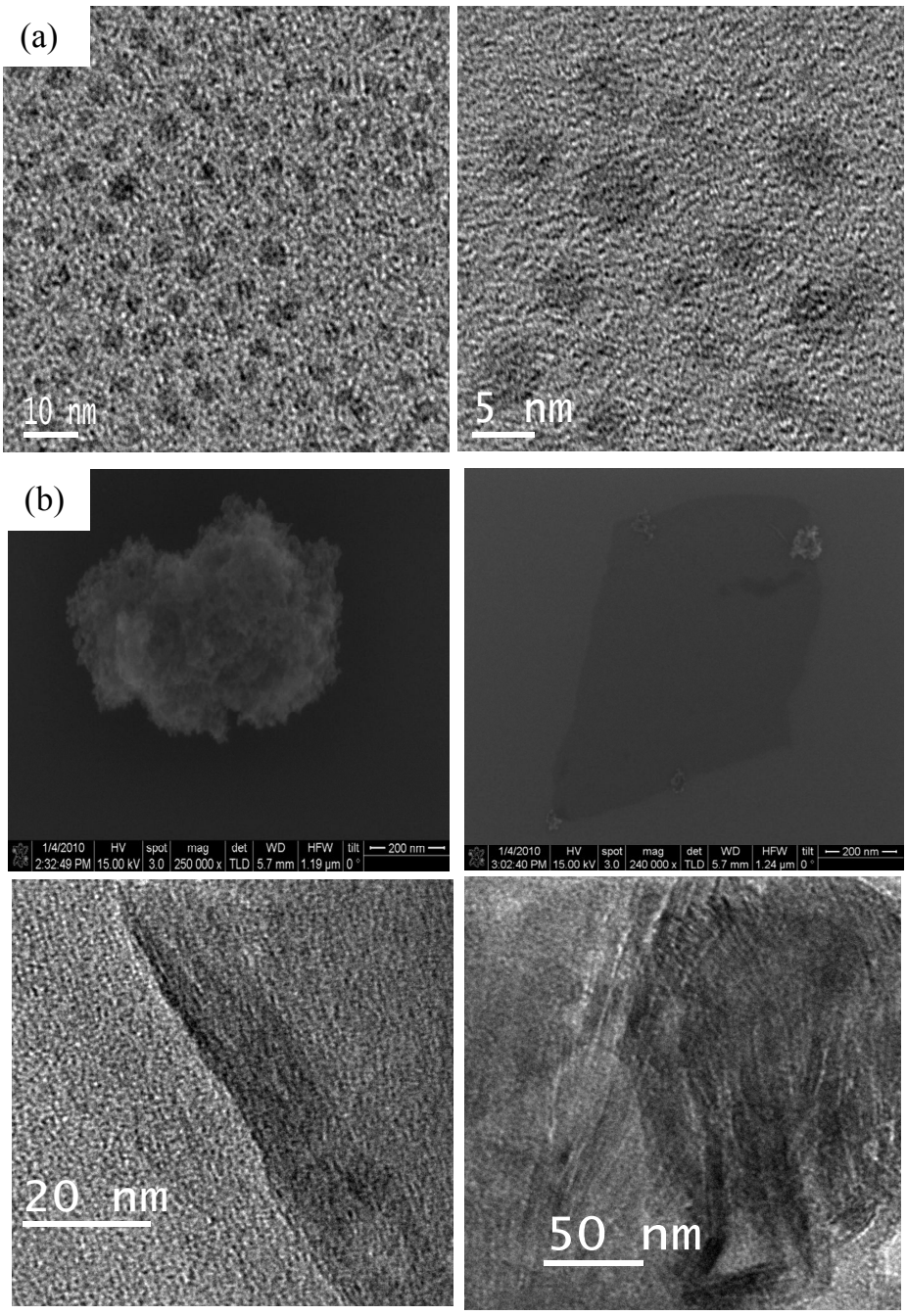

Figure 9. (a) TEM images of nanodiamond, (b) FESEM (top panel) and TEM images (bottom panel) of DG-1650.

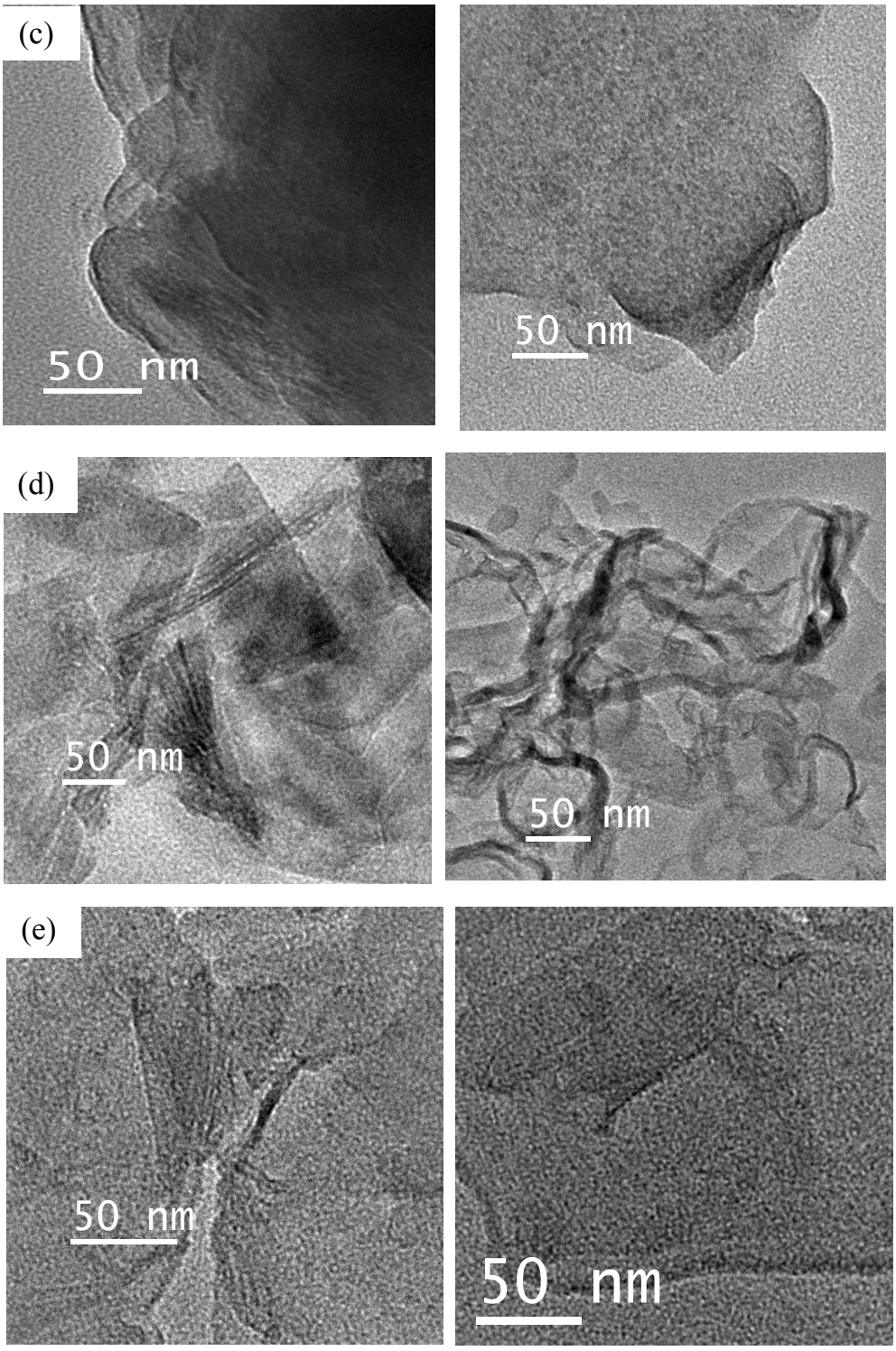

Figure 9. TEM images of (c) DG-1850, (d) DG-2050 (1hr) and (e) DG-2050. (1.5 hr).

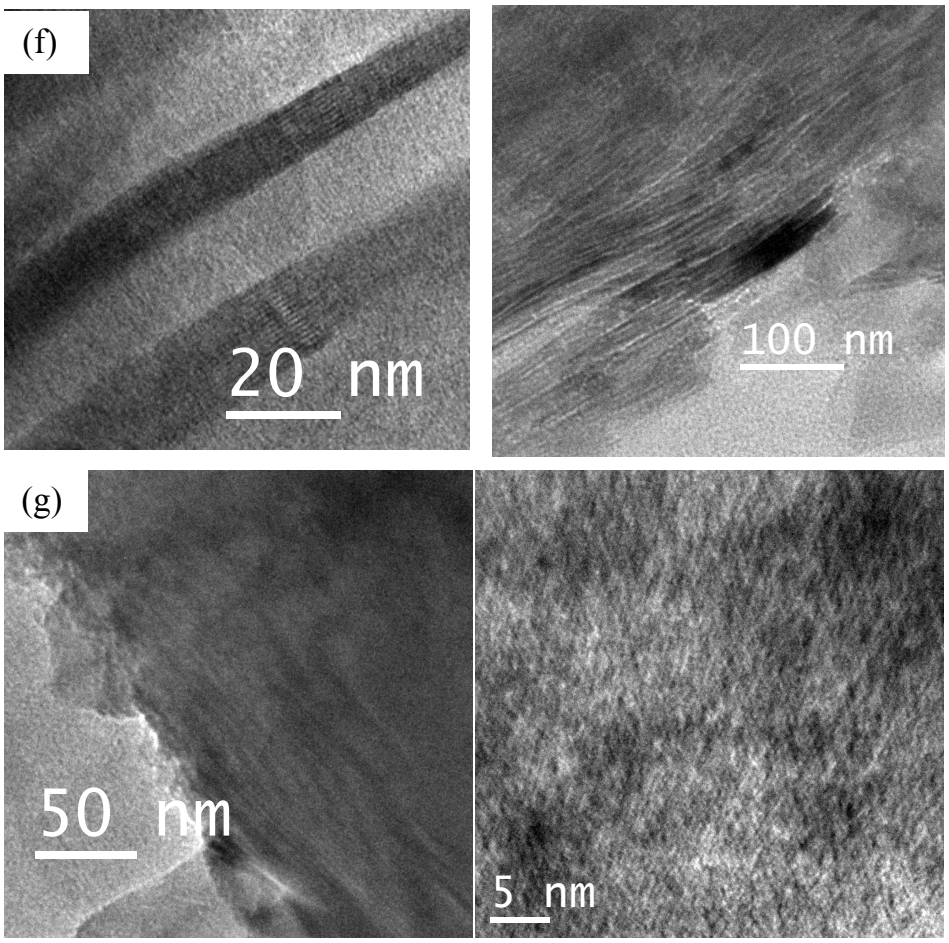

Figure 9. TEM images of (f) DG-2050 (2 hr) and (g) DG-2200.

TEM analysis shows that the size of starting nanodiamond (ND) is around 5 nm. On heating, ND undergoes transition to graphitic structures.

We show the AFM images in Figure 10 and in Figure 11a and b corresponding histograms of the number of layers and of the lateral dimensions of DG-1650 and DG-2200. AFM analysis indicates that DG comprises 3-9 layers having lateral dimension around 600 nm. It shows a slight increase in the number of layers and a decrease in lateral dimensions in the samples heated at 2200 ºC.

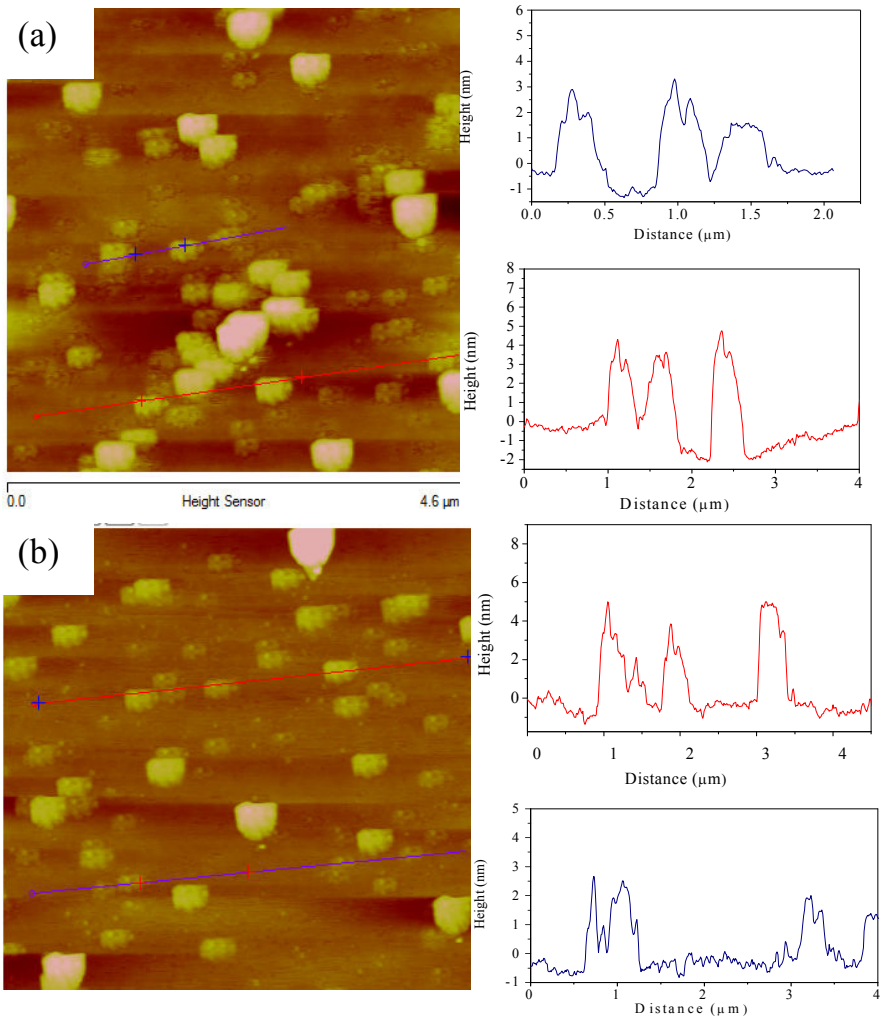

Figure 10. AFM images of (a) DG-1650 and (b) DG-2200.

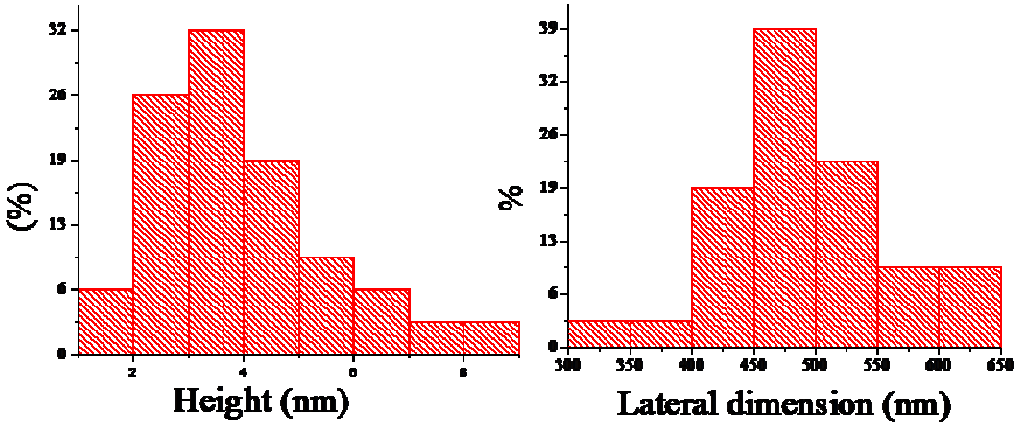

Figure 11a. Histograms of the height (left panel) and of the lateral dimensions (right panel) of DG-1650.

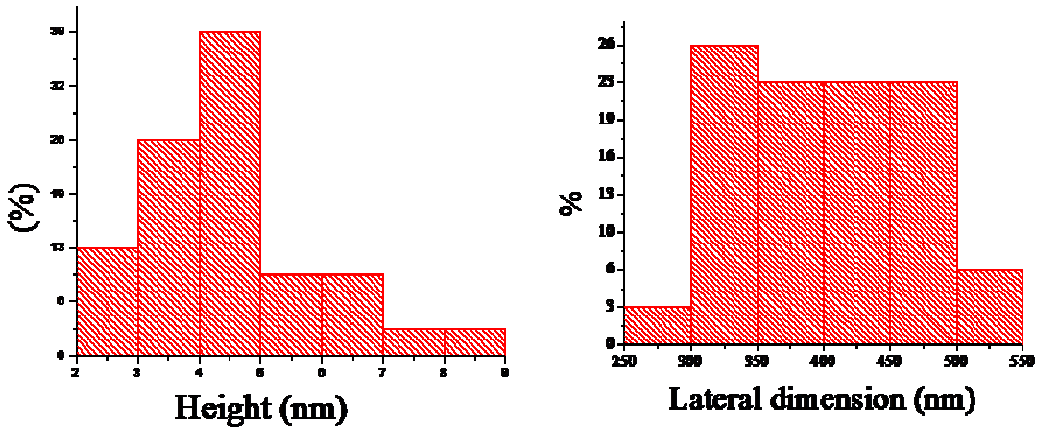

Figure 11b. Histograms of the height (left panel) and of the lateral dimensions (right panel) of DG-2200.

Raman spectra of all DG samples were recorded by employing 532 nm Ar laser. They show the characteristic D, G and 2D bands of graphene at 1340 cm^{-1}, 1580 cm^{-1} and 2680 cm^{-1} respectively. In Figure 12 we show Raman spectra of DG-1850, DG-2050 (1 hr) samples. The Raman band positions of all DG samples are summarized in Table 2. The D band is quite intense in the DG samples.

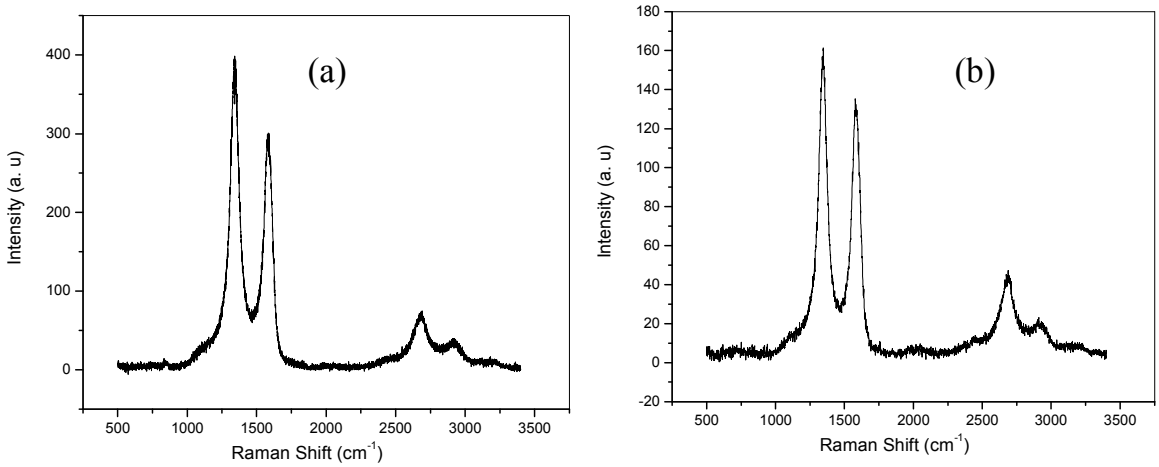

Figure 12. Raman spectra of (a) DG-1850 and (b) DG-2050 (1 hr).

Table 2. Raman band positions along with $I_D/_G$, $I_{2D}/_G$ ratios.

Sample	D (cm^{-1})	G (cm^{-1})	2D (cm^{-1})	I_D/I_G	I_{2D}/I_G
DG-1650	1342	1582	2681	1.25	0.2
	1342	1583	2679	1.17	0.16
DG-1850	1342	1582	2679	1.3	0.16
	1342	1582	2677	1.25	0.2
DG-2050 (1 hr)	1343	1580	2682	1.2	0.25
	1342	1580	2686	1.28	0.15
DG-2050 (1.5 hr)	1340	1580	2682	1.2	0.2
	1342	1582	2686	1.4	0.35
DG-2050 (2hr)	1340	1582	2682	1.4	0.2
	1342	1582	2683	1.4	0.3
DG-2200	1346	1584	2690	1.3	0.2
	1339	1581	2680	1.25	0.25

Graphene (DG) was prepared by annealing of nanodiamond at high temperatures (1650-2200°C) employing graphite furnace. During the annealing process, nanodiamond undergoes phase transition to form graphene. AFM analysis indicated that DG possesses 2-9 layers showing an increase in thickness with an increase in the annealing temperature. These samples have intense D band as compared to EG samples owing to their more defective structure.

2.5.3 Graphene from CVD (CG)

We have carried out CVD of camphor in a two-stage furnace, employing micron sized nickel particles as catalyst. To free from the catalytic Ni particles, the product was thoroughly washed with dilute HCl and characterized by employing different techniques. In Figure 13 we show TEM and AFM images of the graphene sample (CG). Figure 14 shows Raman spectra of CG. The Raman band positions are listed in Table 3.

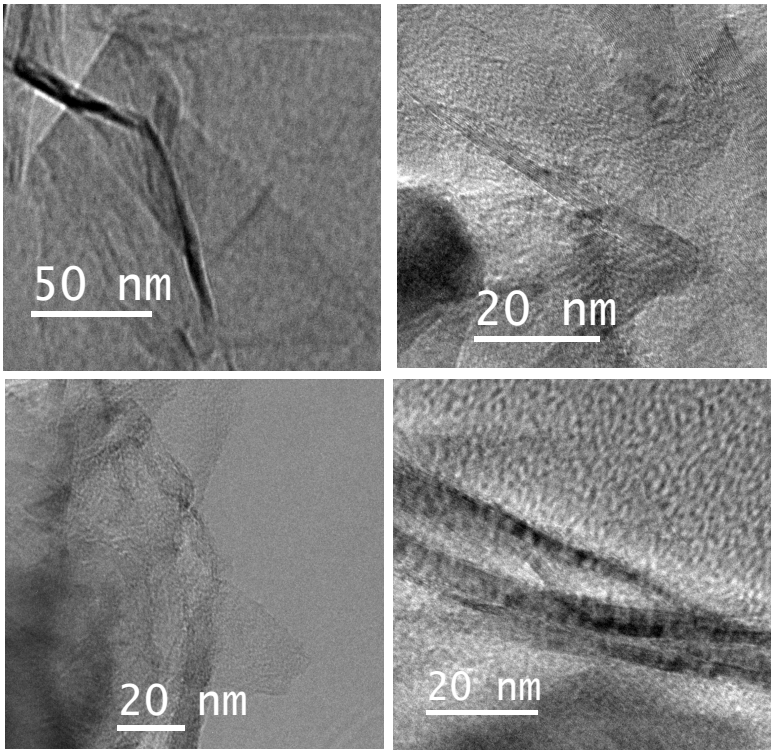

Figure 13a. TEM images of CG.

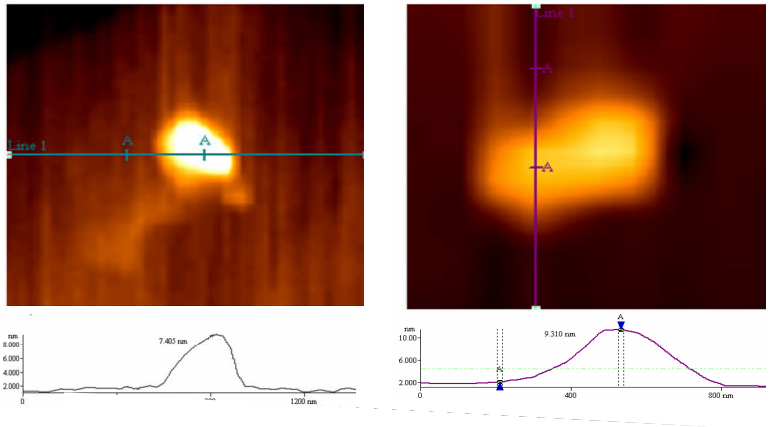

Figure 13b. AFM images of CG.

TEM images of CG show the samples to be comprised of crystalline sheets. AFM cross-section height profile analysis indicates that CG possesses more number of layers than EG and DG containing greater than 20 layers.

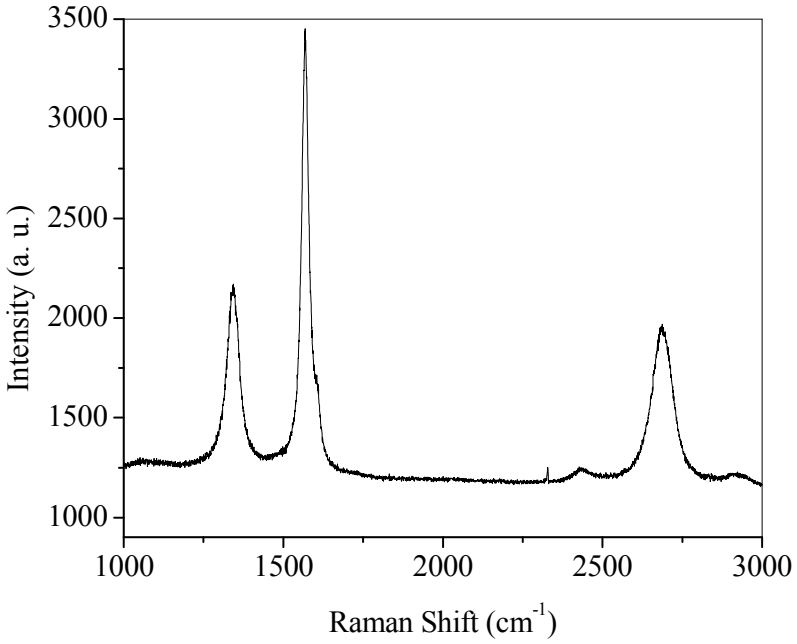

Figure 14. Raman spectrum of CG.

Table 3. Raman band positions along with $I_D/_G$, $I_{2D}/_G$ ratios.

Sample	D (cm^{-1})	G (cm^{-1})	D' (cm^{-1})	2D (cm^{-1})	I_D/I_G	I_{2D}/I_G
CG	1342 1345 1345	1569 1571 1569	1605 1605 1605	2687 2691 2692	0.4 0.55 0.35	0.3 0.3 0.2

We have also carried out CVD to grow large area graphene films on different metal sheets. To obtain quality graphene films, we employed different hydrocarbons, systematically changing the growth conditions. Figure 15a shows FESEM and TEM images of graphene sheets obtained by the thermal decomposition of benzene on nickel

sheet. Figures 15 b and c show the FESEM and TEM images respectively, of graphene sheets obtained by thermal decomposition of methane on nickel sheet.

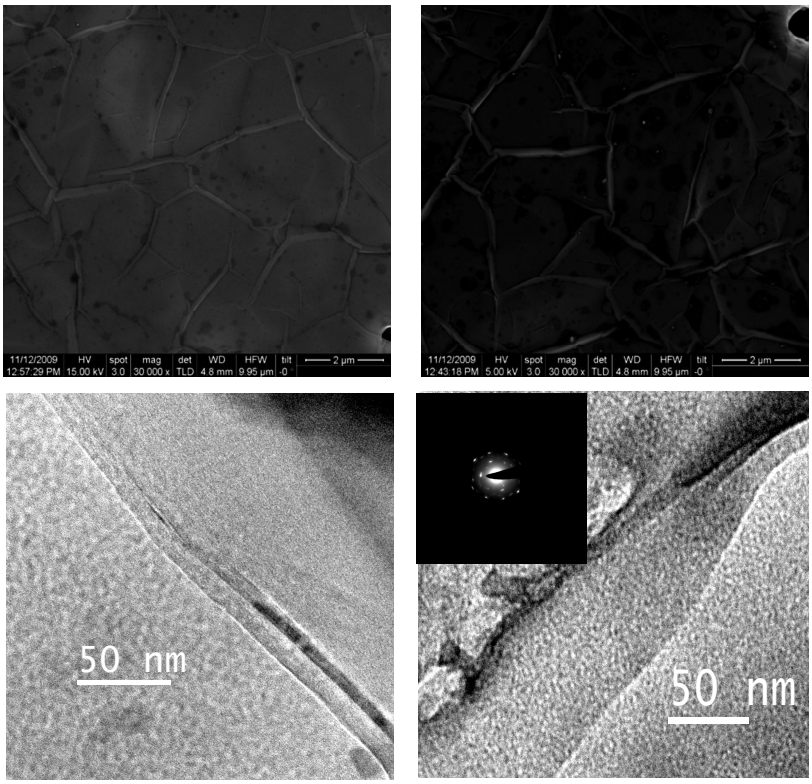

Figure 15. (a) FESEM (top panel) and TEM (bottom panel) images of graphene on a nickel sheet prepared by the thermal decomposition of benzene (argon passed through benzene with flow rate of 200 sccm at 1000 ºC. Inset in Figure shows selected area electron diffraction (SAED) pattern.

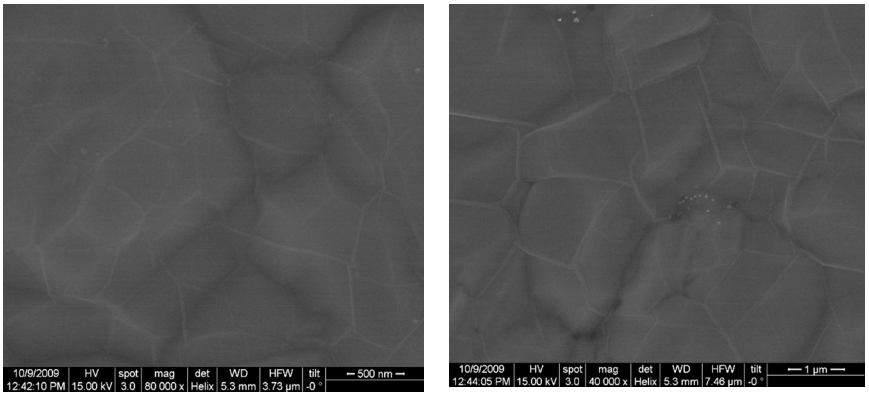

Figure 15b. FESEM images of graphene on a nickel sheet prepared by the thermal decomposition of methane (70 sccm) at 1000 ºC.

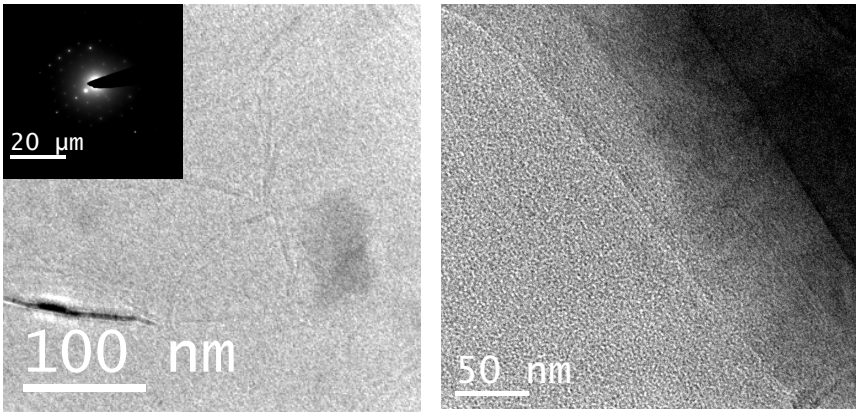

Figure 15c. TEM images of graphene on a nickel sheet prepared by the thermal decomposition of methane (70 sccm) at 1000 ºC. Inset in Figure shows selected area electron diffraction (SAED) pattern.

In Figures 15a, and c we clearly see the edge of the graphene sheet. Insets in Figures a and c show selected area electron diffraction (SAED) patterns. Figures 15(d, e) and f show electron microscopy images of graphenes obtained by thermal decomposition of ethylene on nickel and acetylene on cobalt respectively. In addition to methane, ethylene, acetylene and benzene, liquefied petroleum gas (LPG) has also been employed for graphene growth (Table 5). LPG yielded mainly graphene films comprising few-layers. Growth conditions and the obtained results are summarized in Tables 4 and 5.

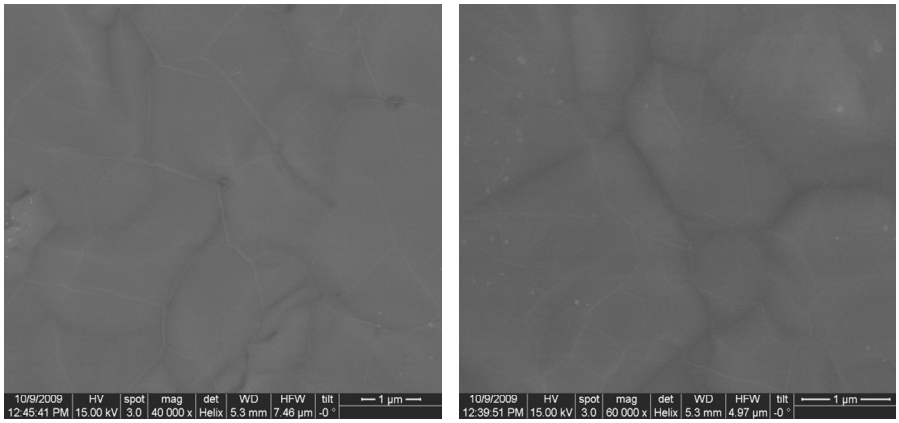

Figure 15d. FESEM images of graphene on a nickel sheet prepared by the thermal decomposition of ethylene (4 sccm) at 900 ºC.

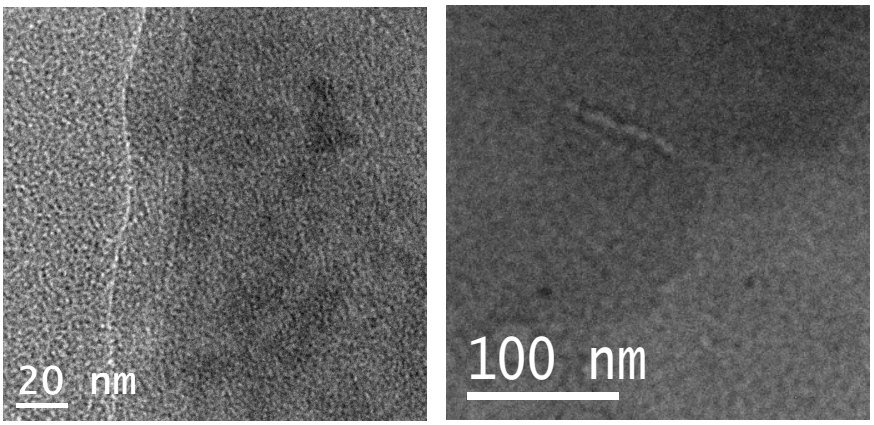

Figure 15e. TEM images of graphene on a nickel sheet prepared by the thermal decomposition of ethylene (4 sccm) at 900 ºC.

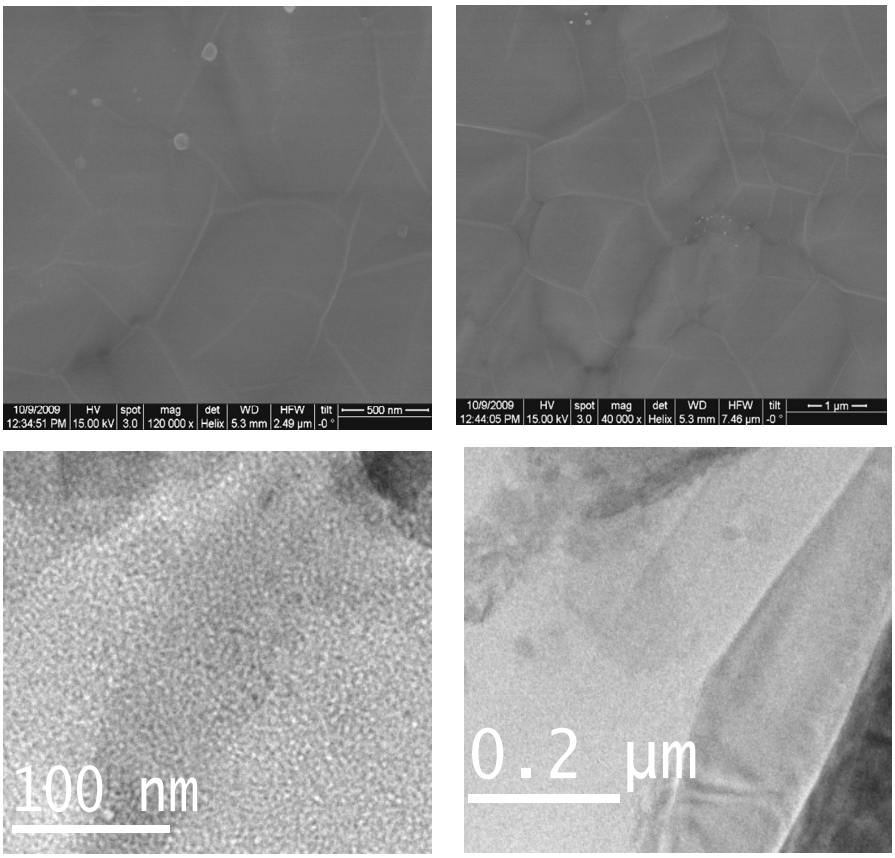

Figure 15f: FESEM (top panel) and TEM (bottom panel) images of graphene on a cobalt sheet prepared by the thermal decomposition of acetylene (4 sccm) at 800 ºC.

Table 4. Growth conditions of graphene films comprising single/few layers.

Precursor (Hydrocarbon)	Annealing temperature (°C)	Reaction temperature(°C) and time (min)	Flow rate (Sccm) (Precursor/ Hydrogen)	**Single/ few layers**
Methane	1100	1000/5	70/400	
Ethylene	1100	900/5	5/400	
Benzene	1100	1000/5	Argon(100)/400	
Benzene	1100	1000/5	Argon (50)/400	
Acetylene	1100	800/5	4/400	

Table 5. Growth conditions of graphene fims comprising few-layers.

Precursor (Hydro carbon)	Annealing Temperature (°C)	Reaction Temperature (°C) and time (min)	Flow Rate (Sccm) (Precursor/Hydrogen)	Few layers
Ethylene	1100	1000/10	50/500	
Ethylene	1100	900/5	15/146	
Ethylene	1100	800/10	15/400	
Ethylene	1100	900/20	30/50	
Ethylene	1100	800/20	15/50	
Ethylene	1100	900/10	15/150	
Ethylene	1100	100/10	10/400	
Ethylene	1100	900/10	10/400	
Benzene	1100	1000/30	100(H_2)	
Benzene	1100	800/15	Argon (60)//700	
Benzene	1100	800/7	Argon(75)/400	
Benzene	1100	800/5	Argon(100)/400	
Benzene	1100	1000/5	Argon(15)/400	
Benzene	1100	700/15	Argon(75)/400	
LPG	1100	800/5	-/700	

In Figures 16 and 17, we show Raman spectra recorded from different graphene samples obtained by CVD method. Raman spectra of graphene obtained on a nickel sheet by the

thermal decomposition of methane, ethylene and benzene, specially the first two hydrocarbons show intense 2 D band relative to the G band with hardly any D band (see Figures 16a and b, clearly indicative of SLGs.[38] Figures 17 a and b show the Raman spectra of graphene prepared on a cobalt foil by the thermal decomposition of methane and acetylene respectively. The spectrum in b is more similar to that of SLG. All these graphene samples show G band at 1580 cm^{-1} and 2 D band around 2670 cm^{-1} with a narrow line width of 30-40 cm^{-1}. The narrow line width and relatively high intensity of 2D band confirm that these Raman spectra correspond to graphenes having 1-2 layers.[38]

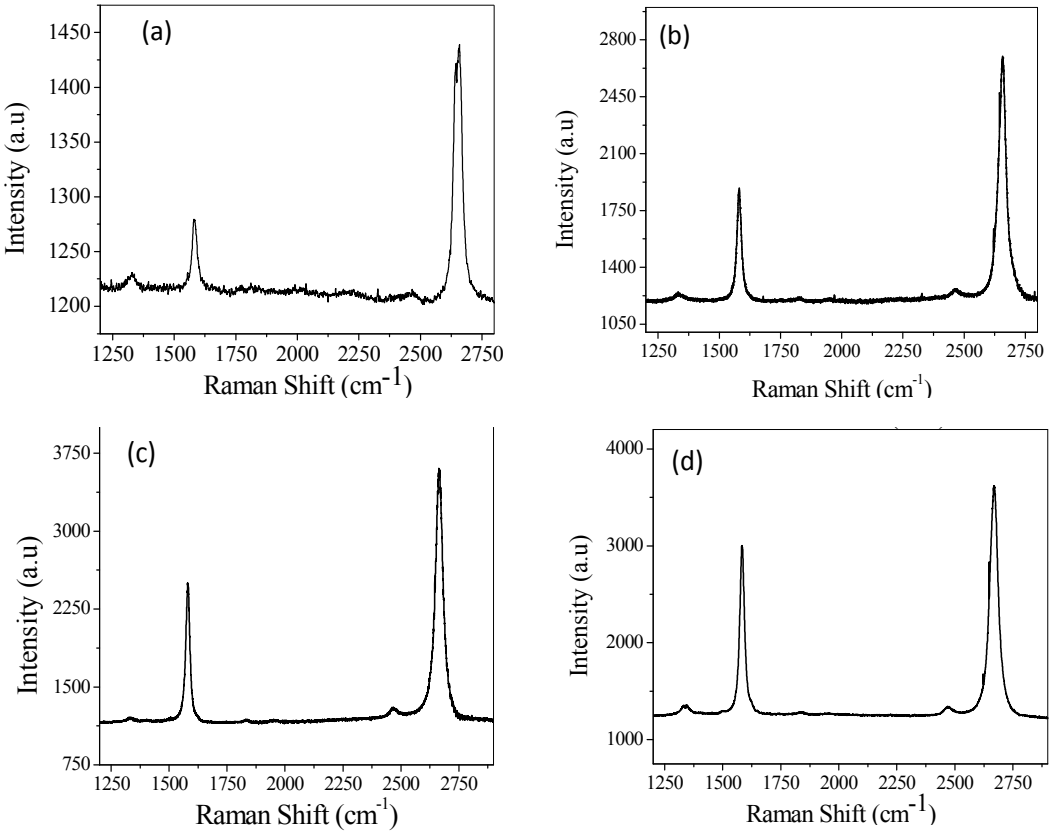

Figure 16: Raman spectra of graphene on a nickel sheet prepared by the thermal decomposition of (a) methane (70 sccm) at 1000 ºC (b) ethylene (4 sccm) at 900 ºC and (c) benzene (argon passed through benzene with flow rate of 200 sccm) at 1000 ºC and (d) benzene (argon passed through benzene with flow rate of 400 sccm) at 1000 ºC.

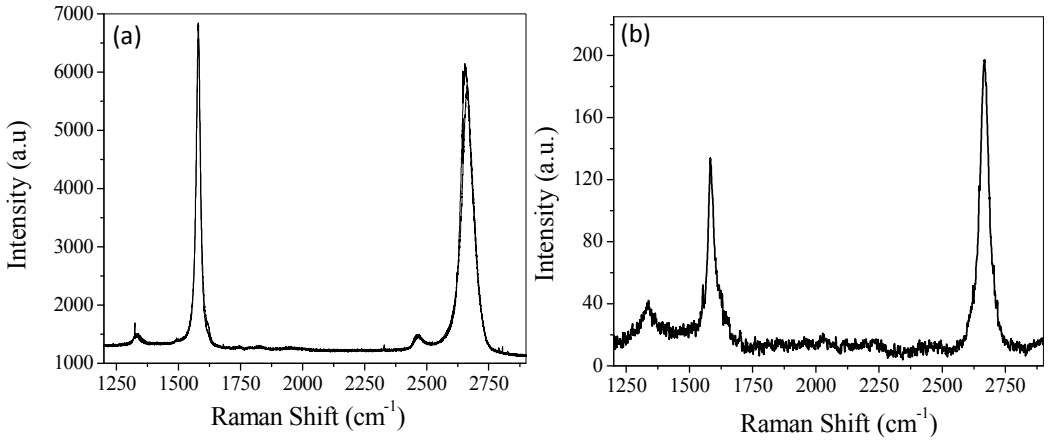

Figure 17. Raman spectra of graphene on a cobalt sheet prepared by the decomposition of (a) methane (64 sccm) at 1000 ºC and (b) acetylene (4 sccm) at 800 ºC.

Thermal CVD process has been effectively employed to prepare graphene. In this process, pyrolysis of camphor was carried out on nickel particles. AFM analysis showed that graphene samples contain more than 10 layers. Using CVD, we have also grown large area graphene films on nickel and cobalt sheets by decomposing different hydrocarbons. Raman study of these films revealed that graphene films comprise single- and bi- layer graphenes.

2.5.4 Graphene by arc discharge in a H_2 atmosphere (HG)

To prepare HG, arc discharge experiments were carried out in a stainless steel chamber that was filled with hydrogen and helium or methane and helium without using any catalyst. In Figure 18 we show schematic representation of arc-discharge apparatus. The proportions of H_2 and He used in our experiments are H_2 (70 torr)/He (500 torr), H_2 (100 torr)/He (500 torr), H_2 (200 torr)/ He (500 torr), H_2 (400 torr)/He (300 torr) and CH_4 (300 torr)/He (300 torr) and the corresponding samples are designated as HG 1, HG 2, HG 3, HG 4 and HG 5 respectively. In addition to the different proportions of H_2 we have also carried out the experiments at different currents and found that at low currents, arc discharge does not occur in the presence of hydrogen. Before characterization, these HG

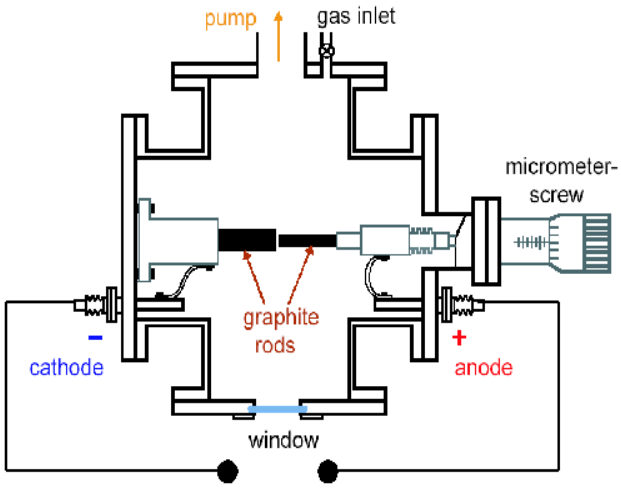

Figure 18. Schematic representation of arc-discharge apparatus.

samples were annealed in hydrogen atmosphere at 1000 ºC for 4 hours. To obtain the TEM images, the so obtained annealed samples were dispersed in CCl_4 and drop casted on TEM grid. In Figure 19 we show TEM images of all the HG samples.

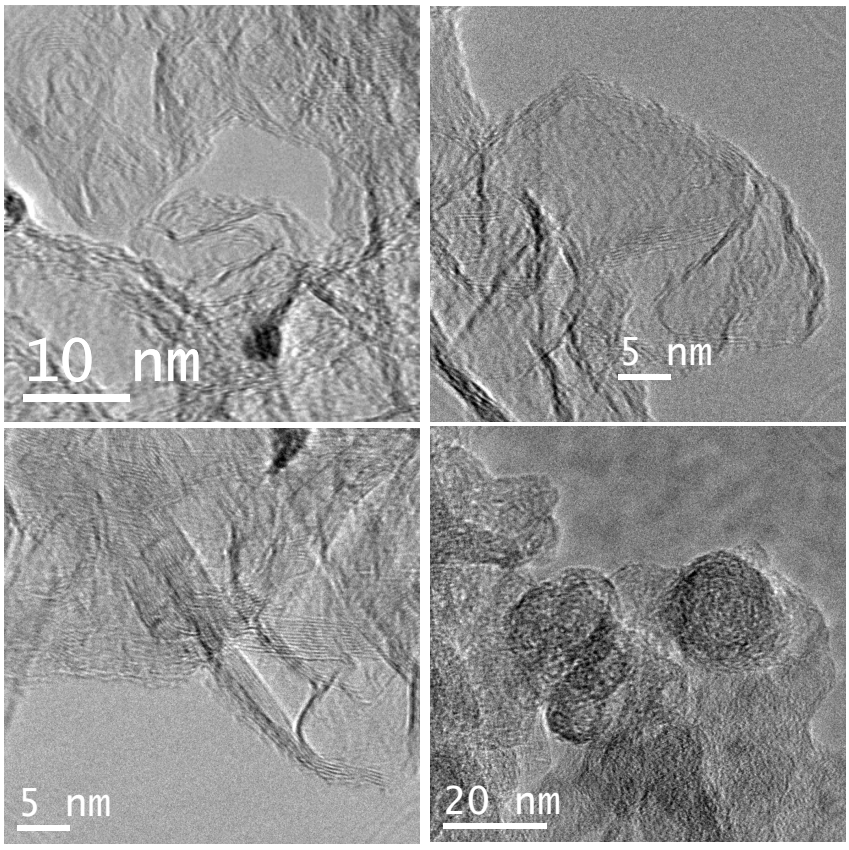

Figure 19 a. TEM images of HG 1.

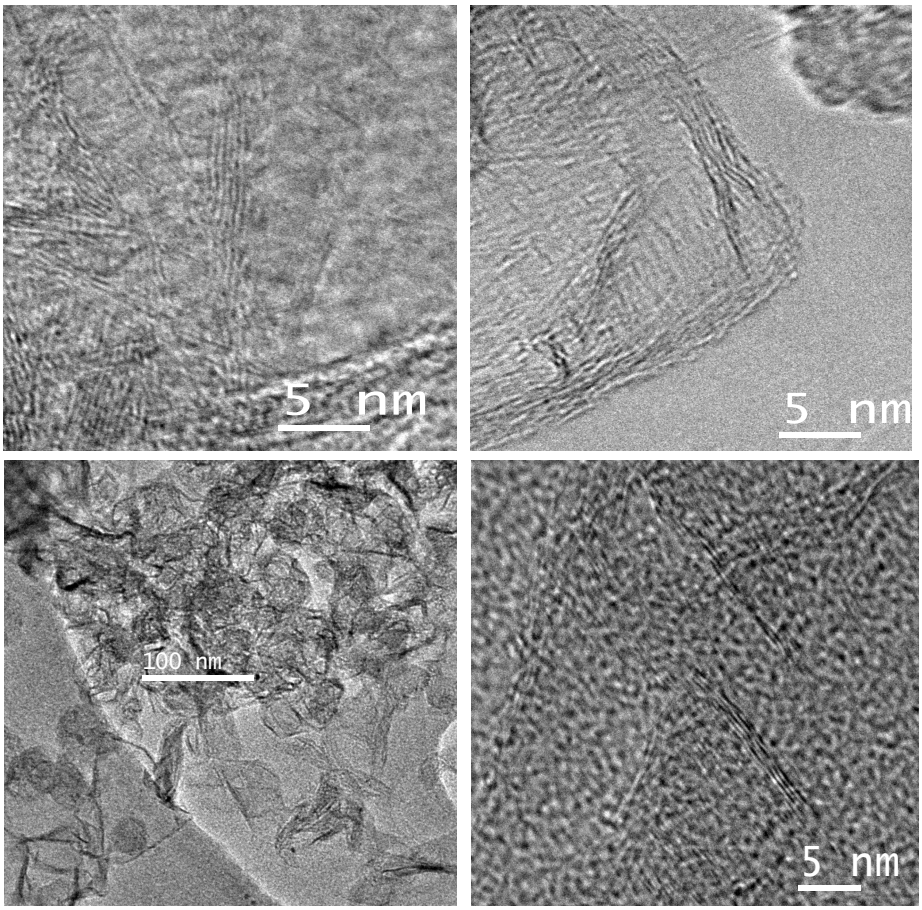

Figure 19b. TEM images of HG 2.

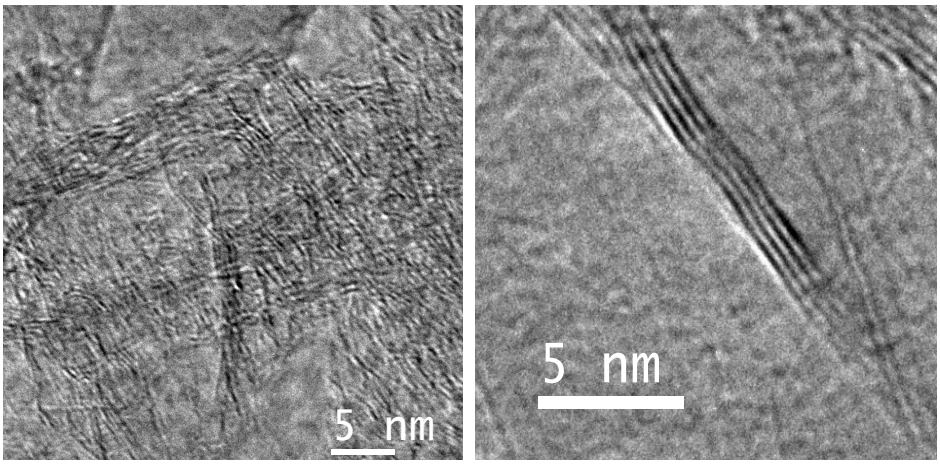

Figure 19 c. TEM images of HG 3.

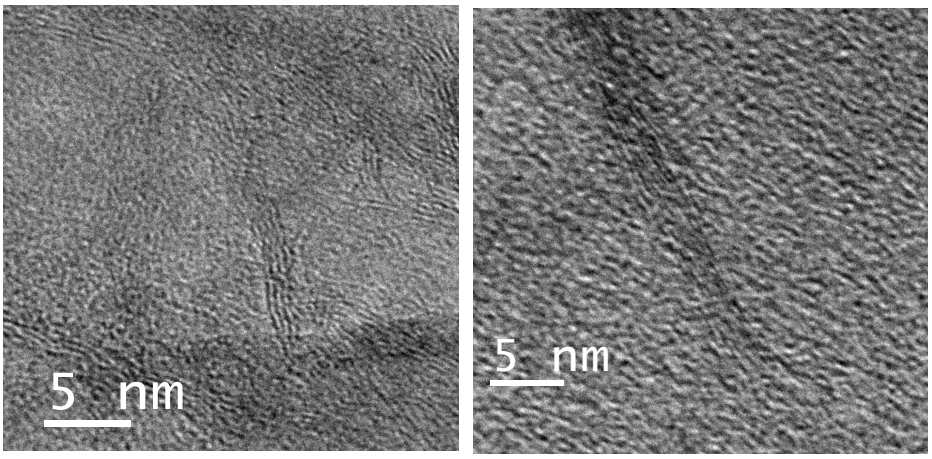

Figure 19d. TEM images of HG 4.

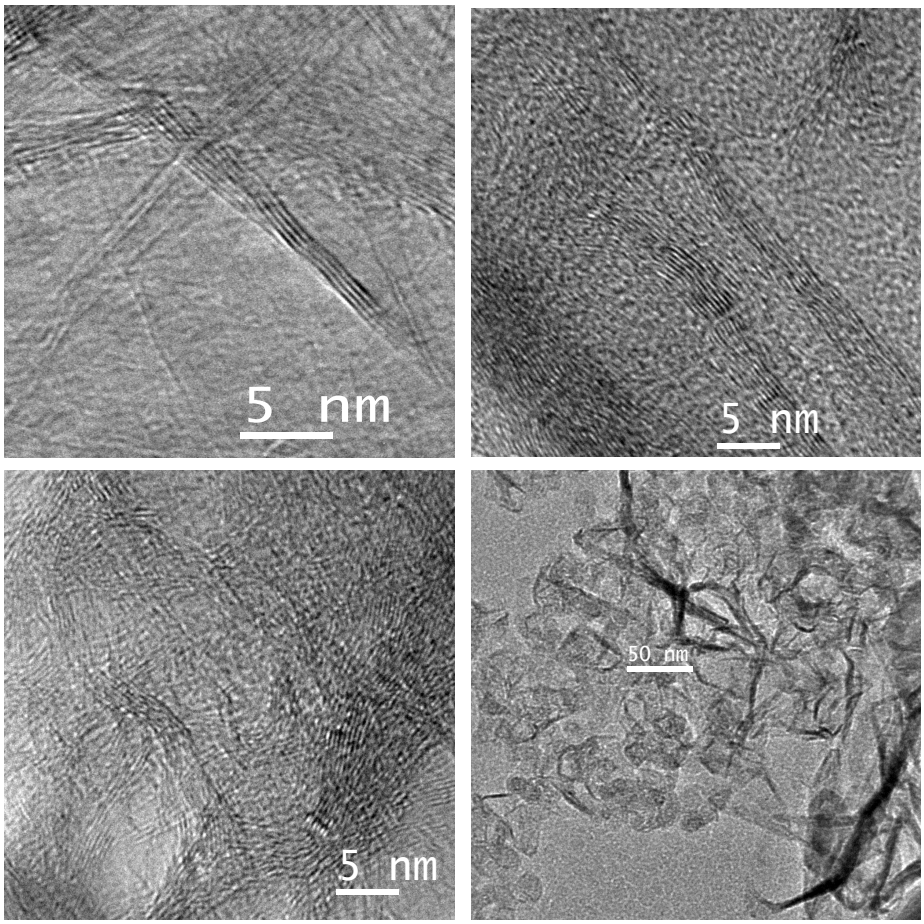

Figure 19 e. TEM images of HG 5.

From the above TEM images we can observe that HG 3 and HG 4 have only graphene sheets whereas remaining samples comprise graphene sheets and onion particles. The HG 3 was obtained in higher yields compared to HG 4. From this we can conclude that, as the content of hydrogen in the arc discharge chamber is decreased, the relative proportion of closed shell polyhedral particles increases. On the other hand, excess hydrogen results in lower yields. We found that under optimal conditions, this method yields 10-20 wt % of graphene with respect to the weight of the anode and the best conditions to obtain the quality samples are: current 100 amp, ratio of H_2 to He is (200 torr)/ (500 torr).

We have also carried out the experiments using nickel as a catalyst, which gave similar results. In these experiments nickel filled graphite rod was employed as consuming anode and the proportion of H_2 and He was maintained at 200 (torr)/500 (torr).We show TEM images of the obtained sample (HG 6) in Figure 19f.

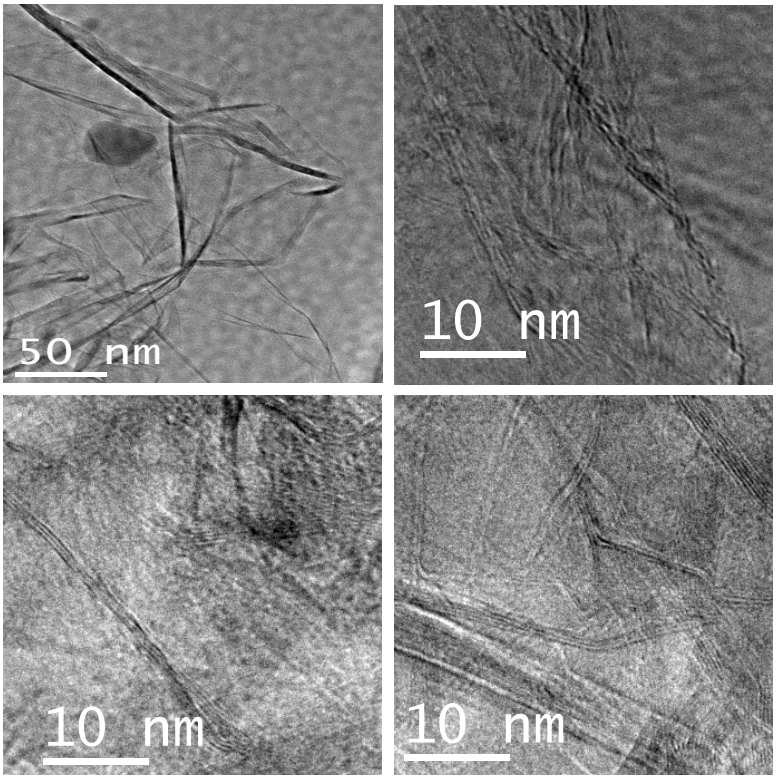

Figure 19f. TEM images of HG 6.

We have recorded AFM images of HG 3 sample using Innova microscope. AFM study indicates that HG 3 (Figure 20) comprises 2-3 layers. Raman spectra of all these samples show characteristic D, G and 2D bands. In Figure 21, we show Raman spectra of HG 1 and HG 3. Raman band positions with I_D/I_G, I_{2D}/I_G values of all the HG samples are listed in Table 6.

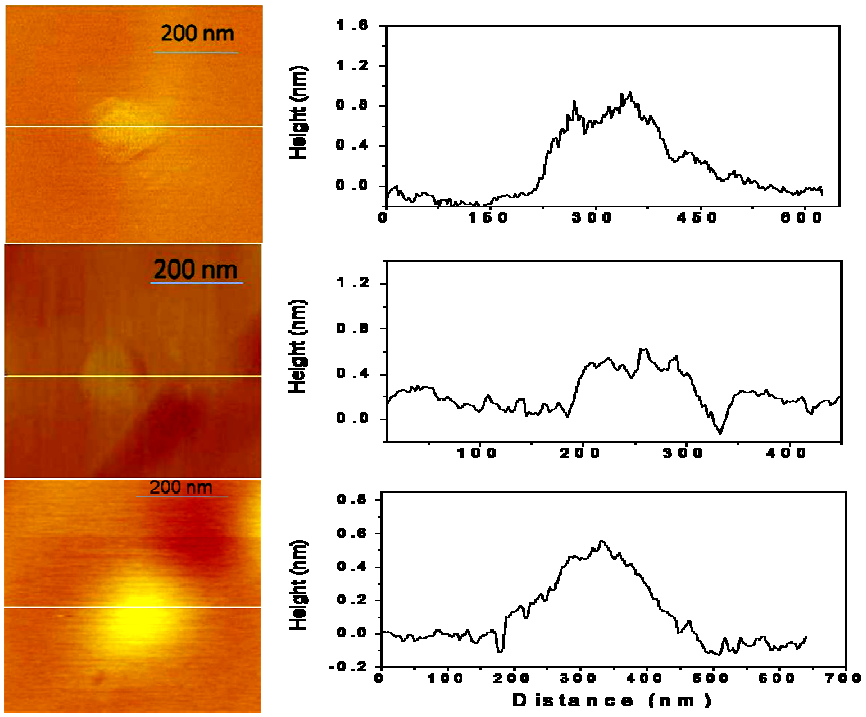

Figure 20. AFM images of HG 3.

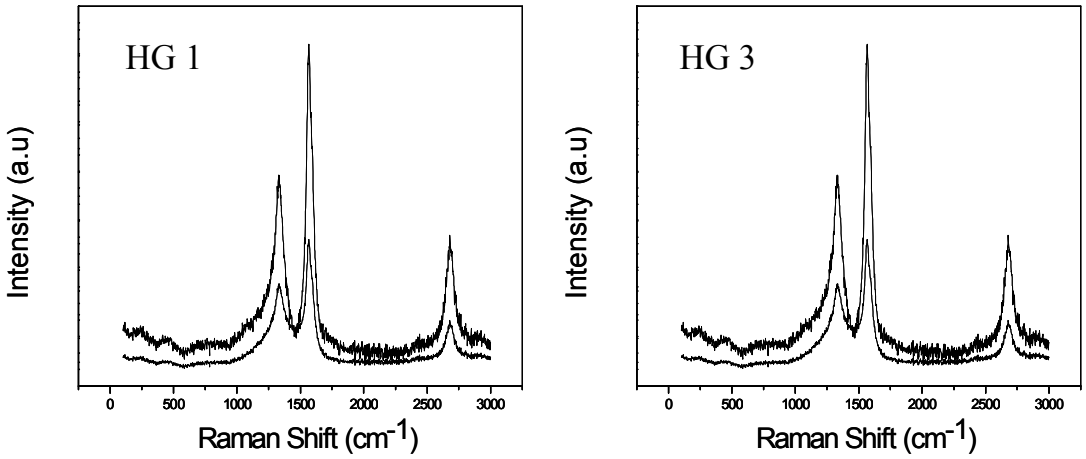

Figure 21. Raman spectra of HG 1 and HG 3.

Table 6. Raman band positions of HG samples

Sample	D (cm^{-1})	G (cm^{-1})	D' (cm^{-1})	2D (cm^{-1})	I_D/I_G	I_{2D}/I_G
HG-1	1329	1560	1597	2665	0.6	0.4
	1328	1560	1597	2660	0.55	0.37
HG-2	1324	1566	1590	2665	0.6	0.3
	1352	1567	1590	26660	0.62	0.32
HG-3	1337	1573	1603	2690	0.56	0.34
	1339	1573	1602	2691	0.52	0.3
HG-4	1335	1566	1597	2684	0.6	0.3
	1336	1565	1597	2684	0.55	0.32
HG-5	1321	1569	1601	2642	0.8	0.7
	1320	1569	1599	2643	0.55	0.5

This new technique to prepare graphene, by arc-evaporation of graphite in hydrogen atmosphere, produces graphene in large quantities. It exploits the fact that the presence of H_2 during the arc discharge terminates the dangling carbon bonds with hydrogen and thus prevents the formation of closed structures. AFM analysis indicated that this process yields graphene samples with mostly 2-4 layers having relatively smaller lateral dimensions ~ 100-200 nm. As this sample has relatively lesser number of layers with small lateral dimensions it may serve as a potential candidate as nanofiller in nanocomposite applications.

2.5.5 Reduced graphene oxide (RGO)

We reduced the SGO using hydrazine hydrate/ethylene glycol as a reducing agent under refluxing conditions and through hydrothermal (HT) and microwave (MW) routes. These samples are designated as RGO, RGO (HT) and RGO (MW) respectively. In Figure 22 we show FESEM and TEM images of SGO, RGO, RGO (MW) and RGO (HT). Raman spectra of RGO, RGO (MW) and RGO (HT) shown in Figure 23 and the corresponding Raman band positions with I_D/I_G values are listed in Table 7.

(a)

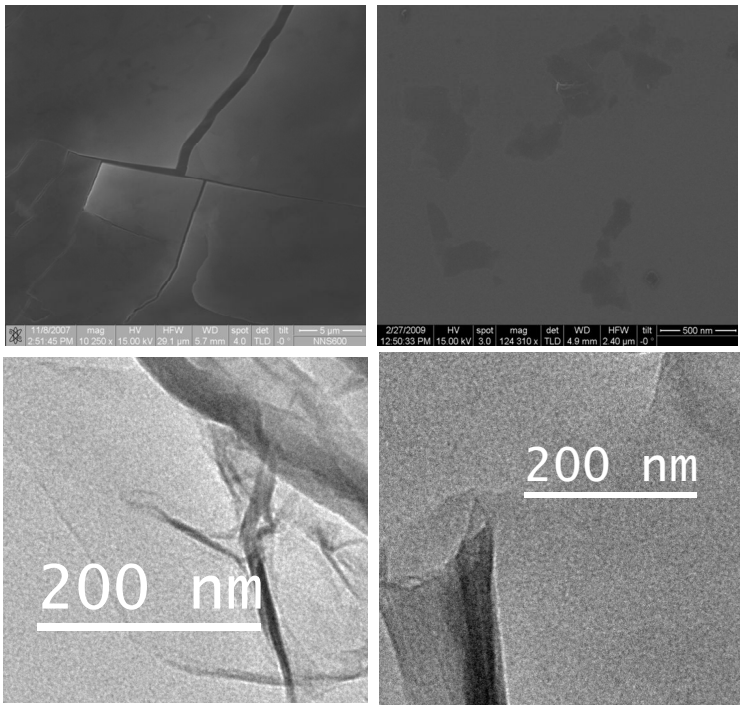

Figure 22a. FESEM (top panel) and TEM (bottom panel) images of SGO.

(b)

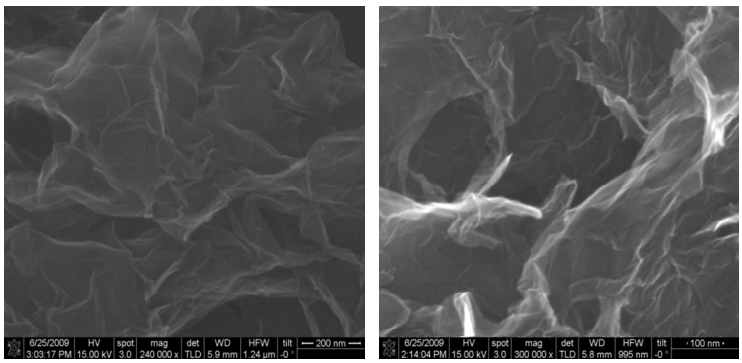

Figure 22b. FESEM images of RGO.

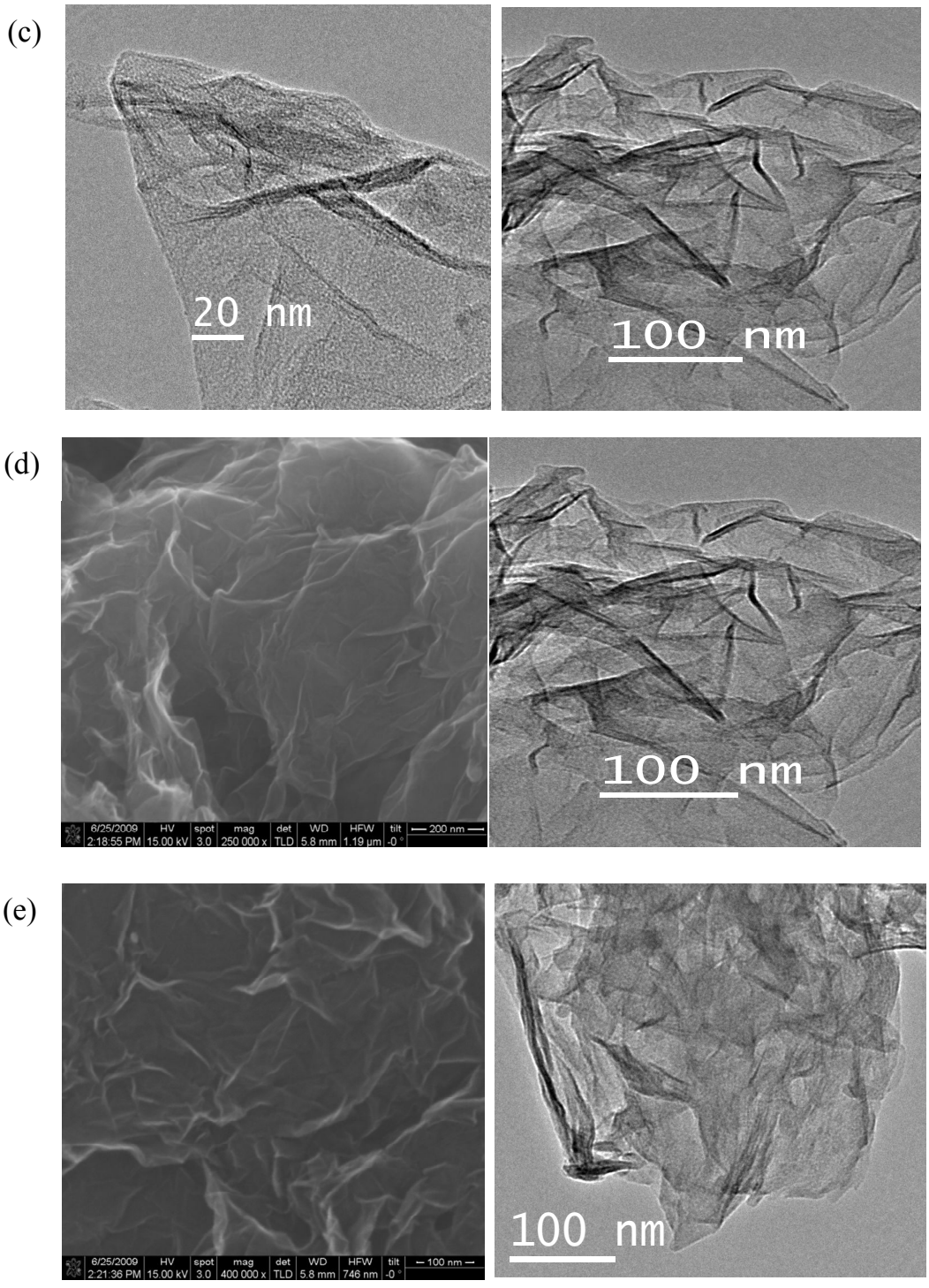

Figure 22. (c) TEM images of RGO, (d) FESEM (left panel) and TEM (right panel) images of RGO (MW) and (e) FESEM (left panel) and TEM (right panel) images of RGO ().

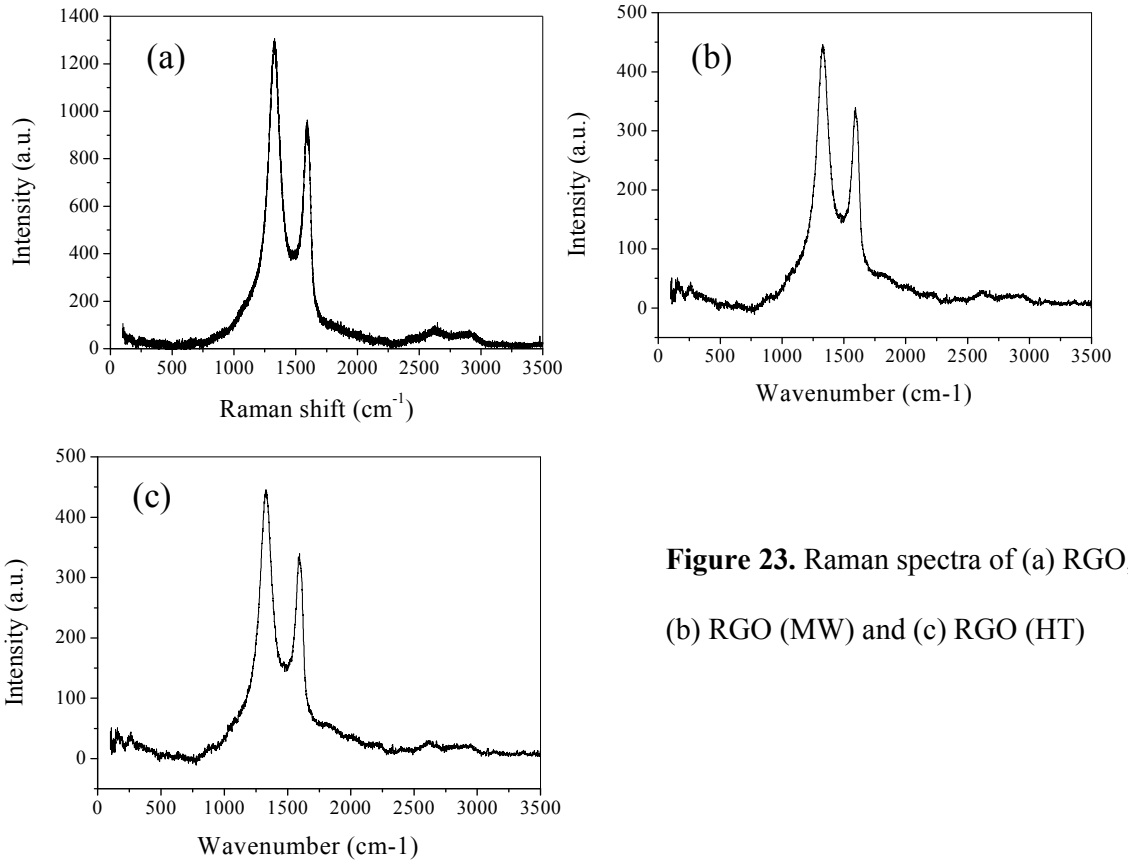

Figure 23. Raman spectra of (a) RGO, (b) RGO (MW) and (c) RGO (HT)

Table 6. Raman band positions and I_D/I_G values of RGO, RGO (MW) and RGO (HT).

Sample	D (cm^{-1})	G (cm^{-1})	I_D/I_G
RGO	1327	1591	1.45
RGO (MW)	1329	1593	1.3
RGO (HT)	1327	1593	1.3

Reduction of SGO produces highly reduced graphene oxide sheets with minimal amount of functionalities remaining on the surface. TEM and AFM analysis concluded that graphene sheets are crumpled and comprise 2-6 number of layers. Raman spectra showed an intense D band and a weak 2D band. The latter might be due to the remaining functionalities on the surface, and defects incorporated in the sample during ultra-sonication.

2.5.6 Radiation induced-RGO

We could reduce SGO employing sunlight, UV and laser. In Figure 24a, we show a photograph of the SGO solution in water medium which is brownish yellow in colour. It gradually turns reddish after 2 hr of irradiation with sunlight, as can be seen from Figure 24b. When the irradiation is continued for 10 hr, it finally turns black in colour, as can be seen from Figure 24c. The colour change of SGO from brownish yellow to black is a clear evidence of the occurrence of reduction.

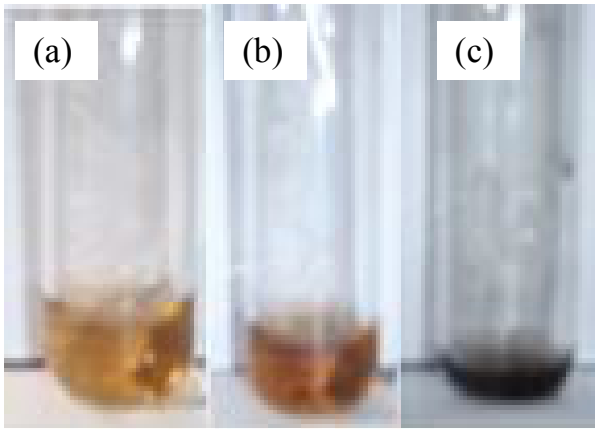

Figure 24. Photographs of SGO solutions (a) before irradiation by sunlight and after irradiation by sunlight for (b) 2 hr and (c) 10 hr.

IR spectra of SGO samples show the decrease in intensity of the carbonyl stretching band after 10 hr of irradiation. Similarly, the intensities of bands due to other oxygen containing functional groups also decrease after prolonged sunlight irradiation. Figure 25 shows FESEM images of graphene oxide before and after irradiation with sunlight (10 hr). We notice only a marginal change in the surface after irradiation, with only minor buckling of the flakes. Irradiation with ultraviolet light yields the same result after irradiation for only 2 hr. In Figure 26 we depict the FESEM images of SGO before and after UV irradiation. UV treatment seems to render the surface buckled. More graphene edges become visible on the surface after irradiation.

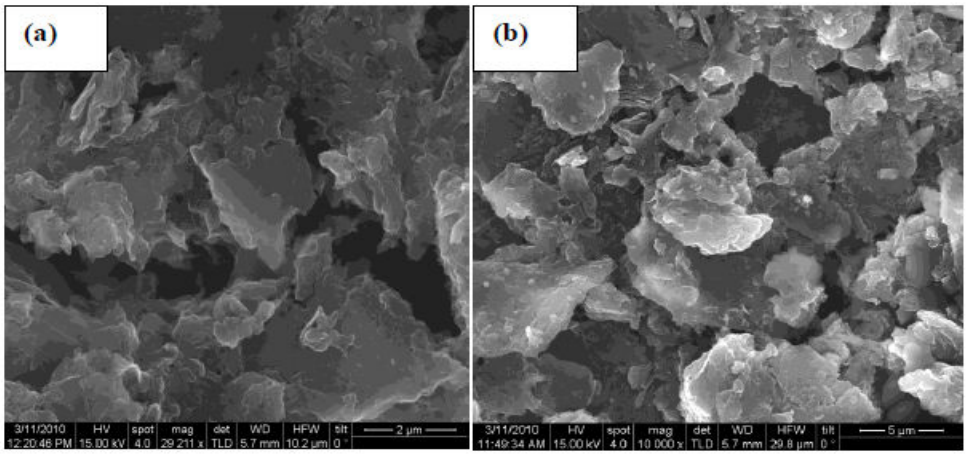

Figure 25. FESEM images of (a) untreated SGO and (b) after 10 hr of irradiation by sunlight.

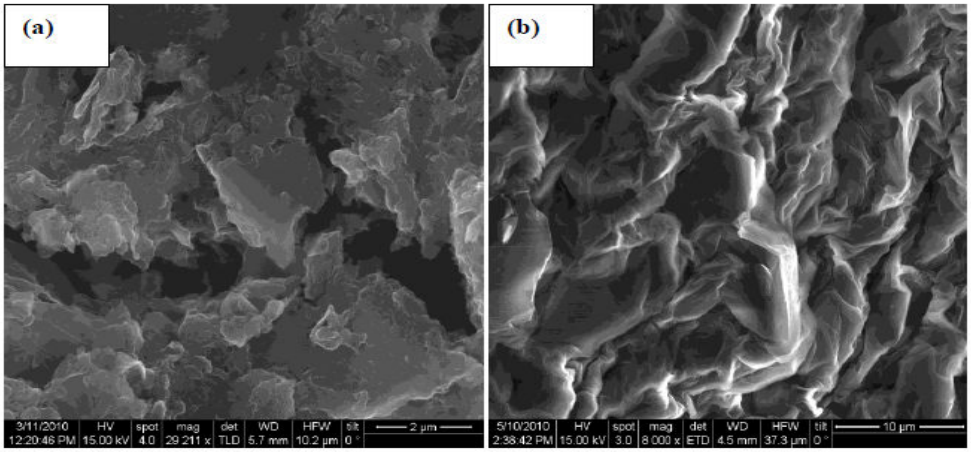

Figure 26. FESEM images of (a) untreated SGO and (b) after 2 hr of UV irradiation.

We have obtained the most interesting results with KrF excimer laser treatment. Brownish yellow colour of the graphene oxide solution becomes deeper brownish red, just after short laser irradiation (approximately 4 minutes of laser treatment, 1000 laser shots at 300 mJ). After 1 hr of laser treatment (18000 laser shots), the graphene oxide solution turns black in colour (Figure 27). The fast colour change obtained with excimer laser is due to large laser fluence as compared to areal energy density for sunlight and ultraviolet light

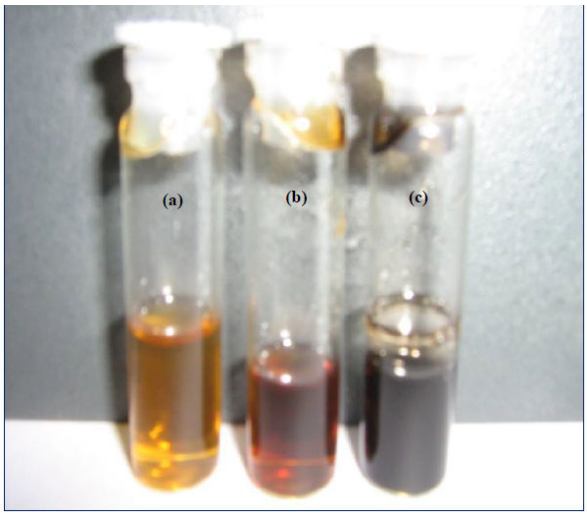

Figure 27. Photographs of (a) untreated SGO and after irradiation with an excimer laser radiation (300 mJ) for (b) 1000 shots and (c) 18000 shots.

IR spectra show the near disappearance of carbonyl stretching band as well as of other bands due to oxygen functionalities, after 1 hr of irradiation. Excimer laser irradiation not only reduces the graphene oxide effectively but also fragments the graphene as can be seen from Figure 28a. Excimer laser irradiation of a solid graphene oxide disc gives rise to highly porous surface features with large number of edges, as can be seen from the FESEM image in Figure 28b. Solid graphene oxide requires only 4-5 laser shots (1 second time for 5 Hz reprate) to be completely reduced to black graphene, devoid of any oxygen containing functional groups. Such reduction of graphene oxide in a few seconds makes excimer laser an excellent choice for reduction. This is noteworthy since no reducing agent is required in this procedure and the extent of reduction is better than that by any other means. Wattage/cm^2 of KrF excimer laser and low pressure UV (254 nm) mercury lamp used in our experiments are 3 mW /cm^2 and 90 μW/cm^2 respectively. Areal power density of the KrF excimer laser is, thus, approximately 33 times larger than that of the mercury lamp.

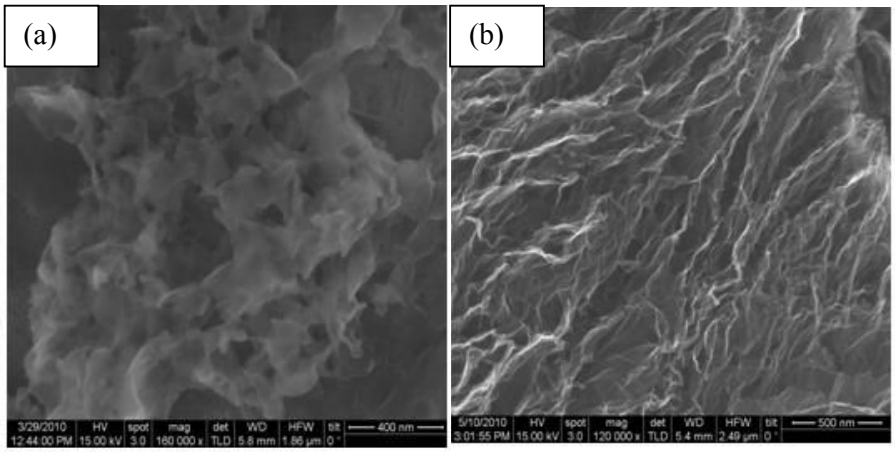

Figure 28. FESEM images of (a) SGO after treatment of solution with excimer laser radiation at 300 mJ laser energy with 1000 shots and (b) the solid with 5 laser shots.

X-ray photoelectron spectroscopy was also carried out on solid graphene oxide and excimer laser-reduced graphene oxide (LRGO). The signals of C 1s and O 1s were analyzed which clearly confirmed the reduction of graphene oxide. Raman spectra of the reduced samples such as LRGO show D, G and 2D bands respectively at 1332, 1580 and 2640 cm^{-1}. Atomic force microscopic image of the laser reduced samples shows a large number of tiny flakes (20-120 nm) with large unbroken flakes comprising 1-7 layers. Electronic properties change after irradiation of SGO as expected. Two-probe resistance measurements show that the resistivity of GO, SRGO and LRGO are 5000, 550 and 41 ohm-cm respectively. This is expected as reduced SGO will have less oxygen containing functionalities which would make the samples more conducting. We have also carried out the irradiation of graphite oxide solutions in water with excimer laser of 300 mJ beam energy. It is found that after 1 h of irradiation, the brownish yellow colour of graphite oxide solution changes to black as can be seen from Figure 29. Thus, the sonication step

is actually not necessary because excimer laser itself can do fragmentation as well as reduction. It also demonstrates the generality of this technique.

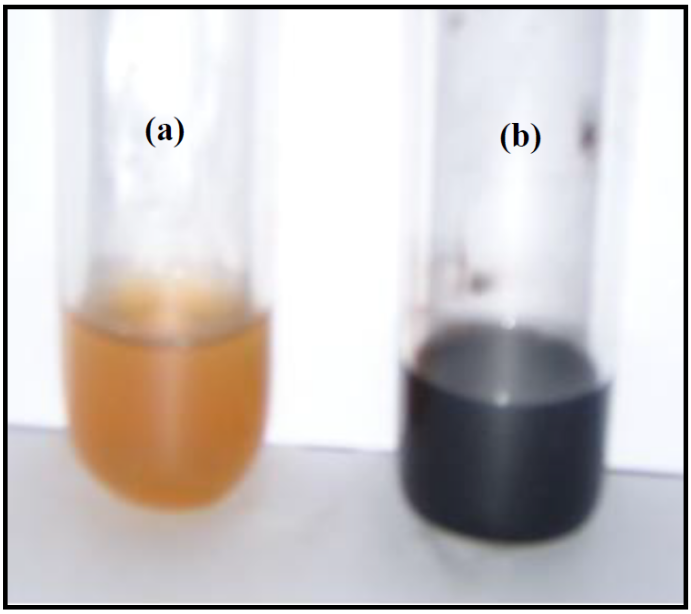

Figure 29. Photographs of (a) graphite oxide solution in water and of (b) excimer laser reduced graphite oxide.

Without employing any reducing agent, reduction of SGO has been achieved utilizing various sources of radiation viz. sunlight, UV and laser. Reduction of SGO has been confirmed from visible color change of the SGO solution, as well as from its UV absorption and IR spectra. In comparison to other synthetic methods of preparing graphene, this process would be an easy and cost effective technique.

2.5.7 TGA analysis of graphenes

We have carried out the thermogravimetric analysis of CG, EG and DG (Figure 30). CG undergoes sharp oxidation around 750°C while DG gets oxidized at 700 °C. EG exhibits the lowest oxidation temperature of ~520 °C, exhibiting a sharp mass loss at this temperature followed by gradual mass loss. The low oxidation temperature of EG is ascribed to the presence of functional groups while the other graphenes consist of

pure carbon and are more crystalline in nature as observed in the x-ray diffraction patterns.

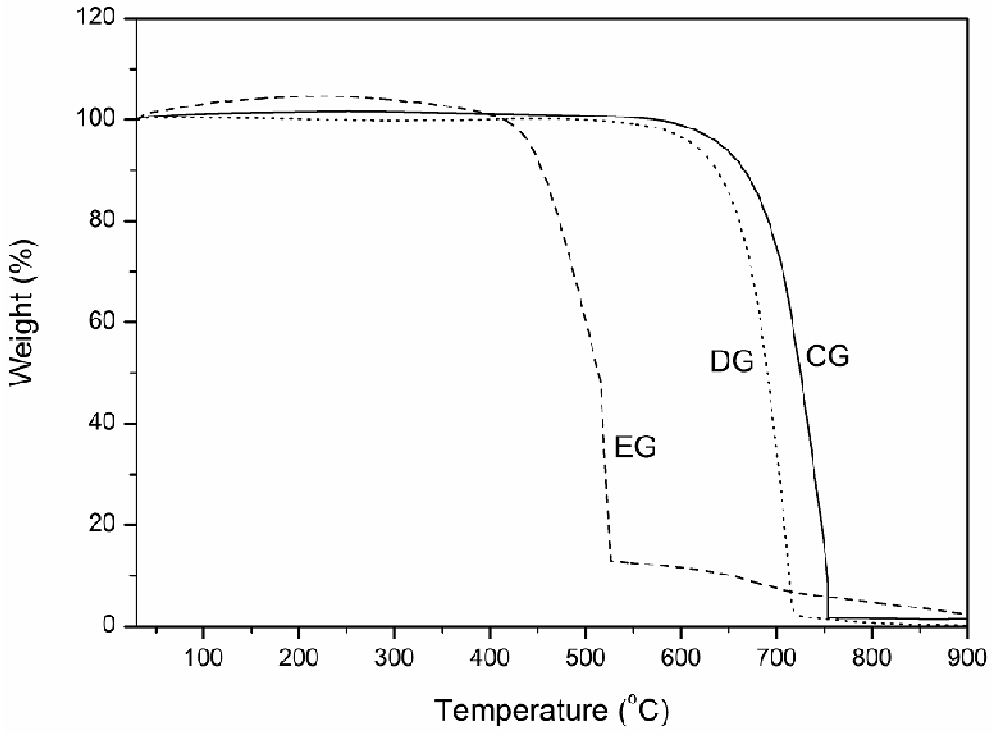

Figure 30. Thermogravimetric analysis of the different graphenes.

2.6 Conclusions

In conclusion, graphene samples were prepared by different procedures and characterized utilizing various techniques such as, field emission scanning electron microscopy (FESEM), transmission electron microscopy (TEM), atomic force microscopy (AFM), Raman spectroscopy and thermo gravimetric analysis (TGA). The procedures employed for the preparation of graphene are thermal exfoliation of graphite oxide, conversion of nanodiamond, chemical vapour deposition and reduction of single-layer graphene oxide. The graphene sample EG was prepared by giving sudden thermal shock to graphite oxide at higher temperatures. AFM analysis indicated that EG possesses 2-6 number of layers. DG was prepared by annealing of nanodiamond at 1650-2200 °C employing graphite furnace. DG comprises 2-9 layers showing an increase in thickness

with the increase in the annealing temperature. CG was obtained by pyrolysis of camphor and possesses more than 10 layers. Using CVD process, large area graphene films were grown on nickel and cobalt sheets. Raman study concluded that these films comprise single- and bi-layers graphenes. Reduction of SGO was carried out using hydrazine hydrate/ethylene glycol as a reducing agent under refluxing conditions and through hydrothermal or microwave treatments. RGO samples are observed to have 2-6 layers, which are mostly crumpled. In addition to the aforementioned, common synthetic procedures, we have developed two new routes viz. arc-evaporation of graphite in H_2 and He atmosphere and radiation induced reduction of graphene oxide to prepare graphene. It appears that in the former method, H_2 plays a key role in the formation of graphene sheets by avoiding to roll into tubular form. Graphene samples obtained by this process contain mostly 2-4 layers. For the first time, SGO has been reduced by various sources of radiation such as sunlight, UV light and KrF excimer laser. Among these, laser irradiation has proven to be an efficient procedure for large-scale synthesis of graphene in shorter time scales.

2.7 References

[1] P. R. Wallace, *Phys. Rev.* **1947**, *71*, 622.

[2] C. Schafhaeutl, *Journal für Praktische Chemie* **1840**, *21*, 129.

[3] D. R. Dreyer, S. Park, C. W. Bielawski, R. S. Ruoff, *Chem. Soc. Rev.* **2010**, *39*, 228.

[4] W. Gao, L. B. Alemany, L. Ci, P. M. Ajayan, *Nat. Chem.* **2009**, *1*, 403.

[5] C. Schafhaeutl, *Phil. Mag* **1840**, *16*, 570.

[6] H.-P. Boehm, E. Stumpp, *Carbon* **2007**, *45*, 1381.

[7] D. R. Dreyer, R. S. Ruoff, C. W. Bielawski, *Angew. Chem. Int. Ed.* **2010**, *49*, 9336.

[8] M. Inagaki, *J. Mater. Res.* **1989**, *4*, 1560.

[9] C. Herold, A. Herold, P. Lagrange, *J. Phys. Chem. Solids* **1996**, *57*, 655.

[10] M. Noel, R. Santhanam, *J. Power Sources* **1998**, *72*, 53.

[11] N. E. Sorokina, I. V. Nikol'skaya, S. G. Ionov, V. V. Avdeev, *Russ. Chem. Bull.* **2005**, *54*, 1749.

[12] Z. H. Liu, Z. M. Wang, X. J. Yang, K. T. Ooi, *Langmuir* **2002**, *18*, 4926.

[13] B. C. Brodie, *Philos. Trans. R. Soc. Londo* **1859**, *149*, 249.

[14] B. C. Brodie, *Quarterly Journal of the Chemical Society of London* **1860**, *12*, 261.

[15] D. R. Dreyer, H. P. Jia, C. W. Bielawski, *Angew. Chem. Int. Ed.* **2010**, *49*, 6813.

[16] S. Stankovich, D. A. Dikin, R. D. Piner, K. A. Kohlhaas, A. Kleinhammes, Y. Jia, Y. Wu, S. T. Nguyen, R. S. Ruoff, *Carbon* **2007**, *45*, 1558.

[17] L. Staudenmaier, *Berichte der deutschen chemischen Gesellschaft* **1898**, *31*, 1481.

[18] G. Ruess, F. Vogt, *Monatsh. Chem.* **1948**, *78*, 222.

[19] H.P. Boehm, *Angew. Chem. Int. Ed.* **2010**, *49*, 9332.

[20] A. K. Geim, K. S. Novoselov, *Nat. Mater.* **2007**, *6*, 183.

[21] X. Fan, W. Peng, Y. Li, X. Li, S. Wang, G. Zhang, F. Zhang, *Adv. Mater.* **2008**, *20*, 4490.

[22] P. Nemes-Incze, Z. Osvath, K. Kamaras, L. P. Biro, *Carbon* **2008**, *46*, 1435.

[23] H. P. Boehm, A. Clauss, G. O. Fischer, U. Hofmann, *Zeitschrift für anorganische und allgemeine Chemie* **1962**, *316*, 119.

[24] A. E. Morgan, G. A. Somorjai, *Surf. Sci.* **1968**, *12*, 405.

[25] J. W. May, *Surf. Sci.* **1969**, *17*, 267.

[26] T. A. Land, T. Michely, R. J. Behm, J. C. Hemminger, G. Comsa, *Surf. Sci.* **1992**, *264*, 261.

[27] A. J. van Bommel, J. E. Crombeen, A. van Tooren, *Surf. Sci.* **1975**, *48*, 463.

[28] D. V. Badami, *Carbon* **1965**, *3*, 53.

[29] X. K. Lu, M. F. Yu, H. Huang, R. S. Ruoff, *Nanotechnology* **1999**, *10*, 269.

[30] C. Roscoe, J. M. Thomas, *Proc. R. Soc. London Ser. A* **1967**, *297*, 397.

[31] K. S. Novoselov, A. K. Geim, S. V. Morozov, D. Jiang, Y. Zhang, S. V. Dubonos, I. V. Grigorieva, A. A. Firsov, *Science* **2004**, *306*, 666.

[32] K. S. Novoselov, A. K. Geim, S. V. Morozov, D. Jiang, M. I. Katsnelson, I. V. Grigorieva, S. V. Dubonos, A. A. Firsov, *Nature* **2005**, *438*, 197.

[33] Y. Zhang, J. W. Tan, H. L. Stormer, P. Kim, *Nature* **2005**, *438*, 201.

[34] K. S. Novoselov, Z. Jiang, Y. Zhang, S. V. Morozov, H. L. Stormer, U. Zeitler, J. C. Maan, G. S. Boebinger, P. Kim, A. K. Geim, *Science* **2007**, *315*, 1379.

[35] H. C. Schniepp, J. L. Li, M. J. McAllister, H. Sai, M. Herrera-Alonso, D. H. Adamson, R. K. Prud'homme, R. Car, D. A. Saville, I. A. Aksay, *J. Phys. Chem. B* **2006**, *110*, 8535.

[36] O. E. Andersson, B. L. V. Prasad, H. Sato, T. Enoki, Y. Hishiyama, Y. Kaburagi, M. Yoshikawa, S. Bandow, *Phys. Rev. B* **1998**, *58*, 16387.

[37] P. R. Somani, S. P. Somani, M. Umeno, *Chem. Phys. Lett.* **2006**, *430*, 56.

[38] A. Reina, X. T. Jia, J. Ho, D. Nezich, H. B. Son, V. Bulovic, M. S. Dresselhaus, J. Kong, *Nano Lett.* **2009**, *9*, 30.

[39] L. Staudenmaier, *Ber. Dtsch. Chem. Ges.* **1898**, *31*, 1481.

[40] W. Hummers, R. E. Offeman, *J. Am. Chem. Soc.* **1958**, *80*, 1339.

[41] A. C. Ferrari, *Solid State Commun.* **2007**, *143*, 47.

CHAPTER 3

FUNCTIONALIZATION AND SOLUBILIZATION OF GRAPHENE

Summary*

Solubilization of graphene in organic solvents has been accomplished through covalent functionalization, involving the preparation of a long-chain alkylamide derivative and by interaction with an organosilane or an organotin reagents such as hexadecyltrimethoxysilane and dibutyldimethoxytin. Water-soluble graphene has been produced by extensive acid treatment or treatment with polyethylene glycol. Non-covalent modification of graphene has been done through π-π interaction by using 1-pyrenebutanoic acid succinimidyl ester, which gives stable dispersions in dimethylformamide. Interaction of graphene with surfactants polyoxyethylene-40-nonylphenyl ether (IGPAL), sodium dodecyl sulfate (SDS) and cetyl trimethyl ammonium bromide (CTAB) produced stable aqueous dispersions, IGPAL being effective even at low concentrations.

*Papers based on this work have been published in *Nanosci. Nanotechnol. Lett. (2009)and Angew. Chem. Int. Ed. (2009)*.

3.1 Introduction

Chemistry occurs in solution. Modern synthetic chemistry and biological processes primarily take place in solution phase. But unfortunately pristine graphene is insoluble in many liquids such as water, polymer resins, and most solvents. Thus it is difficult to evenly disperse in a liquid matrix such as epoxies and other polymers. To make graphene more easily dispersible in liquids, it is necessary to physically or chemically attach certain molecules or functional groups to graphene without significantly changing its desirable properties. This process is called functionalization. The production of robust composite materials requires strong covalent chemical bonding between the filler particles and the polymer matrix, rather than the much weaker van der Waals physical bonds which occur if graphene is not properly functionalized.

Even though much progress has not been occured on graphene functionalization, plenty of investigations have been carried out on functionalization of single-walled carbon nanotubes (SWNTs), which are considered as rolled form of graphene. SWNTs are extremely resistant to wetting.[1] They typically exist as ropes or bundles with 10-25 nm diameters and a few micrometers long. SWNT ropes are entangled together in the solid state to form a highly dense, complex network structure. These factors, coupled with the fact that these pseudo-1D graphitic cylinders do not have any surface functional groups, make them very difficult to disperse in organic media.[2]

It is possible to wet the SWNT raw soot in refluxing nitric acid[3, 4] whereby the end caps of the tubes are oxidized to carboxylic acid and other weakly acidic functionalities.[4-6] These “acid-purified” SWNTs can be dispersed in various amide-type organic solvents under the influence of an ultrasonic force field.[7] However, the nitric acid treatment introduces

defects on the nanotube surface,[8] oxidizes the carbon nanotubes, and produces impurity states at the Fermi level of the nanotubes.[9] The defect sites that are introduced into the carbon nanotubes can be used to shorten and eventually destroy the carbon nanotubes under similar oxidizing conditions.[4, 10-13] The shortened tubes (s-SWNTs) are better solvated by amide solvents than the full-length SWNTs. The addition of a long-chain hydrocarbon at the ends of the shortened (100-300 nm) carbon nanotubes could render the functionalized SWNTs soluble in organic solvents.

Covalent functionalization described above would significantly rupture the conjugation. So to avoid this limitation it is necessary to functionalize through non-covalent modification. The formation of non-covalent aggregates with surfactants or wrapping with polymers has shown themselves to be suitable methods to functionalize SWNTs without affecting its electronic structure. In the search for non-destructive purification methods, it has been shown that nanotubes can be transferred to the aqueous phase in the presence of surface-active benzylalkonium chloride.[14-16] It is believed that the nanotubes are in the hydrophobic interiors of the corresponding micelles, which results in stable dispersions. When the hydrophobic part of an amphiphile contains aromatic group, especially strong interaction results, because effective stacking interactions can then form with the graphitic sidewalls of the SWNTs. This effect was demonstrated in the aggregation with N-succinimidyl-1-pyrenebutanoate.[17] In these aggregates, the succinimidyl group could be substituted with amino groups from proteins such as ferritin or streptavidin, which caused immobilization of the biopolymers on the tubes. This effect could be interesting for the development of biosensors, because the electronic properties of the tubes can be combined with the recognition properties of the immobilized biosystems.

Polymers have also been used in the formation of supramolecular complexes of SWNTs. Suspension of purified tubes in the presence of polymers such as poly (m-phenylene- co-2,5-dioctoxy-p-phenylenevinylene) (PmPV, 2), in organic solvents such as $CHCl_3$, leads to polymer wrapping around the tubes.[18-20] Properties of these supramolecular compounds are markedly different from those of individual components. For example, the SWNT/PmPV complex exhibits conductivity eight-times higher than that of pure polymer, without any restriction of its luminescence properties. The wrapping of SWNTs with polymers that bear polar side-chains, such as polyvinylpyrrolidone (PVP) or polystyrenesulfonate (PSS), leads to stable solutions of the corresponding SWNT/polymer complexes in water.[21] The bundles are again broken up by complex formation in this case. The thermodynamic driving force for complex formation is the need to avoid unfavorable interactions between the apolar tube walls and the solvent water.

3.2 Scope of the present investigations

Graphene is one of the most interesting materials being explored today.[22, 23] It exhibits exotic physical properties such as quantum Hall effect at room temperature and ballistic conduction with high mean free path.[24, 25] Chemical and other properties of graphene also seem to be fascinating. Polymer composites based on graphene are expected to show interesting electronic and mechanical properties.[26] In many of the investigations, it becomes necessary to prepare dispersions or solutions of graphene in organic or aqueous media. Dispersions of single-walled carbon naotubes are generally prepared by covalent or non-covalent functionalization.[27-29] We felt that it would be worthwhile to functionalize graphene to utilize graphene's outstanding physical properties in the manufacture of composite materials, as well as in other practical applications which require preparation of

uniform mixtures of graphene with many different organic, inorganic, and polymeric materials.

We have carried out functionalization of graphene by employing both covalent and non-covalent means (Chart 1).The functionalized samples were characterized by employing infrared (IR) spectroscopy, transmission electron microscopy and Raman spectroscopy. Covalent functionalization has been carried out through the following three independent routes. (a) amidation[27] (b) silane and tin coating[30, 31] (c) acidification. Amidation makes graphene soluble in organic solvents like THF, CCl_4 and DCM, where as silane or tin coating

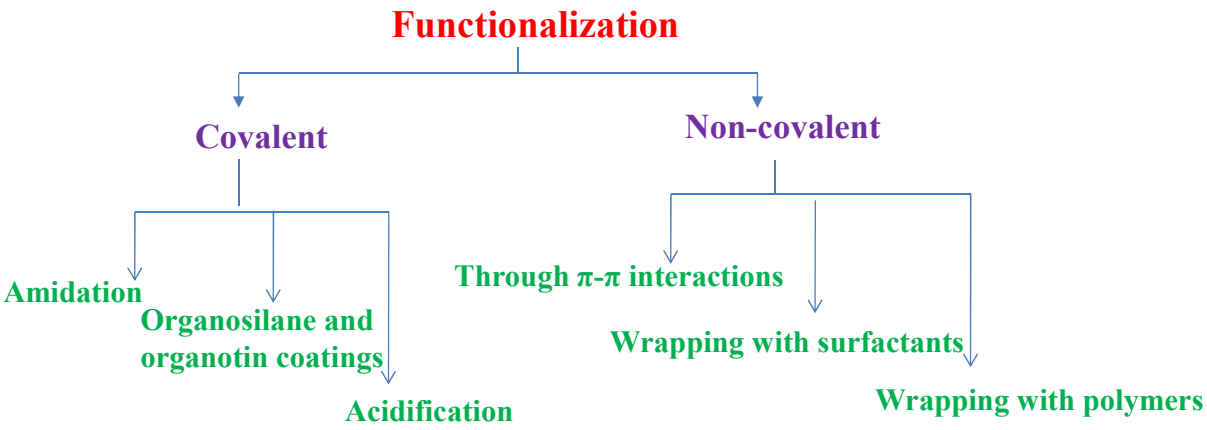

Chart 1: Different means of functionalization of graphene.

gives stable dispersions in non polar solvents such as CCl_4. The dispersions were stable up to 6 hours or more. Acidification of graphene produces aqueous graphene solutions which are stable up to months. While non-covalent functionalization of graphene attained through (a) polymer wrapping[32] (b) π-π interaction[17] and supamolecular approach using surfactants (c). In these three routes polymer wrapping and suppramolecular approach solubilize graphene in water where as π-π interaction with 1-pyrenebutanoic acid succinimidyl ester (PYBS) gives

dispersion of graphene in DMF. These non-covalently functionalized dispersions are stable up to several days.

3.3 Experimental section

3.3.1 Amidation

To solubilize graphene samples (EG and DG) in non-polar solvents, amidation has been carried out. The procedure is as follows. In the first step, conc. nitric acid (2 ml), conc. sulfuric acid (2 ml) and water (16 ml) was added to graphene (50 mg) and subsequently heated in a microwave oven for 10 minutes. Further, the sample was heated at 100 °C for 12 hours under hydrothermal conditions. The product was washed with distilled water and centrifuged repeatedly to remove traces of acid. This yielded graphene that was functionalized with –OH and –COOH groups. The acid treated graphene was refluxed with excess $SOCl_2$ for 12 hours and the unreacted $SOCl_2$ was removed under vacuum. The product was treated with dodecylamine (5 ml) under microwave radiation for 10 minutes and thermally heat treated at 100 °C for 12 hours.

3.3.2 Silane and tin coating

We have used hexadecyltrimethoxysilane (HDTMS) and dibutyldimethoxytin (DBDT)[31] for the covalent modification of graphene. The reaction was carried out as follows. Dry pristine graphene (1 mg), subjected to acid treatment and was placed in a round-bottom flask, to which 15 ml of toluene was added. This mixture was sonicated for 15 minutes and the organosilicon or organotin reagent added to the mixture (1:1 molar ratio) in a nitrogen atmosphere. The reaction mixture was stirred and maintained at 55 °C over night. The product was washed with dry toluene and dried.

3.3.3 Acidification

In order to solubilize graphene in water using acidification, EG (5 mg) was stirred with (1:1) mixture of conc. nitric acid (2ml) and conc. sulfuric acid (4 ml) at room temperature for 2 days. This gave some water-soluble graphene in addition to an insoluble fraction.

3.3.4 Polymer wrapping

To prepare polyethylene glycol (PEG)-functionalized EG, the mixture of mild acid treated graphene (3 mg), excess of PEG (6 ml) and conc. HCl (2 ml) was heated in microwave oven for 10 minutes. The resulting product was further heated at 100 °C for 12 hours.

3.3.5 Functionalization through π-π interaction

Non-covalent functionalization by the interaction of 1-pyrenebutanoic acid succinimidyl ester (PYBS)[33] with graphene was carried out in dimethylformamide (DMF) at different temperatures in the 150-300 °C range. Typically, 5 ml of 12 mM PYBS solution in dry DMF was added to 1 mg graphene and the mixture was ultra-sonicated for 15 minutes at room temperature. To obtain stable dispersions for several days, the mixture of graphene and PYBS was heated in a sealed tube at 150 °C, 180 °C, 200 °C and 300 °C for 3 hours.

3.3.6 Supramolecular approach

To get dispersions of graphene in water, we prepared surfactant solutions having different concentrations and checked for dispersibility. The procedure is as follows. 1.5 mM, 3 mM, 6 mM and 9 mM solutions of CTAB (Cetyl trimethyl ammonium bromide) were prepared in distilled water and to 5 ml of each of these solutions 1 mg graphene was added. These solutions were ultra-sonicated for 15 minutes and kept for observation. Similar to

CTAB, 1 mM, 2 mM and 4 mM, solutions of IGPAL (polyoxyethylene-40-nonylphenyl ether) and 10 mM, 20 mM, 40 mM, solutions of SDS (sodium dodecyl sulfate) were prepared. To 5 mL of each of these solutions, 1 mg graphene was added and ultra-sonicated for 15 minutes.

3.4 Results and discussion

3.4.1 Amidation

By carrying out the amidation reaction similar to that reported for carbon nanotubes, we have obtained dispersions of EG in various non-polar solvents. The results are similar to those reported by Haddon and co-workers.[34]. In Figure 1, we show photographs of the dispersions of amide-functionalized EG in dichloromethane, carbon tetrachloride and tetrahydrofuran. In Figure 2, we show photographs of similar dispersions prepared with DG. The product dodecyl-amido graphene has solubility of 0.5 mg/ml and stable up to 6 hours.

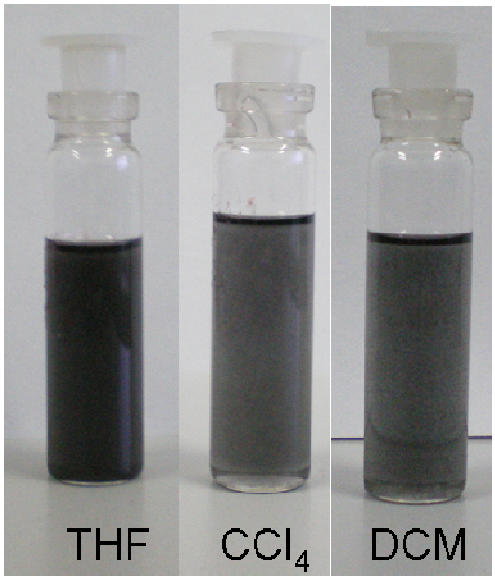

Figure 1. Amide functionalized-EG in THF, CCl_4 and DCM.

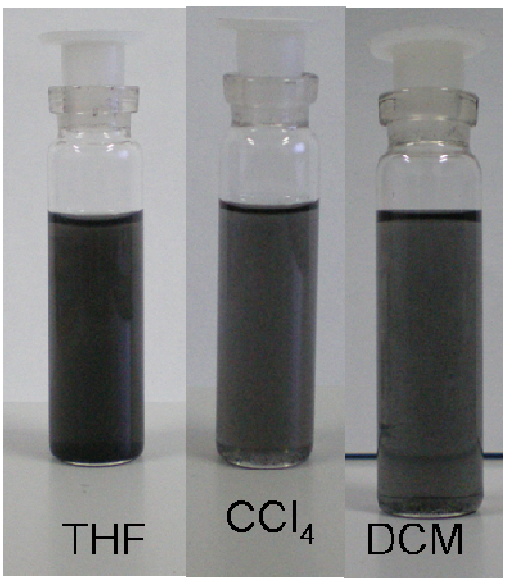

Figure 2. Amide functionalized-DG in THF, CCl_4 and DCM.

In Figure 3, we show the infrared spectra of EG at various stages of the solubilization process. After acid treatment, EG show a carbonyl stretching band at 1710 cm^{-1} due to the carboxyl groups. On functionalization with dodecylamine, the C=O stretching band shifts to 1650 cm^{-1} due to the formation of amide band, in addition to C-H and N-H stretching bands around 2800 and 3300 cm^{-1} respectively are observed.

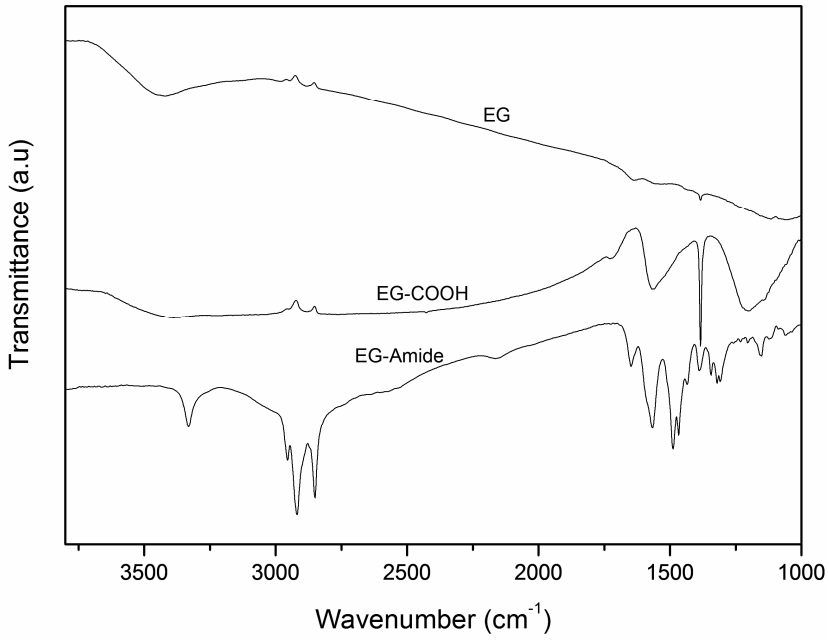

Figure 3. Infrared spectra of pristine EG, acid treated EG (EG-COOH) and amide functionalized EG (EG-amide).

3.4.2 Organosilane and organotin coating

We have accomplished covalent functionalization of EG and DG graphene samples by reaction with hexadecyltrimethoxysilane (HDTMS) and dibutyldimethoxytin (DBDT).[30, 31] Functionalized samples were characterized by IR spectroscopy. The functionalized samples were dispersible in CCl_4 and the dispersions were stable for 6 hours or more. In Figure 4, we show photographs of the dispersions of organosilane and organotin functionalized graphenes.

The IR spectrum of the sample functionalized with HDTMS shows the Si-O vibration band at 1100 cm^{-1} along with the bands due to alkyl groups at around 2950 cm^{-1}. The sample functionalized with dibutyldimethoxytin shows the presence of Sn-O band at

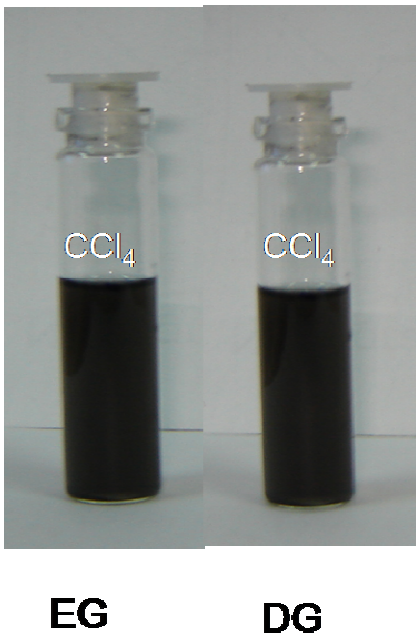

Figure 4a. Organosilane coated EG and DG.

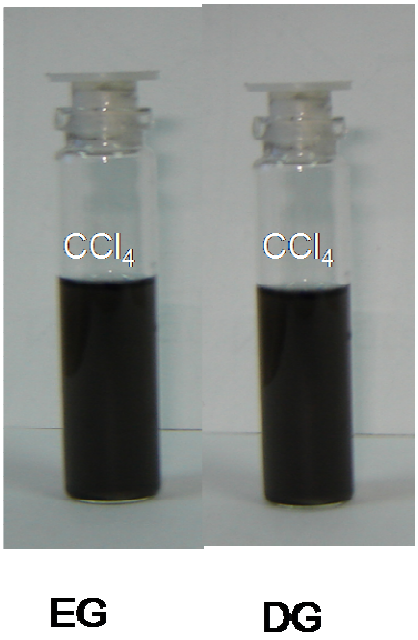

Figure 4b. Organotin coated EG and DG.

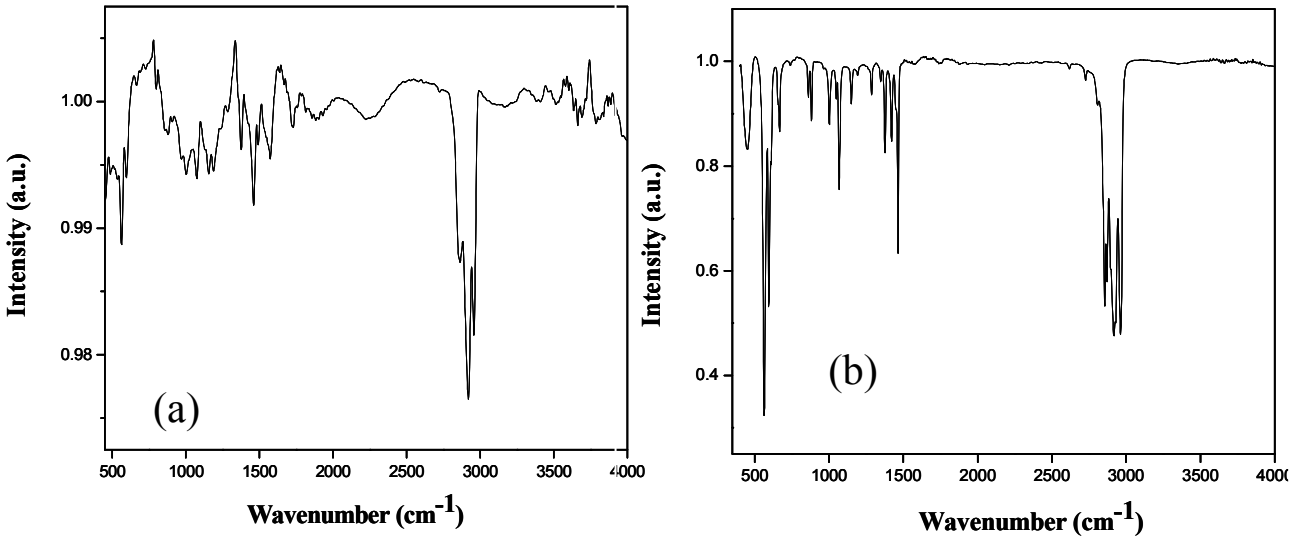

Figure 5. IR spectra of EG functionalized by the (a) organosilane and (b) organotin reagents.

500-600 cm^{-1} and alkyl bands at 2850 and 2950 cm^{-1} [Figures 5 and 6]. It clearly indicates the formation of organo silane and organo tin coating on graphene surface.

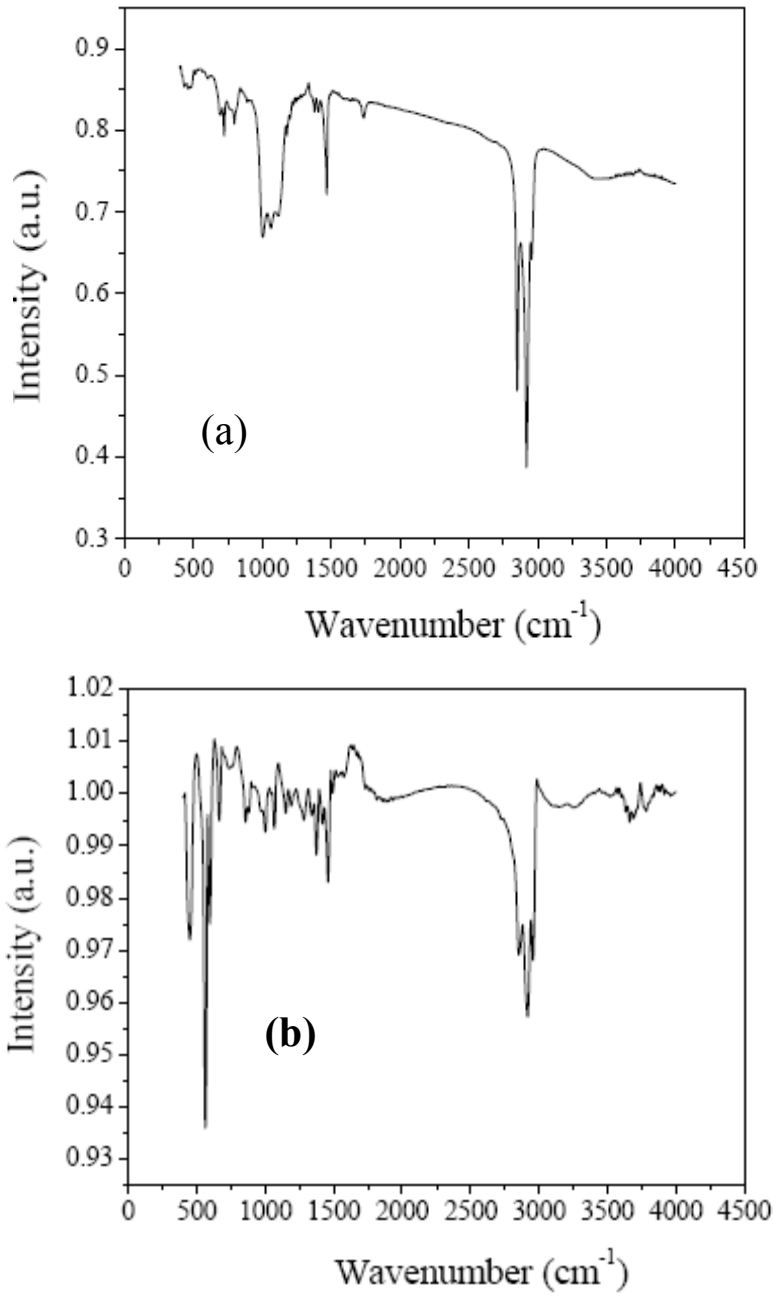

Figure 6. IR spectra of DG functionalized by the (a) organosilane and (b) organotin reagents.

3.4.3 Acidification

As-prepared EG shows evidence for the presence of carbonyl and hydroxyl groups on the surface. After further treatment of EG with nitric and sulfuric acid mixture, we obtain a water solution of EG, along with the insoluble portion of the sample which settles down. The infrared (IR) spectrum of the soluble part obtained after drying shows a prominent band due to carbonyl group in addition to a broad band due to –OH groups is observed as shown in Figure 7.

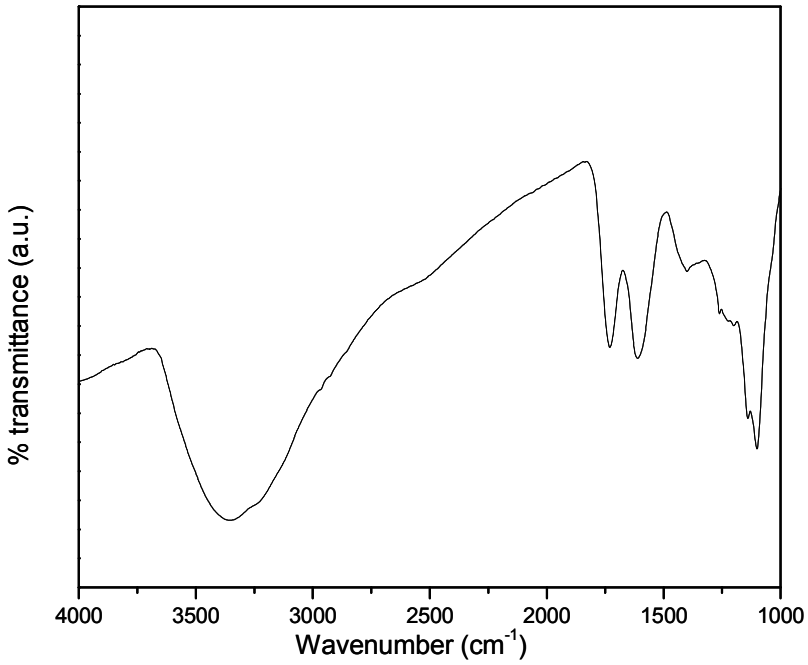

Figure 7. Infrared spectrum of water-soluble EG.

The Raman spectrum of the water-soluble EG shown in Figure 8a exhibits the characteristic G, D and 2D bands and shows that L_a of the sample is 4 nm on an average (as calculated from the intensity ratio of the D and G bands). In Figure 8b, we show photograph of the water-soluble graphene.

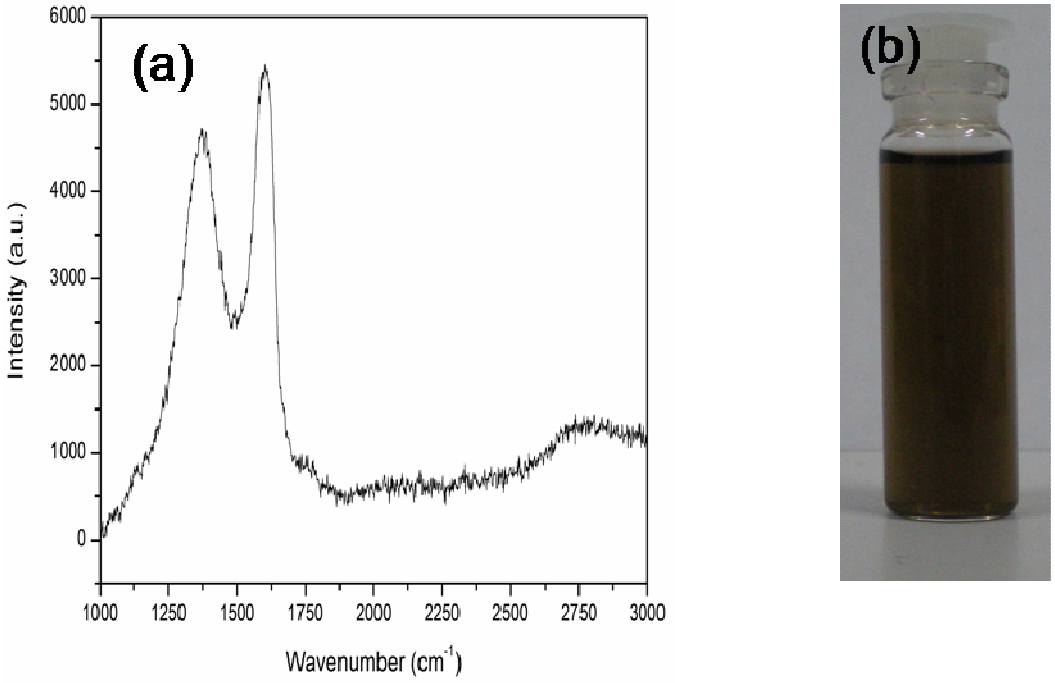

Figure 8. (a) Raman spectrum and (b) photograph of water-soluble EG.

3.4.4 Wrapping with PEG

The water-insoluble EG when treated with polyethylene glycol (PEG) yielded water-dispersible graphene. In Figure 9 we show IR spectra and water-dispersion of PEG

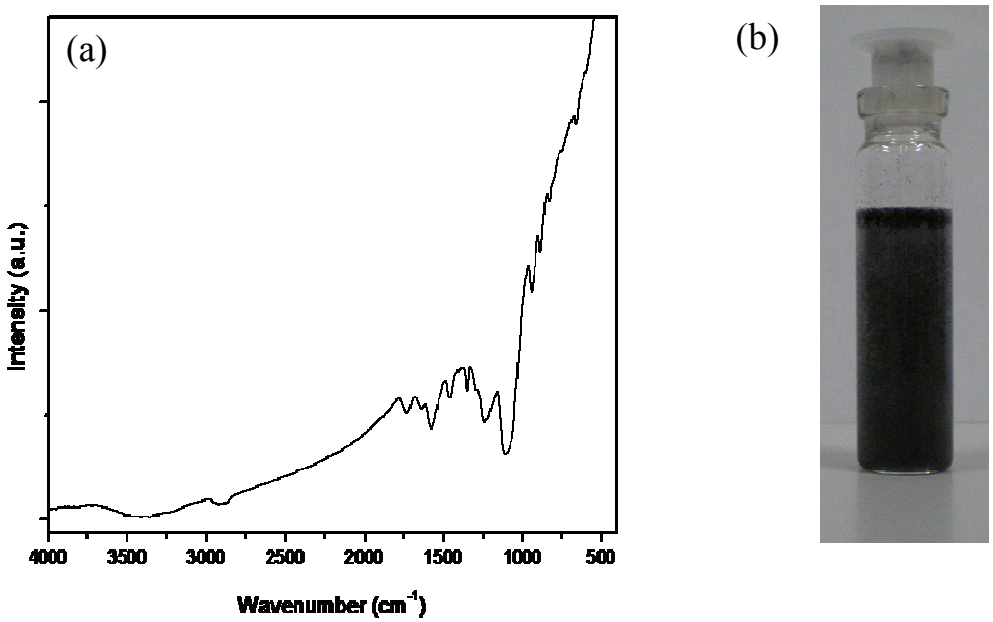

Figure 9. (a) IR spectrum and (b) water dispersion of PEG functionalized graphene.

functionalized graphene.

3.4.5 Functionalization through π-π interactions

We have been able to accomplish the solubilization of both EG and DG in DMF by reacting with PYBS (Figures 10-12).[33] It was necessary to heat the EG sample with PYBS at

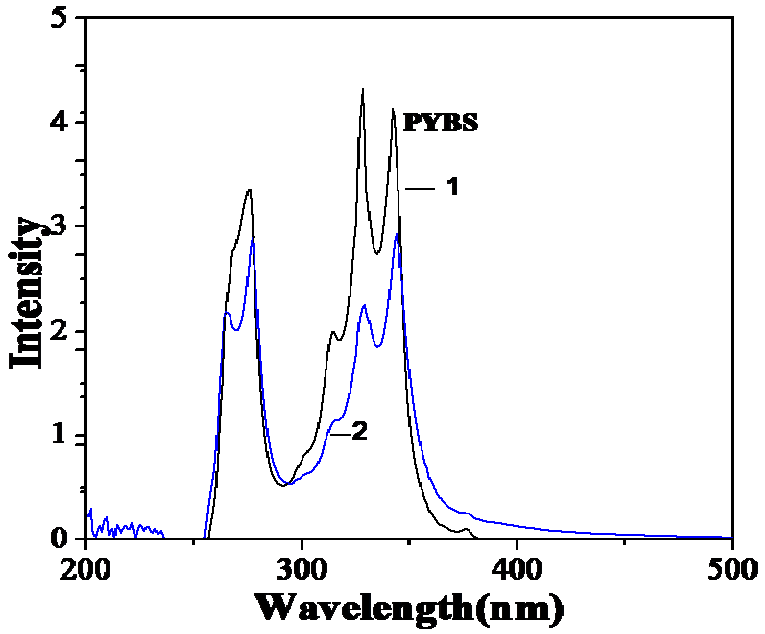

Figure 10. UV absorption spectra of (1) PYBS and (2) PYBS treated EG.

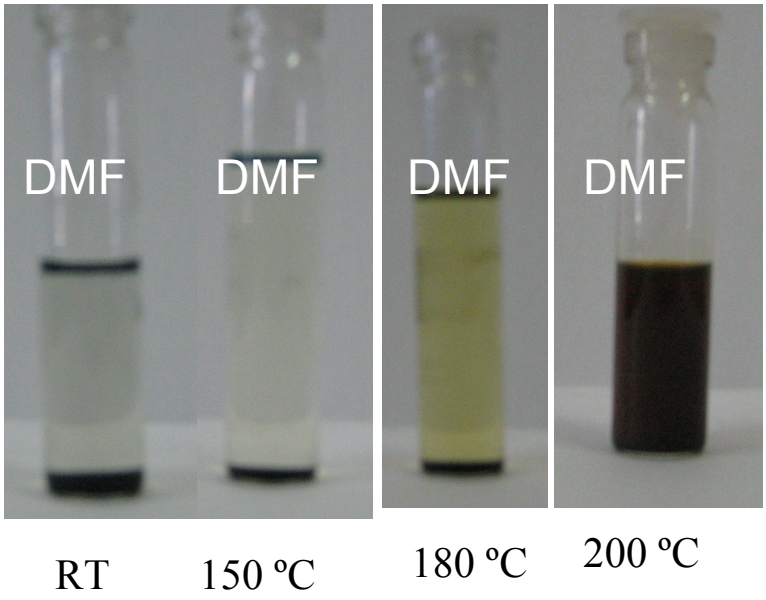

Figure 11: Photographs of DMF dispersions of PYBS treated EG at different temperatures after seven days.

200 °C, and the DG sample at 300 °C to obtain the dispersions which were stable for several days. Samples prepared at low temperatures were stable only up to 2-3 hours. In case of electronic absorption spectra of the PYBS-graphene dispersions show the pyrene bands with changes in the relative intensities because of π-π interactions (see Figure 10). In Figures 11 and 12 we show the photographs of dispersions EG and DG in DMF respectively.

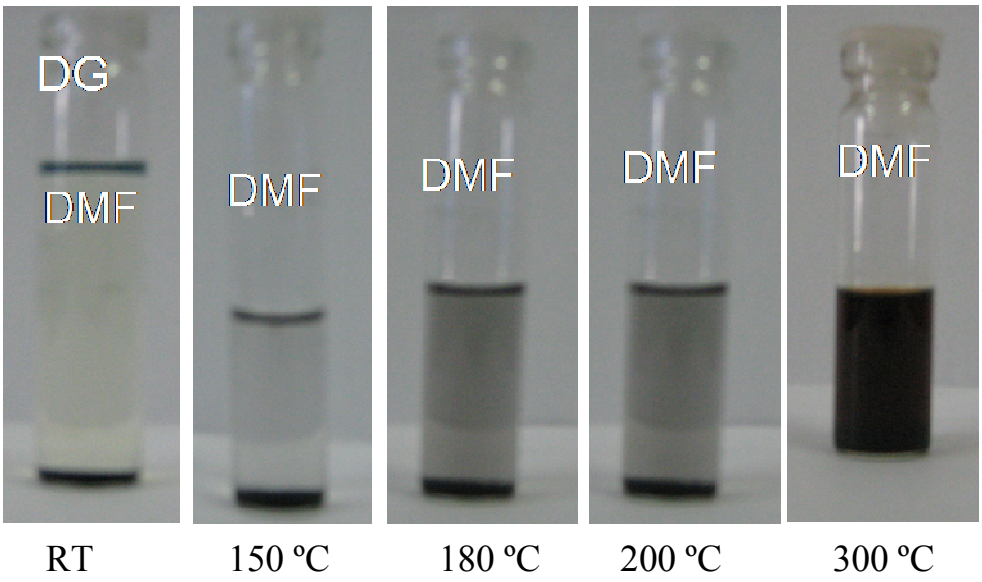

Figure 12. Photographs of DMF dispersions of PYBS treated DG at different temperatures after seven days.

3.4.6 Supramolecular approach

Non-covalent functionalization of graphene was accomplished via supramolecular approach by using different concentrations of surfactants such as CTAB, SDS and IGP. In the case of CTAB, the best dispersions for EG and DG in water were obtained at 6 mM and 9 mM respectively. Photographs of EG and DG dispersions in CTAB are shown in Figure 13. SDS gave good dispersions in water at 20 mM for EG and at 10 mM for DG. The best results were obtained with IGP which gave stable dispersions of EG and DG at a low concentration

of 1 mM. The photographs of the dispersions in SDS and IGP are shown in Figures 14 and 15 respectively. Raman spectra of these dispersions shows the characteristic D, G and 2D bands of graphene [see Figure 16]. In case of EG the obtained dispersions were quite stable up to 7 days, where as the dispersions obtained with DG were stable up to only 2 days.

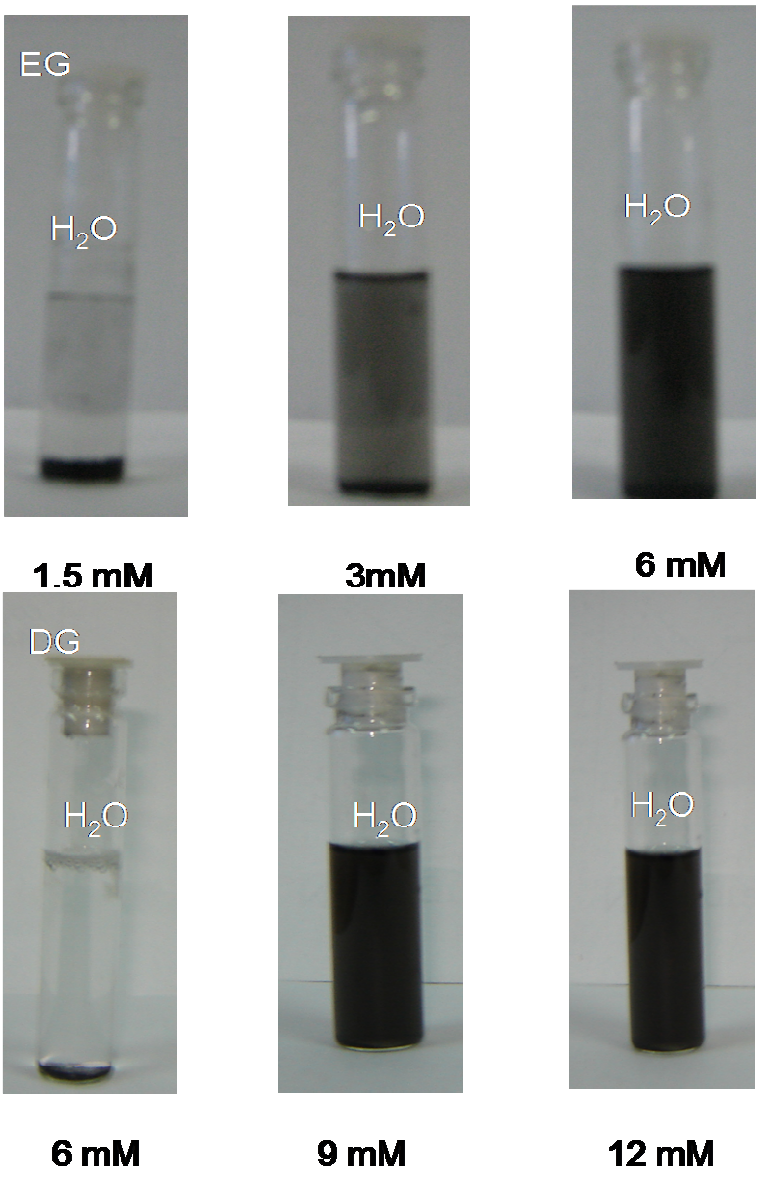

Figure 13. Photographs of water dispersions of EG and DG treated with CTAB at different concentrations.

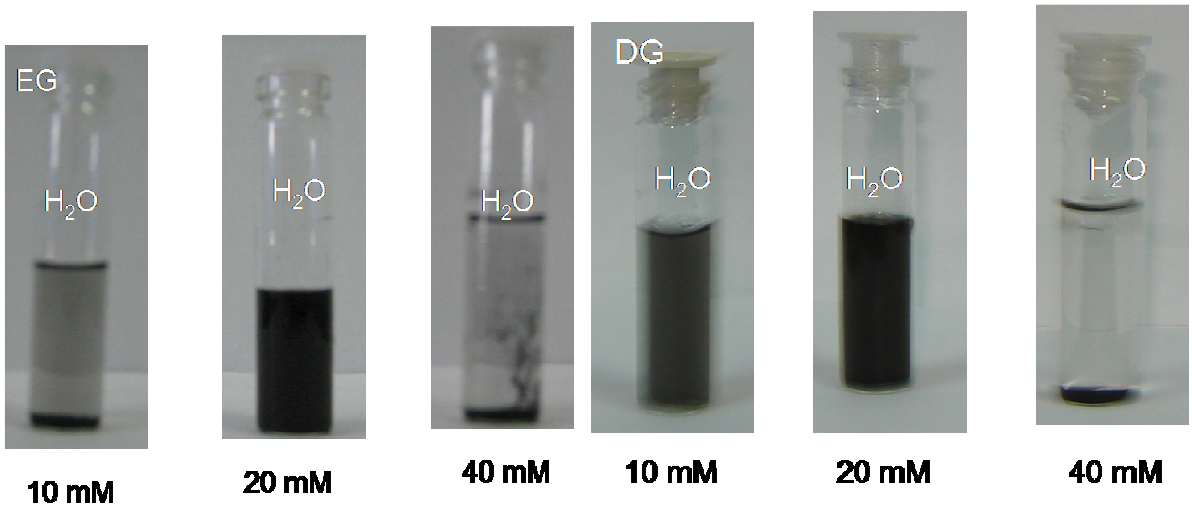

Figure 14. Photographs of water dispersions of EG and DG treated with SDS at different concentrations.

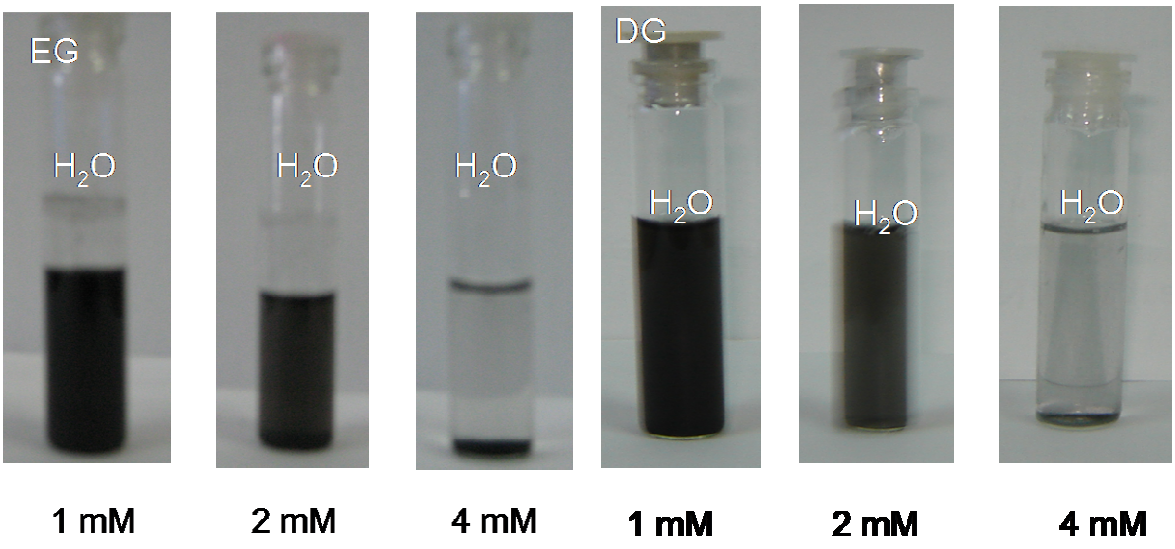

Figure 15. Photographs of water dispersions of EG and DG treated with IGP at different concentrations.

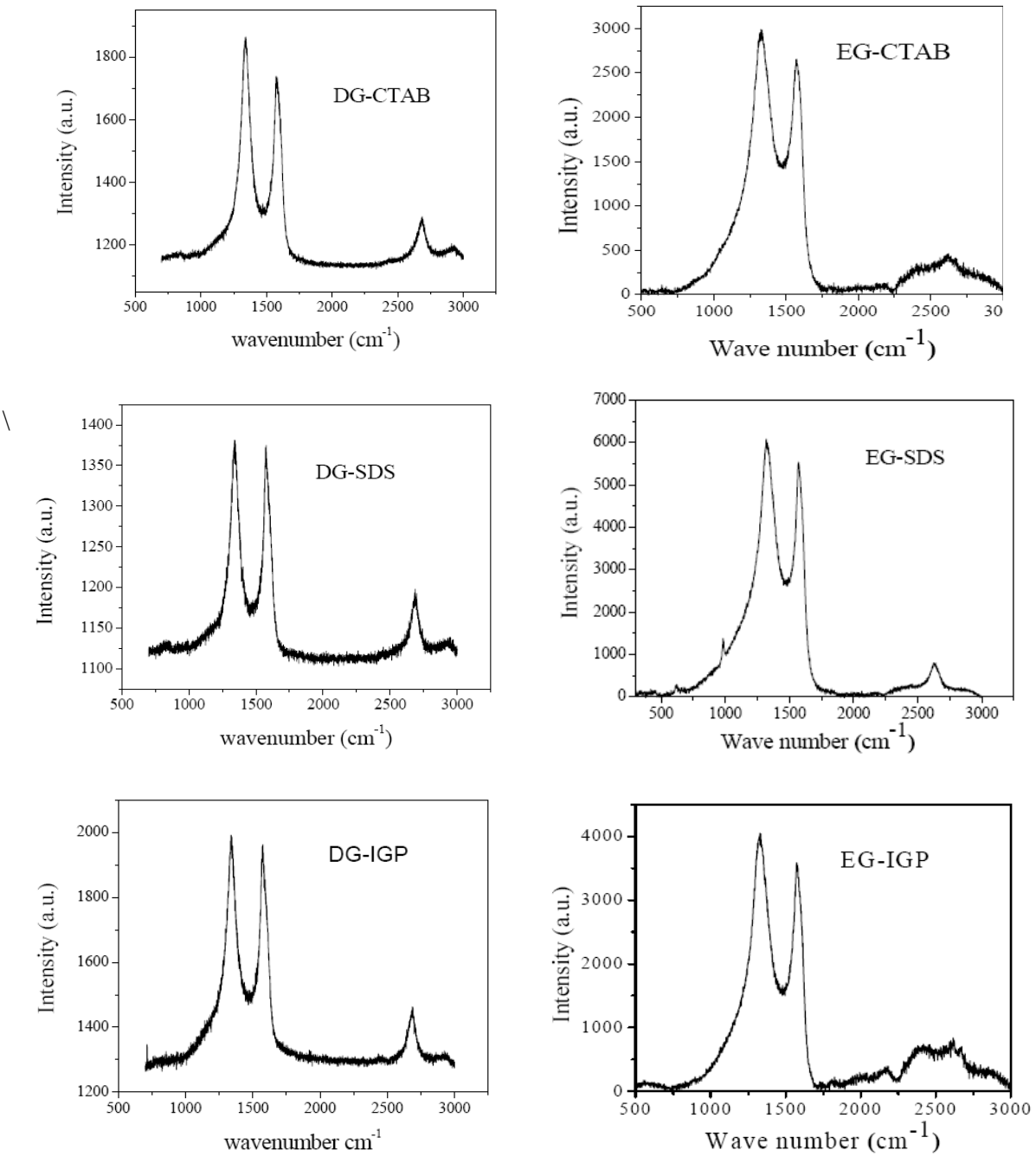

Figure 16. Raman spectra obtained from water dispersions of EG and DG treated with CTAB, SDS and IGP.

3.5 Conclusions

We have been able to functionalize and solubilize graphene prepared by two methods in different media by employing both covalent and non-covalent modifications. Solubilization in non-polar solvents has been accomplished through covalent functionalization using long-chain alkyl amine, organosilane and organotin reagents. Solubilization in polar solvents such as DMF has been accomplished by means of π-π interaction between graphene and a pyrene derivative. Solubilization in water has been attained by using polyethylene glycol and different surfactants such as SDS, CTAB, and IGP.

3.6 References

[1] (a) E. Dujardin, T. W. Ebbesen, A. Krishnan, M. M. J. Treacy, *Adv. Mater.* **1998**, *10*, 1472. (b) S. Niyogi, M. A. Hamon, H. Hu, B. Zhao, P. Bhowmik, R. Sen, M. E. Itkis, R. C. Haddon, *Acc. Chem. Res.* **2002**, *35*, 1105.

[2] Y. Chen, R. C. Haddon, S. Fang, A. M. Rao, P. C. Eklund, W. H. Lee, E. C. Dickey, E. A. Grulke, J. C. Pendergrass, A. Chavan, B. E. Haley, R. E. Smalley, *J. Mater. Res.* **1998**, *13*, 2423.

[3] T. W. Ebbesen, *Acc. Chem. Res.* **1998**, *31*, 558.

[4] J. Liu, A. G. Rinzler, H. Dai, J. H. Hafner, R. K. Bradley, P. J. Boul, A. Lu, T. Iverson, K. Shelimov, C. B. Huffman, F. Rodriguez-Macias, Y. S. Shon, T. R. Lee, D. T. Colbert, R. E. Smalley, *Science* **1998**, *280*, 1253.

[5] D. B. Mawhinney, V. Naumenko, A. Kuznetsova, J. T. J. Yates, J. Liu, R. E. Smalley, *Chem. Phys. Lett.* **2000**, *324*, 213.

[6] H. Hu, P. Bhowmik, B. Zhao, M. A. Hamon, M. E. Itkis, R. C. Haddon, *Chem. Phys. Lett.* **2001**, *345*, 25.

[7] K. D. Ausman, R. Piner, O. Lourie, R. S. Ruoff, M. Korobov, *J. Phys. Chem. B* **2000**, *104*, 8911.

[8] M. Monthioux, B. W. Smith, B. Burteaux, A. Claye, J. E. Fischer, D. E. Luzzi, *Carbon* **2001**, *39*, 1251.

[9] M. E. Itkis, S. Niyogi, M. Meng, M. Hamon, H. Hu, R. C. Haddon, *Nano Lett.* **2002**, *2*, 155.

[10] K. Tohji, H. Takahashi, Y. Shinoda, N. Shimizu, B. Jeyadevan, I. Matsuoka, Y. Saito, A. Kasuya, S. Ito, Y. Nishina, *J. Phys. Chem. B* **1997**, *101*, 1974.

[11] S. Bandow, S. Asaka, X. Zhao, Y. Ando, *Appl. Phys. A* **1998**, *67*, 23.

[12] E. Dujardin, T. W. Ebbesen, A. Krishnan, M. M. J. Treacy, *Adv. Mater.* **1998**, *10*, 611.

[13] A. C. Dillon, T. Gennet, K. M. Jones, J. L. Alleman, P. A. Parilla, M. J. Heben, *Adv. Mater.* **1999**, *11*, 1354.

[14] S. Bandow, A. M. Rao, K. A. Williams, A. Thess, R. E. Smalley, P. C. Eklund, *J. Phys. Chem. B* **1997**, *101*, 8839.

[15] G. S. Duesberg, M. Burghard, J. Muster, G. Philipp, S. Roth, *Chem. Commun.* **1998**, 435.

[16] V. Krstic, G. S. Duesberg, J. Muster, M. Burghard, S. Roth, *Chem. Mater.* **1998**, *10*, 2338.

[17] R. J. Chen, Y. G. Zhang, D. W. Wang, H. J. Dai, *J. Am. Chem. Soc.* **2001**, *123*, 3838.

[18] S. A. Curran, P. M. Ajayan, W. J. Blau, D. L. Carroll, J. N. Coleman, A. B. Dalton, A. P. Davey, A. Drury, B. McCarthy, S. Maier, A. Strevens, *Adv. Mater.* **1998**, *10*, 1091.

[19] A. Star, J. F. Stoddart, D. Steuerman, M. Diehl, A. Boukai, E. W. Wong, X. Yang, S.-W. Chung, H. Choi, J. R. Heath, *Angew. Chem. Int. Ed.* **2001**, *113*, 1771.

[20] J. N. Coleman, A. B. Dalton, S. Curran, A. Rubio, A. P. Davey, A. Drury, B. McCarthy, B. Lahr, P. M. Ajayan, S. Roth, R. C. Barklie, W. J. Blau, *Adv. Mater.* **2000**, *12*, 213.

[21] M. J. O'Connell, P. Boul, L. M. Ericson, C. Huffman, Y. H. Wang, E. Haroz, C. Kuper, J. Tour, K. D. Ausman, R. E. Smalley, *Chem. Phys. Lett.* **2001**, *342*, 265.

[22] A. K. Geim, K. S. Novoselov, *Nat. Mater.* **2007**, *6*, 183.

[23] K. S. Novoselov, A. K. Geim, S. V. Morozov, D. Jiang, Y. Zhang, S. V. Dubonos, I. V. Grigorieva, A. A. Firsov, *Science* **2004**, *306*, 666.

[24] Y. Zhang, Y.-W. Tan, H. L. Stormer, P. Kim, *Nature* **2005**, *438*, 201.

[25] K. S. Novoselov, Z. Jiang, Y. Zhang, S. V. Morozov, H. L. Stormer, U. Zeitler, J. C. Maan, G. S. Boebinger, P. Kim, A. K. Geim, *Science* **2007**, *315*, 1379.

[26] S. Stankovich, D. A. Dikin, G. H. B. Dommett, K. M. Kohlhaas, E. J. Zimney, E. A. Stach, R. D. Piner, S. T. Nguyen, R. S. Ruoff, *Nature* **2006**, *442*, 282.

[27] S. Niyogi, E. Bekyarova, M. E. Itkis, J. L. McWilliams, M. A. Hamon, R. C. Haddon, *J. Am. Chem. Soc.* **2006**, *128*, 7720.

[28] J. Chen, M. A. Hamon, H. Hu, Y. Chen, A. M. Rao, P. C. Eklund, R. C. Haddon, *Science* **1998**, *282*, 95.

[29] M. A. Hamon, J. Chen, H. Hu, Y. Chen, A. M. Rao, P. C. Eklund, R. C. Haddon, *Adv. Mater.* **1999**, *11*, 834.

[30] P. Asuri, S. S. Karajanagi, J. S. Dordick, R. S. Kane, *J. Am. Chem. Soc.* **2006**, *128*, 1046.

[31] Y. Zhang, Y. Shen, D. Han, Z. Wang, J. Song, L. Niu, *J. Mater. Chem.* **2006**, *16*, 4592.

[32] O. Matarredona, H. Rhoads, Z. Li, J. H. Harwell, L. Balzano, D. E. Resasco, *J. Phys. Chem. B* **2003**, *107*, 13357.

[33] R. J. Chen, Y. Zhang, D. Wang, H. Dai, *J. Am. Chem. Soc.* **2001**, *123*, 3838.

[34] S. Niyogi, E. Bekyarova, M. E. Itkis, J. L. McWilliams, M. A. Hamon, R. C. Haddon, *J. Am. Chem. Soc.* **2006**, *128*, 7720.

CHAPTER 4

SOME PROPERTIES OF FEW-LAYER GRAPHENES

Summary*

In this chapter, results of various investigations related to the properties of few-layer graphenes are presented.

Surface areas and uptake of H_2, CO_2 and CH_4: Graphene samples prepared by the exfoliation of graphite oxide (EG), conversion of nanodiamond (DG), arc-evaporation of graphite in a hydrogen atmosphere (HG) and reduction of graphene oxide (RGO) have been investigated for gas adsorption properties. These samples show high Brunauer-Emmett-Teller (BET) surface area values ranging from 238 to1550 m^2/g at 1 atm and 77 K. Graphene samples prepared by us exhibit good hydrogen uptake at 1 atm and 77 K, the uptake going up to 1.7 wt %. The H_2 uptake at 100 atm, 298 K is found to be 3 wt % or more, suggesting thereby the single-layer graphene would exhibit much higher uptakes. Graphene samples prepared by us show high uptake of CO_2, the value reaching up to 35 wt % at 1 atm and 195 K whereas uptake of CH_4 is quite low showing in the range of 0.0-2.8 wt % at 50 bar and 298 K. Interestingly, the uptake of all these gases varies linearly with the surface area of graphenes**.** The first principles calculations show that hydrogen molecule sits parallely on

each six-membered ring of the graphene layer and can accommodates up to 7.7 wt % of hydrogen on single-layered graphene. CO_2 molecules sit alternatively in a parallel fashion on the rings to give a maximum uptake of 37.93 wt % in single-layer graphene. The present study shows that the H_2 uptake by graphene is comparable to that of single-walled carbon nanotubes and other carbon-based materials. Presence of more than one layer of graphene in our samples causes a decrease in the resultant uptake.

Novel magnetic properties: Investigations of the magnetic properties of graphenes reveal that dominant ferromagnetic interactions coexist along with antiferromagnetic interactions in all the samples. Thus, all the graphene samples exhibit room-temperature magnetic hysteresis. Room-temperature ferromagnetism in graphene is affected by the adsorption of molecules. The value of the magnetization drastically decreases on adsorption of TTF and TCNE, having greater effect in case of TTF.

Graphene as a supercapacitor material: Electrochemical redox properties of different graphene samples have been studied. Among all the graphene sampes, EG behaves similar to that of basal plane in graphite, where as DG and CG exhibit slightly better kinetics. Graphene samples were investigated as electrode materials in electrochemical supercapacitors. The samples EG and DG exhibit high specific capacitance in aq. H_2SO_4, the value reaching up to 117 F/g. By using an ionic liquid, the operating voltage has been extended to 3·5 V (instead of 1 V in the case of aq. H_2SO_4), the specific capacitance and energy density being 75 F/g and 31·9 $Whkg^{-1}$ respectively. This value of energy density is one of the highest values reported to date. The performance characteristics of graphenes which are directly related to quality, in terms of the number of layers and the surface area, are superior to that of single-walled and multi-walled carbon nanotubes.

Blue-light emission from graphene-based materials: Acid-treated graphene samples as well as reduced graphene oxide show fairly intense blue-emission centered around 440 nm. Reduction of graphene oxide can be carried out either chemically or by using different types of radiation. Functionalized graphenes can be combined with graphene oxide to emit white-light.

Patterning and lithography based on graphene: Having discovered that graphene oxide (GO) films subjected to laser or electron beam irradiation gets reduced to graphene, we are able to carry out patterning and nanolithography starting with GO and GO in mixture with gold and platinum salts. Laser irradiation of GO is found to be specially convenient for the purpose. Patterning has also been carried out with hydrogenated graphene which on laser irradiation reverts back to graphene giving out hydrogen.

*****Papers based on these studies have appeared in *J. Chem. Sci. (2008), J. Phys. Chem. C (2009), J. Phys. Chem. C (2009), Solid State Commun.(2010), Mater. Express (2011) and ChemSusChem (2011).*

4.1 Surface areas and uptake of H_2, CO_2 and CH_4

4.1.1 Introduction

High surface area materials have large surface to volume ratios. Thus, for smaller pieces of materials, the surface to volume ratio is larger. For pieces of matter on nanometer scale (nanoparticles), the contribution of their surface to overall properties becomes very important. For example, in a nanoscopic particle with a diameter of 5 nm, about half of its atoms are on its surface. This is why the techniques and methods of surface science are needed to describe properties of nanoscopic matter. Even macroscopic pieces of nanostructured materials can have high surface area, since their nanoscopic constituents can arrange in such a way to still have a large exposed surface. For example, single-walled carbon nanotube materials consist of carbon nanotube bundles.[1] The bundles are made of several tens of carbon nanotubes and thus have a large exposed surface. Bundles in a macroscopic material organized in such a way that their large surface still remains exposed (a particular bundle is not shielded by other bundles in the material). Commercial applications of high surface area materials already are in the multibillion dollar range, primary contributions to this economic basis are air separation, petroleum and petrochemical processing, environmental cleanup, chemical sensing, fine chemical catalysis,[2, 3] packaging,[4, 5] and chemical separation.[6] Economic incentives for development and application of high surface area materials are expected to substantially increase in view of their role as important components of chemical sensors,[7, 8] their potential applications in biotechnology and the increasing environmental stress as well as energy and agricultural consumption demands.

Due to its high energy density, clean burning and environment friendliness hydrogen is considered as an ideal fuel. Its use as a fuel has been limited due to the lack of good storage materials. The most promising hydrogen storage routes are in solid materials that chemically bind or physically adsorb hydrogen at volume densities greater than that of liquid hydrogen. The challenge is to find a storage material that satisfies three competing requirements: high hydrogen density, reversibility of the release/charge cycle at moderate temperatures in the range of 70–100 ºC to be compatible with the present generation of fuel cells, and fast release/charge kinetics with minimum energy barriers to hydrogen release and charge. The first requires strong chemical bonds and close atomic packing, the second requires weak bonds that are breakable at moderate temperature, and the third requires loose atomic packing to facilitate fast diffusion of hydrogen between the bulk and the surface, as well as adequate thermal conductivity to prevent decomposition by the heat released upon hydriding. Although several materials have been found that satisfy one or more of the requirements, none has proven to satisfy all the three. In addition to these basic technical criteria, viable storage media must satisfy cost, weight, lifetime, and safety requirements as well.[9]

Methane and carbon dioxide are the two main gases responsible for global warming and other harmful effects. Most of the emissions of CO_2 to the atmosphere from electricity generation and industrial sectors are currently in the form of flue gas from combustion, in which the CO_2 concentration is typically 4-14 % by volume, although CO_2 is produced at high concentrations by a few industrial processes. It is essential to explore ways to eliminate and minimize the presence of these gases in the atmosphere.

4.1.2 Scope of the present investigations

Depending on the applied pressure and temperature, hydrogen can adsorb on solid surfaces through either van der Waals-type weak physisorption or chemisorptions. At a given pressure, adsorption at or above the boiling point of the adsorbate leads to the formation of a monolayer. On activated carbon with a specific surface area of 1,315 m^2g^{-1}, 2 wt% of hydrogen is reversibly adsorbed at a temperature of 77 K.[10] Dillon *et al*.[11] showed H_2 adsorption capacities of 0.01 wt% on unpurified soot containing 0.1-0.2 wt% SWNTs. Assuming only SWNTs adsorb H_2, the data was extrapolated to 5 wt% uptake of H_2 at 273 K and 300 torr. Liu *et al*.[12] reported H_2 storage capacity of 4.2 wt% at room temperature and 10 MPa pressure in pre-treated SWNTs and showed almost complete desorption under ambient conditions. While Ye *et al*.[13] obtained a maximum of 8.25 wt% of H_2 uptake at 80K and 120 bar in highly pure cut-SWNT ropes. These conflicting results are mainly due to inadequate characterization of the carbon material used. It is often a mixture of opened and unopened, single-walled and multi-walled tubes of various diameters and helicities together with other carbonaceous species. Zuettel *et al*.[14] concluded that H_2 uptake in carbon nanotubes at liquid nitrogen temperature (77 K) or at ambient conditions is due to physisorption. The amount of adsorbed hydrogen is proportional to the specific surface area of the carbon nanotubes.[15]

In the case of CO_2, methods have been proposed to capture it in various materials and utilize it in chemical reactions.[16] While removal of low concentrations of CO_2 from air is rather difficult, removal of CO_2 from flue gases is more practical.[17, 18] With this purpose, CO_2 has been dissolved in solvents such as organic amines.[19-23] This method generally suffers from difficulties related to regeneration of the solvents by heating.[24] Solid sorbents

would be more economical and metal-organic frameworks (MOFs) and other solids have been investigated for this purpose.[25-29] Activated carbons have shown good potential to adsorb CO_2.[30, 31] While considerable amount of work on the removal of CO_2 have been reported, elimination of CH_4 from the atmosphere has received somewhat less attention. Removal of CH_4 by sorbents is generally much less effective than that of CO_2. MOFs have been reported to adsorb reasonable amounts of CH_4.[32-37] Activated charcoal and carbon fibre seem to be reasonably good adsorbers for CH_4.[38]

Preliminary experiments indicated that graphene may have good sorption characterstics for H_2 and CO_2. We have therefore, investigated the BET surface areas and uptake of H_2, CO_2 and CH_4 by the graphene samples prepared by exfoliation of graphite oxide (EG),[39] conversion of nanodiamond (DG),[40] arc evaporation of graphite (HG) and reduction of graphene oxide (RGO).[41] Some of these samples have been subjected to H_2 treatment at high temperature and further acid treatment. We have measured the surface areas and H_2 uptake of the graphene samples by employing QuantaChrome Autosorb-1 instrument at 1 atm and 77 K. Using the same instrument CO_2 uptake experiments were performed at 1 atm and 195 K. High pressure H_2 uptake experiments were carried out employing a custom-built apparatus. CH_4 uptake measurements were carried out employing BELSORP-aqua3 analyzer. These samples showed BET surface area values in the range of 238-1550 m^2/g and H_2 uptake going up to 1.7 wt % at 1 atm, 77 K and 3 wt % at 100 atm, 298 K. These samples also showed good CO_2 uptake, the value reaching up to 35 wt % at 1 atm and 195 K, but quite low CH_4 uptake in the range of 0.0-2.8 wt % at 50 bar and 298 K. To understand these properties, first-principles calculations have been carried out on the interaction of H_2 and CO_2 with single- and multilayered graphene.

4.1.3 Experimental section

Graphene samples were prepared by different methods.[39] N_2, H_2 and CO_2 adsorption studies of the graphene samples were carried out using a QuantaChrome Autosorb-1instrument at 77 K (for N_2 and H_2) and at 195 K (for CO_2). Prior to the adsorption measurements, the graphene samples were subjected to degassing at 200 °C for a period of 18 hours under high vacuum (10^{-1} Pa). The degree of adsorption was monitored by the decrease in pressure at the equilibrium state and all operations were computer-controlled. High pressure hydrogen adsorption experiments were carried out using a custom-built adsorption set-up as reported by Gundiah *et al*.[42] The experiments were performed at 300 K and 100 bar using ultra high pure hydrogen (99.99%), with an impurity (e.g. moisture and nitrogen) content less than 10 ppm. CH_4 uptake measurements were carried out employing BELSORP-aqua3 analyzer at 50 bar and 298 K.

4.1.4 Results and discussion

Surface areas

We prepared several graphene samples (EG 1, EG 2, EG 3, EG 4, and EG 5) by the exfoliation of graphite oxide by following the literature procedure.[39] These samples possesses Brunauer-Emmett-Teller (BET) surface areas in the range of 639 -1550 m^2/g. We treated the graphene sample, EG 3, with hydrogen at 1000 °C for 4 hours to obtain EG 3-H_2, and with a 1:1 mixture of concentrated nitric and sulfuric acids at 100 °C under hydrothermal conditions to obtain EG 3-COOH. The surface area of EG 3-COOH was the lowest (34 m^2/g) while that of EG 3-H_2 was 1258 m^2/g. The surface area values of different graphene samples EG 1, EG 2, EG 3, EG 4, EG 5, including acid treated (EG 3-COOH) and hydrogen treated

(EG 3-H_2), are summarized in Table 1. Nitrogen adsorption isotherms of EG 1, EG 2, EG 3, EG 4, EG3-COOH and EG3-H_2 are shown in Figure 1.

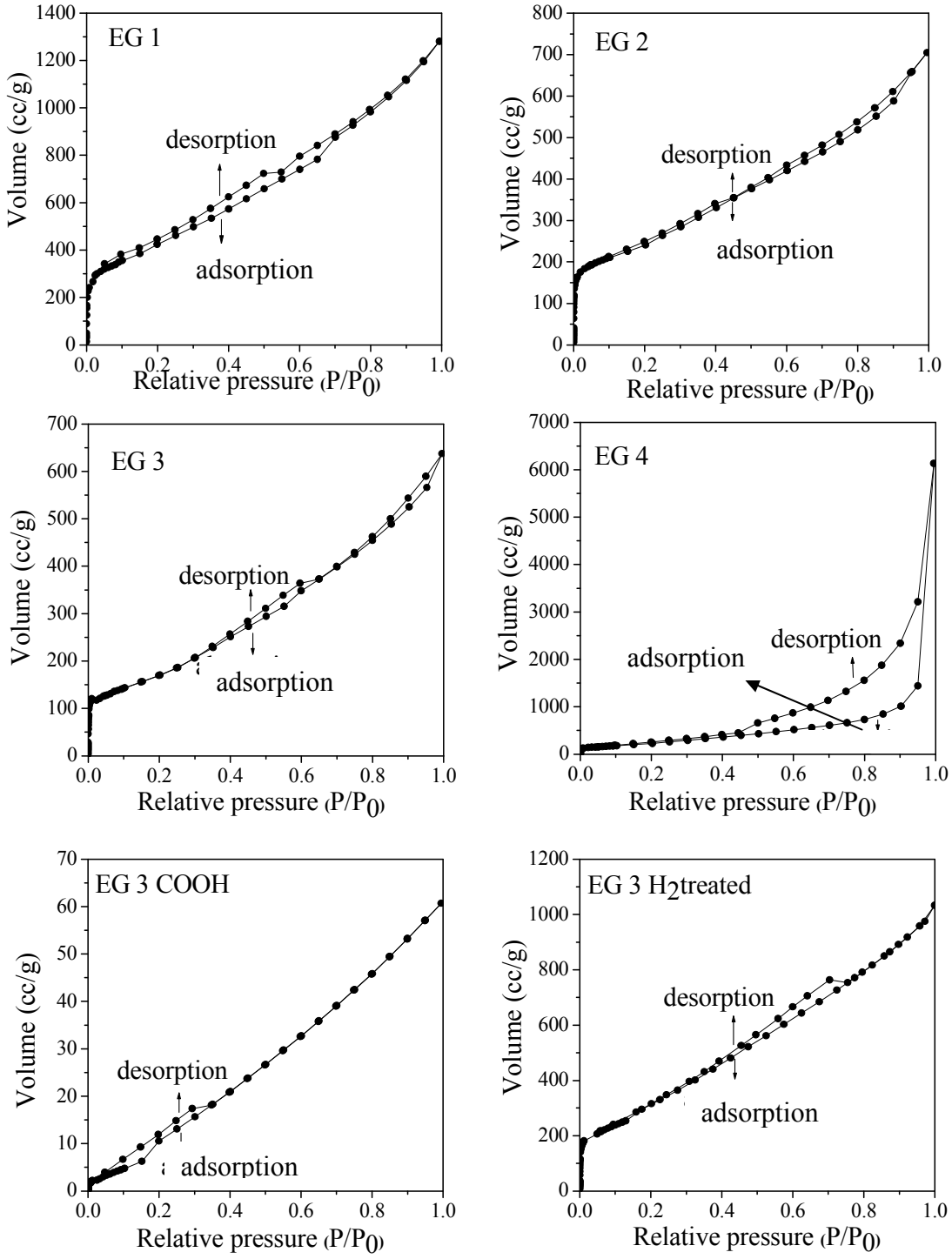

Figure 1. Nitrogen adsorption and desorption curves of EG samples.

Table 1: BET surface area values of EG samples.

Sample	EG 1	EG 2	EG 3	EG 4	EG 5	EG 3-H_2 treated	EG 3-COOH
Surface area (m^2/g)	1550	871	639	925	700	1250	34

We annealed nanodiamond powder employing graphite furnace at 1650 and 1850 ºC for 1 hr, at 2050 ºC for 1hr, 1.5hr and 2 hr and at 2200 ºC for 40 min.[40] These samples are designated as DG-1650, DG-1850, DG-2050 (1 hr), DG-2050 (1.5 hr), DG-2050 (2 hr) and DG-2200 respectively. These samples exhibit surface areas in the range of 400-650 m^2/g and comprise 8-10 graphene layers. Surface areas of the graphene samples depend on the number of layers, the surface area of single-layer graphene being ~2600 m^2/g.[43] In Table 2, we show the surface area values of all the DG samples. BET surface area plots of DG-1650, DG-1850 are shown in Figure 2.

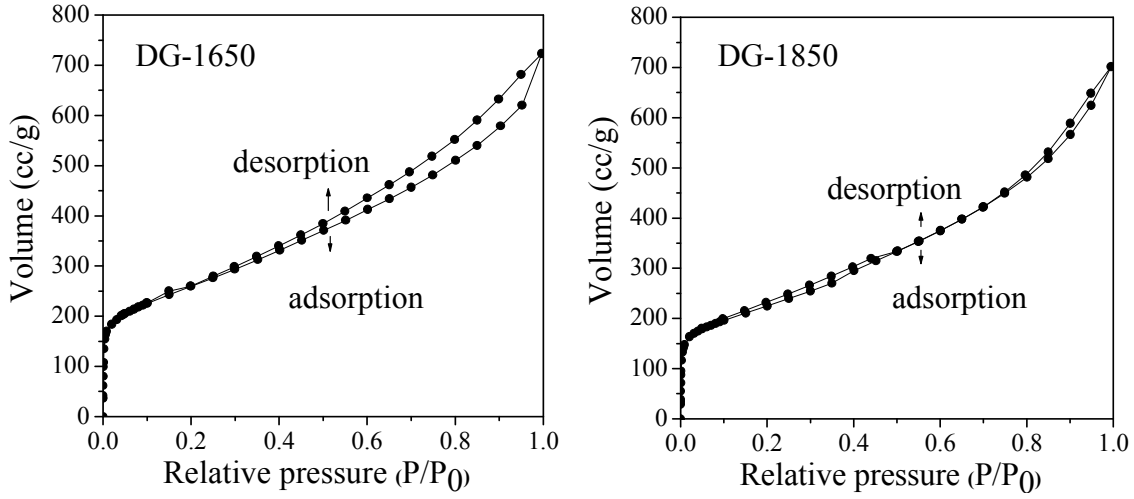

Figure 2. Nitrogen adsorption and desorption curves of DG samples.

Table 2: BET Surface area values of DG samples.

Sample	DG-1650	DG-1850	DG-2050 (1 hr)	DG-2050 (1.5 hr)	DG-2050 (2 hr)	DG-2200
Surface area (m^2/g)	463-650	450	500	430	400	412

We also prepared graphene by employing arc-discharge using graphite rod as consumed anode. Arc discharge chamber was filled with a mixture of hydrogen and helium or methane and helium mixtures, in different proportions. These samples show surface area in the range of 270-680 m^2/g. Among these samples HG 1 shows highest value around 680 m^2/g, next HG 3 comes showing around 480 m^2/g. HG 2, HG 4 and HG 5 show quite low values around 270, 281 and 268 respectively. We show BET surface area plots of HG1 and HG3 in Figure 3.

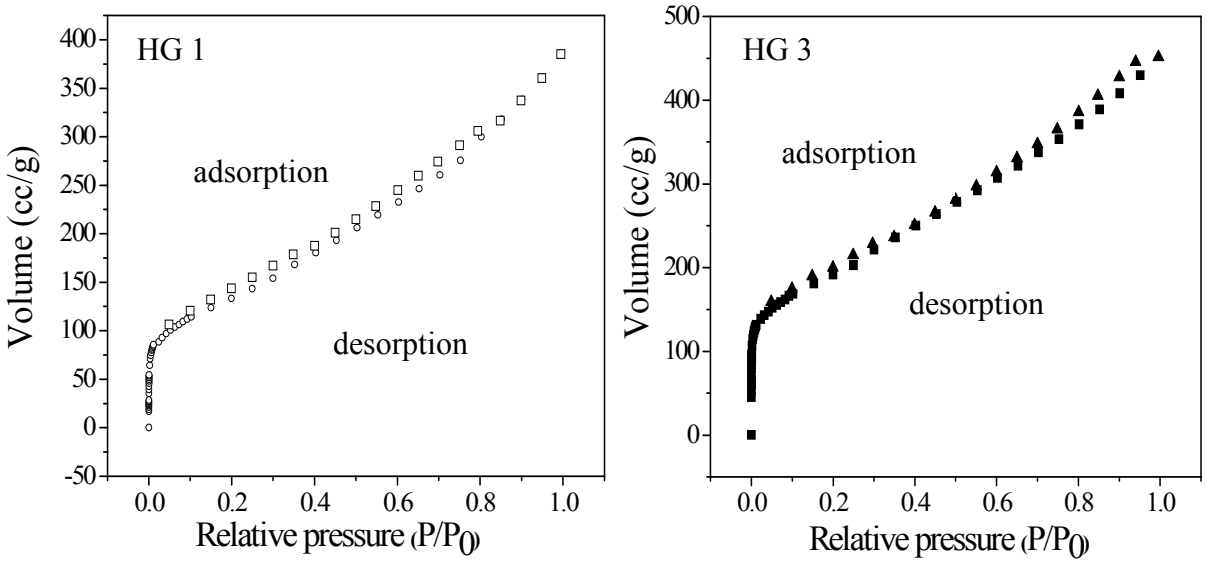

Figure 3. Nitrogen adsorption and desorption curves of HG 1 and HG 3.

We obtained single-layer graphene oxide (SGO) by ultrasonication of graphite oxide (GO) which was prepared by Hummers method. RGO was prepared by the reduction of single-

layer graphene oxide (SGO) under refluxing conditions. We measured surface areas of both SGO and RGO. RGO shows a surface area of around 450 m^2/g, whereas SGO shows a low value of around 5 m^2/g.

Adsorption of H_2

We have studied the uptake of H_2 by the various graphene samples at 1 atm and 77 K by employing a Quanta Chrome Autosorb-1 instrument. In Figure 4, we show typical adsorption and desorption curves of EG, DG, HG 1 and HG 3. EG samples show H_2 uptake in the range of 0.6-1.7 wt % at 1 atm and 77 K. On acidification, EG shows sudden drop in uptake to 0.05 wt %.

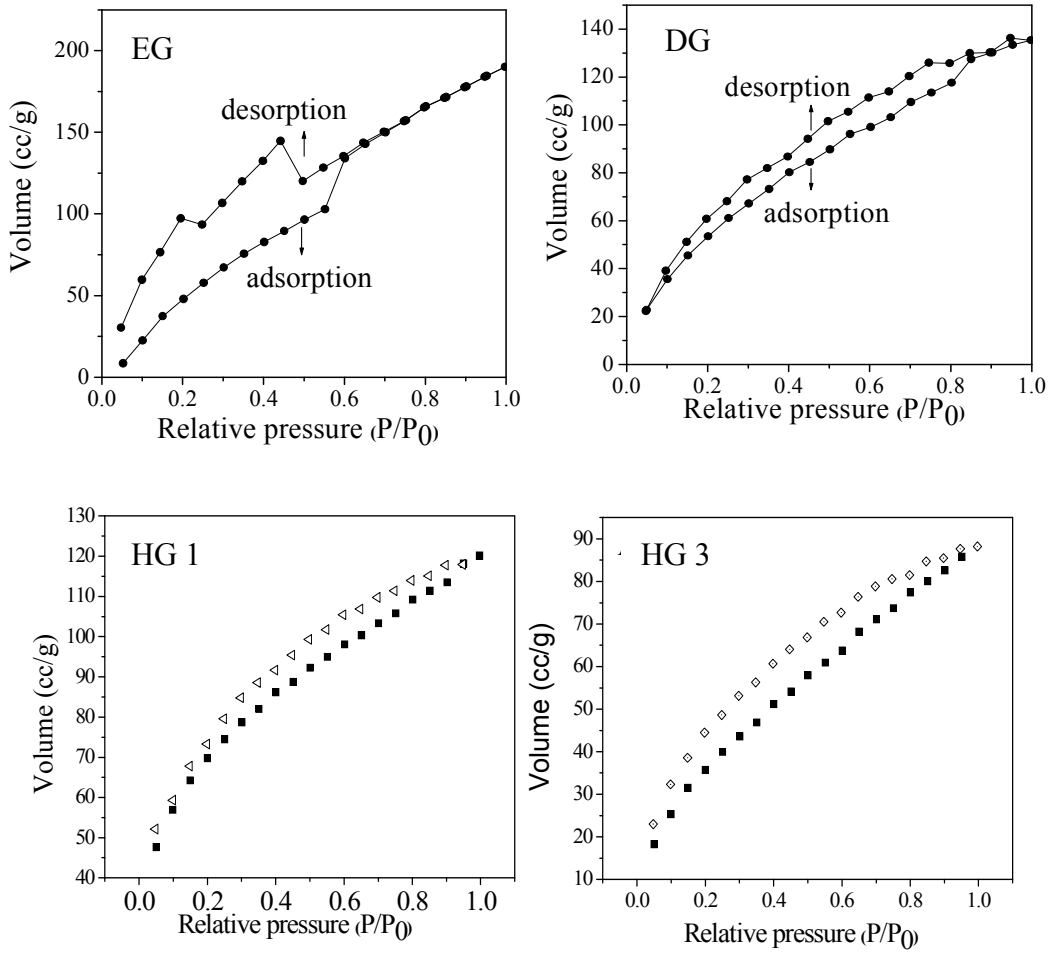

Figure 4. H_2 adsorption and desorption curves of EG, DG, HG 1 and HG 3.

DG samples show H_2 uptake in the range of 0.6-1.21 wt %. Among all the arc discharge samples HG 1 show the highest value of around 1 wt %. HG 3 and HG 2 show around 0.63 and 0.227 wt % respectively. By using a custom-made adsorption set-up,[44] we carried out high pressure hydrogen adsorption measurements. We find that the EG samples with 1.4 wt % (EG 1) and 1 wt % (EG 2) uptake at 1 atm and 77 K, exhibits a hydrogen uptake of 3.1 wt % and 2 wt % at 100 bar pressure and 298 K respectively. DG and HG samples with 1 wt % at 1 atm and 77 K, exhibit 2.5 wt % and 2 wt % of hydrogen uptake at 100 bar pressure and 298 K respectively. High pressure hydrogen uptake curves of EG and DG samples are given in Figure 5.

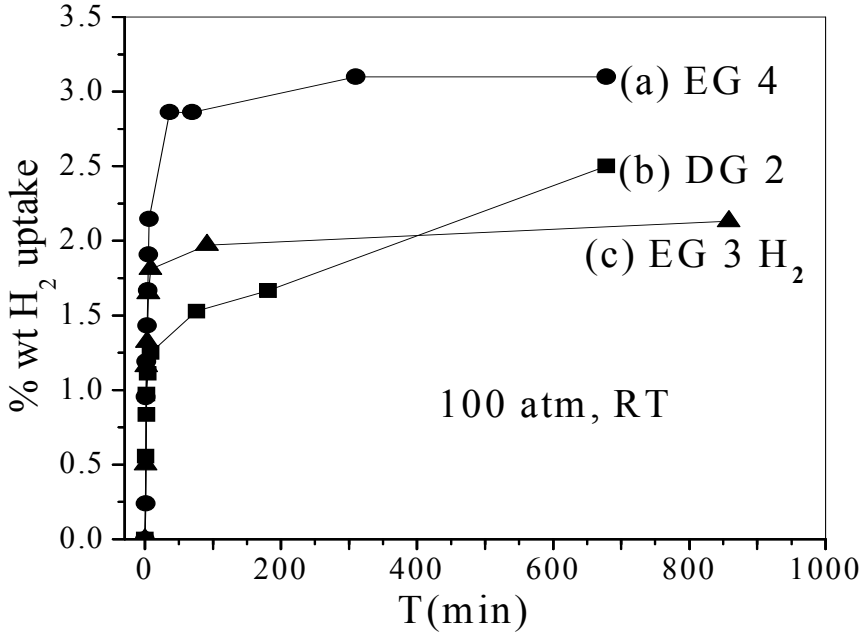

Figure 5. High pressure hydrogen H_2 uptake curves of EG 4, DG 2 and EG 3 H2.

The values of H_2 uptake by the various graphene samples prepared by us vary linearly with the surface area as shown in Figure 6. By extrapolation of the plot in Figure 6 to the surface

area of single-layer graphene, we estimate its hydrogen uptake at 1 atm and 77 K to be around 3 wt%, which is impressive.

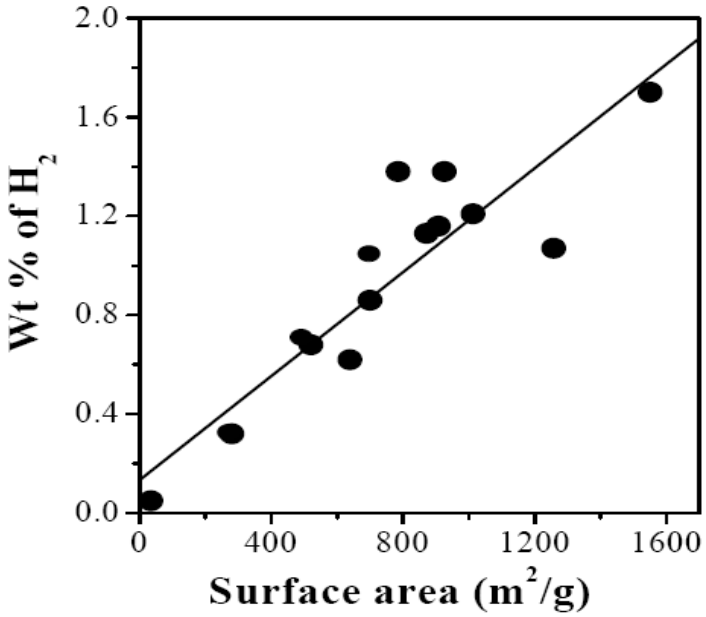

Figure 6. Linear relationship between the BET surface area and the wt% of hydrogen uptake at 1 atm pressure and 77 K temperature.

Though the graphene samples examined by us exhibit lower hydrogen uptake compared to the 6.0 wt% target of Department of Energy (USA), there is significant scope for further improvements, by producing samples with smaller number of layers and significantly higher surface areas. It is possible that single layer graphene will exhibit 5-6 wt % of H_2 uptake at 100 atm and 298 K.

Adsorption of CO_2

We studied the uptake of CO_2 at 1 atm and 195 K by using several samples of graphene prepared by us. Figures 7 and 8 show CO_2 adsorption and desorption curves of EG, DG and HG samples. The EG samples show CO_2 uptake in the range of 21-34 wt %. EG 1 and EG 4 show similar values, close to 34 wt % (Figure 7). EG 2 and EG 3 show around 20

wt % and 26 wt % respectively. The uptake values of CO_2 vary linearly with surface area. The uptake of CO_2 by EG was also measured at room temperature and high pressure. It showed 51 % at 298 K and 50 bar.

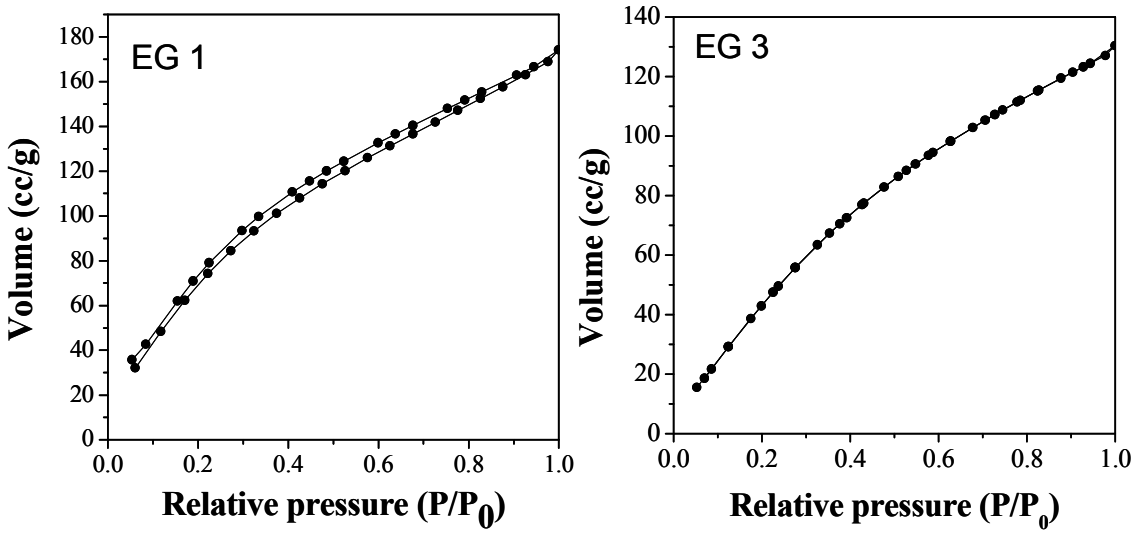

Figure 7. CO_2 adsorption and desorption curves of EG 1 and EG 3.

Among DG and HG samples, DG-1650 sample exhibits around 10 wt %. HG 1 shows 16.8 wt %, where as HG 2 and HG 3 exhibit 10.6 wt % and 11.9 wt % respectively (Figure 8). RGO shows in between EG and DG around 25 wt %, whereas SGO exhibits the lowest uptake (5 wt %) among all the graphene samples. Figure 8 shows CO_2 adsorption and desorption curves of DG, HG 1, HG 2, HG 3, SGO and RGO samples.

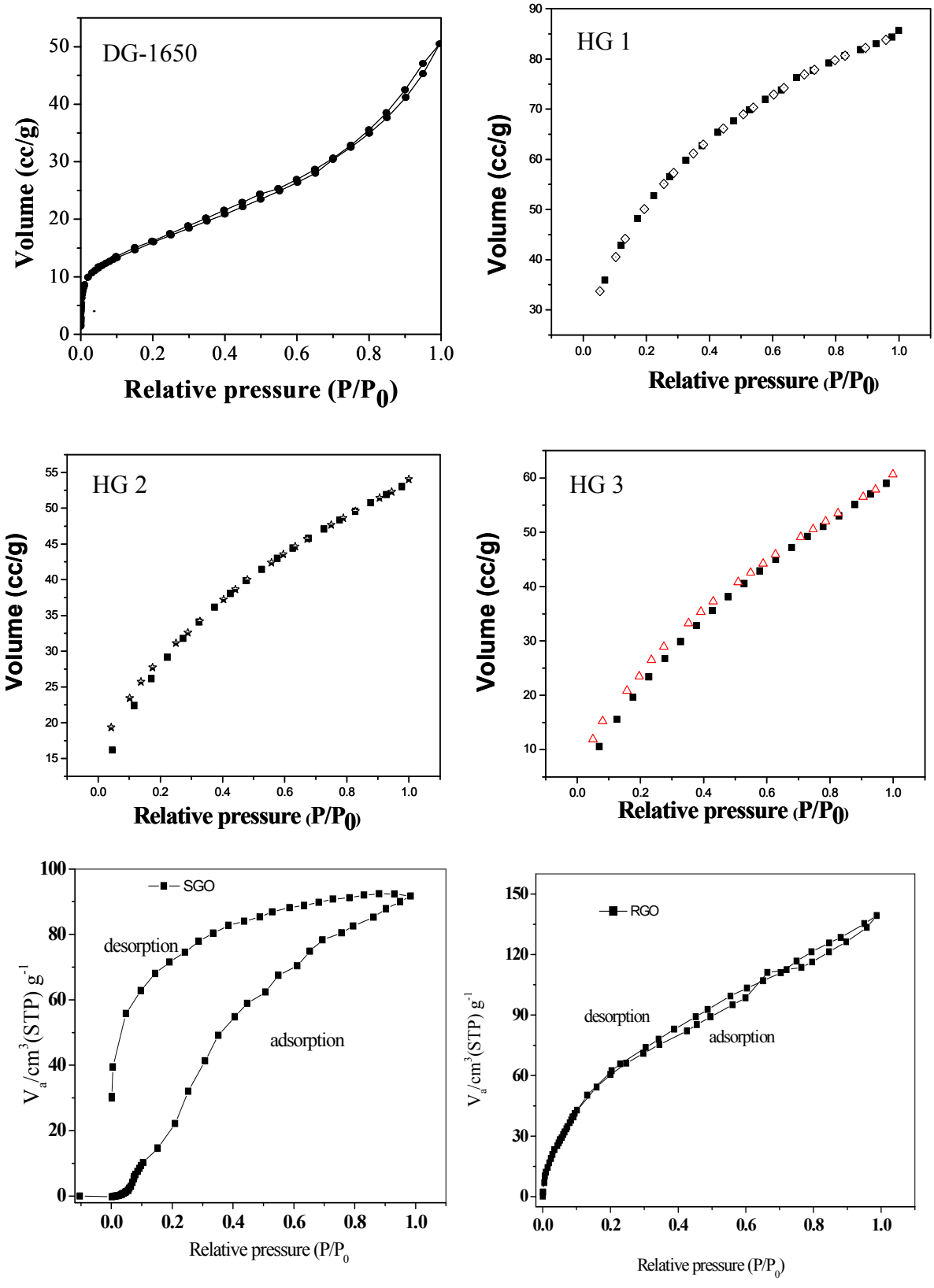

Figure 8. CO_2 adsorption and desorption curves of DG, HG, SGO and RGO samples.

To estimate the H_2 and CO_2 uptake theoretically, Prof. Pati and co-workers considered 2D periodic graphene system with hydrogen and carbon dioxide using an ab initio density functional package, SIESTA[45] and performed calculations within the generalized gradient approximation (GGA). The position and distance of a single H_2/CO_2 molecule are varied separately on the relaxed structure of graphene to determine the most stable position with equilibrium distance for adsorption. Then the density of H_2 and CO_2 molecules are gradually increased on the graphene sheet to determine the maximum weight percentage of uptake. Graphene supercell size and the number of layers are also varied. On the basis of the relaxed geometries, three different orientations of hydrogen molecule namely parallel 1, parallel 2, and perpendicular (upper panel of Figure 9) are considered on the graphene surface. The plot

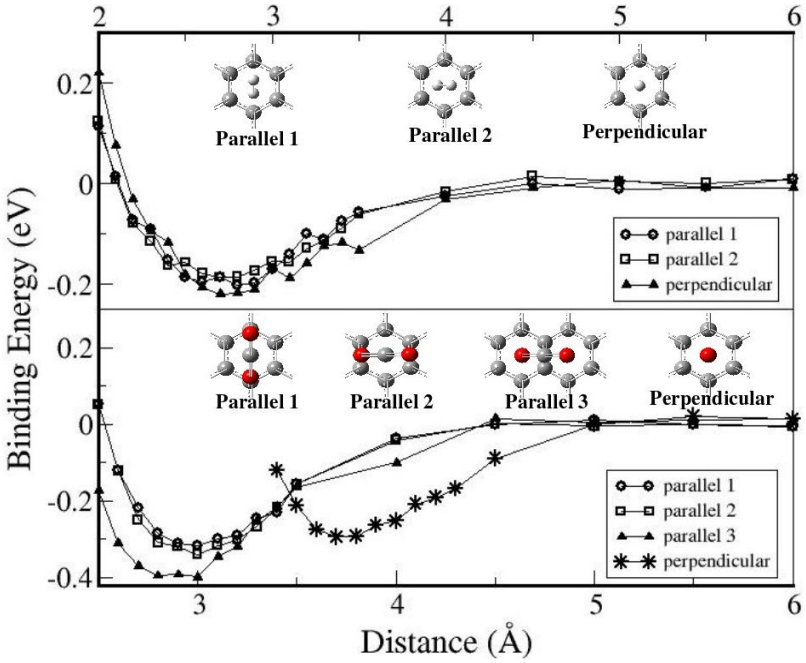

Figure 9. Binding energies of a single molecule on a graphene supercell as a function of distance with different adsorption orientations (shown in insets) for hydrogen (upper panel) and carbon dioxide (lower panel).

of binding energy with varying distance shows that the perpendicular orientation on the center of mass of a benzene ring gives the most stable structure, while other orientations also show similar stabilization energies making all three orientations become almost equally significant. In the case of carbon dioxide, three different positions of parallel orientations, namely parallel 1, 2 and 3 and one perpendicular orientation (lower panel of Figure 9) are considered and the binding energy values show that the parallel 3 structure is the most stable. With the knowledge on the most stable position, orientation and equilibrium distance of hydrogen as well as carbon dioxide, gradually their density has been increased on one side of the graphene surface to estimate the maximum weight percentage of adsorption. Calculations showed that each ring in the graphene plane can stabilize one hydrogen molecule with both parallel 2 and perpendicular orientations on alternative benzene rings of the graphene supercell to accommodate a maximum uptake of 7.69 wt %, suggesting graphene to be a satisfactory hydrogen storage material. However, the weight percentage of H_2 in graphenes with three layers and four layers are estimated to be 2.70 and 2.04 wt % respectively. For carbon dioxide uptake, parallel 3 conformation was considered which showed an adsorption of a maximum 12 molecules on one side of the graphene supercell with 72 carbon atoms. This suggested maximum carbon dioxide uptake of 37.93 wt % on a single-layer graphene. Similar results are also obtained in the case of different choices of supercells, which unambiguously prove that the theoretical estimates of the binding energy and the desorption temperature are hardly affected by the supercell size.

Adsorption of CH_4

Adsorption of methane on different graphenes (EG, HG, SGO and RGO) was carried out at 50 bar, 298 K and 50 bar, 273 K. CH_4 uptake of the graphene samples varies between 0

and 3 wt%. EG and RGO show around 2.4, 1.7 wt% at 298 K and 2.8, 2.4 wt% at 273 K respectively (Figure 10). SGO exhibits negligible uptake and HG shows no uptake at 298 K (Figure 11).

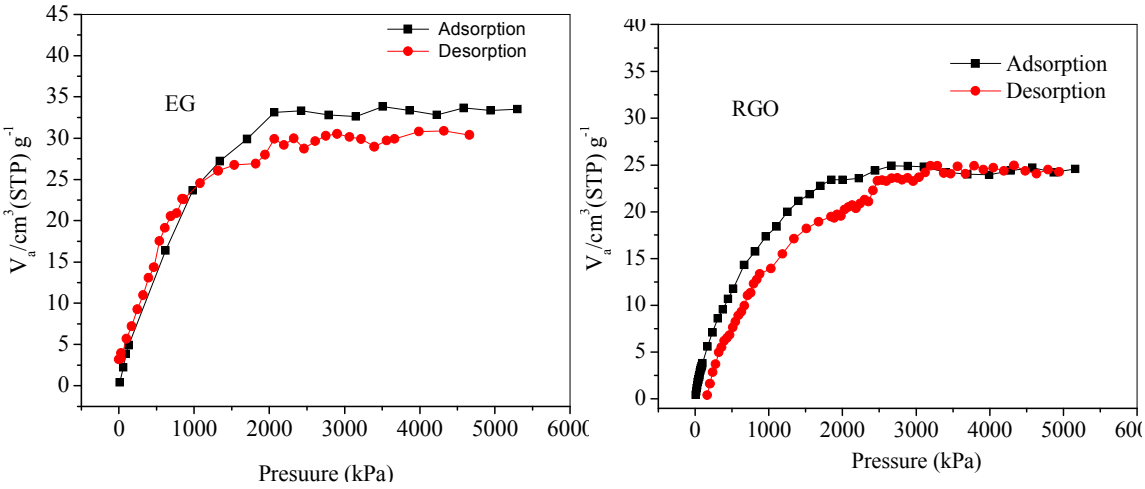

Figure 10. CH_4 adsorption and desorption curves of EG and RGO.

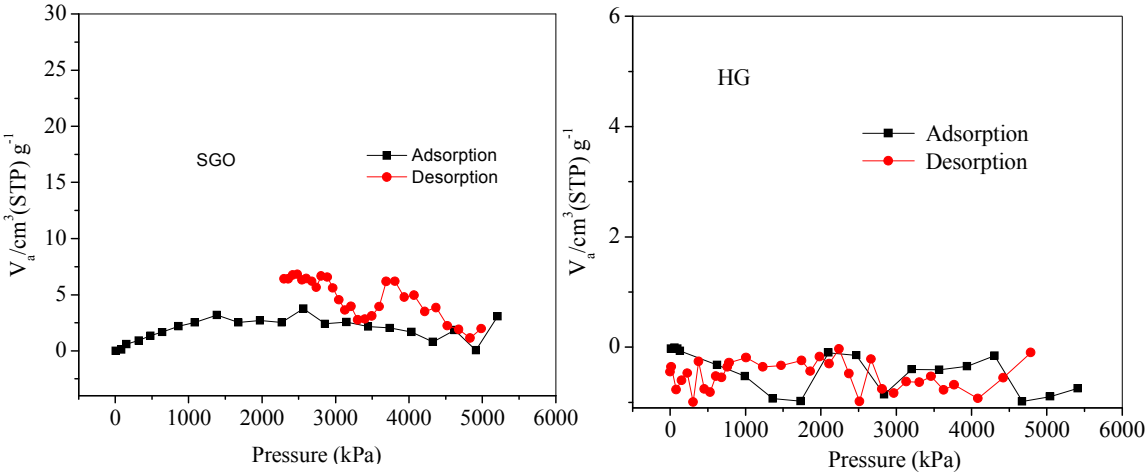

Figure 11. CH_4 adsorption and desorption curves of SGO and HG.

It is interesting that the uptake of CO_2 and CH_4 follow similar trends. CH_4 uptake varies nearly linear with the CO_2 uptake. EG and RGO with relatively high CH_4 uptakes contain

oxygen functionalities on the surface. Interestingly, in the case of HG with little or no uptake of these gases, the surface was clean with negligible oxygen functionalities.

4.1.5 Conclusions

Graphene samples prepared by different methods generally exhibit high surface areas. Graphenes prepared by exfoliation of graphite oxide, conversion of nanodiamond, arc evaporation of graphite and reduction of graphene oxide exhibit significant uptake of H_2 and CO_2. While the maximum H_2 uptake, found by us at 100 atm and 298 K is 3.1 wt %, it should be possible to increase it by preparing better samples and by reducing the average number of graphene layers. Exfoliated graphene sample shows high CO_2 uptake up to 35 wt % at 1 atm and 195 K. Graphene samples show quite low CH_4 uptake values around 3 wt % at 50 bar and 298 K. Interestingly, the uptake of H_2, CO_2 and CH_4 vary linearly with the surface area of the samples. The uptake of H_2 and CO_2 found by us can be of value for storage and separation.

4.1.6 References

[1] C. N. R. Rao, A. Govindaraj, in *Nanotubes and Nanowires, RSC nanoscience & Nanotechnology Series*, RSC, Cambridge, UK, **2005**.

[2] K. J. Klabunde, J. V. Stark, O. B. Koper, C. Mohs, D. G. Park, S. Decker, Y. Jiang, I. Lagadic, D. Zhang, *J. Phys. Chem.* **1996**, *100*, 12142.

[3] S. Decker, K. J. Klabunde, *J. Am. Chem. Soc.* **1996**, *118*, 12465.

[4] G. L. Hornyak, C. J. Patrissi, C. R. Martin, *J. Phys. Chem. B* **1997**, *101*, 1548.

[5] R. Leon, D. Margolese, G. Stucky, P. M. Petroff, *Phys. Rev. B* **1995**, *52*, R2285.

[6] N. P. Blake, V. I. Srdanov, G. D. Stucky, H. Metiu, *J. Chem. Phys.* **1996**, *104*, 8721.

[7] G. Cao, M. E. Garcia, M. Alcala, L. F. Burgess, T. E. Mallouk, *J. Am. Chem. Soc.* **1992**, *114*, 7574.

[8] T. A. Dickinson, J. White, J. S. Kauer, D. R. Walt, *Nature* **1996**, *382*, 697.

[9] S. Satyapal, J. Petrovic, C. Read, G. Thomas, G. Ordaz, *Catalysis Today* **2007**, *120*, 246.

[10] W. J. Nellis, A. A. Louis, N. W. Ashcroft, *Phil. Trans. R. Soc. Lond. A* **1998**, *356*, 119.

[11] A. C. Dillon, K. M. Jones, T. A. Bekkedahl, C. H. Kiang, D. S. Bethune, M. J. Heben, *Nature* **1997**, *386*, 377.

[12] C. Liu, Y. Y. Fan, M. Liu, H. T. Cong, H. M. Cheng, M. S. Dresselhaus, *Science* **1999**, *286*, 1127.

[13] Y. Ye, C. C. Ahn, C. Witham, B. Fultz, J. Liu, A. G. Rinzler, D. Colbert, K. A. Smith, R. E. Smalley, *Appl. Phys. Lett.* **1999**, *74*, 2307.

[14] A. Zuttel, P. Sudan, P. mauron, T. Kiyobayashi, C. Emmenegger, L. Schlapbach, *Int. J.Hydrogen Energy* **2002**, *27*, 203.

[15] M. G. Nijkamp, J. E. M. J. Raaymakers, A. J. Van Dillen, K. P. De Jong, *Appl. Phys. A* **2001**, *72*, 619.

[16] K. M. K. Yu, I. Curcic, J. Gabriel, S. C. E. Tsang, *ChemSusChem* **2008**, *1*, 893.

[17] D. W. Keith, *Science* **2009**, *325*, 1654.

[18] A. Wahby, J. M. Ramos-Fernández, M. Martínez-Escandell, A. Sepúlveda-Escribano, J. Silvestre-Albero, F. Rodríguez-Reinoso, *ChemSusChem 3*, 974.

[19] S. Zhou, X. Chen, T. Nguyen, A. K. Voice, G. T. Rochelle, *ChemSusChem 3*, 913.

[20] J. Zhang, B. Han, Y. Zhao, J. Li, M. Hou, G. Yang, *Chem. Commun.47*, 1033.

[21] R. J. Perry, T. A. Grocela-Rocha, M. J. O'Brien, S. Genovese, B. R. Wood, L. N. Lewis, H. Lam, G. Soloveichik, M. Rubinsztajn, S. Kniajanski, S. Draper, R. M. Enick, J. K. Johnson, H.-b. Xie, D. Tapriyal, *ChemSusChem 3*, 919.

[22] K. Simons, K. Nijmeijer, H. Mengers, W. Brilman, M. Wessling, *ChemSusChem 3*, 939.

[23] E. Sada, H. Kumazawa, M. A. Butt, *Chem. Eng. J.* **1977**, *13*, 213.

[24] S. Chakravarti, A. Gupta, B. Hunek, in *First National Conference on Carbon Sequestration*, Washington DC, **2001**.

[25] A. O. Yazaydin, R. Q. Snurr, T. H. Park, K. Koh, J. Liu, M. D. LaVan, A. I. Benin, P. Jakubczak, M. Lanuza, D. B. Galloway, J. J. Low, R. R. Willis, *J. Am. Chem. Soc.* **2009**, *131*, 18198.

[26] Y.-S. Bae, O. K. Farha, J. T. Hupp, R. Q. Snurr, *J. Mater. Chem.* **2009**, *19*, 2131.

[27] A. O. Yazaydin, A. I. Benin, S. A. Faheem, P. Jakubczak, J. J. Low, J. J. Low, R. Q. Snurr, *Chem. Mater.* **2009**, *21*, 1425.

[28] Y.-S. Bae, O. K. Farha, A. M. Spokoyny, C. A. Mirkin, J. T. Hupp, R. Q. Snurr, *Chem. Commun.* **2008**, 4135.

[29] B. D. Freeman, *Macromolecules* **1999**, *32*, 375.

[30] V. Goetz, O. Pupier, A. Guillot, *Adsorption* **2006**, *12*, 55.

[31] W. R. Alesi, M. Gray, J. R. Kitchin, *ChemSusChem 3*, 948.

[32] M. Eddaoudi, J. Kim, N. Rosi, D. Vodak, J. Wachter, M. O'Keeffe, O. M. Yaghi, *Science* **2002**, *295*, 469.

[33] A. C. Sudik, A. R. Millward, N. W. Ockwig, A. P. Côté, J. Kim, O. M. Yaghi, *J. Am. Chem. Soc.* **2005**, *127*, 7110.

[34] S. Ma, D. Sun, J. M. Simmons, C. D. Collier, D. Yuan, H.-C. Zhou, *J. Am. Chem. Soc.* **2007**, *130*, 1012.

[35] H. Wu, W. Zhou, T. Yildirim, *J. Am. Chem. Soc.* **2009**, *131*, 4995.

[36] J. Lan, D. Cao, W. Wang, *Langmuir* **2009**, *26*, 220.

[37] H. Wu, W. Zhou, T. Yildirim, *J. Phys. Chem. C* **2009**, *113*, 3029.

[38] D. L. Castello, J. A. Mongea, M. A. d. l. Casa-Lillob, D. C. Amoro´sa, A. L. Solano, *Fuel* **2002**, *81*, 1777.

[39] H. C. Schniepp, J. L. Li, M. J. McAllister, H. Sai, M. Herrera-Alonso, D. H. Adamson, R. K. Prud'homme, R. Car, D. A. Saville, I. A. Aksay, *J. Phys. Chem. B* **2006**, *110*, 8535.

[40] O. E. Andersson, B. L. V. Prasad, H. Sato, T. Enoki, Y. Hishiyama, Y. Kaburagi, M. Yoshikawa, S. Bandow, *Phys. Rev. B* **1998**, *58*, 16387.

[41] S. Stankovich, D. A. Dikin, R. D. Piner, K. A. Kohlhaas, A. Kleinhammes, Y. Jia, Y. Wu, S. T. Nguyen, R. S. Ruoff, *Carbon* **2007**, *45*, 1558.

[42] G. Gundiah, A. Govindaraj, N. Rajalakshmi, K. S. Dhathathreyan, C. N. R. Rao, *J. Mater. Chem.* **2003**, *13*, 209.

[43] L. C. F. E. B. R. R. Peigney A, A. Rousset, *Carbon* **2001**, *39*, 507.

[44] G. Gundiah, A. Govindaraj, N. Rajalakshmi, K. S. Dhathathreyan, C. N. R. Rao, *J. Mater. Chem.* **2003**, *13*, 209.

[45] J. M. Soler, E. Artacho, J. D. Gale, A. García, J. Junquera, P. Ordejón, D. S.-Portal, *J. Phys. : Condens. Matter* **2002**, *14*, 2745.

4.2 Novel magnetic properties

4.2.1 Introduction

Magnetism is one of the most intriguing phenomena observed in nature. Magnetism is relevant to physics, geology, biology and chemistry. Traditional magnets, an ubiquitous part of many everyday gadgets, are made of heavy iron- or nickel based materials. Recently, metal-free nanocarbon structures exhibiting magnetic ordering represent a new class of materials and open a novel field of research that could lead to many new technologies. The most important issue in characterizing the electronic features of nanocarbon materials is their geometry dependence, which is clearly understood when we recall the shapes of carbon nanotubes. Indeed, the diameter and chirality of carbon nanotubes are the key parameters characterizing their electronic structure, which varies from semiconducting to metallic depending on the interplay between these parameters.[1] A similar geometry dependence exists in other members of p-electron-based nanocarbon materials also; however, it appears in a manner different from that observed in carbon nanotubes. Among these members, nanographene has an interesting geometry dependence: the electronic structure depends on geometry of the edge structures,[2-6] since a flat nanographene sheet is surrounded by the open edges. The circumference of an arbitrarily shaped nanographene sheet having open edges is described in terms of a combination of armchair and zigzag edges, as shown in Figures 1a and b.[7] According to theoretical and experimental studies on the electronic structure of nanographene, a non-bonding π-electron state (so-called edge state) exists in the region of zigzag edge at the Fermi energy at which the bonding π- and antibonding π*-bands touch each other.[2-4] In contrast, the electronic structure of armchair edge is described merely in terms of the bonding π- and antibonding π*-bands similar to that of an infinite graphene sheet having the feature of zero-gap semiconductor.[8] The non-bonding edge states that are localized

around the zigzag edge region have localized spins, contributing to creation of spin magnetism, which is in sharp contrast to diamagnetic nature of graphene and bulk graphite. Therefore, nanographene is an intriguing building block that can be used in designing carbon-based magnetic systems in which even ferromagnetism can be involved.[9]

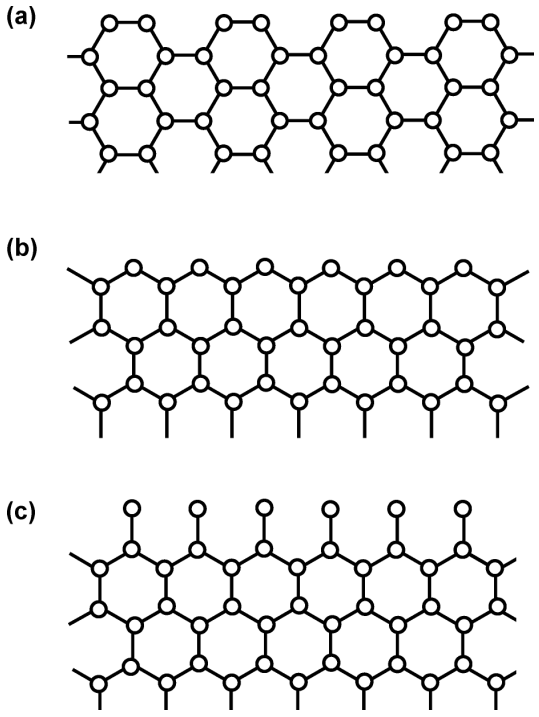

Figure 1. Graphene edges: (a) armchair edge, (b) zigzag edge and (c) zigzag edge with its all edge carbon atoms bonded to an additional carbon atom that participates in the π-conjugated system; (b) and (c) are called 'Fujita edge' and 'Klein edge', respectively. Carbon atoms are denoted by open circles. Each edge carbon atom is terminated by a hydrogen atom or another atom and has no σ-dangling bond. [From ref. [7]).

Chemists know that the electronic structure of benzene, comprising a carbon hexagon network of π-electrons, is given by a combination of three bonding π-levels and three antibonding π*-levels that are split with a large HOMO–LUMO gap as a consequence of resonance in the electronic structure of aromatic molecules. Polycyclic

condensed aromatic molecules such as naphthalene and anthracene which are created by fusing benzene rings have a structure similar to that of π-electrons in benzene. In these molecules, the HOMO–LUMO gap decreases with an increase in the number of benzene rings, and the graphene sheet present in the infinite extreme is featured as a zero-gap semiconductor without the gap. These aromatic molecules, which are classified into Kekule molecules having a close shell, are nonmagnetic, as shown in Figure 2a. However, in polycyclic-condensed aromatic molecules, there is a sub-family that cannot be featured only with the bonding π- and antibonding π*-states.[6, 10, 11] Typical examples are phenalenyl radical, trigangulene radical and 1H,4H,5Htribenzo[bc,hi,no]coronene-1,4,5-triyl consisting of three, six and ten benzene rings, respectively, as shown in Figures 2b, c and d. In these molecules (named non-Kekule molecules), extra π-states, which are

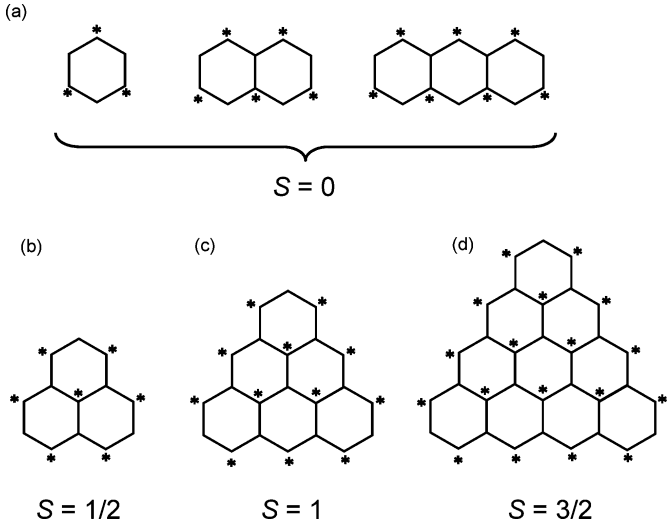

Figure 2. (a) Simple Kekul´e molecules, (b) phenalenyl free-radical, (c) triangulene free-radical and (d) 1H,4H,5H-tribenzo[bc,hi,no]coronene- 1,4,5-triyl free-radical; (b), (c) and (d) are classified as non-Kekul´e molecules. The carbon sites, which are directly bonded to a site belonging to a subgroup (starred), belong to another subgroup (unstarred). (From ref. [7]).

characterized as non-bonding π-electron states at the Fermi level in the gap between π- and π*-states, are added to the electronic structure. The presence of singly occupied nonbonding states in these open shell structures tends to destabilize these molecules, since they occur at the Fermi level. This can be confirmed by the experimental finding that the phenalenyl and trigangulene radicals are chemically active.[10, 11] The number of non-bonding states can be counted on the basis of Lieb's theorem.[6] In general, we can group all the carbon sites of a condensed polycyclic aromatic hydrocarbon molecule into two subgroups where neighbouring sites directly bonded to the site belonging to a subgroup (subgroup A or starred) belong to the other subgroup (subgroup B or unstarred), as shown in Figure 2. According to Lieb's theorem, the number of non-bonding states *N*n is given by the difference in number of the starred and unstarred sites: $N\mathrm{n} = |N\mathrm{A} - N\mathrm{B}|$. The electrons occupying these non-bonding states degenerate at the Fermi level obey the Hund's rule with the parallel spin arrangement. Hence, the half-filled nonbonding states that are populated around the peripheral region of the molecules[6, 10, 11] have localized spins, thereby contributing to the occurrence of strong spin magnetism, in spite of the absence of spin magnetism in Kekul´e molecules. Lieb's theorem states that the spin state is given by $S = N\mathrm{n}/2$, that is, $S = 1/2$, 1 and 3/2 in the doublet, triplet and quartet states for phenalenyl, triangulene and 1*H*,4*H*,5*H*-tribenzo[*bc*,*hi*,*no*]coronene-1,4,5-triyl radicals, respectively, as exhibited in Figure 2b, c and d.[6] An interesting factor emerges from the comparison between anthracene and phenalenyl radical, both of which consist of three fused benzene rings. The former is diamagnetic, whereas the latter has spin magnetism. This demonstrates that the presence or absence of spin magnetism is crucially dependent on the association of benzene rings, which are the building blocks.

A similar situation occurs in nanographene, as can be deduced by extrapolating the size of molecule to nano-dimensions. As mentioned in introduction, non-bonding

edge states appear only in the zigzag edge region of nanographene sheet, but not in the armchair edge region.[2, 3, 12] Figure 3 shows a typical example of a nanographene sheet comprising zigzag or armchair edges. The spatial distribution of populations of the HOMO level for nanographene sheets with their edges having (a) armchair and (b) zigzag edges. We can clearly observe the essential difference in electron populations of the HOMO levels between the zigzag edged nanographene sheet and the armchair-edged

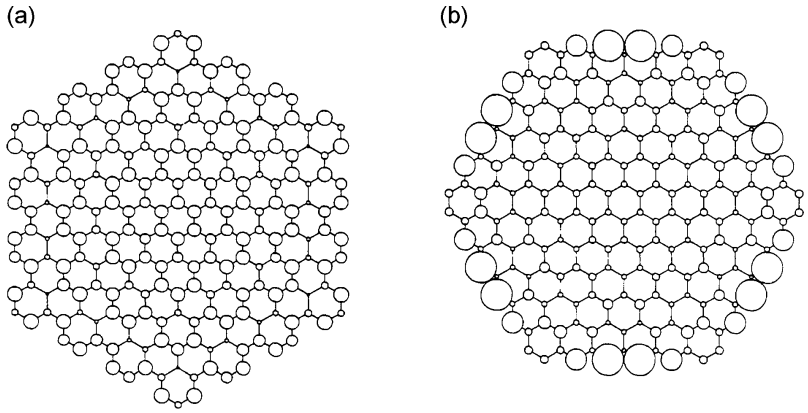

Figure 3. The spatial distribution of the populations of the HOMO level for nanographene sheets with their edges having (a) armchair and (b) zigzag structures. (From ref. [2]).

nanographene sheet. Indeed, the populations are homogeneously distributed in entire region for the armchair-edged nanographene, whereas the HOMO level, which is assigned to non-bonding edge state that is singly occupied, has the largest populations in the edge region of zigzag-edged nanographene sheet. This proves that zigzag edges have edge states that are well localized around the edge region. The presence of an edge state around zigzag edges is experimentally evidenced by ultra-high vacuum (UHV) scanning tunnelling microscopy/spectroscopy (STM/STS) observations of graphene edges whose carbon atoms are hydrogen terminated as shown in Figure 4.[13]

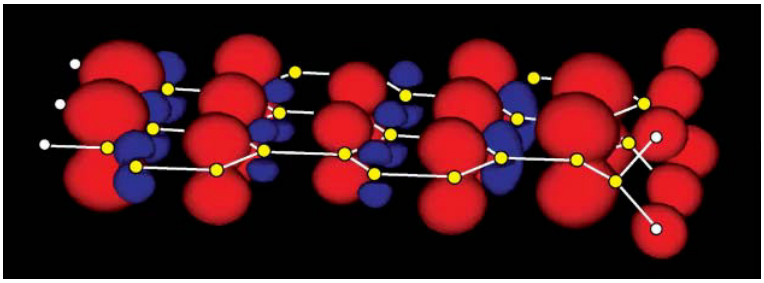

Figure 4: Spin polarizations of a zigzag-edged nanographene ribbon where all the edge carbon atoms on one edge side (right side) are di-hydrogenated and those on the opposite edge side (left side) are mono-hydrogenated. The large red circles represent the densities of up-spins, while the small blue circles denote those of down-spins. (From ref. [13]).

The first experimental work showing high-temperature ferromagnetism in a graphitelike material was reported by Kopelevich, Esquinazi and co-workers.[14] They discovered highly anisotropic behaviour in highly oriented pyrolytic graphite: ferromagnetic-like hysteresis loops for a magnetic field applied parallel to the graphite sheets, which has a large diamagnetic response superposed for fields applied normal to the sheets. The signal was enhanced by heating up to 800 K in a He atmosphere. Absence of correlation with impurity content implied that this was an intrinsic property of the pure carbon.[15] Further experimental evidence that pure carbon can form a structure with long-range magnetic order was reported by Tatiana Makarova and co-workers.[16, 17] They prepared a number of samples of pressure-polymerised rhombohedral fullerenes (poly-C_{60}) at a pressure of 60 GPa in a narrow temperature range (1020 K – 1075 K) and measured positive susceptibility, nonzero static magnetic moment and a hysteresis loop with remnant magnetisation of Mr = 0.015 emu/g and coercive field Hc = 300 Oe although not all the samples showed ferromagnetic behaviour.[18]

Causes of Para- and Ferromagnetism in Pure Carbon

Comparison of the local structure and bonding in polymerised fullerenes and nanofoams was leads to suggest specific structure types for carbon in which unpaired spins can be generated and preserved.[19] In both nanofoams and polymerised fullerenes, the carbon atoms are arranged in a sheet which has graphite-like regions but is distorted so as to show non-zero Gaussian curvature. In the polymerised form, some of the links within the cage are undone, to produce rings that are larger than hexagons. It is therefore possible to find regions of carbon sheet with saddle-like negative curvature in this structure. The nanofoam is also constituted of hyperbolic sheets. The presence of carbon rings other than 6-rings has a disruptive effect on the regular alternation of double and single C-C bonds, characteristic of ideal graphite. The delocalisation of π -electron clouds of graphite may be partially suppressed or very markedly suppressed as in C60. The topology and energetics may be such that satisfaction of all four bonds per atom is frustrated, and the electronic ground state contains unpaired spins. These may be delocalised over finite areas of carbon sheet, but pinned by a barrier of localised bonding electrons at the boundaries of such regions. This is the situation calculated for tetrapod, and such a model accounts well for the spin density observed in the nanofoam. Spectroscopic data for the nanofoam shows clearly that a substantial fraction of carbon atoms are sp^3 rather than sp^2 hybridised. Structural models that are proposed for interconnections between the partially opened cages of poly- C60 also contain some 4-coordinate carbon atoms. In both cases, the implication is that the resulting structures are not just highly convoluted two-dimensional sheets, but contain some cross-links, connecting different “folds” of sheet. In the case of nanofoam, it seems most likely that the sp^3 carbons provide links between spheroidal building units, which contain the hyperbolic schwarzite sheets. There is a third factor shared by polymerised fullerene and

the nanofoam that is important in maintaining long-term magnetization. The unpaired electrons that are responsible for the spin are valence electrons that are not participating in bonding. Therefore, it is possible for the free energy to be lowered if they establish bonds to one another, or to other foreign atoms such as hydrogen or oxygen derived from the air or from moisture. For magnetism to be retained permanently, it is essential to prevent this possibility. Therefore, the carbon structure should be locally rigid, to prevent close juxtaposition of spins occurring by deformation. Chemical attack by foreign species is best prevented by locating the spins inside densely space-filling parts of the structure, so that reactive atoms are unable to get close to the spins by diffusion. The structure thus protects the spins by steric hindrance, a stablisation mechanism that has been known for molecular carbon radicals such as for over a century.[19] The convoluted sheets of nanofoam, with an interlayer spacing of 5.6Å, and the dense packing of cross-linked cages in poly-C60, are both good examples of matrices that are likely to be quite impenetrable to diffusive species. There remains the question of whether paramagnetic spins, which may be separated by distances of several Å, are able to couple so as to produce ferromagnetic ordering. Modelling studies on poly-C60 have shown that both ferro and antiferro coupling pathways can exist between such spins, and that competing pathways can occur in the same structure.[20] Therefore, the overall resultant magnetic behaviour will vary from one material to another material.

Adsorption of different guest molecules on graphene gives rise to a reversible low-spin/high-spin magnetic switching phenomenon which depends on the nature of the guest species. Adsorption of H_2O,[21] interaction with acids[22] and intercalation with potassium clusters reduce the magnetization of nanographite.[23] The reduction in magnetization has been interpreted as due to the interaction with lone pair orbitals as well as charge-transfer with graphene sheets. The edge sites participating in host–guest

interactions can give rise to a variety of interaction giving to rise to magnetic phenomenon. Guest molecules accommodated through physisorption can mechanically compress the flexible nanographite domains, leading to a significant reduction in the inter-nanographene-sheet distance. Such a reduction in intersheet distance could align the magnetic moments antiparallely and reduce the net magnetic moment.[7] Interaction of non-carbon foreign species on the measured magnetic moment is potentially dramatic, as demonstrated by the experiments of Pablo Esquinazi and co-workers [24]. They irradiated a sample of ultra-pure highly-oriented pyrolytic graphite with a beam of protons (2.25 MeV). The protons distorted the graphite structure and formed carbon-hydrogen bonds. Magnetic force microscope images show a classic ferromagnetic signature in the irradiated spots of graphite, which are hydrogenated and hence cannot be considered pure carbon structures. The specific importance of hydrogenation as a means of inducing ferromagnetism was demonstrated by comparison with experiments using α-particles as the irradiating beam; in this case, the irradiated spots did not show the same magnetic response. The ability of hydrogenation to induce magnetism in a carbon-rich material can be understood in terms of the effect of attached hydrogen on the C-C bonding. For example, bonding of a hydrogen atom to one of the carbons of graphite leaves the carbon at the other end of a C+C double bond with one unsatisfied “dangling bond” (Figure 6). This is an electron with unpaired spin, with its associated paramagnetic contribution to the susceptibility. Furthermore, the carbon that has acquired a hydrogen is now in tetrahedral fourfold coordination by other atoms rather than planar threefold, as it would be in pure graphite. The C-C-C bond angles on the hydrogenated carbon are less than 120º, and the graphite sheet is puckered in its vicinity.

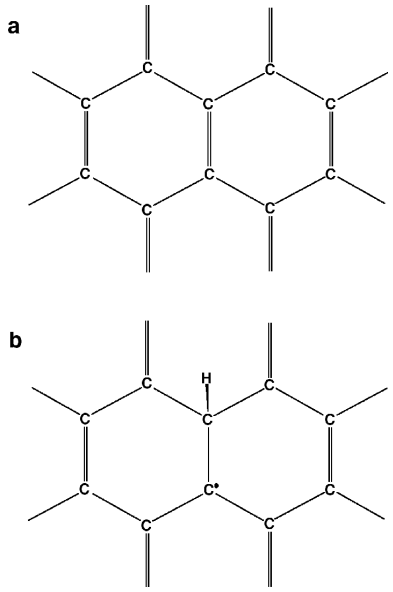

Figure 6. (a) Intact graphite sheet, (b) generation of unpaired spin by hydrogenation.

This deviation away from planarity reduces the efficiency of π-overlap between adjacent atoms, and tends to break up the π-sheet into discrete π-bonds. The reduced connectivity of π -sheet, and the larger π-π* energy gap associated with spatially localised double bonds, conspire to reduce the ring current diamagnetism. The possibility of promoting electrons between these bands also allows a Van Vleck term to contribute to the paramagnetism. Hence, several changes in structure and bonding cooperate, enabling a small degree of hydrogenation to cause a large positive shift in magnetic susceptibility. Theoretical calculations have indicated other pure-carbon structures that may support strong paramagnetism and magnetic ordering.[25] The mechanism is based on a mixture of planar 3-fold coordinated sp^2- and tetrahedral sp^3-hybridized carbon atoms, some of which do not employ all their valence electrons in bonding.

Magnetoresisitance

Hwang and Das Sarma[26] proposed a theory for graphene magnetotransport in the presence of carrier spin polarization and predicted a negative magnetoresistance (MR)

for graphene. Negative tunnel magnetoresistance has been observed in ferromagnetic graphene (FG) and normal graphene (NG) employing FG/NG/FG junctions.[27] The magnetoresistance of Co/ multilayer graphene/ Co spin valve structure has been studied by Nishioka and Goldman[28] who find a positive MR of up to 0.39 % at 2 K. Spin-dependent properties of single-layer graphene have been studied by spin-valve measurements at room temperature and the nonlocal magnetoresistance found to be proportional to conductivity. This study also shows electron-hole symmetry.[29] A study of tunneling spin junction from Co to single-layer graphene has yielded a large value of MR.[30] Suspended bilayers graphene devices are shown to exhibit quantam Hall states that are fully quantized at low magnetic fields and show extremely high magnetoresistance that scales as the magnetic field divided by temperarture.[31] Linear MR is found in multi-layer epitaxial graphene grown on SiC exhibits [32] with MR varies between 80-250 % at 12 T. In dilute fluorinated graphene large MR has been observed.[33] Tunable magnetometers have been deviced by combing Hall effect and MR of graphene.[34]

Graphene quantum sheets with zigzag edge states obtained from GNRs by ultra sonication show room temperature ferromagnetism with strong exchange bias field and around 35% of magnetoresistance at moderate fields and at room temperature.[35] These authors proposed these properties can be used for the spintronic devices. Based on first-principle calculations, magnetized zig-zag nanoribbons are shown to thermally induced spin transport and substantial MR.[36] Zigzag GNR bridging two metallic graphene electrodes appear to show spin-polarized electron transport and large magentoresistance.[37] Theoretical studies show GNRs can exhibit large MR. A GNR field-effect transistor has been found to exhibit negative magnetoresistance.[38] The MR could be tuned by source drain bias. The maximum current ratio decreases from more

than 10,000 at 1.6 K (magnetoresistance = −95%) as the conductance suppression due to the conduction bandgap and/or Coulomb blockade effect is weakened with the increase in temperature. The conduction bandgap apparently disappears at room temperature as the device shows the linear transport behavior.[38]

4.2.2 Scope of the present investigations

Occurrence of intrinsic magnetism in carbon-based materials possessing sp^2 networks has been somewhat a controversial subject. Although there has been doubt as to whether the ferromagnetic features of some of the graphitic materials was due to magnetic impurities such as iron, there is also evidence for ferromagnetism in materials related to highly orient pyrolytic graphite (HOPG).[39] For example, proton irradiated HOPG seems to show room temperature magnetism. It was pointed sometime ago that edges in graphene ribbons play a crucial role in determining the electronic structure.[5] There have been a few studies on the properties of nanographite particles and ribbons which demonstrate the importance of the edge states arising from the nonbonding electrons. Nanographite particles are reported to exhibit unusual magnetic properties including spin-glass behavior and magnetic switching phenomena and their properties have been reviewed by Enoki et al.[40, 41] and the main message is that edge states as well as adsorbed or intercalated species affect the magnetic properties. Bi-layer graphene is predicted to be ferromagnetic.[42] Theoretical studies have predicted the existence of a ferromagnetically ordered ground state in graphene, specially at the zig-zag edges[43] longer than 3-4 repeat units are predicted to be magnetic, irrespective of whether the edges are regular or irregular.[44] Theoretical studies also show the importance of crystallographic nature of graphene in determining its electronic properties and the possibility of half-metallicity in graphene ribbons.[45] We have carried out an experimental study of the magnetic properties of graphene samples prepared by different

methods ensuring that they were devoid of transition metal impurities. We have also investigated the effect of electron donor and acceptor molecules on the magnetic properties of graphene. For this purpose, we have measured the effect of interaction of graphene with tetrathiafulvalane (TTF) and tetracyanoethylene (TCNE). These molecules are known to significantly affect the electronic properties and Raman spectra of graphene because of charge-transfer. Significantly, we find that all the graphene samples show evidence for ferromagnetism with well-defined hysteresis, along with antiferromagnetic features. Electron-donating TTF markedly affects the magnetic properties of graphene.

4.2.3 Experimental section

Synthesis of graphenes

Graphene samples were prepared by thermal exfoliation of graphitic oxide (EG), conversion of nanodiamond (DG),[46] arc evaporation of graphite in hydrogen (HG) and reduction of single-layer graphene oxide (RGO).[47] EG was obtained by thermal exfoliation of graphite oxide and DG was prepared by annealing the nanodiamond powder at 1650 and 2050 ºC for 1hr and at 2200 ºC for 40 min. To prepare RGO, at first single-layer graphene oxide (SGO) was prepared by ultra-sonication of graphite oxide (GO). The so obtained SGO was reduced employing hydrazine hydrate /ethylene glycol as a reducing agent at refluxing conditions and through hydrothermal routes. These samples are designated as RGO and RGO (HT) respectively. In order to ensure that there were no magnetic transition metal impurities, we washed the GO solution with 8-hydroxy-quinoline-5-sulfonic acid prior to the reduction. In this process, 8-hydroxy-quinoline-5-sulfonic acid was added to GO solution in ethanol and the mixture was subjected to sonication followed by stirring for 12 hr. The product obtained by filtration and through washing was employed for reduction. The reduced graphene so obtained by this process is designated as RGO (W). The samples were characterized using

transmission electron microscopy (TEM), atomic force microscopy (AFM), Raman spectroscopy and Brunauer-Emmett-Teller (BET) surface areas.

Preparation of TTF(TCNE) adsorbed HG

For the synthesis of TTF(TCNE) adsorbed HG sample, we have dispersed 7 mg of HG sample in each 10 ml of benzene solutions of having 0.120(0.065)g and 0.024 (0.013)g of TTF(TCNE)(0.05 M and 0.01 M) and sonicated for 30 min. The TTF(TCNE) adsorbed HG sample was filtered using anodic filter paper and then dried at room temperature for 6 hrs.

Magnetic measurements were performed with a vibrating sample magnetometer (VSM) in physical property measuring system (Quantum Design, USA). Electron paramagnetic resonance (EPR) spectra were recorded using a Bruker EMX X-band continuous wave (CW) EPR spectrometer.

4.2.4 Results and discussion

Magnetization data of graphenes

In Figure 7, we show the temperature-dependence of magnetization of graphene samples EG, DG-1650 °C and HG measured at 500 Oe. Inset shows temperature-

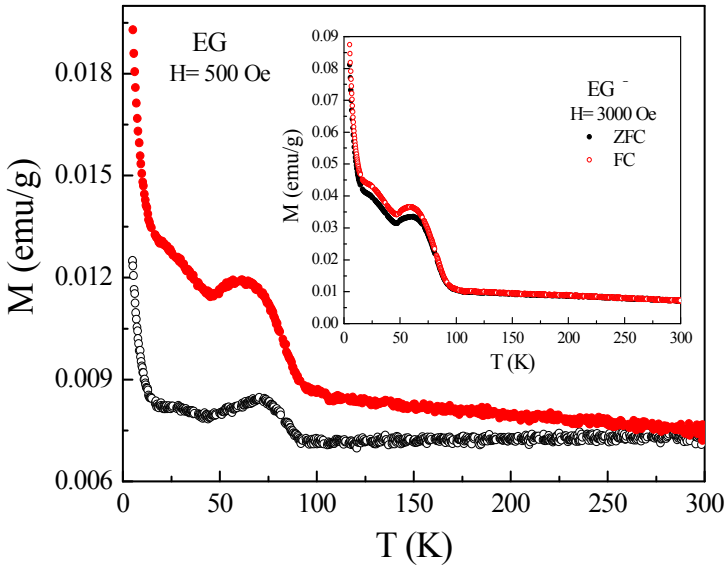

Figure 7a. Temperature variation of magnetization of EG at 500 Oe showing the ZFC and FC data. The inset shows the magnetization data at 3000 Oe.

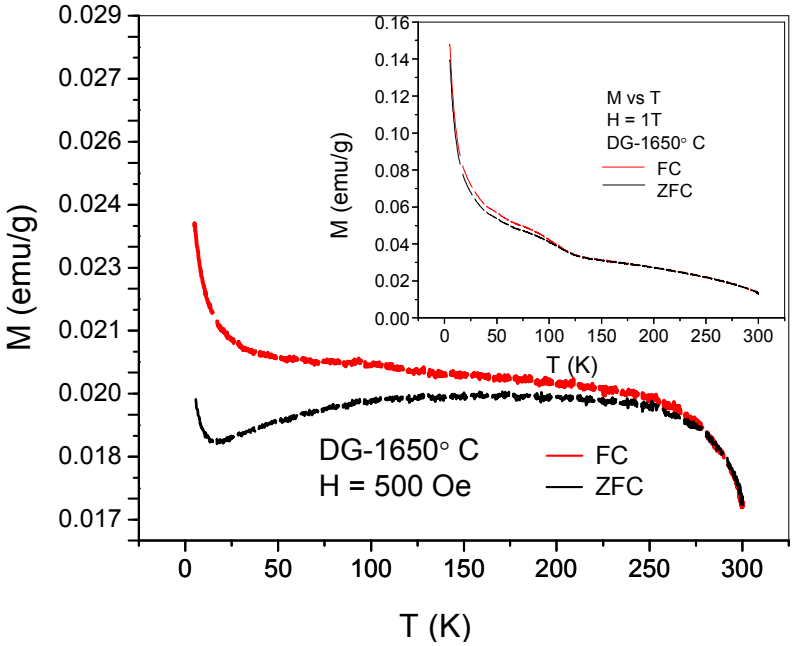

Figure 7b. Temperature variation of magnetization of DG-1650 °C at 500 Oe showing the ZFC and FC data. The inset shows the magnetization data at 1 T.

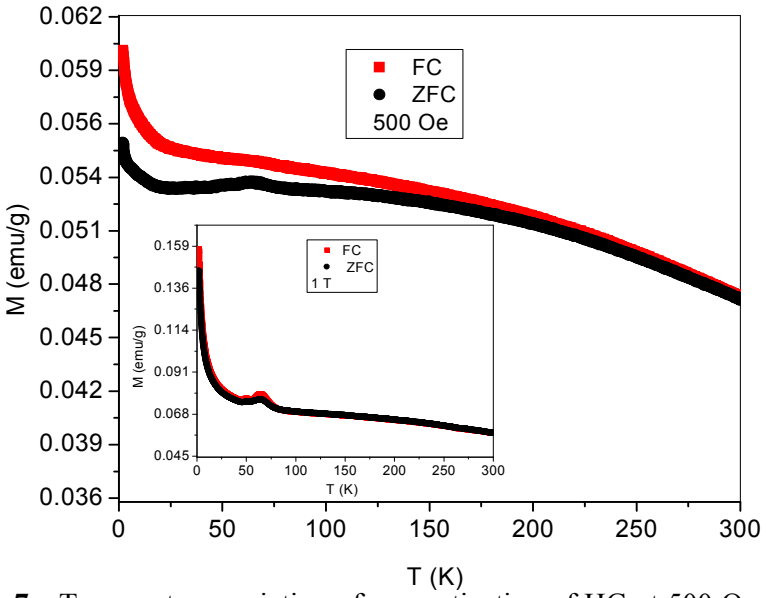

Figure 7c. Temperature variation of magnetization of HG at 500 Oe showing the ZFC and FC data. The inset shows the magnetization data at 1 T.

dependence of magnetization measured at higher field. All the samples show divergence between the field-cooled (FC) and zero-field-cooled (ZFC) data, starting around 300 K. The divergence nearly disappears with the increase in the field as can be seen from the insets in Figure 7. Divergence between the FC and ZFC data in these graphene samples is comparable to that in magnetically frustrated systems such as spin-glasses and superparamagnetic materials. In Figure 8 we show temperature-dependence of

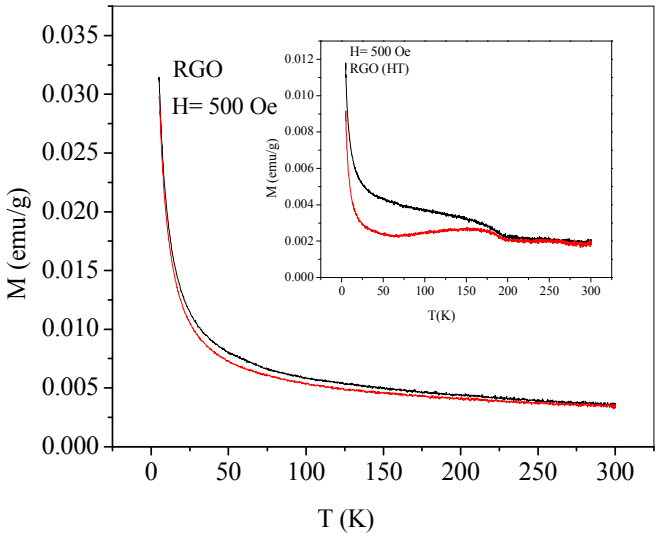

Figure 8. Temperature variation of magnetization of RGO at 500 Oe showing the ZFC and FC data. The inset shows the magnetization data of RGO (HT).

magnetization of RGO and RGO (HT). Even though enough care was taken during the preparation of the various graphene samples, in order to ensure that there were no magnetic transition metal impurities, we washed some of the graphene samples with complexing agents. Thus, in the case of RGO, we washed the GO solution with 8-hydroxy-quinoline -5-sulfonic acid prior to the reduction. The graphene so obtained is designated as RGO (W). In Figure 9, we show the temperature-dependence of

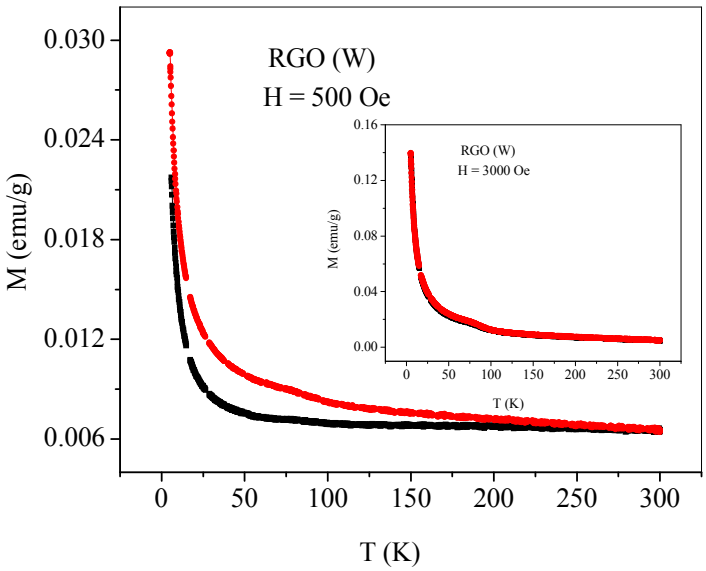

Figure 9. Temperature variation of magnetization of RGO (W) at 500 Oe showing the ZFC and FC data. The inset shows the magnetization data at 3000 Oe.

magnetization of RGO (W) measured at 500 Oe. Inset in the figure shows temperature-dependence of magnetization measured at 3000 Oe. Clearly the basic features of the graphene samples described earlier are preserved.

The Curie-Weiss temperatures obtained from the high-temperature inverse susceptibility data were negative in all these samples, indicating the presence of antiferromagnetic interactions. Interestingly, we observe well-defined maxima in the magnetization at low temperatures, the maxima becoming prominent with the increase in the field. Such magnetic anomalies are found when antiferromagnetic correlations

compete with ferromagnetic (FM) order. Application of high fields aligns the FM clusters and decreases the divergence between FC and ZFC data as indeed observed. It is possible that the data corresponds to percolation type of situation, where in different types of magnetic states coexist. The FM clusters in such a case would not be associated with a well-defined global ferromagnetic transition temperature. This behavior is similar to that of microporus carbon and some members of the rare earth manganite family, $Ln_{1-x}A_xMnO_3$ (Ln=rare-earth, A=alkaline earth).[48-51] Recent theoretical calculations do indeed predict the presence of antiferromagnetic states in the sheets and ferromagnetic states at the edges of graphene.[52]

All the graphene samples EG, DG, HG, RGO, RGO (HT) and RGO (W) show magnetic hysteresis at room temperature (Figure 10). In the case of DG, we see a

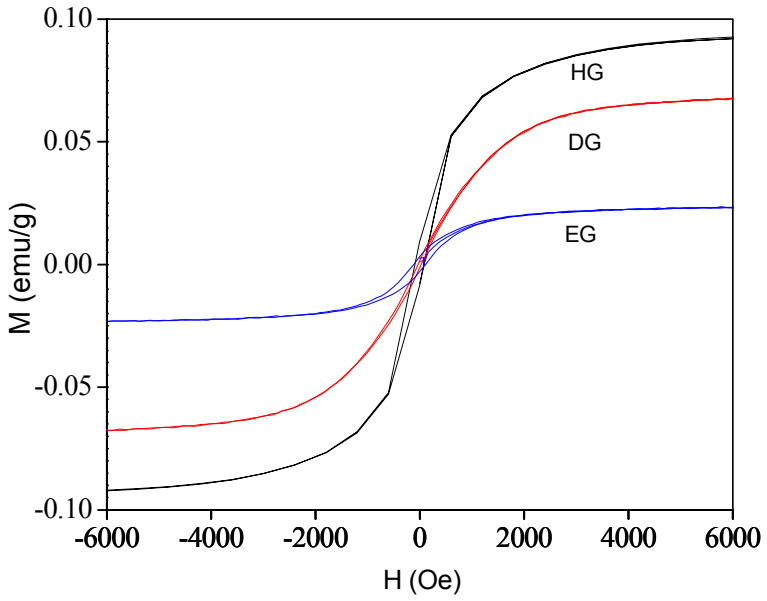

Figure 10a: Magnetic hysteresis in EG, DG-1650 °C and HG at 300 K.

systematic decrease in magnetization with increase in temperature of preparation. Thus in DG-1650 saturation magnetization (M_s), remnant magnetization (M_r) and coercive field (H_c), are 0.05 emu/g, 0.0015 emu/g and 41 Oe respectively whereas in DG-2200 they are

0.02 emu/g, 0.001 emu/g and 213 Oe respectively. Table 1 shows the values of M_s, H_c and M_r at room temperature of all the measured samples. The values shown in parenthesis in table correspond to values obtained at 5 K. It is likely that edge effects would be

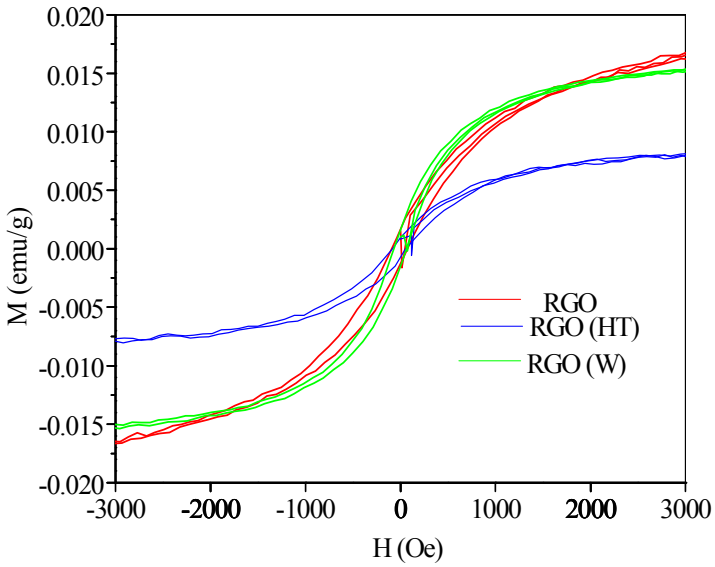

Figure 10b: Magnetic hysteresis in RGO, RGO (HT) and RGO (W) at 300 K.

Table 1. The values of M_s, H_c and M_r at room temperature of all the measured samples. The values shown in parenthesis in table correspond to values obtained at 5 K.

Sample	H_c (Oe)	M_r (emu/g)	M_s (emu/g)
EG	139 (213)	0.003 (0.0055)	0.01 (0.07)
RGO	185 (78)	0.001 (0.0031)	0.003 (0.71)
RGO (E)	145 (214)	0.001 (0.004)	0.002 (0.25)
RGO (W)	80 (96)	0.002 (0.006)	0.009 (1.35)
DG-1650 ºC	41 (136)	0.002 (0.007)	0.05 (0.13)
DG-1850 ºC	-(154)	0.0013 (0.002)	0.0016(0.16)
DG-2200 ºC	200 (213)	0.001 (0.003)	0.002 (0.05)
HG	100 (150)	0.01 (0.018)	0.08 (0.14)

greater in samples with smaller number of layers as well as small areas. In the case of HG, hydrogenation could have occurred to some extent, thereby favouring ferromagnetism. As mentioned earlier, the graphene samples studied by us did not contain detectable levels of transition metal impurities. The unusual magnetic properties reported here are, therefore, considered to be intrinsic to the graphene samples.

EPR mesurements and ac susceptibility measurements

Occurrence of intrinsic magnetism in carbon-based materials comprising sp^2 networks has been somewhat a controversial due to doubts raised, whether the ferromagnetic features are due to magnetic impurities such as iron, cobalt and nickel etc. Albeit, special care has been taken during the synthesis of graphene samples, still to confirm further whether there are any detectable impurities are present in the sample, we have investigated the electron paramagnetic resonance measurements of all the samples from the temperature ranging from 2.5 K to 300 K. In figure 11 we show EPR plots of EG sample. We observe a signal with a line-width of $\Delta H \approx 0.7\text{-}2.9$ mT with a g- value is in the 2.006-2.013 range. The small value of the line-width and the small deviation in the g value from the free-electron value suggest that the spins do not originate from transition-metal impurities but from only carbon-inherited spin species in the graphene sheets. We have measured the temperature dependence of ac susceptibility at different frequencies. We have carried out this experiment since we find the presence of AFM interactions as well as magnetic hysteresis in our graphene samples, a behaviour somewhat like that of frustrated magnetic systems. The measurements on DG and HG samples in the frequency range from 97 to 9997 Hz did not showed any frequency-dependent features in the temperature range of 3-300 K range, ruling out the observed ferromagnetism is not due to spin-glass behavior.

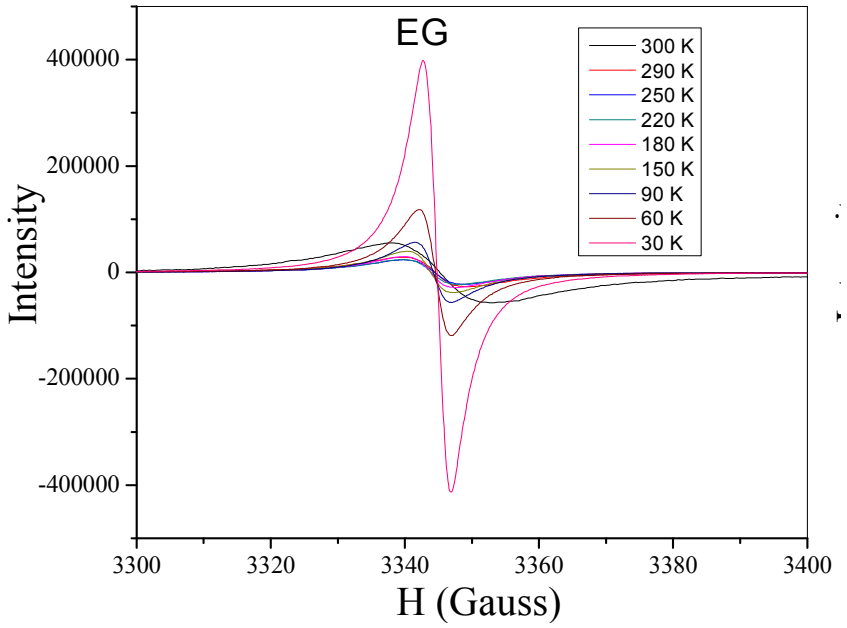

Figure 11. EPR plots of EG sample.

Adsorption of electron-donor and electron acceptors

In order to design more subtle magnetic carbon devices, proper control on the magnetization of these materials essential. For this purpose, we have developed a method for fine-tuning of the magnetization in graphene samples through adsorption of TTF, TCNE and hydrogen. Adsorption of benzene solutions of TTF and TCNE has a profound effect on the magnetic properties of graphene (Figure 12). This method is easy to synthesis, reliable and highly reproducible. The large reversible concentration-dependent effects of adsorbing TTF and TCNE on the magnetic properties of graphene lend evidence to the fact that the magnetic properties of the graphene samples observed by us are intrinsic to them. In Figure 12, we show typical results on the effect of 0.05 M solutions of TTF. On increasing the concentration of TTF or TCNE, the magnetization value decreases progressively. Interestingly, TTF has a greater effect than TCNE, even though the magnitude of adsorption of TCNE on HG is greater. Magnetic hysteresis

of HG persists even after adsorption of TTF and TCNE. On adsorption of TTF and TCNE on graphene, Ms, Mr, and Hc decrease with the concentration of TTF and TCNE. In case

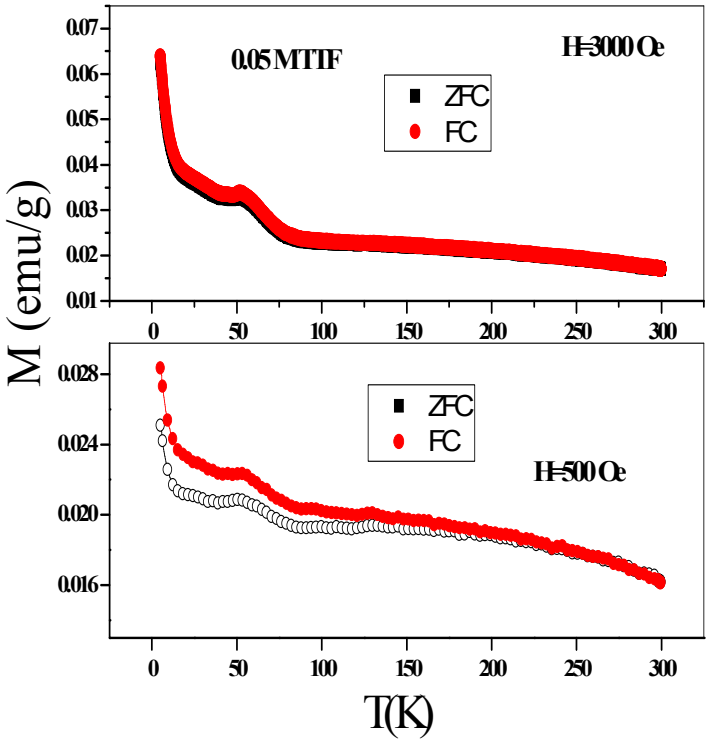

Figure 12. Temperature-variation of the magnetization of HG samples (at 3000 Oe and 500 Oe) after adsorption of 0.05 M TTF solutions. The magnetization data given in the figure are corrected for the weight of adsorbed TTF. Magnetization data of HG with adsorbed TCNE are similar to those with TTF, except that the decrease in magnetization relative to pure HG is smaller.

of TCNE, the Curie-Weiss temperature, θ_p, also decreases markedly on adsorption of these molecules. Clearly, charge-transfer interaction between graphene and TTF (TCNE)[53] is responsible for affecting the magnetic properties. In the literature, there is some evidence to show that adsorption of H_2O[21] and interactions of acids[54] reduce the magnetization of nanographite. Potassium clusters also reduce the magnetization of nanographite.[23] In these cases, the reduction in magnetization has been interpreted as due to the interaction with lonepair orbitals as well as charge-transfer with graphene sheets.

The large reversible concentration-dependent effects of adsorbing TTF, TCNE and hydrogen on the magnetic properties of graphene lend additional evidence to the fact that the magnetic properties of the graphene samples observed by us are intrinsic to them.

4.2.5 Conclusions

In conclusion, graphene samples prepared by different methods, show prominent ferromagnetic features along with the antiferromagnetic characteristics. The value of magnetization as well as the other magnetic properties varies from sample to sample. All the graphene samples exhibit room-temperature magnetic hysteresis. Magnetization of graphene could be tuned by the adsorption of molecules. The value of the magnetization drastically decreases on adsorption of TTF and TCNE having greater effect in case of TTF.

4.2.6 References

[1] R. Saito, G. Dresselhaus, M. S. Dresselhaus, in *Physical Properties of Carbon Nanotubes*, Imperial College Press, London, **1998**.

[2] S. E. Stein, R. L. Brown, *J. Am. Chem. Soc.* **1987**, *109*, 3721.

[3] K. Yoshizawa, K. Okahara, T. Sato, K. Tanaka, T. Yamabe, *Carbon* **1994**, *32*, 1517.

[4] K. W. Mitsutaka Fujita, Kyoko Nakada and Koichi Kusakabe, *J. Phys. Soc. Jpn.* **1996**, *65* 1920.

[5] K. Nakada, M. Fujita, G. Dresselhaus, M. S. Dresselhaus, *Phys. Rev. B* **1996**, *54*, 17954.

[6] E. H. Lieb, *Phys. Rev. Lett.* **1989**, *62*, 1201.

[7] T. Enoki, K. Takai, *Dalton Trans.* **2008**, 3773.

[8] B. T. Kelly, *Physics of Graphite, Applied Science*, London, **1981**.

[9] K. Kusakabe, M. Maruyama, *Phys. Rev. B* **2003**, *67*, 092406.

[10] K. Goto, T. Kubo, K. Yamamoto, K. Nakasuji, K. Sato, D. Shiomi, T. Takui, M. Kubota, T. Kobayashi, K. Yakusi, J. Ouyang, *J. Am. Chem. Soc.* **1999**, *121*, 1619.

[11] J. Inoue, K. Fukui, T. Kubo, S. Nakazawa, K. Sato, D. Shiomi, Y. Morita, K. Yamamoto, T. Takui, K. Nakasuji, *J. Am. Chem. Soc.* **2001**, *123*, 12702.

[12] K. Nakada, M. Fujita, G. Dresselhaus, M. S. Dresselhaus, *Phys. Rev. B* **1996**, *54*, 17954.

[13] Y. Kobayashi, K.-i. Fukui, T. Enoki, K. Kusakabe, Y. Kaburagi, *Phys. Rev. B* **2005**, *71*, 193406.

[14] Y. Kopelevich, P. Esquinazi, J. H. S. Torres, S. Moehlecke, *Journ. Low Temp.Phys.* **2000**, *119*, 691.

[15] P. Esquinazi, A. Setzer, R. Hoene, C. Semmelhack, Y. Kopelevich, D. Spemann, T. Butz, B. Kohlstrunk, M. Loesche, *Phys. Rev. B* **2002**, *66*, 024429.

[16] T. L. Makarova, B. Sundqvist, R. Hohne, P. Esquinazi, Y. Kopelevich, P. Scharff, V. A. Davydov, L. S. Kashevarova, A. V. Rakhmanina, *Nature* **2001**, *413*, 716.

[17] T. L. Makarova, K. H. Han, P. Esquinazi, R. R. d. Silva, Y. Kopelevich, I. B. Zakharova, *Carbon* **2003**, *41*, 1575.

[18] T. L. Makarova, *Journ. of Magn. & Magn. Mater* **2004**, *E1263* 272.

[19] (a) Rode, A, Christy, A, Gamaly, E *et al* 2006, 'Magnetic Properties of Novel Carbon Allotropes', in TL Makarova and F Palacio (ed.), Carbon Based Magnetism: An Overview of the Magnetism of Metal Free Carbon-based Compounds and Materials, Elsevier, Netherlands, pp. 463-482. (b) M. Gomberg, *J. Am. Chem. Soc.* **1900**, *22*, 757.

[20] J. A. Chan, B. Montanari, J. D. Gale, S. M. Bennington, J. W. Taylor, N. M. Harrison, *Phys. Rev. B* **2004**, *70*, 041403.

[21] H. Sata, N. Kawatsu, T. Enoki, M. Endo, R. Kobori, S. Maruyama, K. Kaneko, *Solid State Commun.* **2003**, *125*, 641.

[22] S. Hao, K. Takai, K. Feiyu, T. Enoki, *Carbon* **2008**, *46*, 110.

[23] K. Takai, S. Eto, M. Inaguma, T. Enoki, H. Ogata, M. Tokita, J. Watanabe, *Phys. Rev. Lett.* **2007**, *98*, 017203.

[24] P. Esquinazi, D. Spemann, R. Hoehne, A. Setzer, K. H. Han, T. Butz, *Phys. Rev. Lett.* **2003**, *91*, 227201.

[25] A. A. Ovchinnikov, L. I. Shamovsky, *J. Mol. Struct.: Theochem* **1991**, *251*, 133.

[26] E. H. Hwang, S. Das Sarma, *Phys. Rev. B* **2009**, *80*, 5.

[27] J. F. Zou, G. J. Jin, Y. Q. Ma, *J. Phys.-Condes. Matter* **2009**, *21*, 6.

[28] M. Nishioka, A. M. Goldman, *Appl. Phys. Lett.* **2007**, *90*, 252505.

[29] W. Han, W. H. Wang, K. Pi, K. M. McCreary, W. Bao, Y. Li, F. Miao, C. N. Lau, R. K. Kawakami, *Phys. Rev. Lett.* **2009**, *102*, 4.

[30] W. Han, K. Pi, K. M. McCreary, Y. Li, J. J. I. Wong, A. G. Swartz, R. K. Kawakami, *Phys. Rev. Lett.* **2010**, *105*, 4.

[31] B. E. Feldman, J. Martin, A. Yacoby, *Nat. Phys.* **2009**, *5*, 889.

[32] A. L. Friedman, J. L. Tedesco, P. M. Campbell, J. C. Culbertson, E. Aifer, F. K. Perkins, R. L. Myers-Ward, J. K. Hite, C. R. Eddy, G. G. Jernigan, D. K. Gaskill, *Nano Lett.* **2010**, *10*, 3962.

[33] X. Hong, S. H. Cheng, C. Herding, J. Zhu, *Phys. Rev. B* **2011**, *83*, 5.

[34] S. Pisana, P. M. Braganca, E. E. Marinero, B. A. Gurney, *Nano Lett.* **2009**, *10*, 341.

[35] S. K. Saha, M. Baskey, D. Majumdar, *Adv. Mater.* **2010**, *22*, 5531.

[36] M. G. Zeng, Y. P. Feng, G. C. Liang, *Nano Lett.* **2011**, *11*, 1369.

[37] F. Munoz-Rojas, J. Fernandez-Rossier, J. J. Palacios, *Phys. Rev. Lett.* **2009**, *102*, 4.

[38] J. W. Bai, R. Cheng, F. X. Xiu, L. Liao, M. S. Wang, A. Shailos, K. L. Wang, Y. Huang, X. F. Duan, *Nat. Nanotechnol.* **2010**, *5*, 655.

[39] K. H. Hans, D. Spemann, P. Esquinazi, R. Holine, V. Reide, T. Butz, *Adv. Mater.* **2003**, *15*, 1719.

[40] T. Enoki, K. Takai, *Dalton Trans.* **2008**, 3773.

[41] T. Enoki, Y. Kobayashi, *J. Mater. Chem.* **2005**, *15*, 3999.

[42] E. V. Castro, N. M. R. Peres, T. Stauber, N. A. P. Silva, *Phys. Rev. Lett.* **2008**, *100*, 186803.

[43] H. Lee, Y. W. Son, N. Park, S. W. Han, J. J. Yu, *Phys. Rev. B* **2005**, *72*, 1745431.

[44] S. Bhowmick, V. B. Shenoy, *J. Chem. Phys.* **2008**, *128*, 244717.

[45] V. Barone, O. Hod, G. E. Scuseria, *Nano Lett.* **2006**, *6*, 2748.

[46] O. E. Andersson, B. L. V. Prasad, H. Sato, T. Enoki, Y. Hishiyama, Y. Kaburagi, M. Yoshikawa, S. Bandow, *Phys. Rev. B* **1998**, *58*, 16387.

[47] S. Stankovich, D. A. Dikin, R. D. Piner, K. A. Kohlhaas, A. Kleinhammes, Y. Jia, Y. Wu, S. T. Nguyen, R. S. Ruoff, *Carbon* **2007**, *45*, 1558.

[48] Y. Kopelvich, R. R. Dasilva, J. H. S. Torres, A. Penicaud, *Phys. Rev. B* **2003**, *68*, 092408.

[49] K. W. S. Dho J, N. H. Hur, *Phys. Rev. Lett.* **2002**, *89*, 027202.

[50] V. B. Shenoy, C. N. R. Rao, *Phil. Trans. R. Soc. A* **2008**, *366*, 63.

[51] M. Ghosh, K. Biswas, A. Sundaresan, C. N. R. Rao, *J. Mater. Chem.* **2006**, *16*, 106.

[52] S. Dutta, S. Lakshmi, S. K. Pati, *Phys. Rev. B* **2008**, *77*, 073412.

[53] R. Voggu, B. Das, C. S. Rout, C. N. R. Rao, *J. Phys.: Condens. Matter* **2008**, *20*, 472204.

[54] S. Hao, K. Takai, F. Kang, T. Enoki, *Carbon* **2008**, *46*, 110.

4.3 Graphene as a supercapacitor material

4.3.1 Introduction

In recent years, ultracapacitors have drawn significant attention, owing to their high power density, long lifecycle, and bridging function for the power/energy gap between traditional dielectric capacitors and batteries/fuel cells.[1, 2] The main function of an electrochemical supercapacitors (ES) could be to boost the battery or fuel cell in a hybrid electric vehicle to provide the necessary power for acceleration.[3] The major drawback of ES is its low energy density and high production cost. To overcome this problem, development of new materials would be one of the most intensive approaches. Most popular today are carbon materials, which have high surface areas for charge storage. An ES is a charge-storage device similar to batteries in design and manufacturing. As shown in Figure 1, it consists of two electrodes, an electrolyte, and a separator that electrically isolates the two electrodes. The most important component in an ES is the electrode material. Generally nanomaterials which have high surface area and high porosity considered as electrode materials. It can be seen fr-om Figure 1 that charges can be stored and separated at the interface between the conductive solid particles (such as carbon particles or metal oxide particles) and the electrolyte.[4] This interface can be treated as a capacitor with an electrical double-layer capacitance, which can be expressed as equation (1)

$$C = A\varepsilon/4\pi d \quad \text{..... (1)}$$

Where A is the area of the electrode surface, which for a supercapacitor should be the active surface of the electrode porous layer; e is the medium (electrolyte) dielectric constant, which will be equal to 1 for a vacuum and larger than 1 for all other materials, including gases; and d is the effective thickness of the electrical double layer.

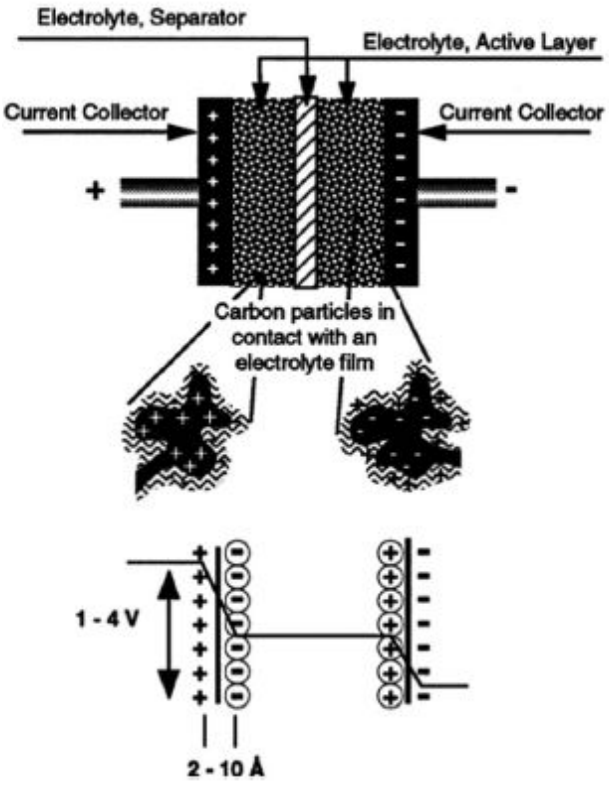

Figure 1. Principles of a single-cell double-layer capacitor and illustration of the potential drop at the electrode/electrolyte interface. (From ref. [4]).

Electrostatic supercapacitors (EDLS): The capacitance of the electrode/interface in an electrostatic or EDLS is associated with an electrode-potential-dependent accumulation of electrostatic charge at the interface. The mechanism of surface electrode charge generation includes surface dissociation as well as ion adsorption from both the electrolyte and crystal lattice defects.[5] These processes operate solely on the electrostatic accumulation of surface charge. As shown in Figure 1, this electrical double-layer capacitance comes from electrode material particles, such as at the interface between the carbon particles and electrolyte, where an excess or a deficit of electric charges is accumulated on the electrode surfaces, and electrolyte ions with counterbalancing charge are built up on the electrolyte side in order to meet electroneutrality. During the process of charging, electrons travel from negative

electrode to positive electrode through an external load. Within the electrolyte, cations move towards the negative electrode while anions move towards the positive electrode. During discharge, the reverse processes take place. In this type of ES, no charge transfers across the electrode/ electrolyte interface, and no net ion exchanges occur between the electrode and the electrolyte. This implies that the electrolyte concentration remains constant during the charging and discharging processes. In this way, energy is stored in the double-layer interface. When ES is charged, a voltage (V) will build up across the two electrodes. The theoretical energy (E) and power densities (P) of this ES can be expressed as equations (2) and (3):[6, 7]

$$E = \frac{1}{2} CV^2 = QV/2 \quad .....(2)$$

$$P = V^2/4R_S \quad ..... \quad (3)$$

Where Q is the total charge stored in the ES and R_S is for the equivalent inner resistance of ES. From above equations it is evinced that V, C and R_S are three important variables which controls the ES's performance. In order to increase ES's energy density and power density, one can increase the values of both V and C or reduce the value of R_S. Here the value of the ES voltage (V) is dependent on the materials used for the electrode and electrolyte (e.g. when carbon is used as the electrode material for aqueous electrolytes, the cell voltage or supercapacitor voltage window is about 1 V, while in organic electrolytes the cell voltage is in the range of 3–3.5 V), whereas the operating voltage is determined by the electrolyte's stability window. From both equations (2) and (3), it can be seen that both energy and power densities are proportional to the square of voltage, therefore, increasing the voltage may be more effective than increasing capacitance or reducing inner resistance in terms of raising the ES's energy and power densities. To enhance the ES's cell voltage within the electrolyte's stability window, selecting the type of electrode materials and optimizing electrode structures

can achieve high cell voltages. To increase the power density of ES, reducing cell's internal resistance, should be the major focus. In general, ES's inner resistance is much smaller than that of batteries due to the rapid combination of positive and negative charges (even in a faradaic-type ES, the redox processes involving electron and ion transfers are also very fast), the power density of an ES is normally much higher than in batteries. Even so, reducing inner resistance can always benefit the ES's performance in terms of power density improvement. From equation (2) it is clear that increasing the capacitance is an effective way to improve energy density. In order to increase overall cell capacitance, both electrode capacitances have to be increased. Therefore, developing electrode materials should be one of the key approaches in ES research and development. In evaluating an electrode material for ES, another generally used definition is the specific capacitance (Cs), with a unit of Faraday per gram (Fg^{-1}), which can be expressed as equation 4: $C_s = Ci/W$ where W is the weight in grams of the electrode material in the electrode layer, and C_i is the electrode capacitance (anode or cathode). A higher specific capacitance does not necessarily mean that this material will be a better ES electrode material, because electrode capacitance is also strongly dependent on the electrode layer structure and the electron and ion transfers within the layer. An electrolyte which resides inside the active material layers is one of the most important ES components. The requirements for an electrolyte are wide voltage window, high electrochemical stability, high ionic concentration and low solvated ionic radius, low resistivity, low viscosity, low volatility, low toxicity, low cost as well as availability at high purity. The electrolyte used in an ES can be classified into three types: (1) aqueous electrolyte, (2) organic electrolyte, and (3) ionic liquids (ILs).

Advantages of ES: Compared to batteries, ES have several advantages: They are: high power density, long life expectancy, long shelf life, high efficiency, wide range of operating

temperatures, environmental friendliness, safety. In normal circumstances, Although ES have many advantages over batteries and fuel cells, they also face some challenges at the current stage of technology. They are Low energy density, High self-discharging rate and industrial standards for commercialization. As capacitance and charge storage of ES intimately depend on the electrode materials used, developing new materials with high capacitance and improved performance relative to existing electrode is indispensable. Apparently, the capacitance of ES heavily depends on specific surface area of the electrode materials. Since not all the specific surface area is electrochemically accessible when the material is in contact with an electrolyte, the measured capacitance of various materials does not linearly increase with increasing specific surface area. Thus, for those electrochemically accessible surface area or useful surface area, a definition called the electrochemical active surface area may be more accurate in describing the electrode capacitance behavior. The pore size of electrode material plays an important role in the electrochemical active surface area. According to Largeot *et al*.[1] the pore size of electrode materials that yielded maximum double-layer capacitance was very close to the ion size of the electrolyte (with respect to an ionic liquid electrolyte), and both larger and smaller pores led to a significant drop in capacitance. Therefore, ES capacitance strongly depends on surface area of the electrode accessible to the electrolyte. In general, the electrode materials of ES can be categorized into three types:[8, 9] (1) carbon materials with high specific surface area,[10, 11] (2) conducting polymers,[12-14] and (3) metal oxides.[15, 16]

4.3.2 Scope of the present investigations

Several workers have focused on understanding the factors that govern electron-transfer kinetics on carbon electrodes. The surface structure of solid carbon electrodes directing electron transfer (ET) reactions in electrochemistry has been well recognized, and it

is found that the creation of specific surface structures, through pretreatments such as plasma activation[17] can drive the ET faster. The surface preparation and hence, the final surface structure is often found to be critical to the performance of the electrodes, its stability and reproducibility of results. The surface modification effects are also sensitive to the reaction that is being conducted at the electrodes.[18] Thus, different reactions should be considered when addressing the role of the electrode surface on the ET mechanism.

The oxidation of potassium ferrocyanide has served as a benchmark in investigating electrochemistry at different carbon electrodes.[19] The electrochemical oxidation generates ferricyanide, and the redox couple $Fe(CN)_6^{4-}$ /$Fe(CN)_6^{3-}$ is close to an ideal system with quasi-reversibility, especially on electrodes (such as carbon) where there is minimum bonding interaction between the electrode material and the cations in solution. The importance of this redox couple in electrochemistry also stems from its role in instrument calibration, determination of diffusion coefficients and the electrochemical area of the electrode. This reaction on most electrodes precludes any effect of surface adsorption (oxide layer formation) on the ET kinetics and hence provides a straightforward correlation of the surface structure and reaction rates.

Here we report on the electrochemical study of graphene electrodes made from three different graphene samples named CG, EG and DG. Cyclic voltammetry was used in 1M KCl containing 100 mM potassium ferrocyanide to obtain information on electron transfer rate from the faradaic reaction of the redox species.

Electrochemical supercapacitors are passive and static electrical energy storage devices for applications requiring high power density such as energy back-up systems, consumer portable devices and electrical/hybrid automobiles.[20, 21] Electrochemical supercapacitors store significantly higher amount of energy than conventional capacitors but less than that of batteries, and are similar in construction to conventional capacitors except

that the metal electrodes are replaced by a highly porous electrode. The dielectric film separating the two electrodes is porous and the cell contains a suitable electrolyte such as aqueous (aq.) H_2SO_4. Energy is stored in supercapacitors due to the formation of a electrical double layer at the interface of electrode (electrical double layer capacitors, EDLCs) or due to electron transfer between the electrolyte and the electrode through fast Faradiac redox reactions (psuedocapacitors). In the latter type of supercapacitors, the amount of charge stored is proportional to the voltage. Porous carbon materials such as activated carbon[22] xerogels,[23] carbon nanotubes,[24] mesoporous carbon,[25] and carbide-derived carbons[26] have been investigated for use as electrodes in EDLCs. In the last few years, there has been great interest in graphene, which constitutes an entirely new class of carbon. Electrical characterization of single-layer graphene has been reported.[27]

We have investigated the use of graphene as electrode material in electrochemical supercapacitors. For this purpose, we have employed graphene prepared by different methods and compared their supercapacitor behaviour with aq. H_2SO_4 as the electrolyte. Furthermore, we have explored the use of ionic liquids as electrolytes. Thus, by employing the ionic liquid, N-butyl-N-methylpyrrolidinium bis(trifluoromethanesulfonyl)imide (PYR14TFSI), we have been able to extend the operating voltage up to 3.5 V compared to 1 V normally obtained with aq. H_2SO_4.

4.3.3 Experimental section

Electrochemical measurements were performed using a PG262A potentiostat/ galvanostat, (Technoscience Ltd, Bangalore, India). Voltammetric properties of graphenes were investigated using a three electrode electrochemical cell containing a graphene paste electrode, platinum foil as the counter electrode and calomel as the reference electrode using 1M KCl solution containing 100 mM potassium ferrocyanide. All graphene paste electrodes were prepared using mineral oil as a binder (25 wt%).[28]

Graphene-based supercapacitor cells were fabricated following Conway.[20] The measurements were carried out with a two-electrode configuration, the mass of each electrode being 5 mg and the ionic liquid, N-butyl-N-methylpyrrolidinium bis(trifluoromethanesulfonyl)imide ($PYR_{14}TFSI$) was dried at 80 °C under vacuum for a day prior to the experiment. The fabrication and characterization of cell was done at 60 °C in a mBraun glove box keeping the oxygen and water levels at less than 0.1 ppm. We have performed cyclic voltammetry to characterize the two-electrode supercapacitor cells with the different graphenes. The specific capacitance is given by the following equation:

$$C_{CV} = 2(i_{+} - i_{-})/(m \times \text{scan rate})$$

Where i_{+} and i_{-} are maximum current in the positive scan and negative scan respectively and m is the mass of electrode. The energy density is given as $E= CV^2$, where C is the capacitance taking into account both the electrode masses and V is the operational voltage.

4.3.4 Results and discussion

We have investigated the electrochemical properties of the CG, EG and DG using the redox reactions with potassium ferrocyanide. The peak to peak separation is known to be significantly depend on the microstructure of the carbon electrode used.[29] A small peak to peak separation (~ 70 mV) is achieved when the edges of graphite are exposed to the electrolyte while it is significantly larger (even close to 1 V) when the basal planes are involved. In Figure 2, we show typical cyclic voltammograms of the redox reaction of 100 mM potassium ferrocyanide (in 1 M KCl) carried out using working electrodes of different

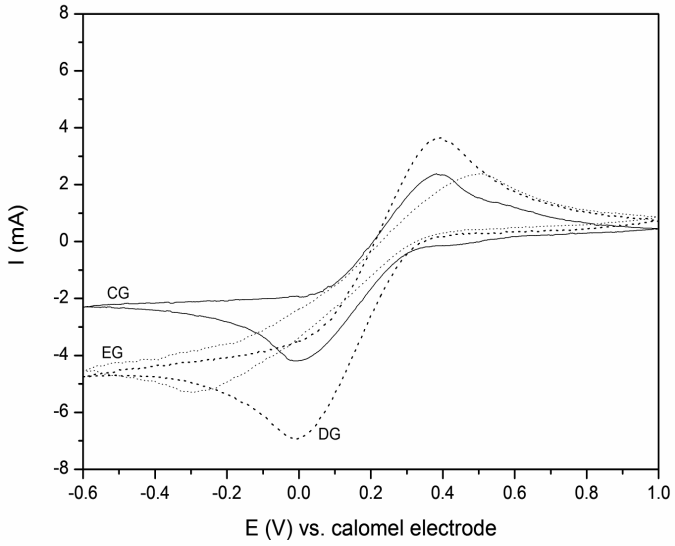

Figure 2. Cyclic voltammograms of the different graphene electrodes (at a scan rate of 20 mV/s) for 100mM $K_4Fe(CN)_6$ in 1M KCl.

graphenes. While the peak to peak separation depends on the scan rate, and it is found to be the largest in the case of EG. DG and CG exhibit similar peak separations. The behavior of EG is similar to that of basal plane in graphite. On the other hand, DG and CG exhibit slightly better kinetics.

We fabricated supercapacitors cells using aq. H_2SO_4 and an ionic liquid, N-butyl-N-methylpyrrolidinium bis(trifluoromethanesulfonyl)imide ($PYR_{14}TFSI$) as the electrolytes. In Figure 3, we show cyclic voltamograms (CVs) at a scan rate of 100 mV/s for capacitors built using graphene as electrodes and 1 M H_2SO_4 as electrolyte. EG and DG exhibit 117 F/g and 35 F/g where as CG exhibits low value of 6 F/g. In PYR14TFSI, specific capacitance values of 75 F/g and 40 F/g were obtained with EG and DG respectively. The maximum values of energy density stored in these capacitors are 31.9 and 17.0 $Whkg^{-1}$ respectively for EG and DG. These are some of the highest values reported to date and are comparable to those of microporous carbons reported by Balducci et al.[30]

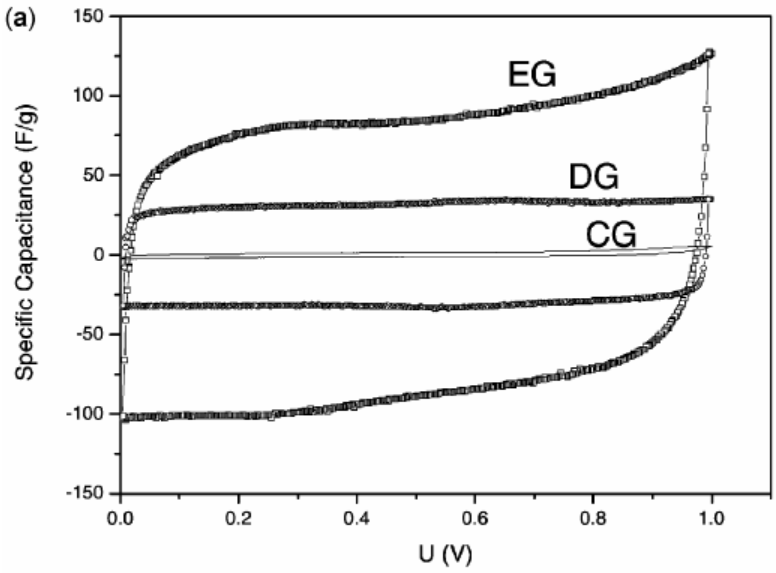

Figure 3. Voltammetry characteristics of a capacitor built from graphene electrodes (5 mg each) at a scan rate of 100 mV/s using aqueous H_2SO_4 (1 M).

4.3.5 Conclusions

The electrochemical properties of different graphenes (CG, EG and DG) have been investigated using the redox reactions with potassium ferrocyanide. The behavior of EG is similar to that of basal plane in graphite. DG and CG exhibit slightly better kinetics. Graphenes acts as a good electrode material for application in supercapacitors. The specific capacitance of the exfoliated graphene in the aqueous electrolyte is comparable to that obtained with activated carbons and superior to that of carbon nanotubes while value of the energy density of the graphene capacitors is one of the highest known to date. The supercapacitor characteristics are directly related to the quality of graphene specifically the number of layers and the associated surface area.

3.6 References

[1] (a) C. Largeot, C. Portet, J. Chmiola, P.-L. Taberna, Y. Gogotsi, P. Simon, *J. Am. Chem. Soc.* **2008**, *130*, 2730, (b) G. Wang, L. Zhang, J. Zhang, Chem. Soc. Rev. 2012, 41, 797.

[2] S. G. Kandalkar, D. S. Dhawale, C.-K. Kim, C. D. Lokhande, *Synth. Met.* **2010**, *160*, 1299. (b) M Jayalakshmi, K. Balasubramanian, Int. J. Electrochem. Sci. 2008, 3, 1196

[3] R. Kötz, S. Müller, M. Bärtschi, B. Schnyder, P. Dietrich, F. N. Büchi, A. Tsukada, G. G. Scherer, P. Rodatz, O. Garcia, P. Barrade, V. Hermann, R. Gallay, *Electrochem. Soc. Proc.* **2001**, *21*, 564.

[4] R.Koetz, M. Carlen, *Electrochim. Acta* **2000**, *45*, 2483.

[5] P. Simon, Y. Gogotsi, *Nat. Mater.* **2008**, *7*, 845.

[6] L. L. Zhang, X. S. Zhao, *Chem. Soc. Rev.* **2009**, *38*, 2520.

[7] H. Pan, J. Li, Y. Feng, *Nanoscale Res. Lett.* **2010**, *5*, 654.

[8] H. Lee, M. S. Cho, I. H. Kim, J. D. Nam, Y. Lee, *Synth. Met.* **2010**, *160*, 1055.

[9] D. Choi, P. N. Kumta, *J. Electrochem. Soc.* **2006**, *153*, A2298.

[10] E. Frackowiak, S. Delpeux, K. Jurewicz, K. Szostak, D. Cazorla-Amoros, F. Béguin, *Chem. Phys. Lett.* **2002**, *361*, 35.

[11] V. Ruiz, C. Blanco, E. Raymundo-Piñero, V. Khomenko, F. Béguin, R. Santamaría, *Electrochim. Acta* **2007**, *52*, 4969.

[12] C. Peng, S. Zhang, D. Jewell, G. Z. Chen, *Prog. Nat. Sci.* **2008**, *18*, 777.

[13] A. Malinauskas, J. Malinauskiene, A. Ramanavičius, *Nanotechnology* **2005**, *16*, R51.

[14] S. I. Cho, S. B. Lee, *Acc. Chem. Res.* **2008**, *41*, 699.

[15] A. Young Rack, Mi Yeon Song, Seong Mu Jo, C. R. Park, D. Y. Kim, *Nanotechnology* **2006**, *17*, 2865.

[16] V. D. Patake, C. D. Lokhande, O. S. Joo, *Appl. Surf. Sci.* **2009**, *255*, 4192.

[17] J. F. Evans, T. Kuwana, *Anal. Chem.* **1977**, *49*, 1632.

[18] P. Chen, R. L. McCreery, *Anal. Chem.* **1996**, *68*, 3958.

[19] R. L. McCreery, in *Electroanalytical Chemistry, Vol. 17* (Ed.: A. J. Bard), Marcel Dekker, New York, **1991**, p. 191.

[20] B. E. Conway, in *Electrochemical supercapacitors*, Kluwer Academic, Plenum New York, **1999**

[21] R. Kötz, M. Carlen, *Electrochim. Acta* **2000**, *45*, 2483.

[22] M. Endo, T. Maeda, T. Takeda, Y. J. Kim, K. Koshiba, H. Hara, M. S. Dresselhaus, *J. Electrochem. Soc.* **2001**, *148*, A910.

[23] S. T. Mayer, R. W. Pekala, J. L. Kaschmitter, *J. Electrochem. Soc.* **1993**, *140*, 446.

[24] C. M. Niu, E. K. Sichel, R. Hoch, D. Moy, H. Tennent, *Appl. Phys. Lett.* **1997**, *70*, 1480.

[25] S. Yoon, J. Lee, T. Hyeon, S. M. Oh, *J. Electrochem. Soc.* **2000**, *147*, 2507.

[26] J. Chmiola, G. Yushin, Y. Gogotsi, C. Portet, P. Simon, P. L. Taberna, *Science* **2006**, *313*, 1760.

[27] K. S. Novoselov, A. K. Geim, S. V. Morozov, D. Jiang, Y. Zhang, S. V. Dubonos, I. V. Grigorieva, A. A. Firsov, *Science* **2004**, *306*, 666.

[28] F. Valentini, A. Amine, S. Orlanducci, M. L. Terranova, G. Palleschi, *Anal. Chem.* **2003**, *75*, 5413.

[29] C. E. Banks, T. J. Davies, G. G. Wildgoose, R. G. Compton, *Chem. Commun.* **2005**, 829.

[30] A. Balducci, R. Dugas, P. L. Taberna, P. Simon, D. Plée, M. Mastragostino, S. Passerini, *J. Power Sources* **2007**, *165*, 922.

4.4 Blue-light emission from graphene-based materials

4.4.1 Introduction

There have been a few reports in the literature stating certain carbon species emit blue light upon excitation.[1-4] Graphitic forms of carbon have rich chemistry with many different chemical functional groups present on the surface, particularly at defect sites such as steps and edges.[5-10] In particular, oxygen containing carboxyl, carbonyl, ether and such functional groups are speculated to be present on graphitic surfaces.[5, 6, 10-14] C-dots are attracting considerable attention as nascent quantum dots, particularly for applications in which the size, cost, and biocompatibility of the label are critical. Advances in this area are appearing frequently, with a number of significant breakthroughs taking place within the last couple of years. C-dots were discovered serendipitously during the purification process of single-walled carbon nanotubes (SWCNTs) prepared by arc-discharge methods.[15] When processing a suspension of these SWCNTs by gel electrophoresis, the suspension separated into three distinct classes of nanomaterials, including a fast-moving band of highly luminescent material. They further found that this carbonaceous material could be fractionated into a number of components with size-dependent fluorescent properties. Nanodiamond is an another important carbon nanomaterial which is similar to the C-dot in size and surface functionality.[16-19] Nanodiamonds are typically made from milling microdiamonds, chemical vapor deposition (CVD), shockwave, or detonation processes. They generally consist of about 98% carbon with residual hydrogen, oxygen, and nitrogen, possesses a sp^3 hybridized core, and have small amounts of graphitic carbon on the surface. Unlike nanodiamonds, C-dots have greater sp^2 character, which is symbolic of nanocrystalline graphite having high oxygen content. Sometimes, because of their high oxygen content, these materials have also been referred to as carbogenic nanodots.[20] While C-dots show spectrally broad

photoluminescence (PL) emission with strong excitation wavelength (λex) dependency. Fluorescent nanodiamonds emit from point defects, particularly the negatively charged nitrogen vacancy site, which absorbs strongly at 569 nm and emits near 700 nm. Although the origin of PL is not yet entirely understood in C-dots, there is mounting evidence that emission arises from the radiative recombination of excitons located at surface energy traps which may or may not require passivation by organic molecules to occur. C-dots have been synthesized through both top-down and bottom-up approaches. Top-down methods consist of arc discharge,[15] laser ablation[21-23] and electrochemical oxidation,[24, 25] where the C-dots are formed or "broken off" from a larger carbon structure. Bottom-up approaches consist, for example, of combustion/thermal,[1, 26, 27] supported synthetic,[26, 28] or microwave methods[29] during which the C-dots are formed from molecular precursors. Typically, their surfaces are oxidized by nitric acid (HNO_3) and further purified by using centrifugation, dialysis, electrophoresis, or another separation technique.

While purifying SWCNTs derived from arc-discharge soot, Xu *et al*. discovered they had also isolated an unknown fluorescent carbon nanomaterial.[15] C-dots have been produced by Sun and co-workers by laser ablation.[21, 22, 30, 31] They prepared a carbon target by hot-pressing a mixture of graphite powder and cement, followed by stepwise baking, curing, and annealing under an argon flow.[3] A Q-switched Nd:YAG laser (1064 nm, 10 Hz) was then used to ablate the carbon target in a flow of argon gas carrying water vapor at 900 ºC and 75 kPa. The sample was then heated at reflux in 2.6 M HNO_3 for up to 12 hr to produce C-dots ranging from 3 to 10 nm in size. At this point, the C-dots were surface passivated by polymeric agents such as diamine-terminated poly(ethylene glycol) (PEG1500N)[3] or poly(propionylethylenimine- co-ethylenimine) (PPEI-EI, with an EI fraction of ca. 20%)[21] and then purified by dialysis against water, followed by a centrifugation step to yield purified C-dots in the supernatant liquid.[30] In a single-step C-dots passivated with diamine hydrate,

diethanolamine, or PEG200N was prepared by Hu *et al*.[4] In this approach, a pulsed Nd:YAG laser was used to irradiate graphite or carbon black dispersed and under ultrasonication to aid in particle dispersal. C-dots were electrochemically prepared from a graphite rod working electrode, a Pt mesh counter electrode, and a Ag/AgCl reference electrode assembly immersed in pH 7.0 phosphate buffer solution (Scheme 1).[32] A variety of carbon-based nanoparticles, including C-dots, were generated by ionic liquid (IL) assisted

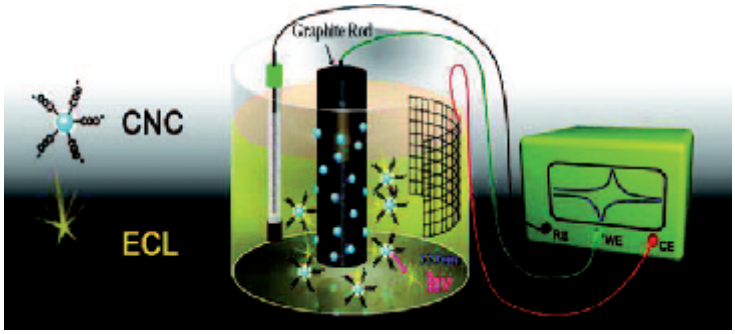

Scheme 1: Electrochemical production of C-dots from a graphite rod which are capable of electrochemiluminescence (ECL). (From reference 32).

electrooxidation of graphite using the water-soluble IL 1-butyl-3-methylimidazolium tetrafluoroborate [bmim][BF4] containing up to 90 wt% water as the electrolyte.[24]

It can generally be concluded that C-dots contain an amorphous to nanocrystalline core with predominantly sp^2 carbon; the lattice spacings are consistent with graphitic or turbostratic carbon. C-dots typically show strong optical absorption in the UV region, with a tail extending out into the visible range. One of the most fascinating features of C-dots is their PL. In any case, one unifying feature of the PL of C-dots is the clear λex dependence of the emission wavelength and intensity. Whether this occurs because of optical selection of differently sized nanoparticles (quantum effect) and/or different emissive traps on the C-dot surface or another mechanism altogether is currently unresolved. Similarly, the requirement

for surface passivation is poorly understood, but appears to be linked to the fabrication method employed.

Gokus *et al*.[33] observed the induction of PL in single- ayer graphene (SLG) flakes with an oxygen plasma treatment. For short treatment times (1–3 s), confocal PL maps reveal bright point like PL features whereas for slightly longer exposures (5–6 s) spatially uniform broadband visible PL was observed across SLG flakes. Remarkably, because oxygen plasma etching proceeds layer-by-layer, bi- and multilayer flakes remained thus implying that emission from the topmost layer is quenched by subjacent untreated layers. Spectral hole burning experiments suggest that the observed large spectral width (ca. 0.5 eV) mainly reflects homogeneous broadening of a single emissive species, that is uniform across the oxidized SLG sheet. This is supported by the fact that the PL transients were nearly uniform across the complete spectrum, thereby indicating that spectral diffusion as a result of energy migration, which is typical for heterogeneously broadened systems, is absent.

4.4.2 Scope of the present investigations

As certain functionalized carbon species emitting blue light, we have investigated in case of graphene-based materials and found that graphene samples oxidized by acids as well as graphene oxide (GO) reduced by various means give excellent blue emission. A possible origin of the blue photoluminescence in reduced graphene oxide (RGO) is the radiative recombination of elecron–hole (e-h) pairs generated within localized states. The energy gap between the π and π^* states generally depends on the size of sp^2 clusters[34] or conjugation length.[35] Interaction between nanometer-sized sp^2 clusters and finite-sized molecular sp^2 domains could play a role in optimizing the blue emission in RGO. The presence of isolated sp^2 clusters in a carbon–oxygen sp^3 matrix can lead to the localization of e–h pairs, facilitating radiative recombination of small clusters.[36] We have investigated the generation

of blue light by graphene-based materials and found that graphene samples oxidized by acids as well as graphene oxide (GO) reduced by various means give blue emission. We have also demonstrated that functionalized graphenes can be combined with graphene oxide to emit white-light.

4.4.3 Experimental section

Few-layer graphene samples were prepared by the thermal exfoliation of graphite oxide at high temperatures (EG),[37] by the conversion of nanodiamond by heating in an inert atmosphere (DG)[38] and by the arc discharge of graphite electrodes in the presence of H_2 and He (HG). Graphene oxide was obtained by prolonged sonication (1hr) of graphite oxide in water medium to yield a brownish stable yellow solution. Pristine graphene samples were treated with a solution of conc.H_2SO_4 and conc. HNO_3 in water (Table 1) under microwave irradiation (2 minutes at 600 W). Before microwave treatment, the solution was sonicated for better mixing. We designate the acid-treated EG, DG and HG as FEG, FDG and FHG respectively. A KrF excimer laser (248 nm, 5 Hz) was employed to irradiate aqueous solutions of GO taken in a quartz vail. The aluminum metal slit (beam shaper) which gives usually a rectangular beam was removed while laser reduction was carried out. This makes laser energy almost uniform throughout the area where graphene oxide is present. It was observed that within half an hour of irradiation at 5 Hz reprate and at 300 mJ beam energy, GO turns black due to the reduction. GO was also exposed to sunlight from the top side in daytime. Graphene oxide after reduction by irradiation with an excimer laser or sunlight settles down at the bottom.

Graphene samples were characterized by employing various techniques like FESEM, TEM, AFM and Raman spectroscopy. HG contains 2-3 layers while EG and DG have 5-6 and 6-10 layers respectively as revealed by AFM measurements.

4.4.3 Results and discussion

The as-prepared graphene samples exhibit weak blue-emission centered around 400 nm upon UV excitation. On acid treatment under microwave irradiation (Table 1), the blue emission band gets slightly red-shifted with the PL emission maximum appearing around 435 nm as can be seen from the Figure 1a. The nature of blue-emission is quantified by the CIE chromaticity diagram in Figure 1b. Another way to obtain blue-emission from graphene

Table 1. Conditions for acid treatment of graphene.

Graphene (5 mg)	Weight (mg)	HNO_3 (ml)	H_2SO_4 (ml)	H_2O (ml)	Microwave treatment (seconds)
EG	5	4	4	8	2
DG	5	4	4	8	2
HG	5	4	4	8	2

materials is via reduction of GO. GO itself exhibits brownish yellow emission with a band centered around 550 nm.[39, 40]

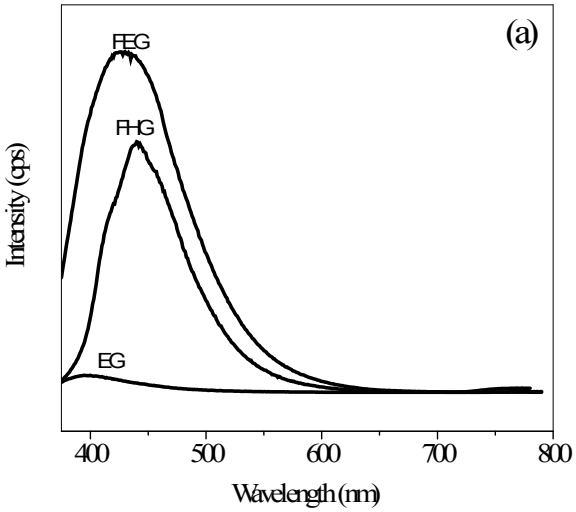

Figure 1a. PL spectra of EG, acid treated EG (FEG) and acid treated HG (FHG).

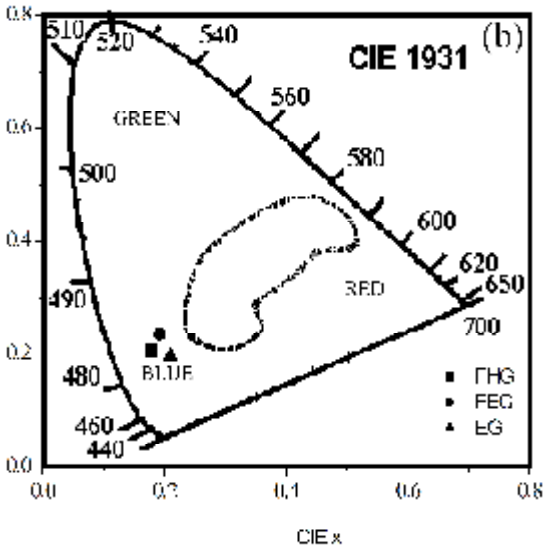

Figure 1b. CIE 1931 color diagram showing the three points due to EG, FEG and FHG in the blue region.

Reduction of GO by chemical means or by radiation gives rise to blue-emitting species. The radiation can be ultraviolet light (Hg lamp), sunlight or a laser. GO upon prolonged irradiation (6 hours) by sunlight gives rise to the same effect achieved by the ultraviolet treatment for 40 minutes. Laser irradiation requires only 10 or 20 min depending on 5 or 10 Hz reprate. Laser irradiation not only reduces GO, but also fragments the graphene sheets into pieces. Reduction of GO by laser radiation and sunlight can be observed visibly by the change in colour as shown in Figure 2. Brownish yellow GO turns black after irradiation. Two-probe resistance measurements showed that the resistivity of GO (5000 Ohm-cm) decreases to 550 and 41 Ohm-cm after reduction with sunlight and laser respectively. This is expected as reduced GO would be more conducting than GO.

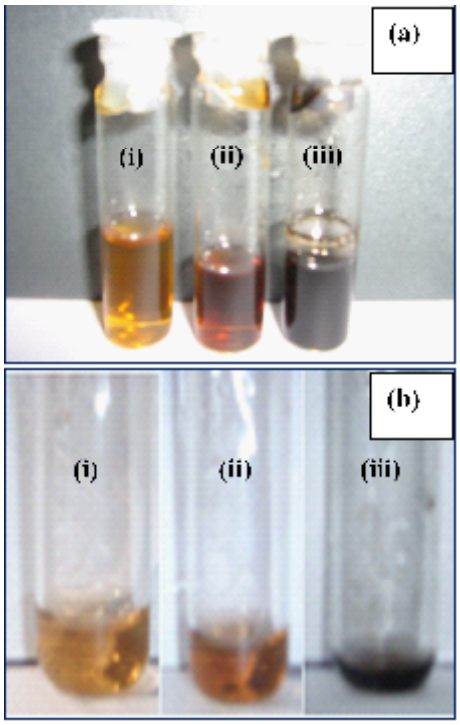

Figure 2. (a) Photographs of (i) GO and laser reduced GO at beam energy of 300 mJ with (ii) 1000 and (iii) 18000shots. (b) Photographs of (i) GO and GO exposed to sunlight for (ii) 2 and (iii) 10 hours.

Infrared spectra of the reduced samples show reduced intensities of the bands corresponding to –OH (~3418 cm^{-1}) and C=O (~1640 cm^{-1}) compared to GO.[39] In Figure 3a, we show the PL spectra for yellow-emitting GO and the blue-emitting light sources achieved by irradiation with different light sources. In Figure 3b, we show CIE chromaticity diagram for GO and the reduced GO samples obtained by different means. Chemically reduced GO also shows similar blue emission. The plausible mechanism for photo-assisted reduction of GO is as follows.

$$GO + h\nu \longrightarrow GO(h + e) \quad (1)$$

$$4h + 2H_2O \longrightarrow O_2 + 4H^+ \quad (2)$$

$$4e + GO + 4H^+ \longrightarrow RGO + 2H_2O \quad (3)$$

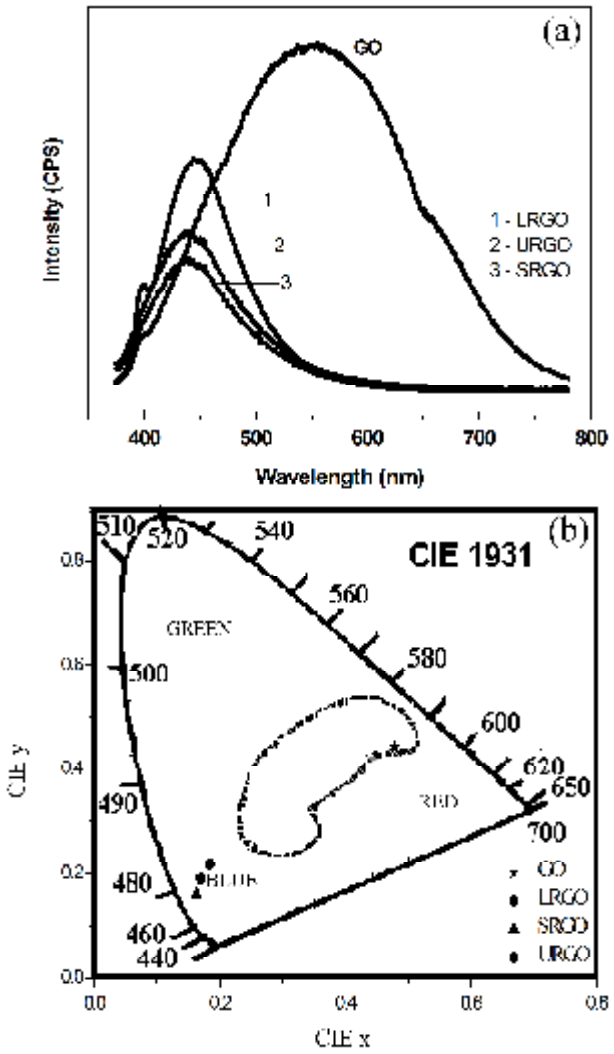

Figure 3. (a) PL spectra of GO and reduced GO obtained by irradiation with laser (LRGO), ultraviolet light (URGO) and sunlight (SRGO). (b) The chromaticity diagram shows the nature of blue emission by the three RGO s.

GO absorbs light generating electron-hole pair. Water acts as a hole scavenger yielding oxygen and protons, whereas the electrons are captured by the sp^2 regions of GO. The captured electrons together with the produced protons reduces the functional groups in GO, extending the π-electron network resulting RGO. Blue emission from laser-reduced graphene oxide (LRGO) or acid treated EG can be combined with the yellow emission from graphene oxide to achieve bluish white light (as shown in Figure 4).

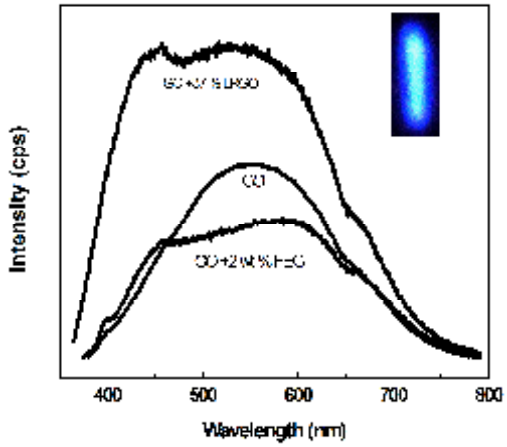

Figure 4. PL spectra of GO and GO admixed with 2 wt % of FEG and 37 wt % of LRGO. Insets in the figure show the photograph of bluish white light emission after mixing LRGO with GO.

4.4.5 Conclusions

It is noteworthy that carbon-based materials such as reduced graphene oxide or oxidized graphene give rise to blue-emission which is similar to inorganic materials such as gallium nitride. The Functionalized graphenes can be combined with single-layer graphene oxide to produce white-light.

4.5.6 References

[1] H. P. Liu, T. Ye, C. D. Mao, *Angew. Chem. Int. Ed.* **2007**, *46*, 6473.

[2] J. Zhou, C. Booker, R. Li, X. Zhou, T.-K. Sham, X. Sun, Z. Ding, *J. Am. Chem. Soc.* **2007**, *129*, 744.

[3] Y.-P. Sun, B. Zhou, Y. Lin, W. Wang, K. A. S. Fernando, P. Pathak, M. J. Meziani, B. A. Harruff, X. Wang, H. Wang, P. G. Luo, H. Yang, M. E. Kose, B. Chen, L. M. Veca, S.-Y. Xie, *J. Am. Chem. Soc.* **2006**, *128*, 7756.

[4] S. L. Hu, K. Y. Niu, J. Sun, J. Yang, N. Q. Zhao, X. W. Du, *J. Mater. Chem.* **2009**, *19*, 484.

[5] C. E. Banks, T. J. Davies, G. G. Wildgoose, R. G. Compton, *Chem. Commun.* **2005**, 829.

[6] R. L. McCreery, in *Electroanalytical Chemistry, Vol. 17* (Ed.: A. J. Bard), Marcel Dekker, New York, **1991**, p. 191.

[7] Y. W. Fan, M. Burghard, K. Kern, *Adv. Mater.* **2002**, *14*, 130.

[8] M. A. Fryling, J. Zhao, R. L. McCreery, *Anal. Chem.* **1995**, *67*, 967.

[9] A. Chou, T. Bocking, N. K. Singh, J. J. Gooding, *Chem. Commun.* **2005**, 842.

[10] X. B. Ji, C. E. Banks, W. Xi, S. J. Wilkins, R. G. Compton, *J. Phys. Chem. B* **2006**, *110*, 22306.

[11] G. G. Wildgoose, C. E. Banks, H. C. Leventis, R. G. Compton, *Microchim. Acta* **2006**, *152*, 187.

[12] K. K. Cline, M. T. McDermott, R. L. McCreery, *J. Phys. Chem.* **1994**, *98*, 5314.

[13] C. A. McDermott, K. R. Kneten, R. L. McCreery, *J. Electrochem. Soc.* **1993**, *140*, 2593.

[14] S. Ranganathan, T. C. Kuo, R. L. McCreery, *Anal. Chem.* **1999**, *71*, 3574.

[15] (a) X. Xu, R. Ray, Y. Gu, H. J. Ploehn, L. Gearheart, K. Raker, W. A. Scrivens, *J. Am. Chem. Soc.* **2004**, *126*, 12736. (b) S. N. Baker, G. A. Baker, Angew. Chem. Int. Ed. 2010, 49, 6726.

[16] S.-J. Yu, M.-W. Kang, H.-C. Chang, K.-M. Chen, Y.-C. Yu, *J. Am. Chem. Soc.* **2005**, *127*, 17604.

[17] A. Krueger, *Adv. Mater.* **2008**, *20*, 2445.

[18] A. Krueger, *J. Mater. Chem.* **2008**, *18*, 1485.

[19] A. Krueger, *Chem. Eur. J.* **2008**, *14*, 1382.

[20] H. Peng, J. Travas-Sejdic, *Chem. Mater.* **2009**, *21*, 5563.

[21] L. Cao, X. Wang, M. J. Meziani, F. Lu, H. Wang, P. G. Luo, Y. Lin, B. A. Harruff, L. M. Veca, D. Murray, S.-Y. Xie, Y.-P. Sun, *J. Am. Chem. Soc.* **2007**, *129*, 11318.

[22] S.-L. Hu, K.-Y. Niu, J. Sun, J. Yang, N.-Q. Zhao, X.-W. Du, *J. Mater. Chem.* **2009**, *19*, 484.

[23] S.-T. Yang, X. Wang, H. Wang, F. Lu, P. G. Luo, L. Cao, M. J. Meziani, J.-H. Liu, Y. Liu, M. Chen, Y. Huang, Y.-P. Sun, *J. Phys. Chem. C* **2009**, *113*, 18110.

[24] J. Lu, J. x. Yang, J. Wang, A. Lim, S. Wang, K. P. Loh, *ACS Nano* **2009**, *3*, 2367.

[25] Q.-L. Zhao, Z.-L. Zhang, B.-H. Huang, J. Peng, M. Zhang, D.-W. Pang, *Chem. Commun.* **2008**, 5116.

[26] A. B. Bourlinos, A. Stassinopoulos, D. Anglos, R. Zboril, V. Georgakilas, E. P. Giannelis, *Chem. Mater.* **2008**, *20*, 4539.

[27] A. B. Bourlinos, A. Stassinopoulos, D. Anglos, R. Zboril, M. Karakassides, E. P. Giannelis, *Small* **2008**, *4*, 455.

[28] R. Liu, D. Wu, S. Liu, K. Koynov, W. Knoll, Q. Li, *Angew. Chem. Int. Ed.* **2009**, *121*, 4668.

[29] H. Zhu, X. L. Wang, Y. L. Li, Z. J. Wang, F. Yang, X. R. Yang, *Chem. Commun.*

2009, 5118.

[30] Y. P. Sun, X. Wang, F. S. Lu, L. Cao, M. J. Meziani, P. J. G. Luo, L. R. Gu, L. M. Veca, *J. Phys. Chem. C* **2008**, *112*, 18295.

[31] Y. P. Sun, B. Zhou, Y. Lin, W. Wang, K. A. S. Fernando, P. Pathak, M. J. Meziani, B. A. Harruff, X. Wang, H. F. Wang, P. J. G. Luo, H. Yang, M. E. Kose, B. L. Chen, L. M. Veca, S. Y. Xie, *J. Am. Chem. Soc.* **2006**, *128*, 7756.

[32] L. Y. Zheng, Y. W. Chi, Y. Q. Dong, J. P. Lin, B. B. Wang, , *J. Am. Chem. Soc.* **2009**, *131*, 4564.

[33] T. Gokus, R. R. Nair, A. Bonetti, M. Bohmler, A. Lombardo, K. S. Novoselov, A. K. Geim, A. C. Ferrari, A. Hartschuh, *ACS Nano* **2009**, *3*, 3963.

[34] J. Robertson, E. P. Oreilly, *Phys. Rev. B* **1987**, *35*, 2946.

[35] J. L. Bredas, R. Silbey, D. S. Boudreaux, R. R. Chance, *J. Am. Chem. Soc.* **1983**, *105*, 6555.

[36] G. Eda, H. E. Unalan, N. Rupesinghe, G. A. J. Amartunga, *Adv. Mater.* **2010**, *22*, 505.

[37] H. C. Schniepp, J. L. Li, M. J. McAllister, H. Sai, M. Herrera-Alonso, D. H. Adamson, R. K. Prud'homme, R. Car, D. A. Saville, I. A. Aksay, *J. Phys. Chem. B* **2006**, *110*, 8535.

[38] O. E. Andersson, B. L. V. Prasad, H. Sato, T. Enoki, Y. Hishiyama, Y. Kaburagi, M. Yoshikawa, S. Bandow, *Phys. Rev. B* **1998**, *58*, 16387.

[39] X. Sun, Z. Liu, K. Welsher, J. Robinson, A. Goodwin, S. Zaric, H. Dai, *Nano Res.* **2008**, *1*, 203.

[40] Z. Luo, P. M. Vora, E. J. Mele, A. T. C. Johnson, J. M. Kikkawa, *Appl. Phys. Lett.* **2009**, *94*, 111909.

4.5 Patterning and lithography based on graphene

4.5.1 Introduction

Fabrication of graphene-based electronics on flexible substrates, is highly desirable since it can greatly extend the applications of graphene in plastic electronics field.[1] Although thermally grown graphene[2-4] has been successfully coated on flexible substrates, these methods generally involves complicated transfer step, which may induce chemical contaminations.[5] Potential applications of graphene in electronics and other areas have been discovered and many of them require patterned graphene.[6] Several methods including plasma etching,[7] dip-pen lithography,[8] nanosphere lithography,[9] photolithography,[10] soft-transfer printing[11] and e-beam lithography[12] have been employed to generate patterned graphene. Existing methods of patterning graphene include mask lithography, transfer printing, and direct-write process. The utilization of masks as sacrificial materials is a convenient way to pattern graphene on a large scale.[13] Using polystyrene (PS) nanosphere as a mask in combination with O_2 reactive ion etching (RIE) was reported to produce periodically ordered graphene nanodisk arrays.[9] A monolayer of highly ordered PS spheres was self-assembled on water surface,[14] this monolayer was then lifted off and transferred onto graphene sheet on SiO_2 /Si (Figure 1a and 1b). O_2 RIE was subsequently carried out to etch a portion of the graphene sheets that was not protected by the PS nanospheres (Figure 1c). The PS spheres were then removed by sonication in chloroform, resulting in periodic graphene nanodisk arrays (Figure 1d and 1e). The dimension of graphene nanodisks can be effectively tuned by varying the size of the PS spheres, which can be scaled down to tens of nanometers. Such graphene nanodisks may be used as microelectrode array in electrochemistry. Aluminum[15] and hydrogen silsesquioxane[16] masks have also been used for the creation of graphene patterns. Charged molecular templates had been employed to transfer and immobilize single-layer graphene onto predefined areas of substrate surfaces.[17]

The molecular templates were generated using microcontact printing of 11-amino-1-undecanethiol self-assembled monolayer on mica-peeled Au substrates.[18] These templates

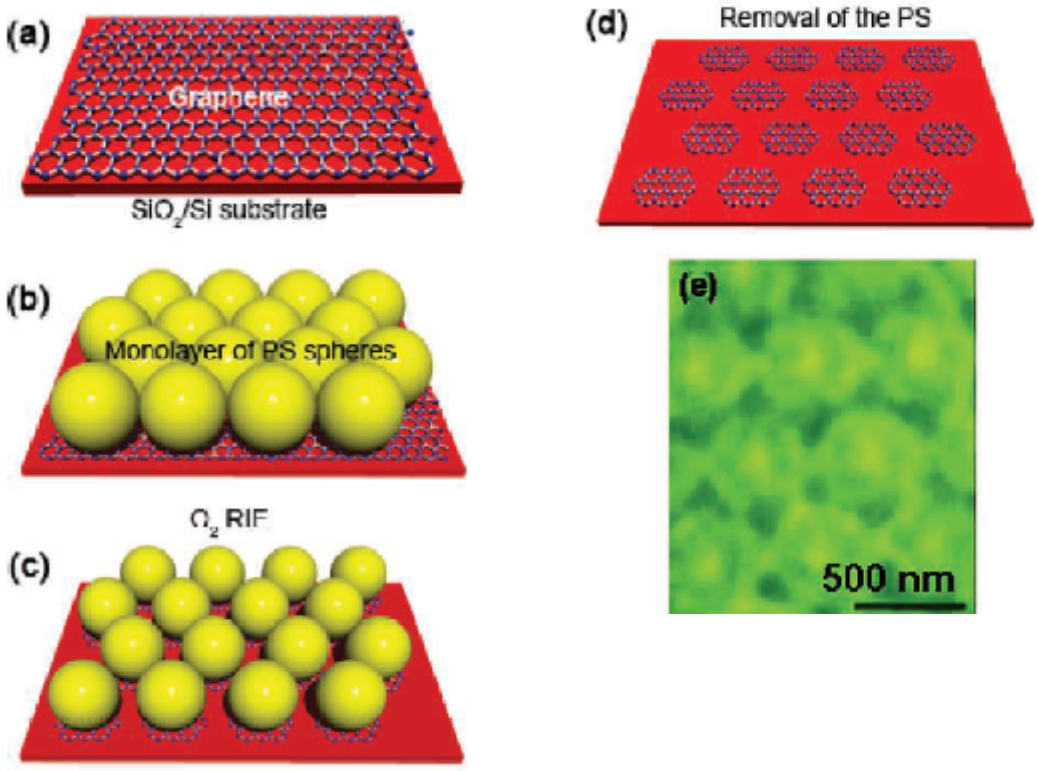

Figure 1 . Schematic illustration for graphene nanodisk arrays fabrication. a) The graphene sheets were transferred to SiO_2 /Si substrate. b) The monolayer PS spheres form an ordered array on the SiO_2 /Si substrate coated with graphene. c) A portion of graphene sheets unprotected by the PS spheres was etched with O_2 RIE. d) Removal of PS spheres by sonication in chloroform. (From ref.[9]).

were then immersed into aqueous graphene oxide (GO) dispersions so that the electrostatic interactions between the negatively charged oxygen-containing functional groups on GO sheets and the positively protonated amine groups of 11-amino-1-undecanethiol transfer the GO sheets onto the patterned functionalized surfaces. The adsorption process can be optimized by tuning various parameters such as pH, immersion time, surface passivation, and the concentration of the GO dispersion. The immobilized GO sheets could be transformed to

graphene sheets by thermal annealing. Hong *et al*. used the CVD process to grow high-quality, few-layer graphene films on nickel-coated SiO_2/Si substrates.[17] By using the pre-patterned nickel substrate, various sizes and shapes of graphene film can be obtained. The average number of graphene layers, the domain size and the substrate coverage can be controlled by changing the nickel thickness and growth time during the growth process. Etching nickel substrate layers with $FeCl_3$ solution allows one to readily transfer patterned graphene films to an arbitrary substrate for device applications. Atomic force microscopy-based nanolithography is used to generate the single-layer graphene oxide (SGO) patterns on Si/SiO_2 substrates. In this process, a Si tip is used to scratch GO films, resulting in GO-free trenches. Using this method, various single-layer GO patterns such as gaps, ribbons, squares, triangles, and zigzags can be easily fabricated. By using the GO patterns as templates, the hybrid GO-Ag nanoparticle patterns were obtained. Our study provides a flexible, simple, convenient method for generating GO patterns on solid substrates, which could be useful for graphene material based device applications. Scanning probe lithography has been used widely to obtain patterns on a variety of substrates, especially to generate single-layer graphene oxide (SGO) patterns.[19] A focused laser beam technique has also been used to construct micropatterned GO and reduced GO multilayers.[20] Patterned GO has been reduced to graphene by exposure to hydrazine or by high-temperature thermal annealing while nanoscopic resolution has been attained by local thermal reduction of GO with a heated AFM tip.[13] The patterning of graphene is necessary for both electrical measurements as well as the fabrication of dimensional graphene devices. Resist-based lithography is a convenient way to define graphene features and patterns for devices but suffers from multiple issues in the high throughput processing of graphene devices due to surface contamination issues. The maskless, contact-free, direct "writing" of patterns in graphene using laser or heium ion beam allows simultaneous lateral and vertical scaling. These technologies allow the fabrication

of microscale and nanoscale features on graphene readily and pave the way for the integration of all-carbon electronics in the semiconductor industries.

4.5.2 Scope of the present investigations

Recently, a focused laser beam technique has been employed to construct an extended area of micropatterned GO and reduced GO multilayers on quartz substrates in a fast and controlled manner.[20] Electrostatic layer-by-layer (LBL) assembly techniques were employed to grow multilayers of GO film on a quartz substrate with polyethylenimine as a linker. The film was placed in the focused laser-beam system. When the focused laser beam was incident on the multilayer GO film, the irradiated area absorbed the laser energy, and the energy was rapidly converted into local heat. The intense heating raised the temperature of the irradiated area above 500 ºC in air and resulted in localized oxidative burning of GO to volatile gases such as CO or CO_2. By moving the computer-controlled sample stage in a programmable step with respect to the focused laser beam, patterns with tunable width and length could be directly written. The patterned GO can be subsequently reduced to graphene by exposure to hydrazine gas or thermal annealing at high temperatures. In other words, direct writing of conductive graphene pattern on GO films, where the graphene domains were isolated by insulating GO matrix, was achieved.

We have carried out patterning and lithography by making use of our recent discovery of a simple means of reducing GO sheets to graphene by irradiation with sunlight, UV radiation, a KrF excimer laser, or an electron beam. Laser irradiation of GO is found to be specially convenient for the purpose. Since excimer laser readily dehydrogenates hydrogenated graphene, therefore we have also carried out excimer laser patterning of hydrogenated graphene.

4.5.3 Experimental section

Graphite oxide (GO) was prepared by the oxidation of graphite powder and subjected the product to an intense sonication for 1 hour to cause exfoliation. The sonicated GO was exposed to excimer laser irradiation (Lambda Physik KrF excimer laser, 248 nm wavelength, 30 ns life time) for possible reduction of graphene oxide. For possible reduction and patterning, GO films deposited on a glass substrate were subjected to excimer laser radiation (300 mJ laser energy, 5 Hz repetition rate, 200 shots), after covering them by a TEM grid as the mask. Gold and platinum compounds ($HAuCl_4$ and H_2PtCl_6) were taken along with graphene oxide for reduction and patterning, in order to achieve higher electrical conductivity. The metal compounds got reduced to metal nanoparticles upon excimer laser irradiation due to photolysis.

To carry out the electron-beam reduction[21] and patterning, GO films were spin-coated onto silicon substrates (n-type, 0.5 mm thick, one side polished). GO films were exposed to electron beams (NOVA NANOSEM 600) at different voltages and currents. Various shapes were selected from the design tools available, to expose selected areas of the GO films to the electron beam. Graphene was hydrogenated by Birch reduction. Dehydrogenation was achieved by exposure to an excimer laser (See chapter 7 for details). To carry out the patterns with hydrogenated graphene, hydrogenated graphene films covered with a TEM grid were exposed to excimer laser.

Atomic force microscopy (Innova SPM) and field scanning electron microscopy (NOVA NANOSEM 600) were carried out to examine the morphology. Fourier transform infrared spectra were recorded using an IFS66v/s Bruker spectrometer. Raman spectroscopy was carried out to investigate the reduction of GO and dehydrogenation of hydrogenated graphene. Electrical conductivity was measured with a Keithley electrometer.

4.5.4 Results and discussion

The GO sheets were 1-3 layer in thickness and 1-2 microns in lateral dimension as evidenced from atomic force microscopy (see Figure 2).

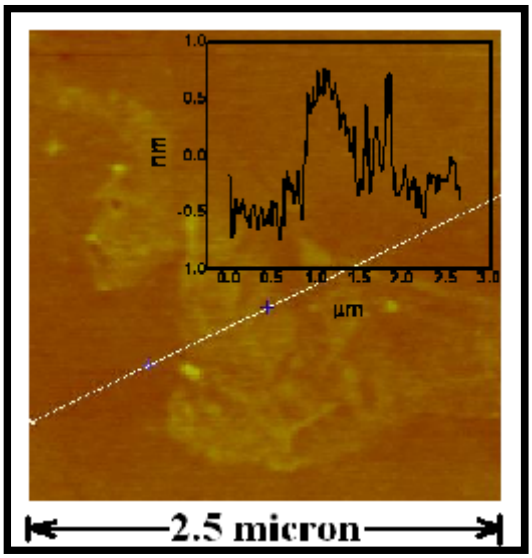

Figure 2. Atomic force microscopy image of GO sheets. Inset shows height profile along the white line shown in the Figure.

Excimer laser irradiation results in the reduction of GO to graphene as evidenced from the change in colour from brownish yellow to black (Figure 3).

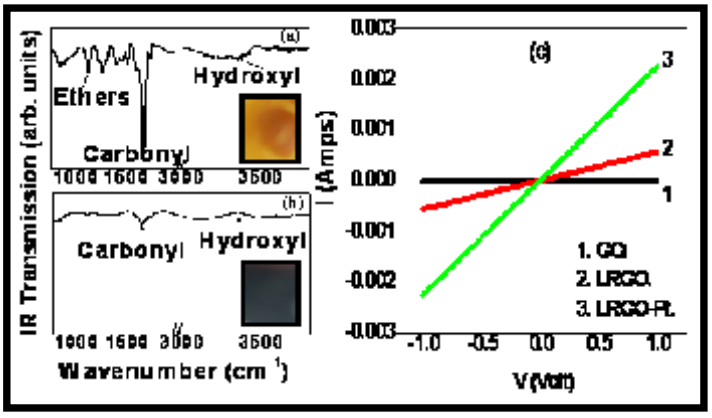

Figure3. FTIR spectra of GO (a) before and (b) after laser reduction (LRGO). Insets show photographs of GO before and after reduction. (c) Current-voltage characteristics of 1, GO; 2, LRGO; 3, LRGO-Pt.

Carbonyl and other oxygen functionalities on the surface of GO nearly disappear after the irradiation as can be seen from the infrared spectra shown in Figures 3a and b. Raman spectra of the laser reduced samples (LRGO) show D, G and 2D bands respectively at 1332, 1580 and 2640 cm^{-1}. The electrical conductivity increases by two orders of magnitude after laser irradiation of GO as shown in Figure 3c. Platinum or gold salts (H_2PtCl_6 or $HAuCl_4$) taken with GO get reduced to metal nanoparticles on irradiation and get deposited on the graphene surface. The conductivity of the metal-decorated graphene is much larger than that of graphene as shown in Figure 3c.

By employing a TEM grid as a mask, we obtained nice patterns formed by graphene in the form of squares on removing the mask as shown in the optical microscopic image in Figure 4a. We show a large-area field-emission scanning electron microscope (FESEM) image of a pattern in Figure 4b.

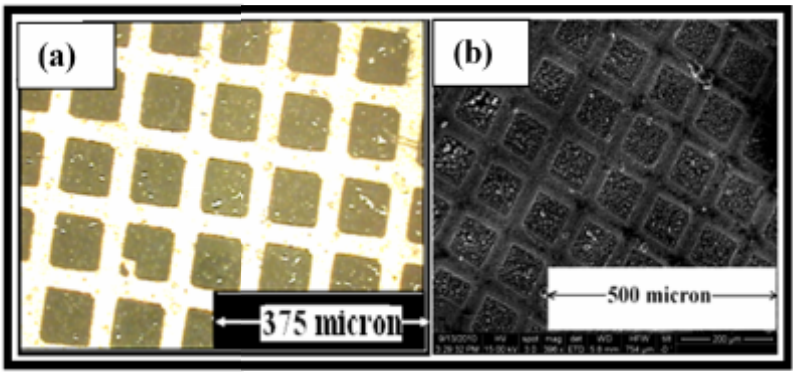

Figure 4. (a) Optical microscopic image of the pattern achieved after excimer laser reduction of graphene oxide surface and (b) Large-area FESEM image of the pattern.

We have generated similar images using GO + $HAuCl_4$ and GO + H_2PtCl_6 as starting materials. In Figures 4c and d, we show large-area FESEM images obtained after laser

irradiation. These graphene samples contain Au and Pt nanoparticles as revealed by the images in Figures 4e and f.

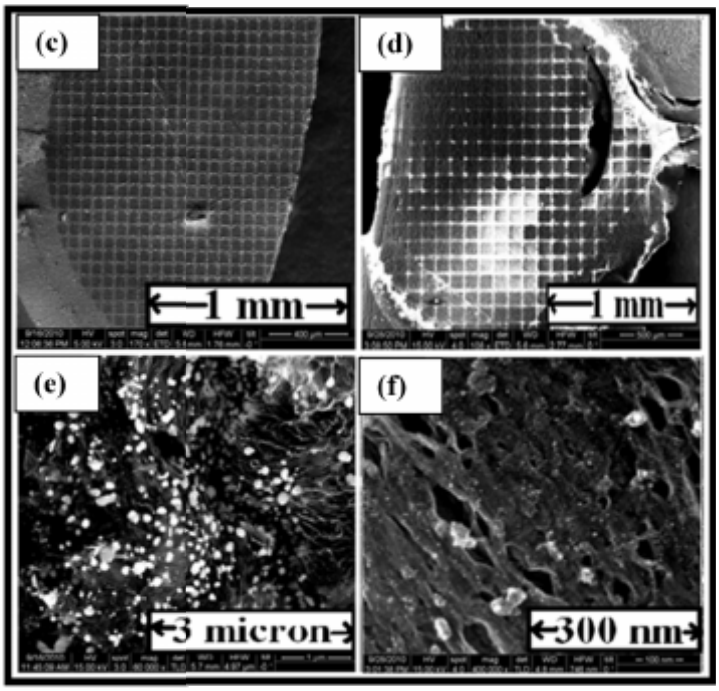

Figure 4. Large-area image of a pattern produced by laser irradiation of the mixture of GO with (c) $HAuCl_4$ and (d) H_2PtCl_6. FESEM images showing (e) Au and (f) Pt nanoparticles on the graphene surface.

Various shapes with controllable sizes could be written by electron beam on GO films. We have obtained excellent nano patterns by electron beam induced reduction and patterning as shown in Figure 5 (a-d), the line width in these images being 250 nm. We could also attain line widths of 100 nm. We could obtain sharp and distinguishable features at 20 kV and 12 nA. We used a Z-dimension depth of 1 micron and exposure times upto 100 microseconds. Lines (100 nm width) and squares (50 micron x 50 micron and 20 micron x 20 micron) were used for the purpose of e-beam reduction and patterning.

The hydrogenated graphene film was spin-coated onto a silicon substrate and the film irradiated through a mask (TEM grid). The pattern obtained was recorded with an optical

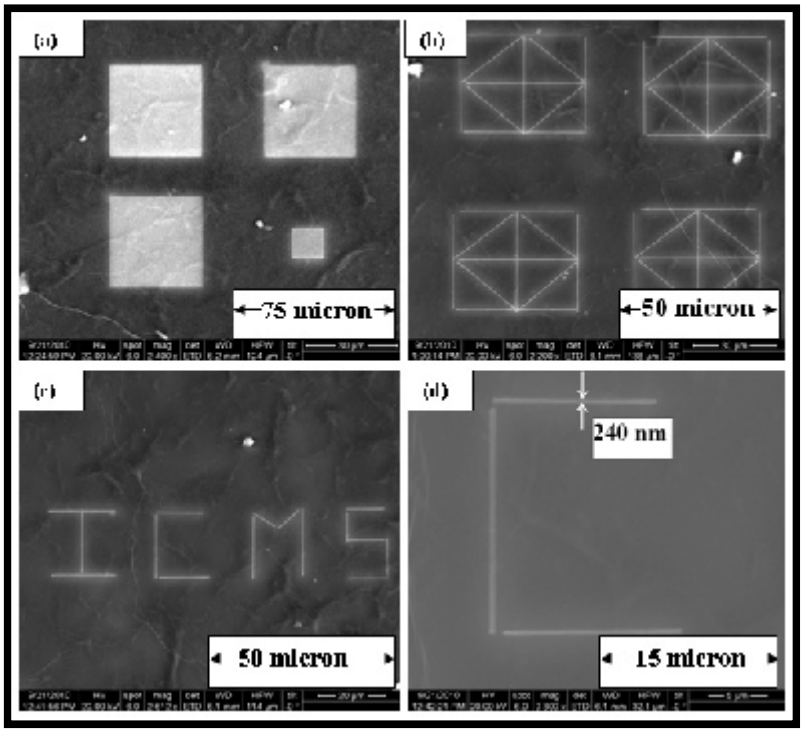

Figure 5. Electron-beam direct writing of (a) micron-sized square patterns, (b) - (d) diagrams with 250 nm wide lines produced with electron beam irradiation.

microscope as well as FESEM. We show these images in Figure 6a. Raman spectroscopy confirms that the D-band intensity reduces relative to the G-band upon laser irradiation

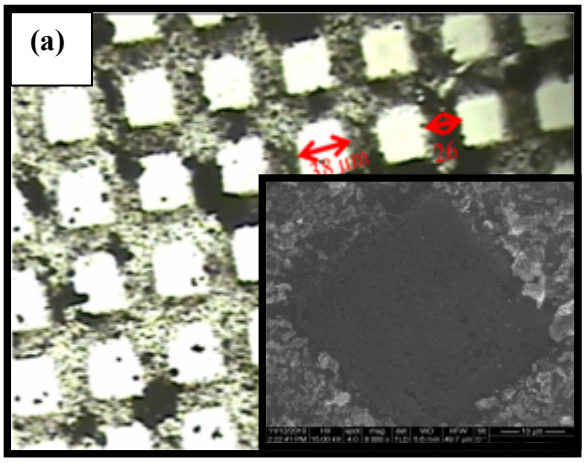

Figure 6a. Optical microscope image of micropattern imprinted on hydrogenated graphene film. Inset shows FESEM image for laser exposed area.

indicating that dehydrogenation has indeed occurred (Figure 5b). Dehydrogenation of hydrogenated graphene can be exploited for patterning in several applications. It should be noted that graphene is electrically conducting while hydrogenated graphene is many orders of magnitude less conducting.

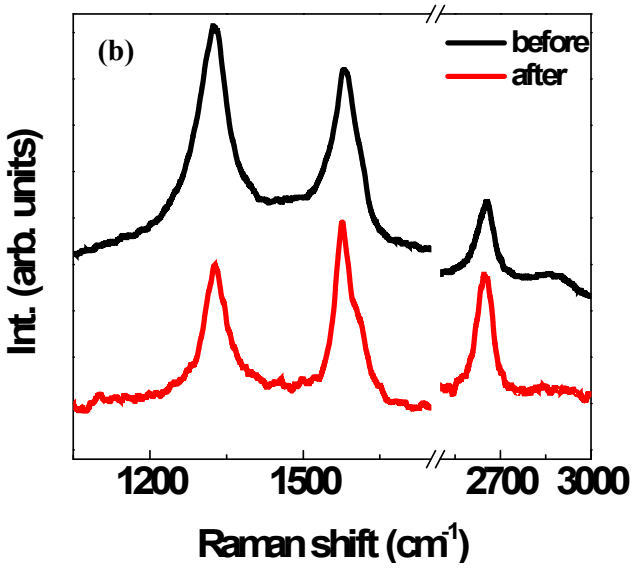

Figure 6b: Raman spectra for hydrogenated graphene before and after laser irradiation.

4.5.5 Conclusions

In conclusion, the present study demonstrates that excimer laser or electron beam irradiation of graphene oxide and hydrogenated graphene films provides an effective means of micropatterning and nanolithography. The patterns of graphenes so produced have higher electrical conductivity. This method of patterning may find useful applications in device technology.

4.5.6 References

[1] J. A. Rogers, *Nat. Nanotechnol.* **2008**, *3*, 254.

[2] K. S. Kim, Y. Zhao, H. Jang, S. Y. Lee, J. M. Kim, K. S. Kim, J.-H. Ahn, P. Kim, J.-Y. Choi, B. H. Hong, *Nature* **2009**, *457*, 706.

[3] X. Li, Y. Zhu, W. Cai, M. Borysiak, B. Han, D. Chen, R. D. Piner, L. Colombo, R. S. Ruoff, *Nano Lett.* **2009**, *9*, 4359.

[4] J. D. Caldwell, T. J. Anderson, J. C. Culbertson, G. G. Jernigan, K. D. Hobart, F. J. Kub, M. J. Tadjer, J. L. Tedesco, J. K. Hite, M. A. Mastro, *ACS Nano*, *4*, 1108.

[5] X. Liang, Z. Fu, S. Y. Chou, *Nano Lett.* **2007**, *7*, 3840.

[6] Y. Zhou, K. P. Loh, *Adv. Mater.22*, 3615.

[7] X. Zhou, G. Lu, X. Qi, S. Wu, H. Li, F. Boey, H. Zhang, *J. Phys. Chem. C* **2009**, *113*, 19119.

[8] B. Li, G. Lu, X. Zhou, X. Cao, F. Boey, H. Zhang, *Langmuir* **2009**, *25*, 10455.

[9] C. X. Cong, T. Yu, Z. H. Ni, L. Liu, Z. X. Shen, W. Huang, *J. Phys. Chem. C* **2009**, *113*, 6529.

[10] V. C. Tung, M. J. Allen, Y. Yang, R. B. Kaner, *Nat. Nanotechnol.* **2009**, *4*, 25.

[11] M. J. Allen, V. C. Tung, L. Gomez, Z. Xu, L.-M. Chen, K. S. Nelson, C. Zhou, R. B. Kaner, Y. Yang, *Adv. Mater.* **2009**, *21*, 2098.

[12] H. Duan, E. Xie, L. Han, Z. Xu, *Adv. Mater.* **2008**, *20*, 3284.

[13] (a) Z. Wei, D. Wang, S. Kim, S.-Y. Kim, Y. Hu, M. K. Yakes, A. R. Laracuente, Z. Dai, S. R. Marder, C. Berger, W. P. King, W. A. de Heer, P. E. Sheehan, E. Riedo, *Science*, *328*, 1373. (b) Y. Zhou, K. P. Loh, Adv. Mater. 2010, 22, 3615.

[14] J. Rybczynski, U. Ebels, M. Giersig, *Colloids Surf. A* **2003**, *219*, 1.

[15] S. Pang, H. N. Tsao, X. Feng, K. Müllen, *Adv. Mater.* **2009**, *21*, 3488.

[16] Z. H. Chen, Y. M. Lin, M. J. Rooks, P. Avouris, *Physica E* **2007**, *40*, 228.

[17] Z. Q. Wei, D. E. Barlow, P. E. Sheehan, *Nano Lett.* **2008**, *8*, 3141.

[18] M. Hegner, P. Wagner, G. Semenza, *Surf. Sci.* **1993**, *291*, 39.

[19] X. Z. G. Lu, H. Li, Z. Yin, B. Li, L. Huang, F. Boey, H. Zhang, *Langmuir* **2010**, *26*, 6164.

[20] Y. Zhou, Q. Bao, B. Varghese, L. A. L. Tang, C. K. Tan, C.-H. Sow, K. P. Loh, *Adv. Mater.* **2010**, *22*, 67.

[21] M. Baraket, S. G. Walton, Z. Wei, E. H. Lock, J. T. Robinson, P. Sheehan, *Carbon* **2010**, *48*, 3382.

CHAPTER 5

INTERACTION OF GRAPHENE WITH ELECTRON DONOR & ACCEPTOR MOLECULES AND METAL NANOPARTICLES

Summary*

Interaction of tetrathiafulvalene (TTF) and tetracyanoethylene (TCNE) with few-layer graphene samples prepared by different methods has been investigated by Raman spectroscopy to understand the role of the graphene surface. The position and full-width at half maximum of the Raman G-band are affected on interaction with TTF and TCNE and the effect is highest with EG and least with HG. The effect of TTF and TCNE on the 2D band is also maximum with EG and least with HG. The observed trend in the magnitude of interaction between the donor and acceptor molecules as found from the Raman spectroscopy, vary in the same order as the surface areas of the graphenes. Interaction of metal nanoparticles such as Ag, Au, Pt and Pd with graphene has been examined by employing Raman spectroscopy and first-principles calculations. There is a significant shift of the G-band as well as of the other bands, in addition to variation in the relative intensities of D and 2D bands when the metal nanoparticles are deposited on graphene. The shifts in the G and D bands show meaningful trends with the ionization energies of the metals as well as the charge-transfer energies. Results from the calculations underscore the importance of charge-transfer between the metal particles and graphene.

*Papers based on these studies have appeared in *Chem. Phys. Lett. (2009), (2010).*

5.1 Introduction

Graphene, exhibits a number of exotic physical properties, previously not observed at nanoscale.[1, 2] In particular, the band structure of graphene exhibits two intersecting bands at two inequivalent K points in the reciprocal space, and its low energy excitations are massless Dirac Fermions near these K points because of the linear (photon-like) energy momentum dispersion relationship. This results in very high electron mobility in graphene, which can be further improved significantly, even up to $\approx 10^5$ $cm^2/V \cdot s$. Electron or hole transport in field-effect devices based on graphene can be controlled by an external electric field. It has been demonstrated theoretically that the chiral massless Dirac Fermions of graphene propagate anisotropically in a periodic potential, which suggests the possibility of building graphene based electronic circuits from appropriately engineered periodic surface potential patterns, without the need for cutting or etching. Graphene-based devices can be expected to have many advantages over silicon-based devices. However, precise control of the carrier type and concentration in graphene is not easy. Up to now, most of the graphene samples were either deposited on a SiO_2 surface or grown on a SiC surface, and these epitaxial graphenes are usually electron doped by the substrate.[3] To control the n-type carrier concentration in the graphene, alkali metal atoms have been deposited on graphene. The single, open-shell NO_2 molecule is found to be a strong acceptor, whereas its equilibrium gaseous state N_2O_4 acts as a weak dopant and does not result in any significant doping effect.[4] Thus, it is desirable and crucial to develop new methods to precisely control the carrier type and concentration in graphene for further development of graphene-based nanoelectronics.

The control of carrier type and concentration has been achieved in SWNTs by electrochemical doping or chemical doping. Through electrochemical top-gating, it was possible to achieve a high level of doping.[5] The electronic structure and phonon frequencies of SWNTs are affected on doping with electrons or holes. Changing the electronic properties

of SWNTs by chemical means has attracted considerable attention. Metal (M) to semiconductor (S) transition in SWNTs has also been induced by helical wrapping of DNA.[6] Water appears to be critical to this reversible transition which accompanied by hybrid formation with DNA. It is predicted that a band gap can open up in metallic SWNTs wrapped with DNA in the presence of water molecules, due to charge-transfer. Kim *et al*.[7] have shown that adsorption of $AuCl_3$ to SWNTs results in high level of p-doping due to strong charge-transfer from the SWNTs to $AuCl_3$ and they have shown that sheet resistance was systematically reduced with the increasing doping concentration. Ehli *et al*.[8] have shown that charge-transfer between SWNTs and perylene dyes leads to individualized nanotubes and they have observed radical ion-pair state is formed in the excited state. There are reports of charge-transfer interaction of SWNTs with I_2 and Br_2.[9, 10] Doping of double-walled carbon nanotubes with bromine and iodine has been investigated.[11, 12] Charge-transfer doping of DWNTs has been used to distinguish between the behavior of the S/M and M/S outer/inner semiconducting (S) and metallic (M) tube configurations. The binding of electron accepting molecules (F4TCNQ (2,3,5,6-Tetrafluoro-7,7,8,8-tetracyanoquinodimethane) and NO_2) to SWNTs leads to a threshold voltage shift toward positive gate voltages, while the binding of electron donating molecules (NH_3 and polyethylenimine) leads to a shift toward negative gate voltages.[13-15] Field-effect transistor (FET) devices made of semiconducting SWNTs have been used to obtain quantitative information on charge-transfer with aromatic compounds.[16] Stoddart *et al*.[17] have fabricated SWNT/ FET devices to investigate the electron/charge-transfer with the donor-acceptor SWNT hybrids. A SWNT/FET device, functionalized noncovaletly with a zinc porphyrin derivative shows that SWNTs act as electron donors and that the porphyrin molecules act as the electron acceptors. There are various efforts in the literature to tune the electronic properties of SWNTs. Charge transfer is well known in molecular systems. This can be achieved either by intramolecular or by

intermolecular charge-transfer pathway. For the intramolecular case, the donor and/or acceptor molecule has to form a new chemical bond with the nanotubes. Obviously, the formation of new covalent bonds through functionalization of nanotubes may significantly modify the structure as well as its electronic properties. On contrary to that, one can self assemble some selective donor or acceptor molecules on the surface of SWNTs developing a possibility of through charge-transfer. Recently, Voggu *et al*.[18] have investigated the interactions of various electron-withdrawing (chlorobenzene, nitrobenzene, tetracyanoquinodimethane (TCNQ), tetracyanoethylene (TCNE)) and electron-donating (anisole, aniline, tetrathiafulvalene (TTF)) molecules with SWNTs to determine the sensitivity of their electronic structure and properties to molecular charge-transfer. They have investigated the effect of these donor and acceptor molecules as measured by both electronic and Raman spectra of the SWNTs and found that donor and acceptor molecules induce opposite effects in the electronic and Raman spectra as well as in electrical resistivity.

Voggu *et al*. have also studied the effect of metal nanoparticles on the electronic structure of SWNTs.[19] For this purpose, SWNTs have been coated with nanoparticles of gold and platinum by microwave treatment[20] and gold nanoparticles were covalently attached through the click reaction.[21] Raman spectra of SWNTs attached to the metal nanoparticles in comparison with the spectrum of pure SWNTs have been studied by made use of the G-band in the Raman spectra to obtain the relative proportions of the semiconducting and metallic species. They have also used the radial breathing mode (RBM) bands in the Raman spectra to affirm the results obtained from the analysis of G-bands. The Raman studies establish that there is an increase in the proportion of the metallic SWNTs on interaction with Au and Pt nanoparticles. In other words, the metal nanopaticles cause a semiconductor to metal transition in the SWNTs-nanoparticle composites.Theoretical calculations which reveal that the interaction of SWNTs with small and reasonably large Au

and Pt clusters, as well as cylindrical monolayers of these metals, leads to the modification of the electronic structure resulting in semiconductor to metal transition of the SWNTs. The primary interaction responsible for electronic transition is Coulombic charge-transfer between the metal particles and SWNT surface. It is noteworthy that metallic SWNTs do not transform into semiconducting nanotubes upon interaction with metal particles.

Pristine graphene is a zero-gap semiconductor, and its Fermi level exactly crosses the Dirac point.[22, 23] For practical application, an energy gap is essential. Raman spectroscopy has emerged as an effective probe to characterize graphene samples in terms of the number of layers and their quality.[24, 25] By combining Raman experiments with in-situ transport measurements of graphene in field-effect transistor geometry, it has been shown that the G-modes of single and bi- layer graphenes blue shift on doping with electrons as well as holes.[26, 27] On the other hand, the 2D band blue-shifts on hole doping whereas it red shifts on doping with electrons. The relative intensity of the 2D band is quite sensitive to doping. Theoretical calculations based on time-dependent perturbation theory have been employed to explain the observed shifts of the G-band. Comparison between theory and experiment, however, is not entirely satisfactory at high doping levels ($>1x10^{13}/cm^2$) and the disagreement is greater for the 2D band. In the case of bi- layer graphene,[27] the blue-shift of the G-band with doping has contributions from phonon-induced inter-band and intra-band electronic transitions, thereby giving an experimental measure of the overlap integral between A and B atoms in the two layers. Furthermore, the in-plane vibration in bi- layer graphene splits into a symmetric Raman active mode (Eg) and an anti-symmetric infrared active mode (Eu). Doping dependence of these modes has been examined by Raman scattering[28] and infrared reflectivity measurements.[29] The latter show a drastic enhancement of intensity and a softening of the mode as a function of doping, along with a Fano-like asymmetric line shape due to a strong coupling of the Eu mode to inter-band transitions. Graphene is a nearly

semimetal membrane, whose extreme physical strength[30] and high electron mobility at room temperature result from extensive electron conjugation and delocalization. Charge transfer to and from adsorbed species can shift[31, 32] the graphene Fermi level by a large fraction of an electron olt. Such adsorption-induced chemical doping adjusts the Fermi level without introducing substitutional impurities, or basal plane reactions, that interrupt the conjugated network. Adsorption induced chemical doping may well become an important aspect of future graphene technologies. In graphenes consisting of only a few layers, chemical doping can result from both surface adsorption and intercalation between layers.

Organic molecules containing aromatic π systems can be used to solubilize and modify the electronic structure of graphene. Charge-transfer with coronene tetracarboxylate (CT) has been exploited recently to solubilize graphene sheets.[33] It was shown that the CT molecules help to exfoliate few-layer graphene and selectively solubilize single- and double-layer graphenes. Graphene quenches the fluorescence of aromatic molecules, probably due to the electron transfer, a feature of possible use in photovoltaics. Charge-transfer from fluorescent molecules to graphene has been utilized in visualization of graphene sheets by fluorescence microscopy[34] and in the use of graphene as a substrate for resonance Raman spectroscopy.[35] This chapter describes our efforts towards understanding the effect of various electron-donor and acceptor molecules and metal nanoparticles on the electronic structure of graphene.

5.2 Scope of the present investigations

The extremely high mobility of electrical carriers in graphene makes it an ideal candidate for next-generation nanoelectronics.[1, 2] However, lacking a band gap, graphene as a semimetal has been limited from some direct applications in electronics such as a channel material for field-effect transistors. Therefore, opening and tuning the bandgap of graphene, a crucial step to the wider device applications of graphene electronics, has attracted great

scientific interest. To date, many methods have been developed to open the band gap of graphene, including hydrogenation,[36] electrically gated bi-layer graphene,[37-42] Stone–Wales defects,[43] graphene-substrate interaction.[44, 45]

We considered it is important to investigate the effects of doping graphene through molecular charge-transfer by the interaction of graphene with electron-donor and -acceptor molecules and compare the results from electrochemical doping. We have, therefore, investigated the effects of TTF and TCNE on the Raman bands with few-layer graphenes prepared by three different methods and hence associated with differences in the nature of the surface. The methods employed for the preparation include the exfoliation of graphite oxide, conversion of nanodiamond and arc-evaporation of graphite in a hydrogen atmosphere, of which the last is a new method. The results do indeed show that the maximum changes in the Raman band positions and widths occur in the case of graphene with the largest surface area. We studied the interaction of graphene with tetrathiafulvalene (TTF) which is a powerful electron-donor and tetracyanoethylene (TCNE) which is an excellent electron-acceptor. We have employed Raman spectroscopy as well as electronic spectroscopy, the former enabling us to monitor the changes with the concentration of the donor and acceptor molecules. Optical absorption spectroscopy gave clear evidence of charge transfer in these systems.

Carbon nanotubes have been decorated by nanoparticles of metals such as gold and platinum. This has been accomplished by different methods and such composite materials have found applications in catalysis and other areas.[46, 47] A specially interesting aspect of such composites is that the nanoparticles of gold and platinum affect the electronic structure of single-walled carbon nanotubes (SWNTs) through Coulombic charge-transfer.[19] In the light of the recent discovery that both SWNTs and graphene interact with electron donor and acceptor molecules through molecular charge-transfer, resulting in changes in their electronic structure,[18, 48-51] we considered it is important to investigate the influence of metal

nanoparticles on the electronic structure of graphene. For this purpose, we have deposited nanoparticles of gold, silver, platinum and palladium on graphene samples prepared by two independent methods. There have been a few reports on the deposition of metal particles on graphene, but the studies generally deal with synthesis, surface plasmon resonance of the metal nanoparticles and other properties.[52-59] There is little known on the nature of interaction between graphene and the metal particles. We have, therefore, employed Raman spectroscopy to examine the interaction between metal nanoparticles and graphene, since it is well-established that Raman spectra reflect changes in the electronic structure of graphene as well as of SWNTs brought about by doping. In order to understand the nature of interaction between the metal particles and graphene, detailed first-principles calculations were carried out by Prof. Pati and co-workers. The calculations along with the changes in the Raman spectra point to the importance of charge-transfer interaction between the metal particles and graphene.

5.3 Experimental section

To study the interaction of electron donor and acceptor molecules, 1 mg of the graphene sample was dispersed in 3 ml of benzene containing appropriate concentrations of TTF and TCNE and sonicated.

To prepare graphene-gold nanoparticle composites, graphene (1 mg) was dispersed in the mixture of ethylene glycol (4 ml), water (4 ml) and aqueous solution of chloroauric acid ($HAuCl_4$) (0.2 ml, 10 mM) by sonication for 0.5 hr. This mixture is transferred to a 50 ml PTFE-lined bomb and sealed. The sealed autoclave was placed in a domestic microwave oven (General Electric model JES738WJ) equipped with a 900 W magnetron operating at 2.45 GHz and subjected to treatment for an hour.[20] To minimize solvent superheating and pressure buildup in the bomb, a two-minute off-time interval was allowed for every 10 minutes of microwave exposure. After this treatment, graphene-Au nanoparticles composites

were obtained by centrifugation followed by washing with deionized water to remove the excess ethylene glycol. Composites with other metal nanoparticles were prepared by a similar procedure. In order to deposite Ag nanoparticles, a mixture of graphene (1 mg) with a solution of silver nitrate ($AgNO_3$) in water (1ml, 5 mM) and ethylene glycol (0.5 ml (or) 1 ml) was subjected to microwave treatment for 15 minutes. To decorate graphene with silver nanoparticles of different diameters, the concentrations of the reactants were varied. To decorate graphene with platinum nanoparticles, the mixture of graphene (1 mg), an aqueous solution of chloroplatinic acid (H_2PtCl_6) (1 ml, 10 mM) and ethylene glycol (1 ml) mixture was treated for 15 minutes. To prepare graphene-Pd nano composite, the mixture of graphene (1 mg), 0.5 ml aqueous solution of tetra-chloropalladic acid (H_2PdCl_4) (10 mM) and 4 ml of ethylene glycol was treated for 45 minutes. Graphene and its composites with metal nanoparticles were characterized using transmission electron microscopy (TEM), atomic force microscopy (AFM), UV-VIS spectroscopy and Raman spectroscopy.

5.4 Results and discussion

5.4.1 Interaction with electron donor and acceptor molecules

In order to study the interaction of TTF and TCNE with graphene, 1 mg of the graphene sample was dispersed in 3 ml of TTF and TCNE solutions of different concentrations (0 M, 0.001 M and 0.1 M) and sonicated for 1 hr. The resultant solution was filtered and the obtained product was employed for Raman studies. In Figure 1, we show the changes in the Raman G-bands of the EG, DG and HG samples brought about by interaction with TTF and TCNE. The band on the right-side of G-band is due to the defect-related D'-band. The D'-band is more prominent in HG than in DG and EG. The full-width at half maximum (FWHM) of the G-band is lowest in HG and highest in EG. We have followed the variation in the G-bands of EG, DG and HG on interaction with different concentrations of

TTF and TCNE. All the samples show an increase in the G-band frequency on interaction with TCNE and a decrease in the G-band frequency on interaction with TTF. Figure 2 shows

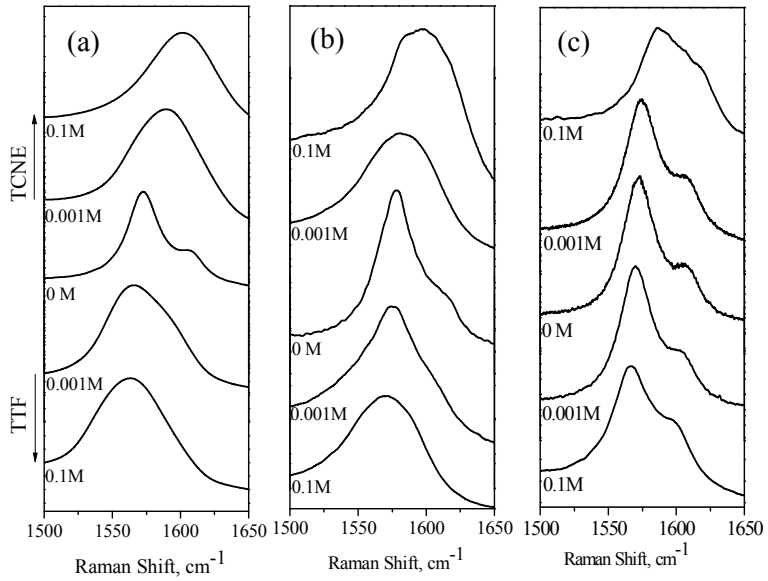

Figure 1. Variation in the Raman G-bands of graphene samples: (a) EG (b) DG and (c) HG, caused by interaction with varying concentrations of TTF and TCNE.

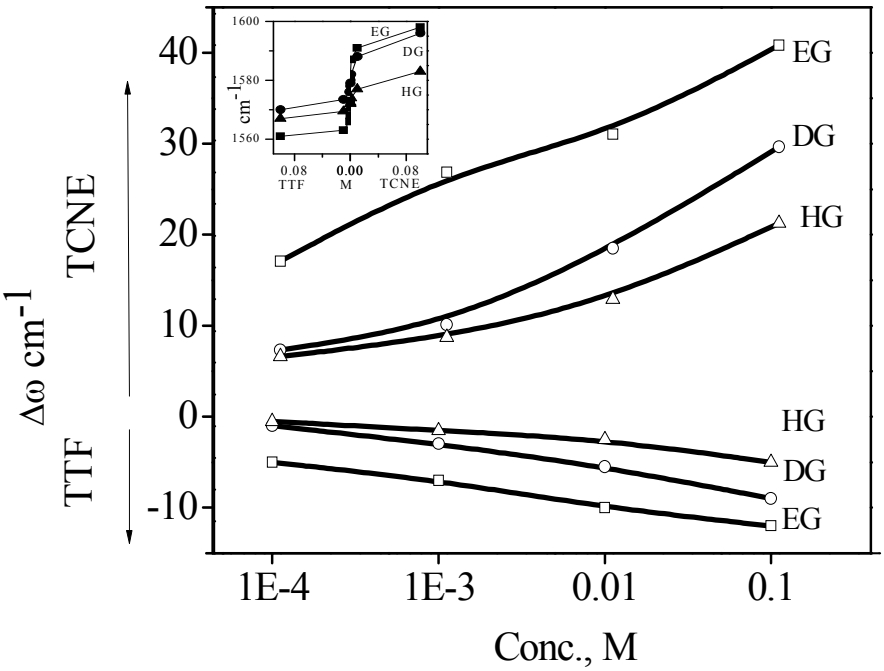

Figure 2. Changes in the position of G-band plotted against the logarithm of concentration of TTF and TCNE. Inset shows the data plotted against the concentration.

the changes in the G-band position of the three graphene samples with varying concentrations of TTF and TCNE. The change in the G-band frequency is maximum in the case of EG and least in the case of HG. Thus, the shifts in the G-band in the EG, DG and HG samples are 25,17 and 11 cm^{-1} respectively on interaction with 0.1M TCNE.

In Figure 3, we show the variation of the FWHM of the G-band of the three graphenes with the concentration of TTF and TCNE. The FWHM of the G-band generally increases on interaction with TTF and TCNE, the magnitude of increase being highest in the case of EG.

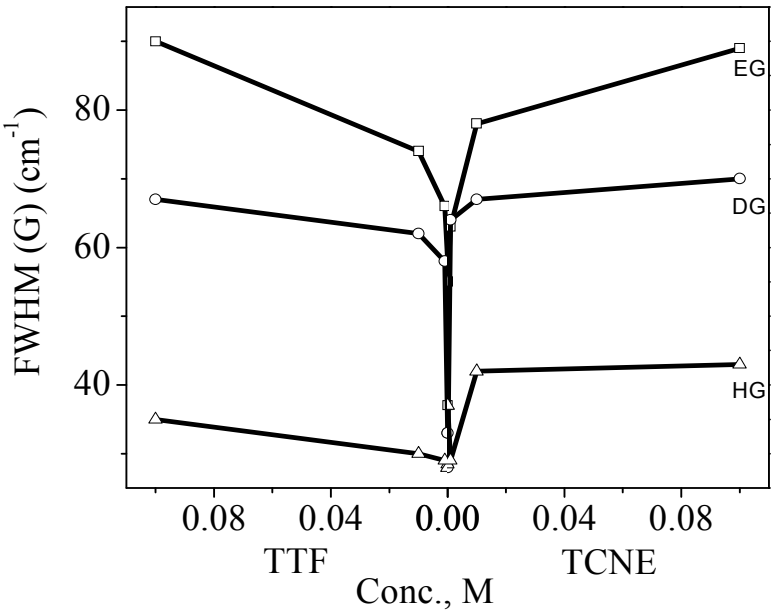

Figure 3. Variation in the FWHM of the G-band with the concentration of TTF and TCNE.

We also notice that initial increase is generally sharp. We could obtain reliable data on the changes in the D' band in the case of HG. The FWHM of D' band also increases with increase in the concentration of TTF and TCNE. It is known that the 2D-band is highly sensitive to electron or hole doping.[26] In Figure 4, we show the effect of interaction of TTF and TCNE on the 2D bands of EG, DG and HG. The 2D-band intensity generally decreases on

interaction with TTF or TCNE. The effect is least in the case of HG. In Figure 5a, we have plotted the ratio of intensities of the of 2D and G bands, I(2D)/I(G) against the concentrations of TTF and TCNE. The 2D-band intensity decreases with the increase in concentration of both TTF and TCNE, the initial decrease being sharp in all the cases.

.

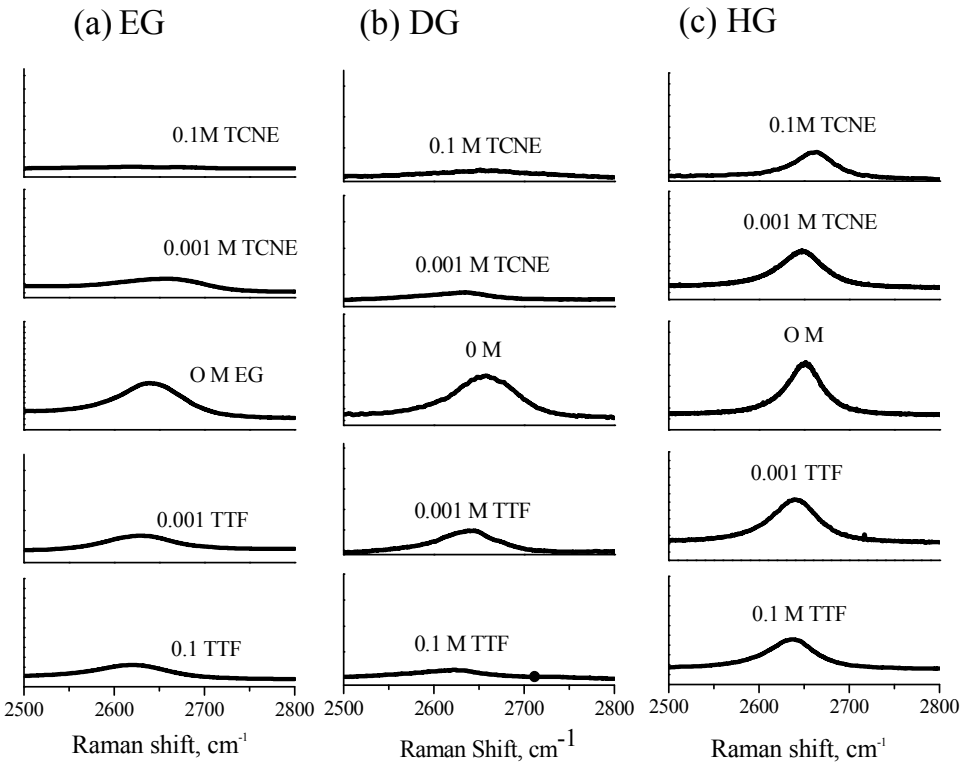

Figure 4. Variation in the Raman 2D-bands of the graphene samples, (a) EG (b) DG and (c) HG, caused by interaction with varying concentrations of TTF and TCNE.

The decrease in intensity is higher with EG and DG when compared to HG. The intensity of the defect-related D band also varies with the TTF/TCNE concentration, but in a direction opposite to that of the 2D-band. This is because the origin of the 2D and D band is different. The D-band, unlike the 2D-band couples preferentially to electronic states with wave vector k such that 2q=k. Two scattering events of which one is an elastic process involving defects and another is inelastic involving a phonon occur in the case of the D-band. In the case of the

2D-band both processes are inelastic. The intensity ratio of I(D)/I(G) increases more markedly in the case of EG and DG compared to HG, the initial increase being sharp in all the cases.

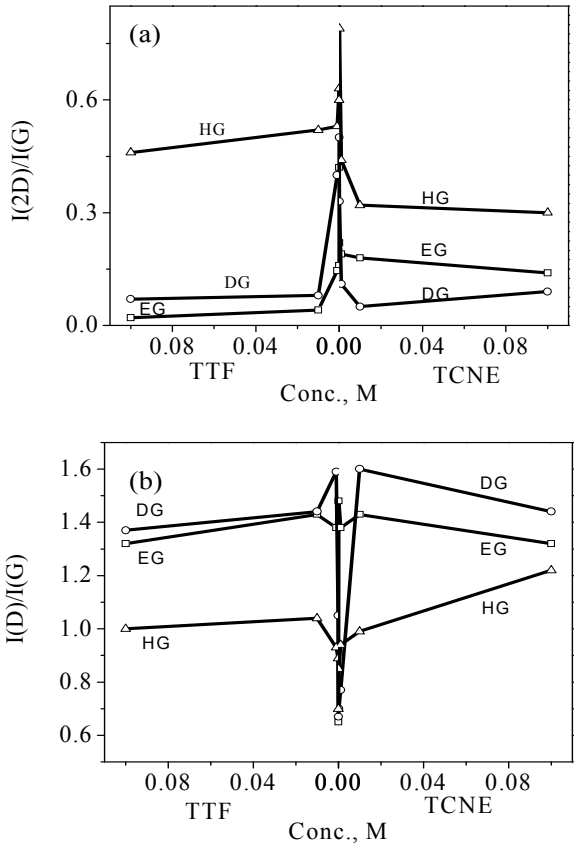

Figure 5: Variation in the (a) 2D/G and (b) D/G intensity ratios with the concentration of TTF and TCNE.

5.4.2 Interaction with metal nanoparticles

Graphene-metal nanoparticle composites prepared by glycol reduction under microwave irradiation were examined by both FESEM and TEM. In Figure 6 we show typical FESEM and TEM images of the graphene (EG) decorated with Au nanoparticles. From Figure 6 we see a uniform coating of spherical gold nanoparticles on the graphene sheet. The insets in Figure show the histogram of the diameter of nanoparticles. The average diameter of the gold nanoparticles is around 14 nm. The UV-Visible spectrum in Figure 7 of the nanocomposite shows the characteristic surface plasmon band due to the Au nanoparticles around 530 nm.[60]

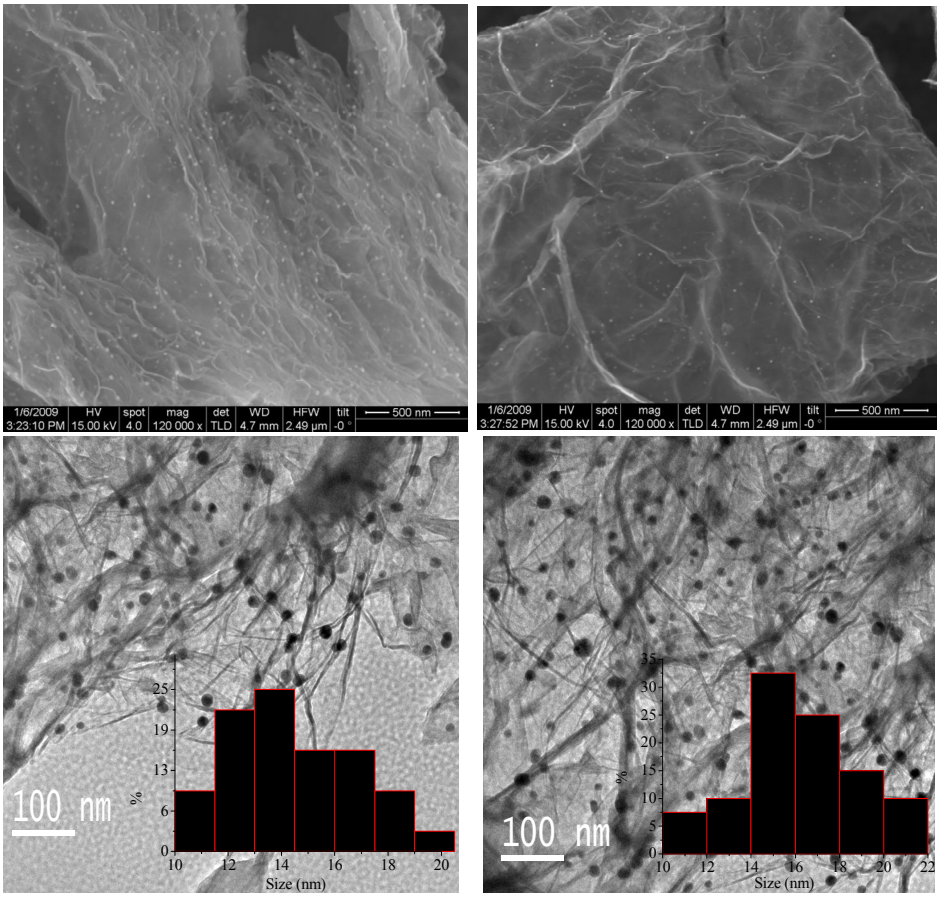

Figure 6. FESEM (top panel) and TEM (bottom panel) images of EG-Au (~14 nm) Insets in bottom panel show the histogram of the diameters of Au nanoparticles.

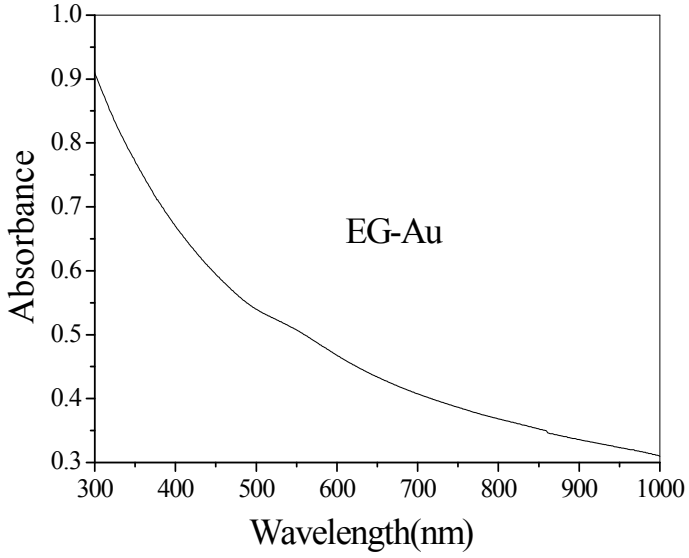

Figure 7. UV-VIS spectrum of EG-Au showing the plasmon band.

We have also decorated graphene prepared by arc-evaporation of graphite (HG) with gold nanoparticles, the average diameter of the nanoparticles being 35 nm (Figure 8). The Au nanoparticles in the HG-Au nanocomposite give rise to a broad plasmon band centered around 550 nm.

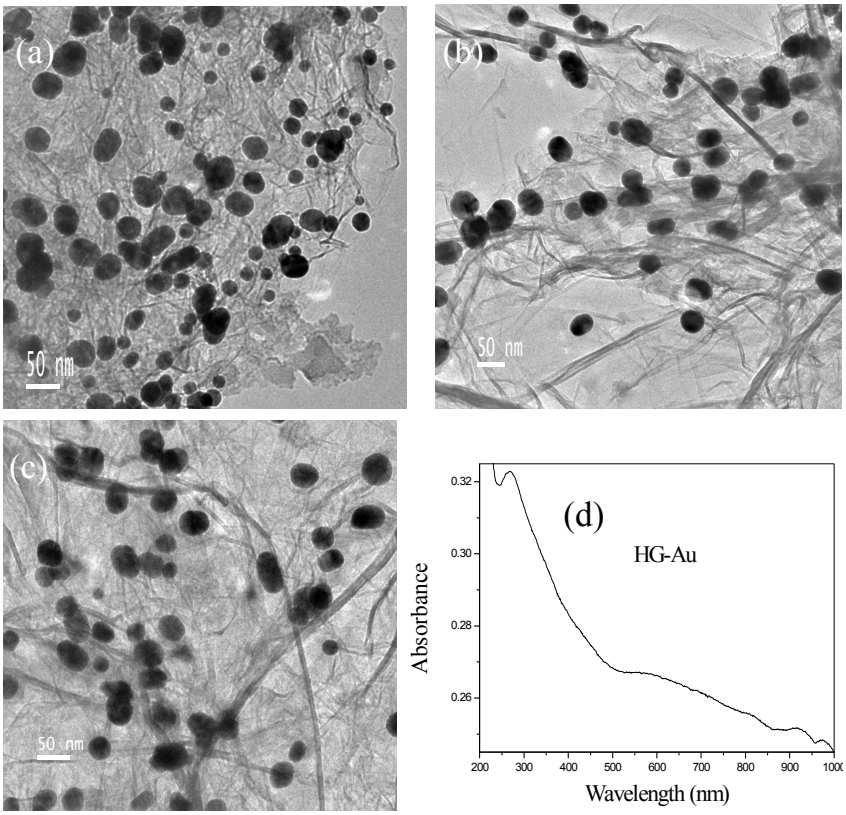

Figure 8. (a, b and c) TEM images and (d) UV-VIS spectrum of HG-Au.

We have decorated graphene with silver nanoparticles of different diameters. To control the diameter of silver nanoparticles, different amounts of ethyleneglycol were added to the 1 ml of silver nitrate ($AgNO_3$) (1mL, 5 mM) solution suspended with graphene. When 1 ml of ethylene glycol was added to the solution, the average diameter of the silver nanoparticles was around 4 nm range as revealed by the TEM image in Figure 9. These particles show a surface plasmon band around 410 nm as shown in Figure 10. When 0.5 ml of ethylene glycol was added for the preparation, the average diameter was in the 17 nm range (Figure 11).

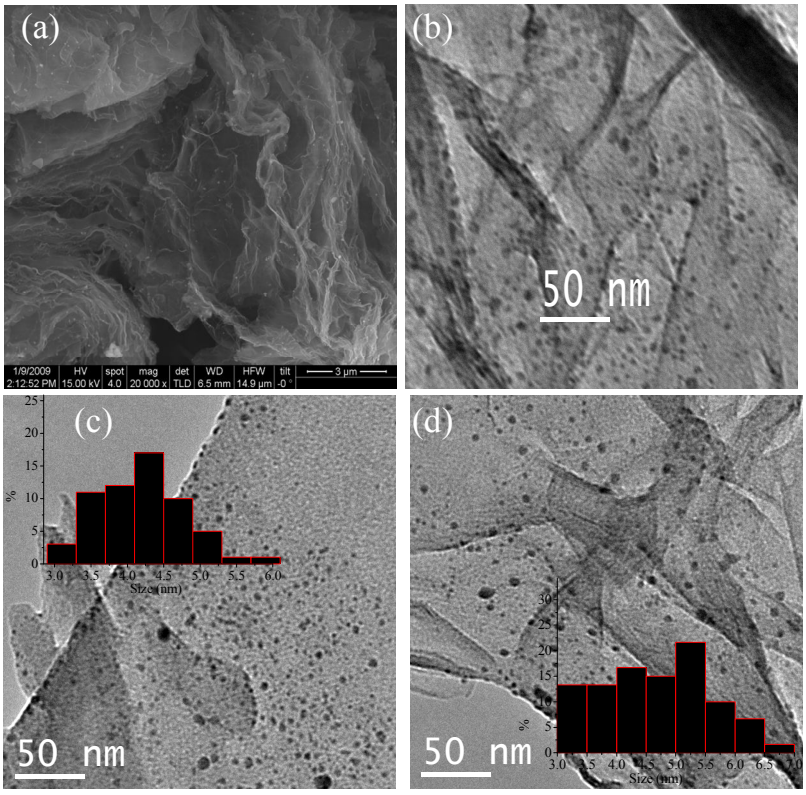

Figure 9. (a) FESEM and (b, c and d) TEM images of EG-Ag (~4 nm). Insets in c and d show the histogram of the diameters of Ag nanoparticles.

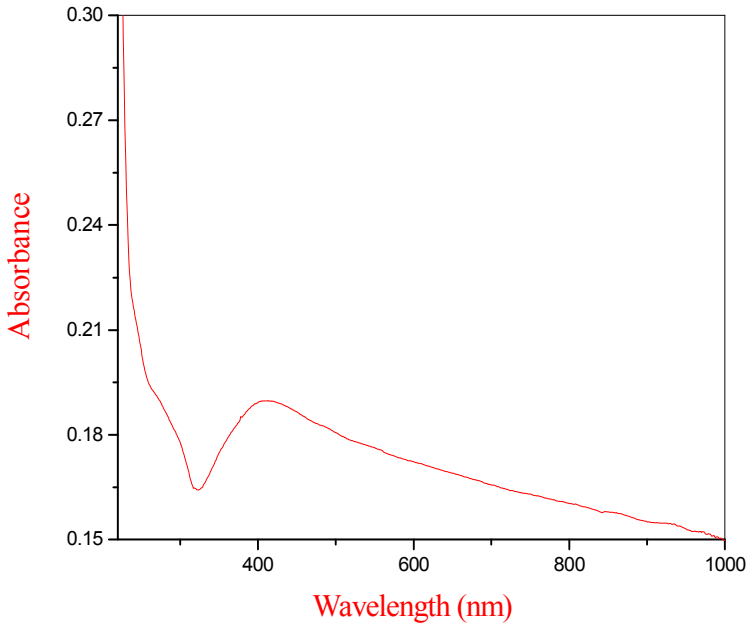

Figure 10. UV-VIS spectrum of EG-Ag showing the plasmon band around 410 nm.

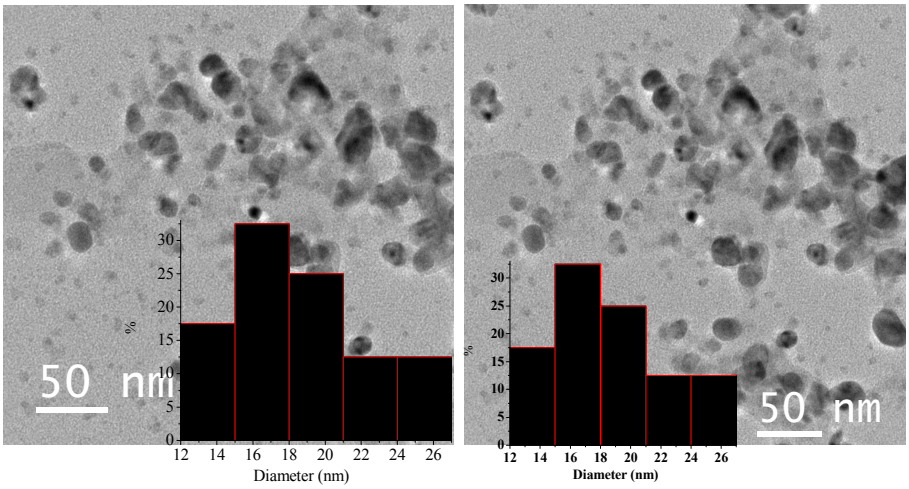

Figure 11. TEM images of EG-Ag (~17 nm). Insets show the histogram of the diameters of Ag nanoparticles.

In Figures 12 and 13 we show typical FESEM and TEM images of graphene decorated with

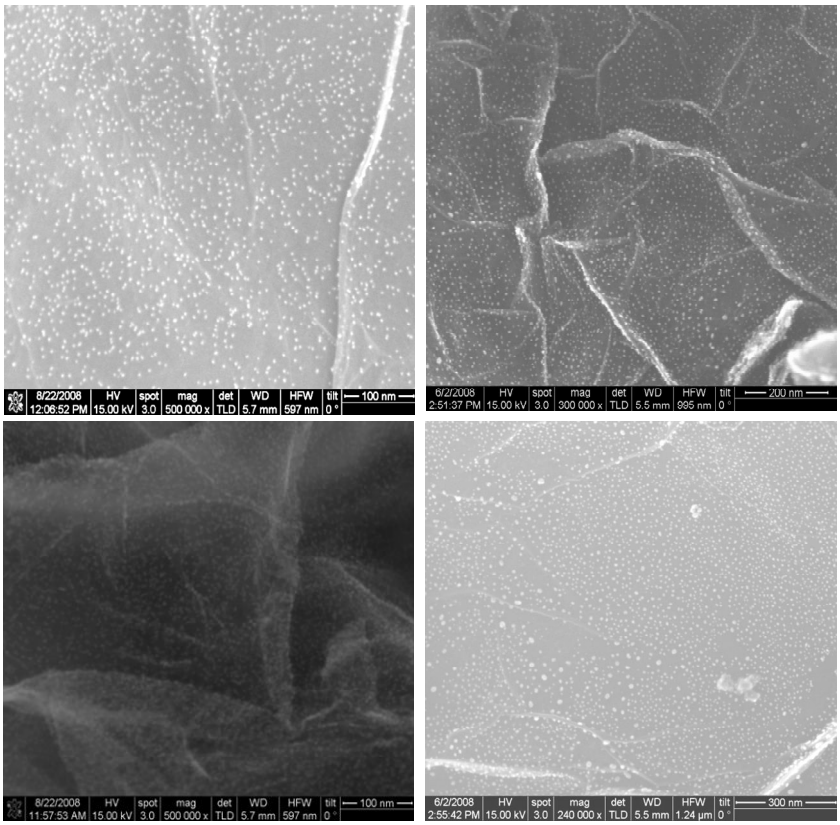

Figure 12. FESEM images of EG-Pt.

Pt respectively. From both FESEM and TEM it is clear that Pt nanoparticles well decorated uniformly on the graphene surface. Histogram analysis show that the size of nanoparticles in the range of 7-12 nm.

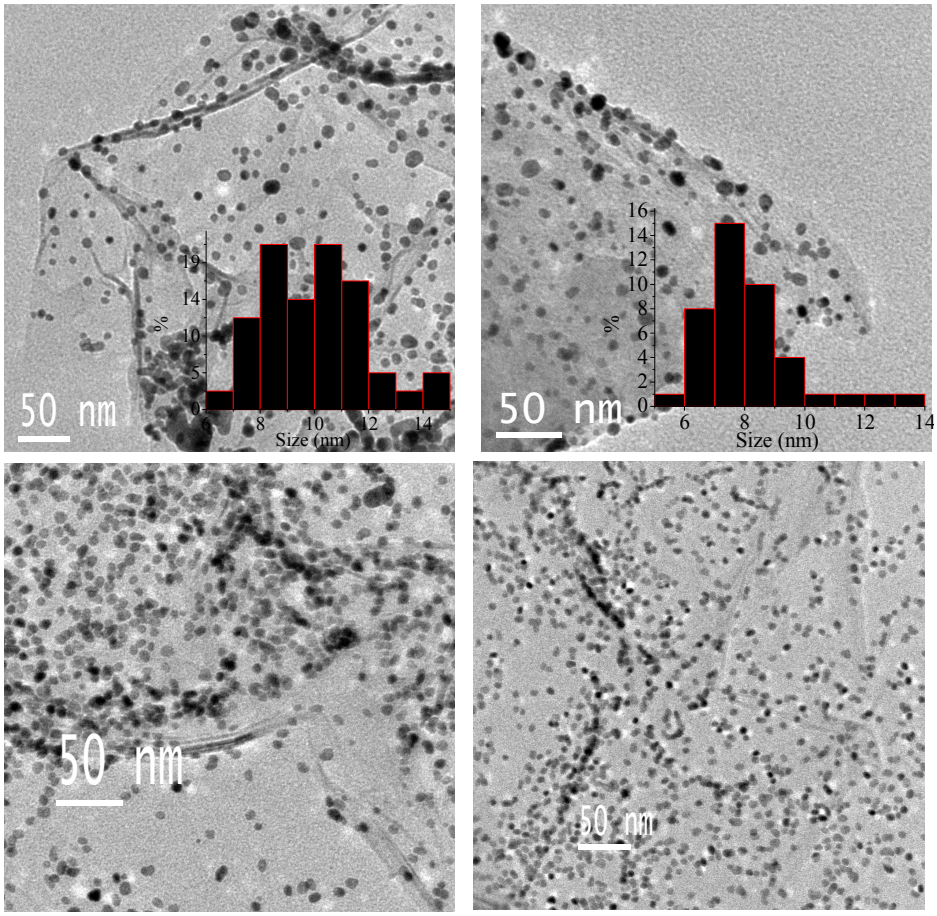

Figure 13. TEM images of EG-Pt. Insets show the histogram of the diameters of Pt nanoparticles.

Figure 14 shows TEM images of Pd decorated graphene (EG-Pd). Histogram analysis showed that the diameter of Pd nanoparticles was in the 7-12 nm range. The TEM images of the graphene-metal nanoparticle composites clearly demonstrate that the graphene sheets are covered by the metal nanoparticles fairly uniformly.

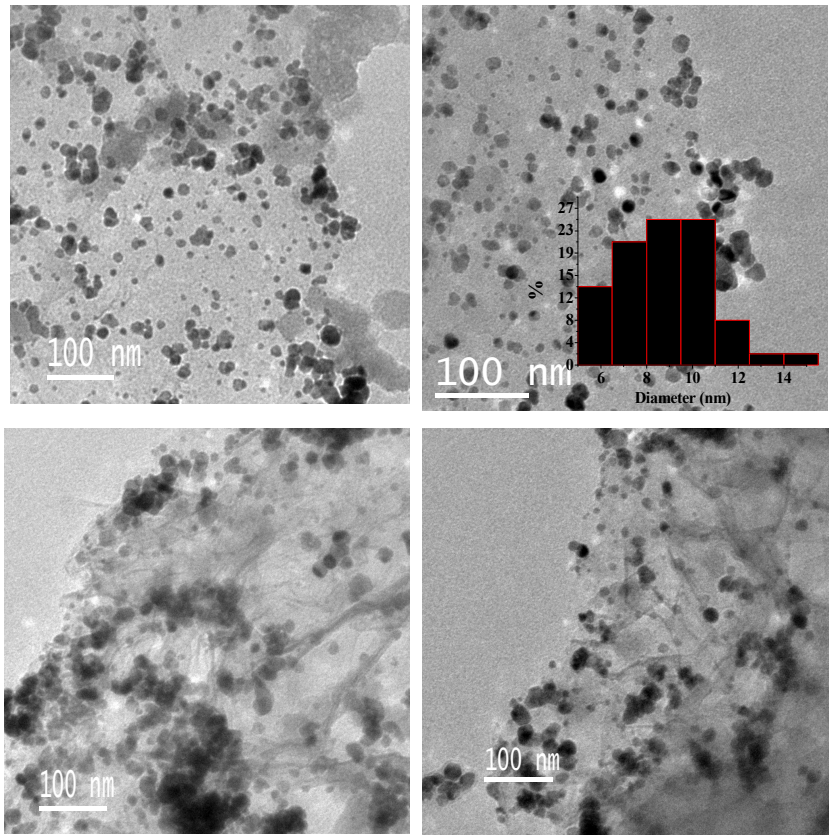

Figure 14. TEM images of EG-Pd. Inset shows the histogram of the diameters of Pd nanoparticles.

We have examined the Raman spectra of the graphene-metal nanoparticle composites by recording the spectra at different locations. The Raman spectrum of graphene exhibits the characteristic D-band (1320 cm^{-1}), G-band (1570 cm^{-1}), D'- band (1620 cm^{-1}) and 2D-band (2635 cm^{-1}).[61] The D and D'-bands are defect-induced features and are absent in defect-free samples. The G-band corresponds to the E_{2g} mode of graphite and arises from the vibration of sp^2 bonded carbon atoms. The 2D band originates from second order double resonant Raman scattering and varies with the number of layers. The intensity of the 2D band is sensitive to doping of graphene by holes or electrons. In Figure 15, we show typical Raman spectra of EG and the EG-metal nanoparticle composites and list typical data in Table 1.

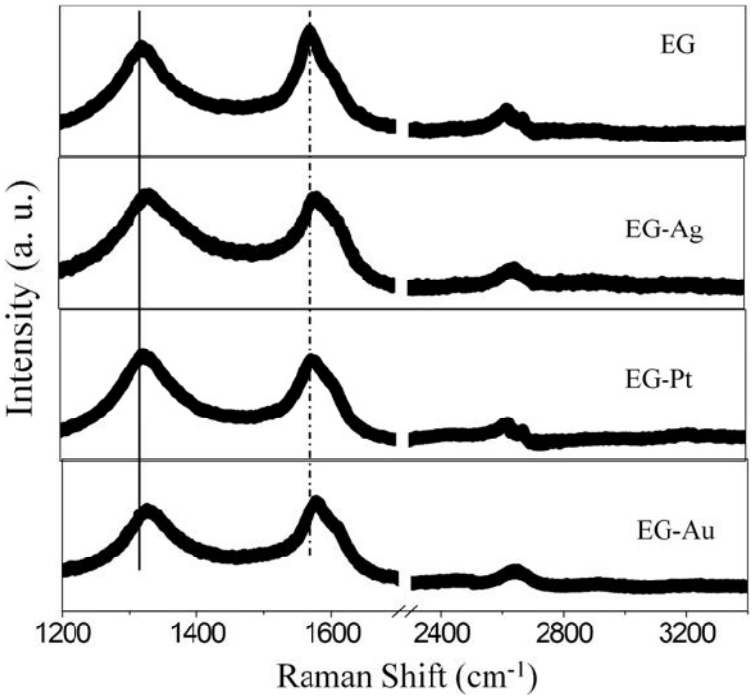

Figure15. Raman spectra of EG, EG-Ag, EG-Pt and EG-Au.

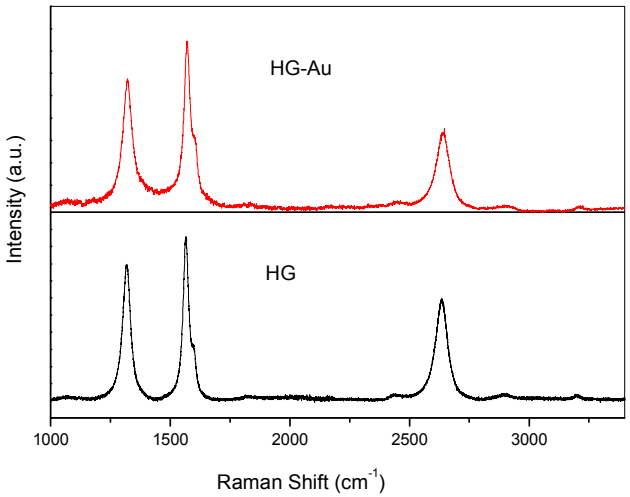

Figure16. Raman spectra of HG and HG-Au.

Table 1. Raman data of EG, EG-Ag, EG-Au, and EG-Pt

	EG [(a)]	EG-Ag	EG-Au [(a)]	EG-Pt
Average diameter of the nanoparticles (nm)	-	4	14	10
D (cm^{-1})	1323	1329	1325	1324
G (cm^{-1})	1571	1577	1574	1574
2D (cm^{-1})	2635	2638	2640	2636
FWHM of G-band (cm^{-1})	32	50	50	46

(a) HG gave D, G and 2D bands at 1319, 1567 and 2636 cm^{-1} respectively while HG-Au (~ 25 nm) gave these bands at 1321, 1571 and 2643 cm^{-1} respectively.

We shall first discuss the effect of silver nanoparticles on the spectrum of EG. On depositing Ag nanoparticles of 4 nm diameter on EG, we see stiffening of the G-band with an increase in frequency of nearly 6 cm^{-1}. The D band also gets shifted to higher frequency by 6 cm^{-1} and the intensity of the D band relative to that of the G band increases by 25%. The intensity of the 2D band relative to that of G band, however, decreases. The decrease in the intensity of 2D band of EG can thus be taken to reflect electronic interaction between the Ag nanoparticles and the graphene. Furthermore, on interaction with the Ag nanoparticles the full-width at half-maximum (FWHM) increases by 21 % in the case of D-band and by 56% in the case of G-band. The FWHM of the 2D band increases by about 10 %. We have also carried out Raman measurements on EG-Ag nanocomposite with Ag nanoparticles of an average diameter of 17 nm particles and found the magnitude of the shifts of Raman bands to be comparable to those of the EG-Ag nanocomposite formed with 4 nm particles.

Raman spectra of the EG-Au nanoparticle composite show effects similar to those of the EG-Ag nanocomposite. Thus, we observe stiffening of both the D- and G-bands though to a smaller extent than in the case of Ag nanoparticles. The increase in frequencies of the D- and G- bands are 3 and 2 cm^{-1} respectively. The intensity of D band relative to that of the G band increases to a smaller extent (7 %) than in case of Ag nanoparticles, and relative intensity of 2D band with respect to the G-band decreases to the same extent. The Raman spectrum of the HG-Au nanocomposite shows similar changes although the magnitudes vary (See Table 1).

Raman spectra of the EG-Pd and EG-Pt nanocomposites exhibit changes similar to EG-Ag and EG-Au with stiffening of Raman bands, increase in the FWHM of the bands as well variation in the relative intensities of the D and 2D bands. Comparing the changes in the Raman spectra of EG caused by the different metal nanoparticles, we find that the effects of Ag and Pd nanoparticles on the G and D bands are similar in that the magnitude of changes is large. Pt and Au nanoparticles, on the other hand, cause smaller changes. Such differences may be related to the intrinsic properties of the metal nanoparticles. We have, therefore, tried to relate the changes in the Raman spectrum of EG to the ionization energy of the metal. In Figure 17 we have plotted the frequency shifts of the G band of EG against the ionization energy (IE) of the metal. Note that the ionization energy varies as Ag<Pd<Pt<Au, the values for Ag and Au being 7.5 and 9.2 eV respectively. Interestingly, the magnitude of the band shifts generally decreases with increase in ionization energy of the metal. The position and FWHM of the D band also show a similar trend. The shift in the 2D band does not show any definitive trend just as in the case of electrochemical or chemical doping. The variation in the G band is better described as follows. In a given group, the shift decreases on going down the group. Thus, the shifts vary as Pd > Pt and Ag > Au, in the same manner as the IEs.

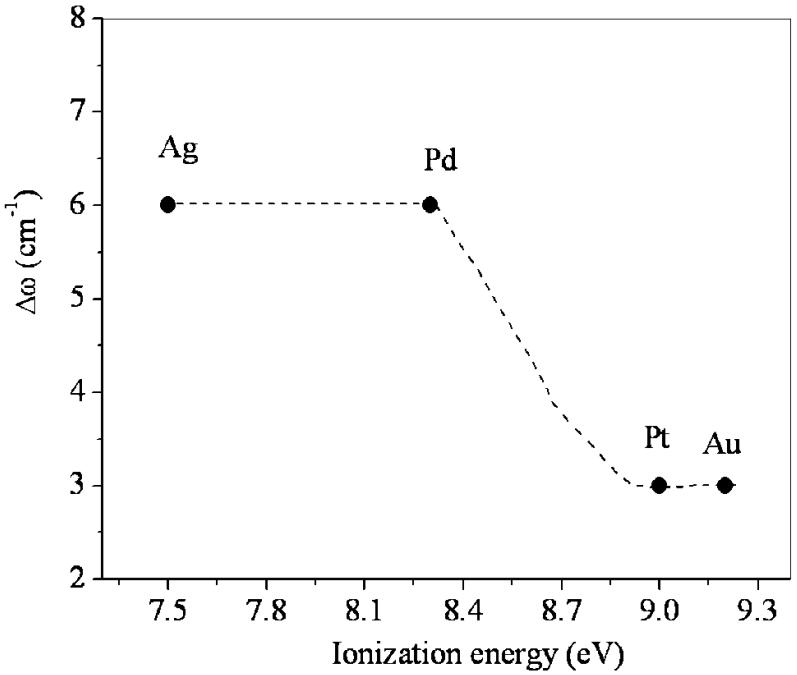

Figure 17. Variation in the position of the G-band with the ionization energy of the metal. The broken curves given as a guide to the eye.

Prof. Pati and co-workers have investigated the energetics as well as the changes in structural and electronic properties of graphene on deposition of metal nanoclusters of Pd, Ag, Pt and Au using first-principles density functional theory (DFT) calculations. The calculations were carried out using the linear combination of atomic orbital density-functional theory (DFT) methods as implemented in the SIESTA package.[62] A supercell (8 × 8 × 1) containing 128 carbon atoms is used for the electronic structure calculations and considered the two dimensional arrays of metal clusters deposited on graphene (Figure 18). The relative stability of the metal nanoclusters embedded on graphene surface (i.e., graphene@M_{40}) is determined by the stabilization energies (ΔE_{stab}) or the binding energy. The larger the stabilization energy, stronger is the binding of the dopant cluster to the graphene surface.

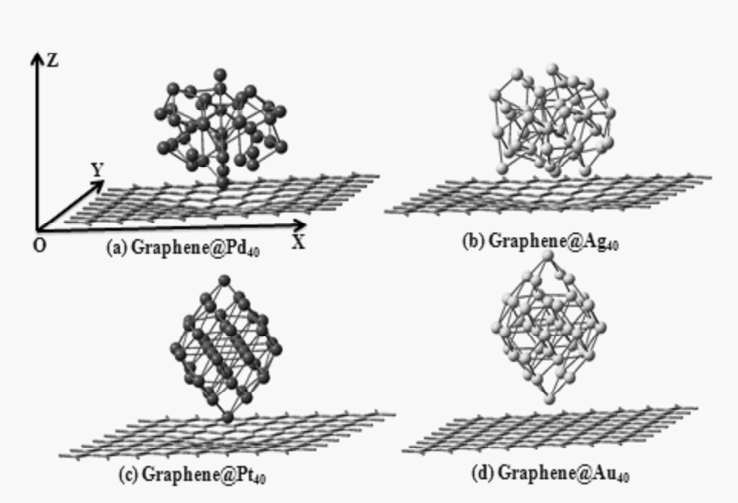

Figure 18. Optimized geometries of four metal nanoclusters deposited on graphene surface.

From the fully optimized geometries, it was find that the relative stabilization energies are higher in magnitude for Pd, Ag, Pt clusters embedded graphene complexes compared to the Au cluster indicating a relatively weak interaction between the Au nanoparticles and the graphene compared to others. An analysis of the Mülliken population suggested that there is an effective charge transfer between the adsorbed metal cluster and graphene. For the Pd, Ag, and Pt clusters, charge transfer occurs from graphene to the metal cluster while for the Au nanoclusters the direction of charge transfer is from the metal cluster to graphene. The extent of charge transfer for Pd, Ag and Pt nanoclusters is larger than that for the Au cluster, with the largest charge transfer in the case of Pd. The stabilization energies found in the present study followed the same trend as IE or EA of the metal clusters belonging to a particular period in the periodic table. The comparatively smaller magnitude of EA and IE make the Au cluster to act as weak electron donor towards graphene. The interaction energy is found to change inversely with the distance between metal cluster and graphene, clearly predicting

that such interactions are mainly due to Coulombic forces as already observed for SWNTs interacting with Pt and Au nanoclusters and for electron donor/acceptor adsorbed on SWNTs.

7.5Conclusions

The G, D and 2D bands in the Raman spectrum of graphenes have been effectively employed to examine the dependence of the interaction of electron donor and acceptor molecules on the graphene surface. Among the three graphene samples, the one with highest surface area is obtained by the exfoliation of graphite oxide (EG), the lowest surface area being found in the sample obtained by the arc evaporation of graphite in a hydrogen atmosphere (HG). The changes in the Raman spectra and hence the magnitude of the charge-transfer interaction are found to be highest in the case of EG and least in the case of HG. The present study shows the importance of the graphene surface in determining doping effects through molecular charge-transfer.

The study on the interaction of Ag, Pd, Au and Pt nanoparticles with graphene demonstrates that there is significant electronic interaction between them giving rise to changes in the Raman spectrum of graphene. First-principles calculations support the conclusions from the Raman study and demonstrate the importance of charge-transfer between the metal particles and graphene. The charge-transfer itself is related to the ionization energy and electron affinity of the metal particles.

5.6 References

[1] A. K. Geim, K. S. Novoselov, *Nat. Mater.* **2007**, *6*, 183.

[2] A. K. Geim, *Science* **2009**, *324*, 1530.

[3] S. Y. Zhou, G. H. Gweon, A. V. Fedorov, P. N. First, W. A. de Heer, D. H. Lee, F. Guinea, A. H. Castro Neto, A. Lanzara, *Nat. Mater.* **2007**, *6*, 770.

[4] T. O. Wehling, K. S. Novoselov, S. V. Morozov, E. E. Vdovin, M. I. Katsnelson, A. K. Geim, A. I. Lichtenstein, *Nano Lett.* **2007**, *8*, 173.

[5] A. Das, A. K. Sood, A. Govindaraj, A. M. Saitta, M. Lazzeri, F. Mauri, C. N. R. Rao, *Phys. Rev. Lett.* **2007**, *99*, 136803.

[6] M. Cha, S. Jung, M.-H. Cha, G. Kim, J. Ihm, J. Lee, *Nano Lett.* **2009**, *9*, 1345.

[7] K. K. Kim, J. J. Bae, H. K. Park, S. M. Kim, H.-Z. Geng, K. A. Park, H.-J. Shin, S.-M. Yoon, A. Benayad, J.-Y. Choi, Y. H. Lee, *J. Am. Chem. Soc.* **2008**, *130*, 12757.

[8] C. Ehli, C. Oelsner, D. M. Guldi, A. Mateo-Alonso, M. Prato, C. Schmidt, C. Backes, F. Hauke, A. Hirsch, *Nat. Chem.* **2009**, *1*, 243.

[9] A. M. Rao, P. C. Eklund, S. Bandow, A. Thess, R. E. Smalley, *Nature* **1997**, *388*, 257.

[10] J. Chen, M. A. Hamon, H. Hu, Y. Cheng, A. M. Rao, P. C. Eklund, R. C. Haddon, *Science* **1998**, *282*, 95.

[11] G. M. do Nascimento, T. Hou, Y. A. Kim, H. Muramatsu, T. Hayashi, M. Endo, N. Akuzawa, M. S. Dresselhaus, *Nano Lett.* **2008**, *8*, 4168.

[12] G. M. do Nascimento, T. Hou, Y. A. Kim, H. Muramatsu, T. Hayashi, M. Endo, N. Akuzawa, M. S. Dresselhaus, *J. Phys. Chem. C* **2009**, *113*, 3934.

[13] M. Shim, A. Javey, N. W. Shi Kam, H. Dai, *J. Am. Chem. Soc.* **2001**, *123*, 11512.

[14] J. Kong, N. R. Franklin, C. Zhou, M. G. Chapline, S. Peng, K. Cho, H. Dai, *Science* **2000**, *287*, 622.

[15] T. Takenobu, T. Kanbara, N. Akima, T. Takahashi, M. Shiraishi, K. Tsukagoshi, H. Kataura, Y. Aoyagi, Y. Iwasa, *Adv. Mater.* **2005**, *17*, 2430.

[16] A. Star, T.-R. Han, J.-C. P. Gabriel, K. Bradley, G. Gruner, *Nano Lett.* **2003**, *3*, 1421.

[17] D. S. Hecht, R. J. A. Ramirez, M. Briman, E. Artukovic, K. S. Chichak, J. F. Stoddart, G. Gruner, *Nano Lett.* **2006**, *6*, 2031.

[18] R. Voggu, C. S. Rout, A. D. Franklin, T. S. Fisher, C. N. R. Rao, *J. Phys. Chem. C* **2008**, *112*, 13053.

[19] R. Voggu, S. Pal, S. K. Pati, C. N. R. Rao, *J. Phys. Condens. Matter* **2008**, *20*, 083202

[20] M. S. Raghuveer, S. Agrawal, N. Bishop, G. Ramanath, *Chem. Mater.* **2006**, *18*, 1390.

[21] R. Voggu, P. Suguna, S. Chandrasekaran, C. N. R. Rao, *Chem. Phys. Lett.* **2007**, *443*, 118.

[22] K. S. Novoselov, A. K. Geim, S. V. Morozov, D. Jiang, Y. Zhang, S. V. Dubonos, I. V. Grigorieva, A. A. Firsov, *Science* **2004**, *306*, 666.

[23] A. K. Geim, K. S. Novoselov, *Nat. Mater.* **2007**, *6*, 183.

[24] A. C. Ferrari, J. C. Meyer, V. Scardaci, C. Casiraghi, M. Lazzeri, F. Mauri, S. Piscanec, D. Jiang, K. S. Novoselov, S. Roth, A. K. Geim, *Phys. Rev. Lett.* **2006**, *97*, 187401.

[25] A. Gupta, G. Chen, P. Joshi, S. Tadigadapa, Eklund, *Nano Lett.* **2006**, *6*, 2667.

[26] A. Das, S. Pisana, B. Chakraborty, S. Piscanec, S. K. Saha, U. V. Waghmare, K. S. Novoselov, H. R. Krishnamurthy, A. K. Geim, A. C. Ferrari, A. K. Sood, *Nat. Nanotechnol.* **2008**, *3*, 210.

[27] A. Das, B. Chakraborty, S. Piscanec, S. Pisana, A. K. Sood, A. C. Ferrari, *Phys. Rev. B* **2009**, *79*, 155417.

[28] L. M. Malard, D. C. Elias, E. S. Alves, M. A. Pimenta, *Phys. Rev. Lett.* **2008**, *101*, 257401.

[29] A. B. Kuzmenko, L. Benfatto, E. Cappelluti, I. Crassee, D. van der Marel, P. Blake, K. S. Novoselov, A. K. Geim, *Phys. Rev. Lett.* **2009**, *103*, 116804.

[30] C. Lee, X. Wei, J. W. Kysar, J. Hone, *Science* **2008**, *321*, 385.

[31] X. Wang, X. Li, L. Zhang, Y. Yoon, P. K. Weber, H. Wang, J. Guo, H. Dai, *Science* **2009**, *324*, 768.

[32] F. Schedin, A. K. Geim, S. V. Morozov, E. W. Hill, P. Blake, M. I. Katsnelson, K. S. Novoselov, *Nat. Mater.* **2007**, *6*, 652.

[33] A. Ghosh, K. V. Rao, S. J. George, C. N. R. Rao, *Chem. Eur. J.* **2010**, *16*, 2700.

[34] J. Kim, L. J. Cote, F. Kim, J. Huang, *J. Am. Chem. Soc.* **2009**, *132*, 260.

[35] L. Xie, X. Ling, Y. Fang, J. Zhang, Z. Liu, *J. Am. Chem. Soc.* **2009**, *131*, 9890.

[36] D. C. Elias, R. R. Nair, T. M. G. Mohiuddin, S. V. Morozov, P. Blake, M. P. Halsall, A. C. Ferrari, D. W. Boukhvalov, M. I. Katsnelson, A. K. Geim, K. S. Novoselov, *Science* **2009**, *323*, 610.

[37] T. Ohta, A. Bostwick, T. Seyller, K. Horn, E. Rotenberg, *Science* **2006**, *313*, 951.

[38] E. V. Castro, K. S. Novoselov, S. V. Morozov, N. M. R. Peres, J. M. B. Lopes dos Santos, J. Nilsson, F. Guinea, A. K. Geim, A. H. Castro Neto, *Phys. Rev. Lett.* **2007**, *99*, 216802.

[39] J. B. Oostinga, H. B. Heersche, X. Liu, A. F. Morpurgo, L. M. K. Vandersypen, *Nat. Mater.* **2008**, *7*, 151.

[40] Y. Zhang, T. T. Tang, C. Girit, Z. Hao, M. C. Martin, A. Zettl, M. F. Crommie, Y. R. Shen, F. Wang, *Nature* **2009**, *459*, 820.

[41] K. F. Mak, C. H. Lui, J. Shan, T. F. Heinz, *Phys. Rev. Lett.* **2009**, *102*, 4.

[42] H. Min, B. R. Sahu, S. K. Banerjee, A. H. MacDonald, *Phys. Rev. B* **2007**, *75*, 155115.

[43] X. Peng, R. Ahuja, *Nano Lett.* **2008**, *8*, 4464.

[44] S. Y. Zhou, G. H. Gweon, A. V. Fedorov, P. N. First, W. A. De Heer, D. H. Lee, F. Guinea, A. H. C. Neto, A. Lanzara, *Nat. Mater.* **2007**, *6*, 770.

[45] G. Giovannetti, P. A. Khomyakov, B. G, P. J. Kelly, J. van den Brink, *Phys. Rev. B* **2007**, *76*, 73103.

[46] B. C. Satishkumar, et al., *J. Phys. D Appl. Phys.* **1996**, *29*, 3173.

[47] V. Georgakilas, D. Gournis, V. Tzitzios, L. Pasquato, D. M. Guldi, M. Prato, *J. Mater. Chem.* **2007**, *17*, 2679.

[48] H. J. Shin, S. M. Kim, S. M. Yoon, A. Benayad, K. K. Kim, S. J. Kim, H. K. Park, J. Y. Choi, Y. H. Lee, *J. Am. Chem. Soc.* **2008**, *130*, 2062.

[49] B. Das, R. Voggu, C. S. Rout, C. N. R. Rao, *Chem. Commun.* **2008**, *41*, 5155.

[50] R. Voggu, B. Das, C. S. Rout, C. N. R. Rao, *J. Phys.: Condens. Matter* **2008**, *20*, 472204.

[51] N. Varghese, A. Ghosh, R. Voggu, S. Ghosh, C. N. R. Rao, *J. Phys. Chem. C* **2009**, *113*, 16855.

[52] R. Muszynski, B. Seger, P. V. Kamat, *J. Phys. Chem. C* **2008**, *112*, 5263.

[53] R. M. S, A. S., B. N., G. Ramanath, *Chem. Mater.* **2006**, *18*, 1390.

[54] P. V. Kamat, *J. Phys. Chem. Lett.* **2009**, *1*, 520.

[55] K. Jasuja, V. Berry, *ACS Nano* **2009**, *3*, 2358.

[56] L. Lu, I. Randjelovic, R. Capek, N. Gaponik, J. Yang, H. Zhang, A. Eychmuller, *Chem. Mater.* **2005**, *17*, 5731.

[57] H. M. A. Hassan, V. Abdelsayed, A. E. R. S. Khder, K. M. AbouZeid, J. Terner, M. S. El-Shall, S. I. Al-Resayes, A. A. El-Azhary, *J. Mater. Chem.* **2009**, *19*, 3832.

[58] J. Li, C.-y. Liu, *Eur. J. of Inorg. Chem. 2010*, 1244.

[59] E. Yoo, T. Okata, T. Akita, M. Kohyama, J. Nakamura, I. Honma, *Nano Lett.* **2009**, *9*, 2255.

[60] S. Link, M. A. El-Sayed, *J. Phys. Chem. B* **1999**, *103*, 4212.

[61] M. A. Pimenta, G. Dresselhaus, M. S. Dresselhaus, L. G. Cancado, A. Jorio, R. Saito, *Phys. Chem. Chem. Phys.* **2007**, *9*, 1276.

[62] J. M. Soler, E. Artacho, J. D. Gale, A. Garcia, J. Junquera, P. Ordejon, D. Sanchez-Portal, *J. Phys. : Condens. Matter* **2002**, *14*, 2745.

CHAPTER 6

BORON AND NITROGEN DOPING OF GRAPHENE

Summary*

Two-dimensional graphene exhibits fascinating electronic properties as exemplified by ballistic electronic conduction and occurrence of quantum Hall effect at room temperature. Graphene can be doped electrochemically and through molecular charge-transfer, both causes marked changes in the Raman spectrum. Clearly, it showed of great importance to dope graphene substituting by boron and nitrogen. We have now found way to prepare doped graphene. Boron-doped graphenes (1-3 at%) prepared by carrying out arc discharge of graphite in an atmosphere of H_2+B_2H_6 and by arc discharge of boron-stuffed graphite electrodes. Nitrogen-doped graphenes (0.6-1 at%) have been prepared by arc discharge of graphite in the presence of H_2+pyridine or NH_3 and also by the transformation of nanodiamond in the presence of NH_3 (or) pyridine. The graphene samples generally had 2-3 layers estimated by atomic force microscopy and transmission electron microscopy. The B- and N-doping in graphenes causes a stiffening of the G-band in the Raman spectra and intensification of the defect related D-band. The stiffening of the G-band depends on the extent of doping.

*A paper based on this work has been published in *Adv. Mater. (2009).*

6.1 Introduction

Tuning physicochemical properties by chemical modification of materials becomes necessary in many applications.[1] One way of achieving this control is by elemental doping, a method effectively used in semiconductor silicon technology.[2, 3] For example, nitrogen atoms in silicon lock dislocations to increase mechanical strength. Effects of doping silicon with phosphorous and other elements with different oxidation states have been well documented. Chemical substitution brings about significant changes in carbon materials as well. In particular, substitution of boron or nitrogen in carbon nanostructures renders them p-type or n-type respectively. Besides the electronic structure, doping affects the Raman spectra and other properties of carbon nanostructures.[1]

Different routes have been reported to dope carbon nanotubes (CNTs). In as early as 1997, substitution of carbon by nitrogen in multi-walled carbon nanotubes (MWNTs) was achieved by the pyrolysis of aza-aromatics (pyridine, triazine).[4] The nitrogen content decreased with increasing temperature of pyrolysis, the estimated nitrogen content being around 5, 3.5, and 3 at.% in nanotubes prepared by the pyrolysis of pyridine at 973, 1123 and 1273 K respectively. Good yields of N-doped MWNTs are obtained by carrying the pyrolysis of a mixture of pyridine and $Fe(CO)_5$ in flowing $Ar+H_2$.[4] In this procedure, the iron particles formed by the decomposition of $Fe(CO)_5$ act as nucleating centres for the growth of carbon nanotubes. N-doped MWNTs were also be prepared by pyrolyzing pyridine over Co powder at 1000 ^oC.[5] Pyrolysis of the organic precursors in the presence of pyridine yields bundles of aligned N-MWNTs. The nitrogen content depends upon the catalyst and the nitrogen content is greater with an iron catalyst rather than a cobalt catalyst.[6] 3 at.% of N in MWNTs has been achieved by this procedure.

Pyrolysis of ferrocene-melamine mixtures at 900-1000 ^{o}C in the presence of Ar produces large arrays of aligned CN_x nanotubes.[7] Incorporation of 2-10 at.% N in MWNTs is achieved by this procedure. The electronic density of states (DOS) of CN_x nanotubes obtained from scanning tunneling spectroscopy (STS) exhibits strong features in the band close to the Fermi level (0.18 eV). Based on tight-binding and ab initio calculations, it is found that pyridine-like N is responsible for introducing donor states close to the Fermi Level.

Boron-doped MWNTs are prepared by the pyrolysis of acetylene–diborane mixtures in a stream of helium and hydrogen.[8] The composition obtained by this procedure is $C_{35}B$. B-CNTs can also be prepared by arc discharge between boron stuffed graphite electrodes.[9] In this method, doping of 1 at.% boron could be achieved. MWNTs with Y-junctions were prepared some time ago by the pyrolysis of nickelocene along with thiophene.[10] N-doped MWNTs (2 at.% N) with Y-junctions have been prepared by the pyrolysis a nickel phthalocyanine–thiophene mixture as well.[11] Tunneling conductance measurements reveal rectifying behavior with regions of Coulomb blockade, the effect being much larger in the N-doped junction nanotubes. CN_x-CNT intramolecular junctions have been produced via chemical vapour deposition with ferrocene and melamine.[12]

N-doped single-walled carbon nanotubes (N-SWNTs) have been prepared by the arc-discharge method by introducing a nitrogen-rich precursor into the anode along with the catalyst and graphite.[13] The nitrogen source is melamine or boron nitride. Up to 1 at.% of nitrogen has been incorporated in SWNTs by this method. Arc-discharge between BN-stuffed graphite electrodes yields 1 at.% of nitrogen in SWNTs but no boron incorporation. The nanotubes so obtained are long. N-SWNTs have also been prepared by chemical vapour deposition of xylene and acetonitrile over catalyst-coated substrates.[14]

Nitrogen concentration in the nanotubes could be varied (2-6 at. %) by changing the concentration of acetonitrile in the feed.

Long strands of nitrogen-doped SWNTs (< 2 at.% N) have been prepared by the thermal decomposition of ferrocene+ethanol+benzylamine (FEB) solutions in an Ar atmosphere at 950 ^{o}C.[15] When the amount of nitrogen present in the starting FEB solution is increased, the formation of large diameter tubes is inhibited. This can be correlated with a study of Choi *et al*.[16] where they report that N-doped (substitutional) inner layers in double-walled nanotubes become more stable as the inner wall is more heavily doped. Water plasma chemical vapor deposition of methane and ammonia is employed to prepare N-SWNTs on SiO_2/Si substrates.[17] Up to 4 at.% nitrogen can be incorporated in SWNTs by this means. SWNTs obtained by this route are small in diameter and are semiconducting in nature. The density of nanotubes formed monotonically decreases with the increase in ammonia content. N-SWNTs are not formed under high doses of ammonia.

N-SWNTs with a defined diameter range can be prepared by chemical decomposition of a 100% benzylamine vapour using ceramic supported bimetallic catalysts (Mo, Fe).[18] A maximum nitrogen content of 2 at.% is obtained by this procedure. The amount of nitrogen incorporated in the nanotubes varies with the temperature employed. SWNTs of up to 15 at.% boron doping are obtained by a substitution reaction. A mixture of B_2O_3 and SWNTs is heated in an NH_3 atmosphere to achieve high doping.[19, 20] Laser vaporization of NiB loaded graphite yields B-SWNTs with boron concentration up to 1.8 at.%.[21] Substitutional boron in a carbon lattice represents an electron-deficient atom, rendering the B-SWNTs p-type in character. Low boron doping (less than 1 at.%) of SWNTs is achieved by the CVD method using tri-isopropyl borate ($C_9H_{21}BO_3$) vapour as the boron as well as the carbon source.[22] Boron

doped SWNTs (up to 10 at.% B) can be prepared by thermal treatment of B_2O_3 and SWNTs at 1600 K in nitrogen flow.[23] N-doped DWNTs are synthesized by chemical vapor deposition of methane and ammonia over the bi-metallic catalyst, $Mo_{0.1}Fe_{0.9}Mg_{13}O$.[24, 25] Decomposition of methane along with pyridine over this catalyst yields nitrogen- doped DWNTs (~ 1 at.%).[26] This method can be used to prepare 1 at.% boron-doped DWNTs using diborane as the boron source.[24] In this chapter we discuss different synthetic routes to prepare boron and nitrogen doped graphenes.

6.2 Scope of the present investigations

N- doped MWNTs exhibit interesting electrical transport properties. Tunneling conductance measurements of these materials have been reported.[5] The conductance of N- doped MWNTs is generally higher than that of undoped ones. The gap estimated from the normalized conductance is smaller in the N- doped MWNTs. Some properties of B- and N-doped MWNTs have been reported. Thus, N-doped MWNTs exhibit excellent electron emission behaviour.[27] The emission efficiency is enhanced by incorporating a larger nitrogen concentration at the nanotube tip, due to the occurrence of a peak in the electronic structure near the Fermi-level. B-doped MWNTs are metallic.[28] There is a closing of the apparent band gap in doped nanotubes and development of a prominent acceptor-like feature on the valence band side close to the Fermi level. This acceptor-like feature results from nanodomains of BC_3 within the nanotube lattice. Field electron (FE) emission properties of boron- and nitrogen- doped carbon nanotubes grown in-situ on tungsten tips and silicon substrates have been studied.[29] For a total emission current of 1 μA, the current density (J) is 4 A/cm^2 at 368 V/μm for B-doped CNTs and at 320 V/μm for N-doped MWNTs grown on W tips, compared with the value of 1.5 A/cm^2 at 290 V/μm for undoped MWNTs. FE currents upto 400 μA drawn from both B- and N-doped MWNTs are stable for more than 3 hours.

Lithium metal has proved to be important in the fabrication of lightweight and energy-efficient batteries. Electrochemical Li insertion into B-doped MWNTs has been investigated in a non-aqueous medium.[30] The reversible capacity observed is 156 mAh/g for undoped and 180 mAh/g for B-doped MWNTs in the first cycle with almost equal Coulomb efficiencies of 55-58%. The Coulomb efficiency increased to more than 90% after the second cycle.

Villalpando-PGez *et al*.[31] designed a NH_3-sensitive device utilizing nitrogen-doped MWNTs. This sensor exhibits response times of the order of a few tenths of a second and reaches a steady state value in 2–3 s. A strong, reversible response to ethanol has been found with vertically aligned nitrogen-doped MWNTs that showed a response time of less than one second. CN_x nanotubes could, therefore, be more efficient in detecting hazardous gaseous species because of the presence of pyridine-type sites on their surface. Theoretical[32] and experimental[33] studies suggest no charge transfer between CO and pure MWNTs. However, calculations suggest the possibility of using doped MWNTs for sensing purposes.[32] N- MWNTs appear to be less toxic than pure MWNTs.[34]

Meissner effect has been found in thin films of B-doped SWNTs.[35] A low boron concentration and a highly homogeneous ensemble of B-SWNTs films leads to Meissner effect with a T_c of 12 K. Ab initio calculations indicate that the work function for B-doped nanotubes to be 1.7 eV lower than compared to that of pure carbon-terminated nanotubes. B-doped nanotubes produced by arc-discharge techniques are found to contain B mainly at the tips and to exhibit stable electron field emission at lower turn-on voltages (1.4 V/μm) compared to undoped single- and multi-walled carbon nanotubes (2.8 and 3.0 V/μm, respectively).[36]

Doping of graphene through molecular charge-transfer caused by electron-donor and –acceptor molecules also gives rise to significant changes in the electronic structure of graphenes composed of a few layers, as evidenced by changes in the Raman and photoelectron spectra.[37, 38] Charge-transfer by donor and acceptor molecules soften and stiffen the G-band, respectively. The difference between electrochemical doping and doping through molecular charge-transfer is noteworthy. It is of fundamental interest to investigate how these effects compare with the effects of doping graphene by substitution with boron and nitrogen and to understand dopant-induced perturbations of the properties of graphene. Secondly, opening the bandgap in graphene is essential for facilitating its applications in electronics, and graphene bi- layers[39] are an attractive option for this. With this motivation, we prepared, for the first time, B- and N-doped graphene (BG and NG) bi- layer samples by employing different strategies and investigated their structure and properties. To prepare BGs and NGs, we employed our newly discovered technique to prepare graphene in which arc discharge between carbon electrodes in a hydrogen atmosphere yields graphenes (HG) composed of two to three layers. The method makes use of the fact that in the presence of hydrogen, graphene sheets do not readily roll into nanotubes. In the case of BG, we carried out the arc discharge using graphite electrodes in the presence H_2 + B_2H_6 (BG1) or using boron-stuffed graphite electrodes (BG2). We prepared NG by carrying out the arc discharge in the presence of H_2 + pyridine (NG1) or H_2 + ammonia (NG2). We also performed the transformation of nanodiamond in the presence of pyridine and ammonia to obtain nitrogen doped DG samples NG3 and NG4 respectively. All doped graphene samples were characterized by a variety of physical methods along with an undoped sample prepared by arc discharge in hydrogen (HG). To understand the effect of substitutional doping on the structure of graphene as well as its

electronic and vibrational properties first-principles density functional theory (DFT) calculations were carried out by Prof. Waghmare and co-workers.

6.3 Experimental section

Synthesis of Boron- and Nitrogen-Doped Graphene: BG1 was prepared by performing the arc discharge of graphite electrodes in the presence of hydrogen, helium, and diborane (B_2H_6). B_2H_6 vapor was generated by the addition of BF_3-diethyl etherate to sodium borohydride in tetraglyme. B_2H_6 vapor was carried to the arc chamber by flowing hydrogen (200 Torr) and subsequently He (500 Torr) through the B_2H_6 generator. BG2 was prepared by carrying out the arc discharge using boron-packed graphite electrodes (3 at.% B) in the presence of H_2 (200 Torr) and He (500 Torr). NG1 was prepared by performing the arc discharge of graphite electrodes in the presence of H_2, He, and pyridine vapor. Pyridine vapour was carried to the arc chamber by flowing hydrogen (200 Torr) and subsequently He (500 Torr) through a pyridine bubbler. NG2 was prepared by carrying out arc discharge of graphite electrodes in the presence of H_2 (200 Torr), He (200 Torr), and NH_3 (300 Torr). The transformation of nanodiamond was carried out in the presence of pyridine and NH_3 vapor at 1650 ºC to obtain NG3 and NG 4 respectively.

6.4 Results and discussion

In Figure 1a, we show the typical core-level X-ray photoelectron spectra (XPS) of BG1 and BG2 along with the elemental mapping from electron energy loss spectroscopy (EELS) of BG2 carried out on transmission electron microscope (TEM) images. The C 1s signal is at approximately 285 eV, while the B 1s peak is around 189 eV. The position of this feature indicates that boron is bonded to carbon in the sp^2 carbon network.[24] Based on the XPS data, we found that BG1 and BG2 contain 1.2 and 3.1 at.% of boron,

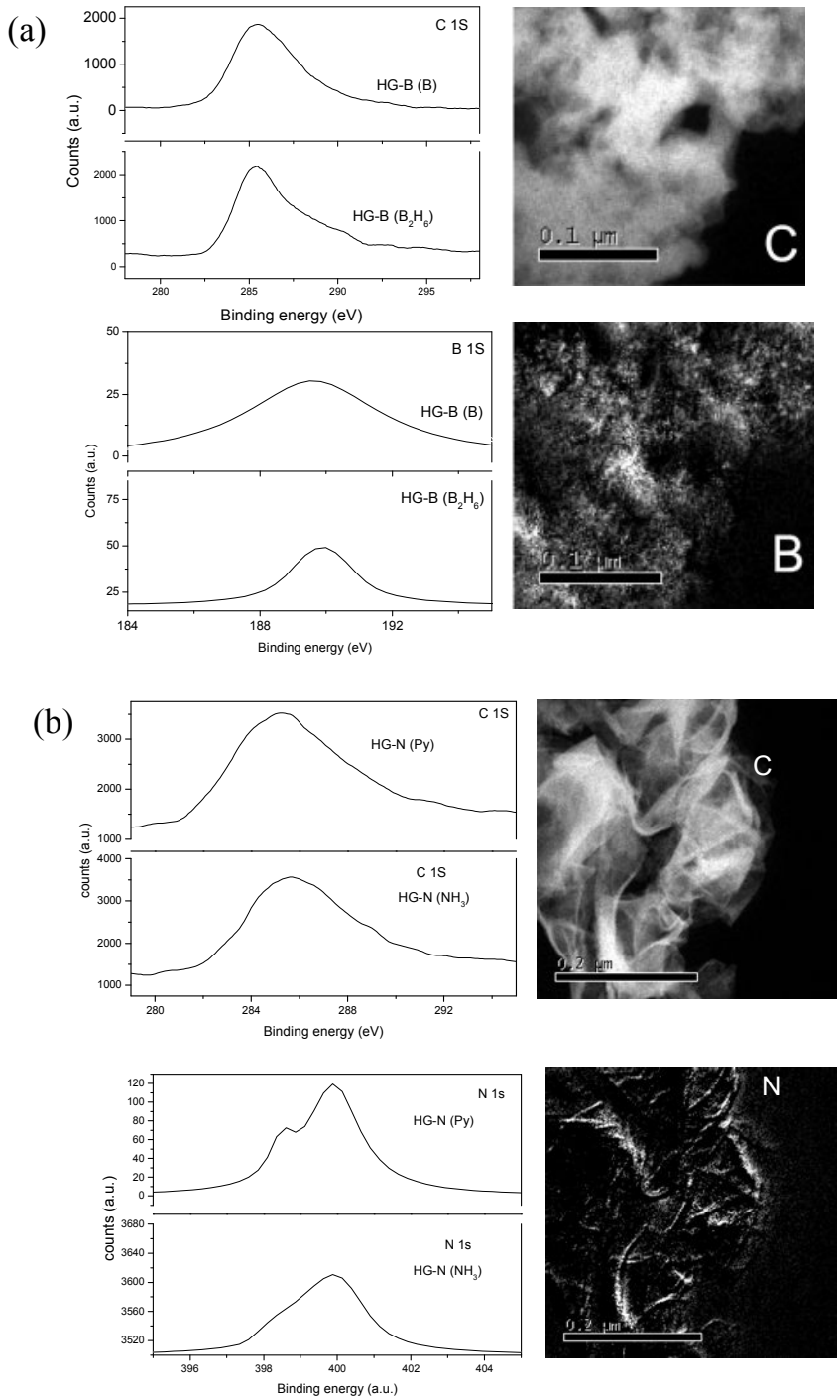

Figure 1. (a) C 1s and B 1s XPS signals of B-doped graphene (BG1 and BG2), EELS elemental mapping of C and B of BG2.(b) C 1s and N 1s XPS signals of N-doped graphene (NG1 and NG2), EELS elemental mapping of C and N of NG2.

respectively. EELS measurements performed on the graphene nanostructures in the electron microscope indicated the content of boron in these samples to be 1.0 and 2.4 at.%, respectively. In Figure 1b, we show the typical XPS data for the NG2 sample along with the EELS elemental mapping. The asymmetric shape of the N 1s peak indicates the existence of at least two components. On deconvolution, we found peaks at 398.3 and 400 eV, the first one being characteristic of pyridinic nitrogen (sp^2 hybridization) and the second due to nitrogen in the graphene sheets.[5, 24] XPS data indicated that NG1, NG2, and NG3 contain 0.6, 1, and 1.4 at.% of nitrogen, respectively. EELS results were comparable, indicating that NG2 contained 0.9 at.% nitrogen. TEM images clearly show the presence of two to three layers in the BG and NG samples. In Figure 2 a,b,c and d we

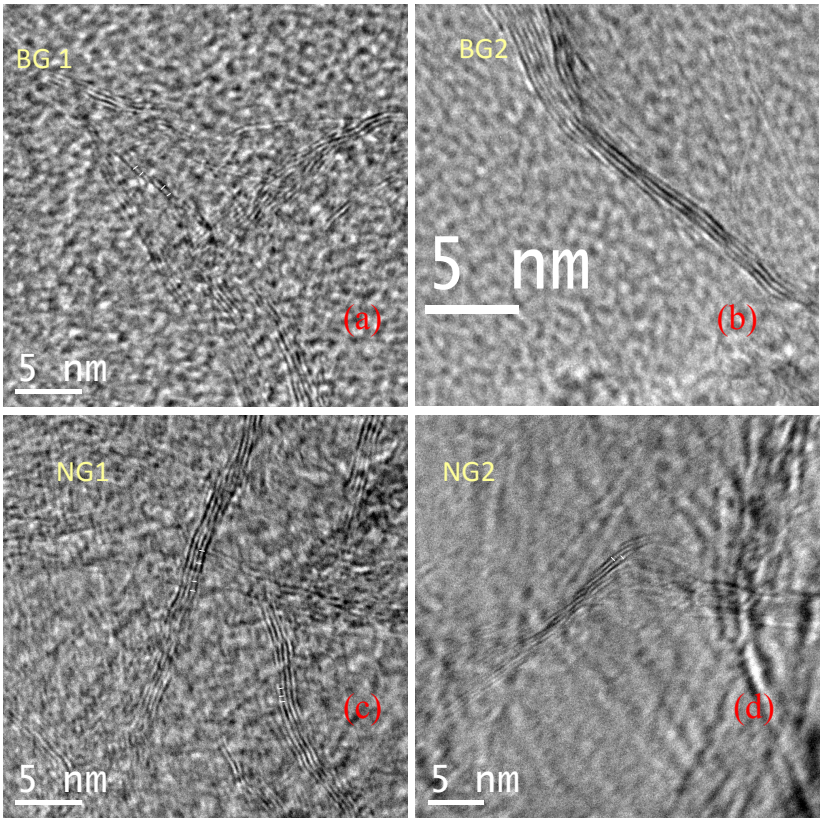

Figure 2. TEM images of B-doped graphene (a) BG1) and (b) BG2 and N-doped graphene (c) NG1 and (d) NG2.

show the high-resolution transmission electron microscopy (HREM) images of the BG1, BG2, NG1and NG2 samples respectively. In Figure 3, we show typical atomic force microscopy (AFM) images of BG1 and NG1. The images correspond to two-layer graphenes. The AFM images generally show the presence of two to three layers in the various BG and NG samples, with the occasional presence of single layers.

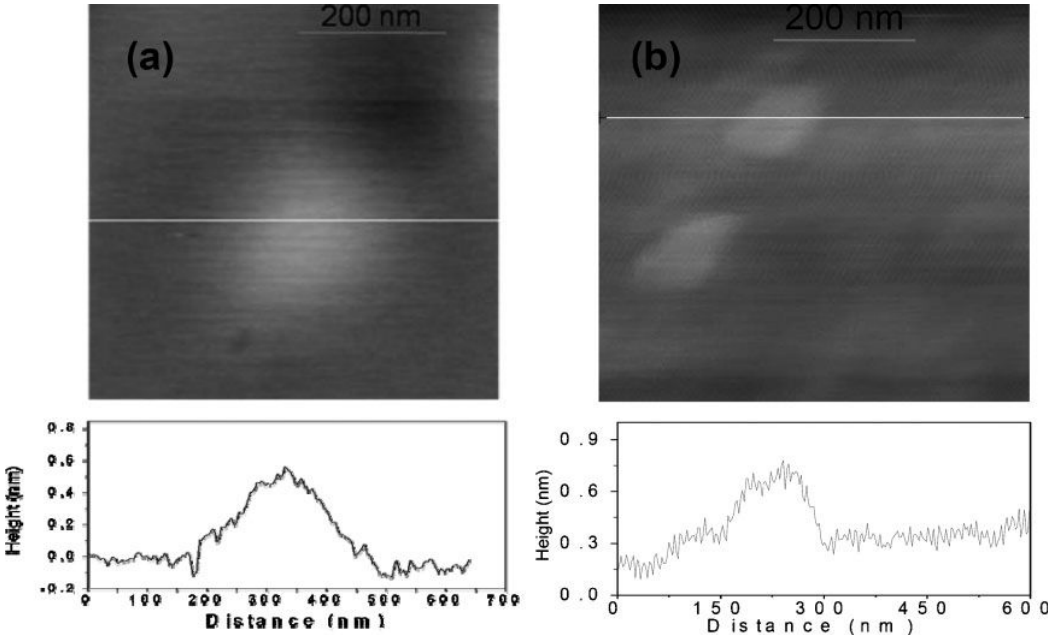

Figure 3. Typical AFM images of flakes of B- and N-substituted graphenes: (a) BG1and (b) NG1.

Thermogravimetric analysis indicated that the BG and NG samples undergo combustion at temperatures only slightly lower than the parent graphene (580 ºC). The BG and NG samples exhibit higher electrical conductivity than the undoped graphene (Figure 4). We examined the Raman spectra of all BG and NG samples in comparison with that of HG, i.e., pure graphene, prepared by the H_2-discharge method (Figure 5a and b). The Raman spectra (with 632.8nm excitation) of these samples show three main features in the 1000–3000 cm^{-1} region,[40-42] the G-band (-1570 cm^{-1}), the defect-related D-band (-1320 cm^{-1})

and the 2D-band (-2640 cm^{-1}). It is noteworthy that the G-band stiffens both with boron and nitrogen doping as can be seen in Figure 5c.

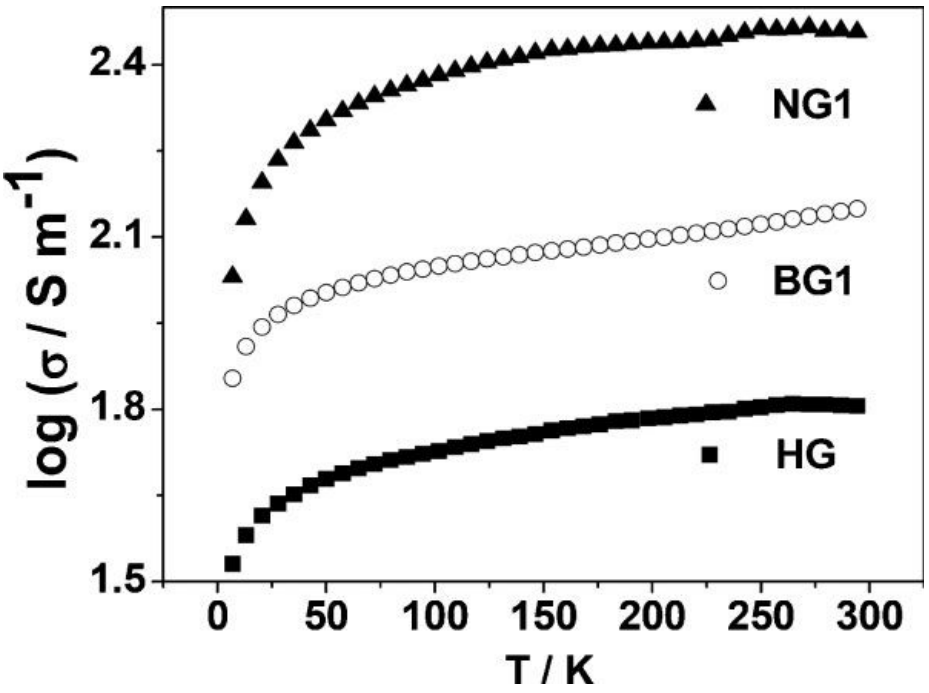

Figure 4. Electrical conducting data of NG1, BG1 and pristine grapene (HG).

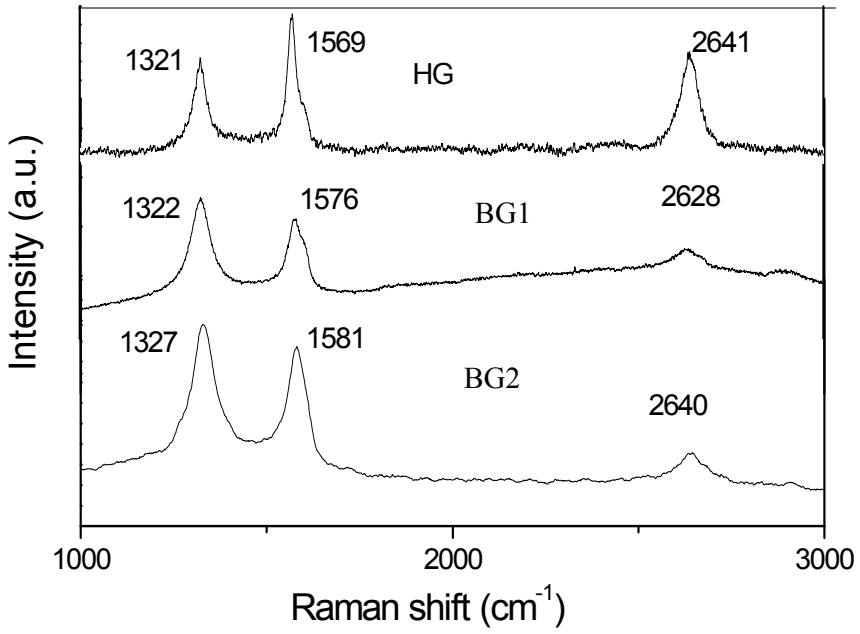

Figure 5a: Raman spectra of HG, and BG2.

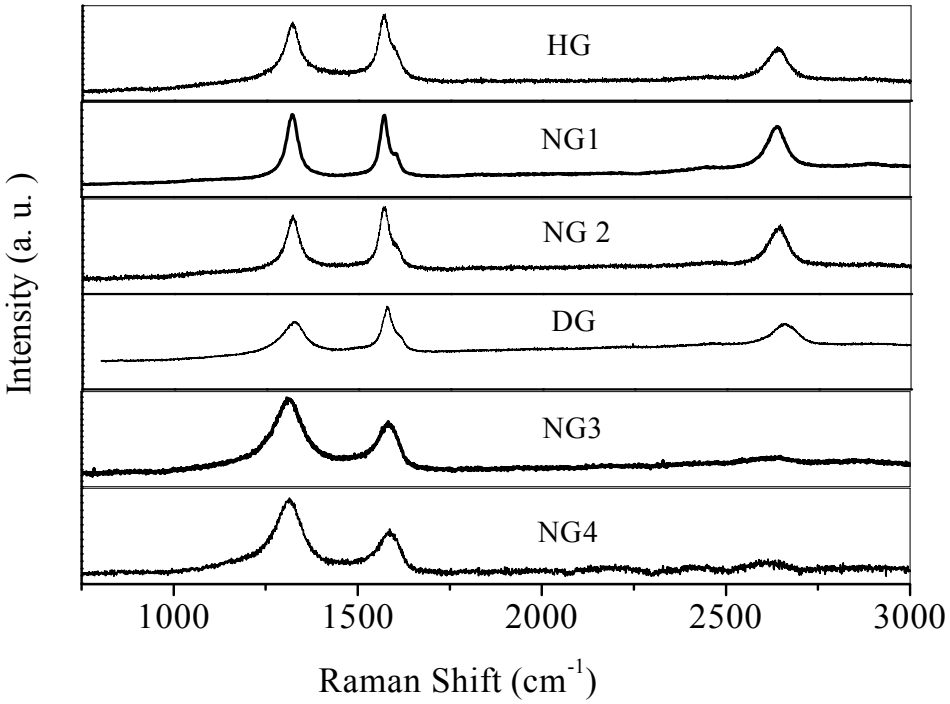

Figure 5b: Raman spectra of HG, Nand NG4.

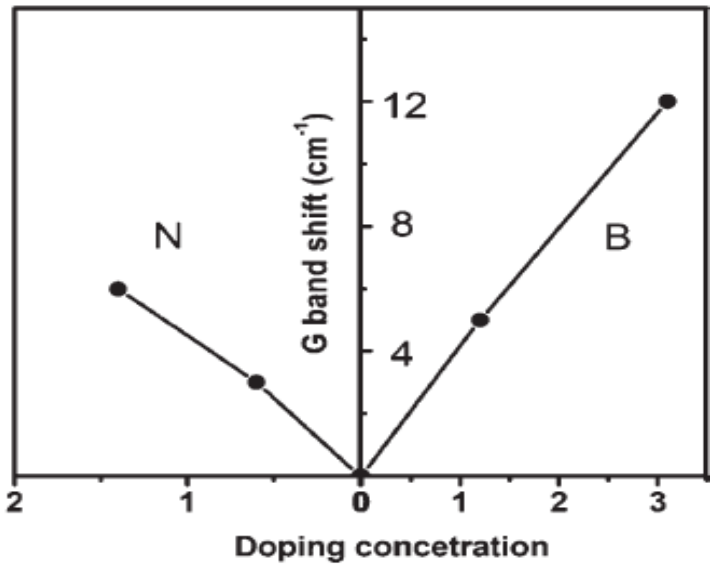

Figure 5c: Shifts of the G-band caused by electron (N) doping (with pyridine) and hole (B) doping.

This is similar to what happens with electrochemical doping[40] but differs from what occurs when the doping is done by molecular charge-transfer.[37, 38] The blue-shift in the case of BG2, which has a higher B-content, is larger than that of BG1 (Table 1). In case of NG, the sample with the highest N content, NG3, shows the largest shift (Table 2).

Table 1. Raman data of HG, BG1 and BG2.

Sample	D (cm^{-1})	G (cm^{-1})	2D (cm^{-1})	I_D/I_G	I_{2D}/I_G
HG	1321	1569	2641	0.6	0.7
BG1	1322	1576	2628	1.3	0.2
BG2	1327	1581	2640	1.2	0.3

Table 2. Raman data of HG, NG1, NG2, DG, NG3 and NG4.

Sample	D (cm^{-1})	G (cm^{-1})	2D (cm^{-1})	I_D/I_G	I_{2D}/I_G
HG	1321	1568	2641	0.6	0.7
NG1	1322	1572	2638	1	0.65
NG2	1321	1570	2641	0.8	0.7
DG	1327	1576	2657	0.6	0.45
NG3	1313	1584	2622	1.7	0.1
NG4	1315	1586	2626	2	0.23

Stiffening of the G-band arises from the nonadiabatic removal of the Kohn anomaly at the G-point, and its broadening is due to the absence of blockage of the decay channels of the phonons into electron–hole pairs.[42] The intensity of the D-band is higher with respect to that of the G-band in all doped samples. On doping, the relative intensity of the 2D-band generally decreases with respect to that of the G-band. It is known that the 2D-band is sensitive to doping.[37, 38, 40] The 2D-band can also be deconvoluted to show the presence of more than one layer (2 and/or 3). The changes in the G-band and the other

bands in the Raman spectra along with the XPS and EELS results mentioned earlier suggest that the dopant B- and N-atoms occur substitutionally.

Prof. Waghmare and co-workers carried out first-principles density functional theory (DFT) calculations to understand the effect of substitutional doping on the structure of graphene as well as its electronic and vibrational properties. In their simulations, two configurations of doped bilayer graphene (4 x 4 supercell), where the substituted atoms (3.125% B or 3.125% N) in the two layers are a) close to and b) far from each other were considered.

Calculations revealed that the linearity in the dispersion of the electronic bands within 1 eV of the Fermi energy is almost unchanged with B- and N-doping indicating that the doped graphenes have the potential to exhibit the interesting properties of pristine graphene. The Fermi energy, which is at the apex of the conical band-structure near the K-point of the Brillouin zone of graphene, is shifted by -0.65 and 0.59 eV in the case of 2 at.% B and N-substitutions. These shifts are of -1.0 and 0.9 eV in 3.125 at.% B- and N-doped bilayers, respectively. A large amount (96%) of shift in Fermi energy arised from substitution with dopants, and the remaining 4% arised from lattice relaxation. The shifts in vibrational frequencies calculated based on only changes in bond length obtained at a fixed lattice constant showed opposite signs. However, after adding the dynamic corrections, the frequency shifts become positive, in agreement with experimental observations.

6. 5 Conclusions

We have demonstrated that different routes are possible for the synthesis of BG and NG. Based on an agreement between experiments and calculations, we conclude that BGs and NGs to exhibit p- and n-type semiconducting electronic properties that can be systematically tuned with the concentration of B and N and characterized by Raman

spectroscopy. Interestingly, elemental doping and electrochemical doping produce similar shifts in the Raman G-band, but molecular charge-transfer gives rise to different effects. Such p-and n-type conducting graphene bilayers should be usable in a variety of devices similar to those based on semiconductors.

6.6 References

[1] C. N. R. Rao, A. Govindaraj, in *Nanotubes and Nanowires, RSC nanoscience & Nanotechnology Series*, RSC, Cambridge, UK, **2005**.

[2] K. Sumino, M. Imai, *Philos. Mag. A.* **1983**, *47*, 753.

[3] K. Sumino, I. Yonenaga, M. Imai, T. Abe, *J. Appl. Phys.* **1983**, *54*, 5016.

[4] R. Sen, B. C. Satishkumar, A. Govindaraj, K. R. Harikumar, M. K. Renganathan, C. N. R. Rao, *J. Mater. Chem.* **1997**, *7*, 2335.

[5] R. Sen, B. C. Satishkumar, A. Govindaraj, K. R. Harikumar, G. Raina, J.-P. Zhang, A. K. Cheetham, C. N. R. Rao, *Chem. Phys. Lett.* **1998**, *287*, 671.

[6] M. Nath, B. C. Satishkumar, A. Govindaraj, C. P. Vinod, C. N. R. Rao, *Chem. Phys. Lett.* **2000**, *322*, 333.

[7] M. Terrones, P. M. Ajayan, F. Banhart, X. Blase, D. L. Carroll, J. C. Charlier, R. Czerw, B. Foley, N. Grobert, R. Kamalakaran, P. Kohler-Redlich, M. Ruhle, T. Seeger, H. Terrones, *Applied Physics a-Materials Science & Processing* **2002**, *74*, 355.

[8] B. C. Satishkumar, A. Govindaraj, K. R. Harikumar, J. P. Zhang, A. K. Cheetham, C. N. R. Rao, *Chem. Phys. Lett.* **1999**, *300*, 473.

[9] S. M. C. Vieira, O. Stephan, D. L. Carroll, *J. Mater. Res.* **2006**, *21*, 3058.

[10] B. C. Satishkumar, P. J. Thomas, A. Govindaraj, C. N. R. Rao, *Appl. Phy. Lett.* **2000**, *77*, 2530.

[11] F. L. Deepak, N. S. John, A. Govindaraj, G. U. Kulkarni, C. N. R. Rao, *Chem. Phys. Lett.* **2005**, *411*, 468.

[12] Y. Chai, Q. F. Zhang, J. L. Wu, *Carbon* **2006**, *44*, 687.

[13] M. Glerup, J. Steinmetz, D. Samaille, O. Stéphan, S. Enouz, A. Loiseau, S. Roth, P. Bernier, *Chem. Phys. Lett.* **2004**, *387*, 193.

[14] G. Keskar, R. Rao, J. Luo, J. Hudson, J. Chen, A. M. Rao, *Chem. Phys. Lett.* **2005**, *412*, 269.

[15] F. Villalpando-Paez, A. Zamudio, A. L. Elias, H. Son, E. B. Barros, S. G. Chou, Y. A. Kim, H. Muramatsu, T. Hayashi, J. Kong, H. Terrones, G. Dresselhaus, M. Endo, M. Terrones, M. S. Dresselhaus, *Chem. Phys. Lett.* **2006**, *424*, 345.

[16] H. C. Choi, S. Y. Bae, J. Park, K. Seo, C. Kim, B. Kim, H. J. Song, H. J. Shin, *Appl. Phy. Lett.* **2004**, *85*, 5742.

[17] Y. S. Min, E. J. Bae, I. P. Asanov, U. J. Kim, W. Park, *Nanotechnology* **2007**, *18*, 4.

[18] P. Ayala, A. Grueneis, T. Gemming, D. Grimm, C. Kramberger, M. H. Ruemmeli, F. L. Freire, H. Kuzmany, R. Pfeiffer, A. Barreiro, B. Buechner, T. Pichler, *J. Phys. Chem. C* **2007**, *111*, 2879.

[19] E. Borowiak-Palen, T. Pichler, G. G. Fuentes, A. Graff, R. J. Kalenczuk, M. Knupfer, J. Fink, *Chem. Phys. Lett.* **2003**, *378*, 516.

[20] G. G. Fuentes, E. Borowiak-Palen, M. Knupfer, T. Pichler, J. Fink, L. Wirtz, A. Rubio, *Phys. Rev. B* **2004**, *69*, 6.

[21] J. L. Blackburn, Y. Yan, C. Engtrakul, P. A. Parilla, K. Jones, T. Gennett, A. C. Dillon, M. J. Heben, *Chem. Mater.* **2006**, *18*, 2558.

[22] P. Ayala, W. Plank, A. Gruneis, E. I. Kauppinen, M. H. Rummeli, H. Kuzmany, T. Pichler, *J. Mater. Chem.* **2008**, *18*, 5676.

[23] D. Golberg, Y. Bando, W. Han, K. Kurashima, T. Sato, *Chem. Phys. Lett.* **1999**, *308*, 337.

[24] L. S. Panchalkarla, A. Govindaraj, C. N. R. Rao, *ACS Nano* **2007**, *1*, 494.

[25] S. Y. Kim, J. Lee, C. W. Na, J. Park, K. Seo, B. Kim, *Chem. Phys. Lett.* **2005**, *413*, 300.

[26] P. L. Gai, O. Stephan, K. McGuire, A. M. Rao, M. S. Dresselhaus, G. Dresselhaus, C. Colliex, *J. Mater. Chem.* **2004**, *14*, 669.

[27] M. Doytcheva, M. Kaiser, M. A. Verheijen, M. Reyes-Reyes, M. Terrones, N. de Jonge, *Chem. Phys. Lett.* **2004**, *396*, 126.

[28] D. L. Carroll, P. Redlich, X. Blase, J. C. Chalier, S. Curran, P. M. Ajayan, S. Roth, M. Ruhle, *Phys. Rev. Lett.* **1998**, *81*, 2332.

[29] R. B. Sharma, D. J. Late, D. S. Joag, A. Govindaraj, C. N. R. Rao, *Chem. Phys. Lett.* **2006**, *428*, 102.

[30] I. Mukhopadhyay, N. Hoshino, S. Kawasaki, F. Okino, W. K. Hsu, H. Touhara, *J. Electrochem. Soc.* **2002**, *149*, A39.

[31] F. Villalpando-Paez, A. H. Romero, E. Munoz-Sandoval, L. M. Martinez, H. Terrones, M. Terrones, *Chem. Phys. Lett.* **2004**, *386*, 137.

[32] S. Peng, K. Cho, *Nanotechnology* **2000**, *11*, 57.

[33] S. Santucci, S. Picozzi, F. D. Gregorio, L. Lozzi, C. Cantalini, L. Valentini, J. M. Kenny, B. Delley, *J. Chem. Phys.* **2003**, *119*, 10904.

[34] J. C. Carrero-Sanchez, A. L. Elías, R. Mancilla, G. Arrellín, H. Terrones, J. P. Laclette, M. Terrones, *Nano Lett.* **2006**, *6*, 1609.

[35] N. Murata, J. Haruyama, J. Reppert, A. M. Rao, T. Koretsune, S. Saito, M. Matsudaira, Y. Yagi, *Phys. Rev. Lett.* **2008**, *101*, 027002.

[36] J. C. Charlier, M. Terrones, M. Baxendale, V. Meunier, T. Zacharia, N. L. Rupesinghe, W. K. Hsu, N. Grobert, H. Terrones, G. A. J. Amaratunga, *Nano Lett.* **2002**, *2*, 1191.

[37] B. Das, R. Voggu, C. S. Rout, C. N. R. Rao, *Chem. Commun.* **2008**, *41*, 5155.

[38] R. Voggu, B. Das, C. S. Rout, C. N. R. Rao, *J. Phys.: Condens. Matter* **2008**, *20*, 472204.

[39] T. Ohta, A. Bostwick, T. Seyller, K. Horn, E. Rotenberg, *Science* **2006**, *313*, 951.

[40] A. Das, S. Pisana, B. Chakraborty, S. Piscanec, S. K. Saha, U. V. Waghmare, K. S. Novoselov, H. R. Krishnamurthy, A. K. Geim, A. C. Ferrari, A. K. Sood, *Nat. Nanotechnol.* **2008**, *3*, 210.

[41] A. C. Ferrari, *Solid State Commun.* **2007**, *143*, 47.

[42] S. Pisana, M. Lazzeri, C. Casiraghi, K. S. Novoselov, A. K. Geim, A. C. Ferrari, F. Mauri, *Nat. Mater.* **2007**, *6*, 198.

CHAPTER 7

CHEMICAL STORAGE OF H_2 BY GRAPHENE

Summary*

Hydrogen can be chemically stored in graphene employing hydrogen plasma treatment and Birch reduction. Hydrogen plasma treatment and Birch reduction of few-layer graphene samples give rise to hydrogenated samples containing up to 1.7 and 5wt % of hydrogen respectively. Hydrogenation of graphene results in the increase of magnetization values with the hydrogen content. Spectroscopic studies reveal the presence of sp^3 C-H bonds in the hydrogenated graphenes. They, however, decompose readily on heating to 500 °C or on irradiation with UV or laser radiation releasing all the hydrogen, thereby demonstrating the possible use of few-layer graphene for chemical storage of hydrogen. First-principles calculations provide the mechanism of dehydrogenation which appears to involve a significant reconstruction and relaxation of the lattice.

* A paper based on these studies has appeared in Proc. Natl Acad. Sci. (USA) (2011).

7.1 Introduction

Energy can be stored in different forms: as mechanical energy, in an electric or magnetic field, as chemical energy of reactants and fuels or as nuclear fuel. Among those forms chemical energy is the one that can be transmitted easily. It is based on energy of the unpaired outer electrons (valence electrons), eager to be stabilized by electrons from other atoms. In the periodic table, of all elements, hydrogen has the best valence electrons to protons (also neutrons) ratio, and a very high energy gain per electron as well. Though hydrogen is the most abundant element on earth, majority is chemically bound with oxygen as H_2O (water), and some bound to liquid or gaseous hydrocarbons. The hydrogen consumed today as a chemical raw material (about $5x10^{10}$ kg per year worldwide) is mainly produced from fossil fuels and by the reaction of hydrocarbon chains ($–CH_2–$) with H_2O at high temperatures, which produces H_2 and CO_2. In fact, most of the world energy consumption is from fossil fuels (Figure 1); the rest mainly comes from nuclear power, hydro power, and also burning of waste and wood. Fossil fuels are generally employed for a wide variety of purposes ranging from cooking to transportation; quite long and exhaustive. Almost every aspect of human life, today, is associated with the use of fossil fuels. There is an ever increasing energy consumption which is caused by population growth and higher living standards. In order to support the growing demand for fossil fuels new reserves need to be discovered. Someday, we will inevitably run out of fossil fuels due to limited availability. Another important issue which might become critical even before we run out of fossil fuels is global warming which can potentially harm the life of many people due to rising sea levels and increasingly harsh weather conditions.

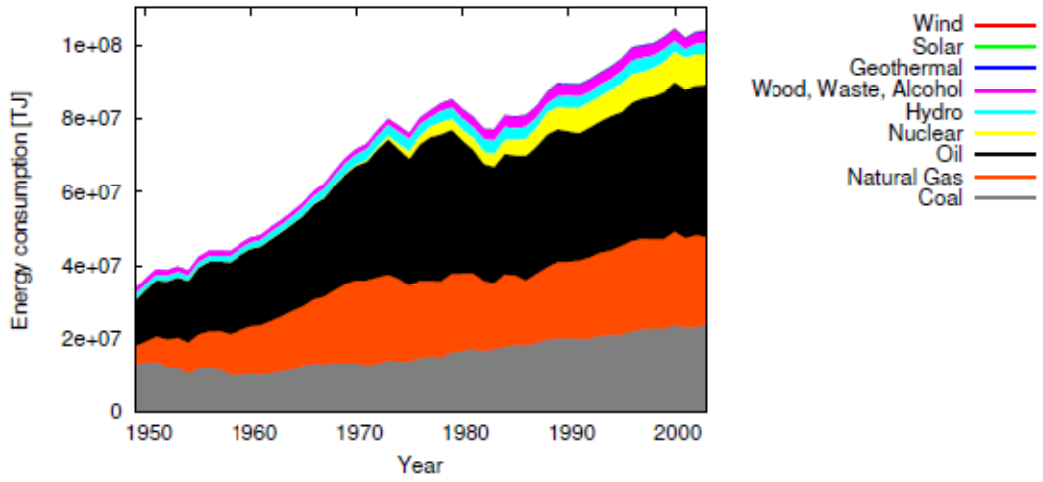

Figure 1: World energy consumption by source 1949-2003. Data are from the Energy Information Administration (EIA), U. S. Department of Energy, Annual Energy Review 2003 (http://www.eia.doe.gov/emeu/aer/txt/ptb0103.html).

A possible way of addressing the above problems is a gradual transformation of our present fossil fuel based society to hydrogen based society viz. a society in which hydrogen is the primary energy carrier. The chemical energy per mass of hydrogen (142 MJ kg^{-1}) is at least three times larger than that of other chemical fuels (for example, the equivalent value for liquid hydrocarbons is 47 MJ kg^{-1}). Hydrogen is a clean synthetic fuel: when burnt with oxygen, the only exhaust gas is water. Primarily, there are two ways to run a road vehicle on hydrogen. One is combustion of hydrogen with oxygen from air in an internal combustion engine. Second one is reaction of hydrogen with oxygen from air in a fuel cell, which produces electricity (and heat) and drives an electric engine. But for on-board energy storage, vehicles need compact, light, safe and affordable containment. Commercially available car requires about 24 kg of petrol to cover a range of 400 km with a combustion engine, whereas, 8 kg hydrogen for the combustion engine version and 4 kg hydrogen for an electric car

equipped with a fuel cell is enough to cover the same range. Hydrogen is a molecular gas. At room temperature and atmospheric pressure, 4 kg of the gas has a volume of 45 m^3. As hydrogen occupies large volume at ambient conditions, packing of hydrogen as compact as possible, possible is required to reach the highest volumetric density (Figure 2).[1]

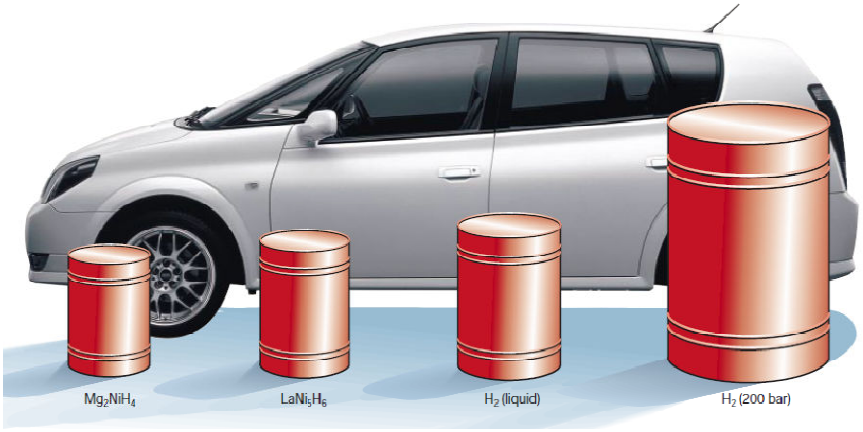

Figure 2. Volume of 4 Kg of hydrogen compacted in different ways, with size relative to the size of a car. (From ref. [1]).

This can be enabled either by compressing the gas or reducing the repulsion by interaction of hydrogen with another material. Importantly, the use of hydrogen for transportation, personal electronics and other portable power applications requires an effective hydrogen storage medium.

High-pressure tanks made of steel are tested up to 300 bar and regularly filled up to 200 bar in most countries. To store 4 kg hydrogen still requires an internal volume of 225 litres (about 60 gallons) or 5 tanks of 45 litres each. Carbon-fibre-reinforced composites based on high-pressure tanks are tested up to 600 bar and filled up to 450 bar for regular use. But they require a special inert inner coating to prevent the reaction of high pressure hydrogen with the polymer. These high-pressure containers, when full, would contain about

4% hydrogen by mass, but with significant disadvantages: the fuel would be available at a pressure dropping from 450 bar to zero overpressure, so additional pressure control would be essential. These standard piston-type mechanical compressors can be employed to compress hydrogen. Theoretical work for the isothermal compression of hydrogen is given by the equation:

$$\Delta G = R \cdot T \cdot \ln(\frac{p}{p_0})$$

Where R is the gas constant, T the absolute temperature, p and p_0 the end pressure and the starting pressure, respectively. Low hydrogen density and high gas pressures in the system are important drawbacks of this storage method. High-pressure vessels pose a considerable risk and the compression itself is the most dangerous and complicated part.

Liquid hydrogen is stored in cryogenic tanks at 21.2 K at ambient pressure. Due to low critical temperature of hydrogen (33 K), the liquid form can be stored only in open systems, as there is no liquid phase existent above the critical temperature. The simplest liquefaction cycle is the Joule-Thompson cycle (Linde cycle). The large amount of energy necessary for liquefaction and the continuous boil-off of hydrogen limit the possible use of liquid hydrogen storage systems in commercial applications. We considered it would be scientifically interesting to do research on the interaction of hydrogen with different graphenes. In this chapter we discuss chemical storage of H_2 by graphenes prepared by different methods.

7.2 Scope of the present investigations

The use of hydrogen for transportation, personal electronics and other portable power applications requires an effective hydrogen storage medium. Existing technology for hydrogen storage is limited to compressed gas and liquefaction, both of which are now used

in demonstration vehicles. Compressed gas, even at the highest practical pressure of 10,000 psi, is still a bulky way to store hydrogen that requires a significant fraction of the trunk space in a small car to enable a 500 km driving range. Liquid hydrogen takes up slightly more than half the volume of 10,000 psi compressed gas, but it loses 30–40% of its energy in liquefaction. Although gas and liquid storage are useful as temporary options in a provisional hydrogen economy, more compact and efficient storage media are needed for a mature hydrogen economy.

Recent developments in nanoscience hold promise for meeting the difficult hydrogen storage challenge. Small dimensions of nanoscale materials minimize the diffusion length and time for hydrogen atoms to travel from the interior to the surface. Their large relative surface area provides a platform for dissociation of molecular hydrogen to atomic hydrogen, a prerequisite for diffusion and chemical bonding with the host. Pekker *et al*.[2] have carried out chemical storage of hydrogen in CNTs by employing Birch reduction. They obtained 0.72 wt% H_2 desorption corresponding to C: H ratio of 10.8:1. Hydrogenation has been attained by Nikitin *et al*.[3] by utilizing atomic hydrogen beam. XPS measurements revealed that 65 atomic % hydrogenation of carbon atoms which corresponds to 5.1 wt% of H_2 has been achieved. The C-H bonds thus formed were stable at ambient temperature and pressure and broke completely above 600 ºC. Molecular H_2 also led to hydrogenation in CNTs at elevated temperature and pressure.[4]

We thought it would be worthwhile to study chemical storage of hydrogen by graphene. For this purpose, we prepared graphene by employing different procedures namely exfoliation of graphite oxide (EG),[5] arc-evaporation of graphite in hydrogen atmosphere (HG) and reduction of graphene oxide (RGO).[6] We reduced the graphene samples by

employing hydrogen plasma treatment and Birch-reduction and the products were then characterized by employing various techniques. Hydrogen plasma treatment was carried out by employing 13.56 MHz radio frequency plasma generator. Birch reduction of graphene was carried out in dry liquid NH_3 in the presence of lithium at -33 ºC. We found that up to 5 wt % of hydrogen could be incorporated in few-layer graphenes by Birch reduction and up to 1.7 wt % of hydrogen by hydrogen plasma treatment. First-principles calculations were carried out to understand the nature of hydrogen in reduced graphene. Magnetic properties of the hydrogenated samples were studied and compared to their pristine counterpart. Magnetization values of the hydrogenated graphenes increased with the hydrogen content. Sp3 C-H bonds formed by the reduction of few-layer graphenes were broken on heating or on irradiation with ultraviolet or laser radiation, releasing all the hydrogen.

7.3 Experimental section

To carry out the hydrogen plasma treatment, graphene samples (HG) coated on glass/Si substrates were exposed to H_2 plasma generated by 13.56 MHz radio frequency plasma generator. [7-10]

Birch reduction of EG, HG and RGO was carried out by taking graphene (70 mg) with lithium in dry liquid NH_3 (40 ml).[11-13] The resulting suspension was maintained at -33 °C by using a liquid ammonia reflux condenser and stirred for 1hr. The amount of lithium was varied between 200 and 700 mg and added in different proportions. At the end of the reaction, 10 ml of 2-methyl 1-propanol was added slowly and gradually heated the reaction mixture to ambient temperature to evaporate NH_3. The resultant black product was washed with methanol, dil. HCl, water and methanol and dried in vacuum at 50 °C.

Hydrogenated EG, HG and RGO samples (designated as EG-H, HG-H and RGO-H respectively) were heated to different temperatures in the 200-500 °C range and the products subjected to chemical analysis and other methods of characterization. To study photolytic decomposition of the hydrogenated samples, the samples were deposited on a KBr crystal and subjected to ultraviolet (Hg lamp, λ=260 nm, 90 W) or Lambda physik KrF excimer laser (λ=248 nm, τ=30 ns, rep. rate 5 Hz, beam energy = 300 mJ) radiation. For laser irradiation, the KBr crystal (coated with the sample) was covered with a quartz plate so that the material did not get delaminated from the substrate. Aluminum metal slit (beam shaper) which usually gives a rectangular beam was removed while laser irradiation was carried out. This makes laser energy almost uniform throughout the area where the sample is present. Excimer laser beam direction was aligned normal to the substrate.

EG, HG, RGO, EGH, HGH and RGOH samples, as well as the dehydrogenated products were characterized by various techniques. Elemental analysis of the samples was carried out using a Perkin Elmer 2400 CHN analyzer. Evolution of hydrogen on heating was followed by employing a gas chromatograph (Mayura 9800). DC resistance measurements were carried out by standard four-probe method, using the resistivity option in the physical property measurement system (PPMS) of Quantum Design, USA. I-V characteristics were recorded with a Keithley electrometer (model 236). Magnetic measurements were performed with a vibrating sample magnetometer (VSM) in physical property measuring system (Quantum Design, USA).

7. 4 Results and discussion

7.4.1 Plasma hydrogenation

To carry out hydrogen plasma treatment of few-layer graphene samples (HG), we employed 13.56 MHz radio frequency plasma generator. Figure 3 depicts schematic illustration of the experimental setup.

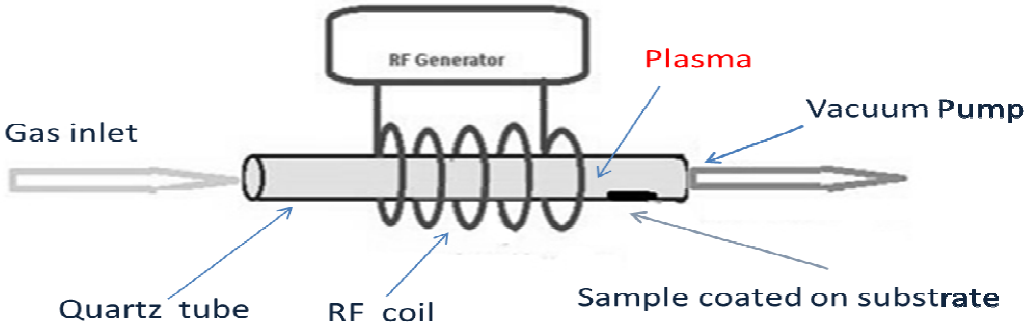

Figure 3. Schematic illustration of the experimental set up.

Graphene (HG) dispersed in 1,2 dichlorobenzene was spin-coated coated on glass/Si substrates and then heated in vacuum at 200˚C for 1 hour, prior to the plasma treatment to free from traces of solvent. Vacuum annealed samples were then placed in hydrogen plasma of power 40 W (at room temperature) and 100 W (at room temperature and 170 ºC).

We have carried out the elemental analysis of plasma treated samples of 100 W for 20 minutes. Elemental analysis indicated that plasma treated samples at room temperature and 170 ºC contain 1.25 and 1.7 wt % of H_2 respectively. In Figure 4 we show Raman spectra of pristine samples and those plasma-treated at 40 W for 5 and 10 min. Figure 5 shows Raman spectra of samples plasma-treated at 100 W for 5, 10 and 20 min at room temperature. After H_2 plasma treatment, Raman spectra of graphene samples change significantly. The I_D/I_G

ratio increases with the increase in plasma power and duration of plasma treatment. On heating at 500 ºC for 4 hrs I_D/I_G ratio in the Raman spectrum reverts to the original value of

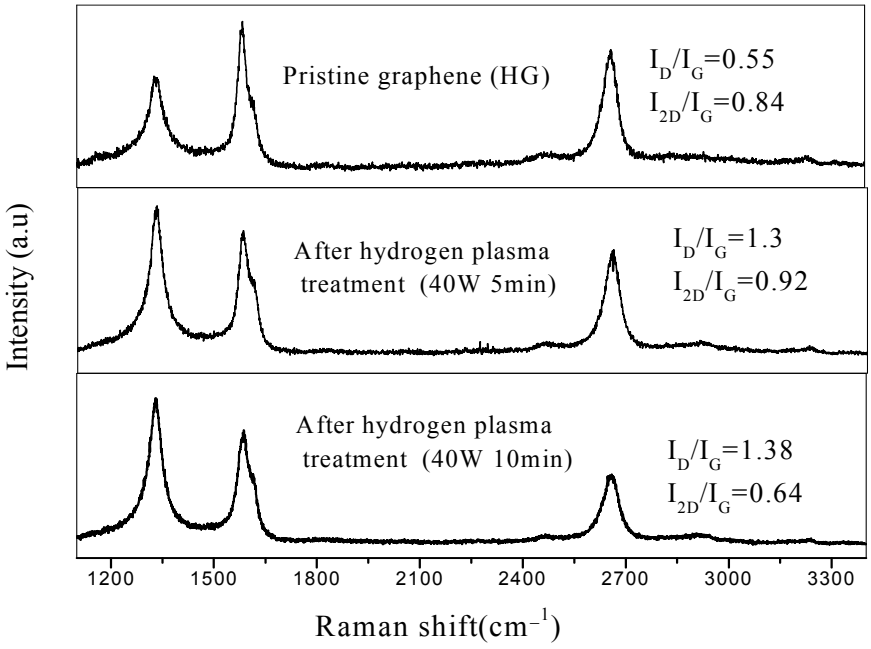

Figure 4. Raman spectra of HG before and after plasma treatment of 40 W for 5 and 10 min.

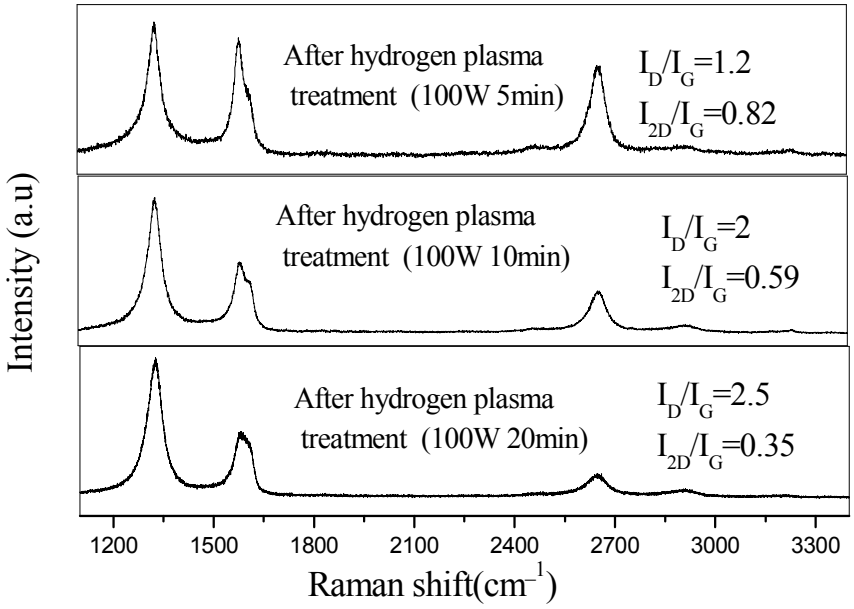

Figure 5. Raman spectra plasma treated samples of 100 W for 5, 10 and 20 minutes at room temperature.

of graphene as in the case of Birch-reduced samples due to dehydrogenation (Figure 6).

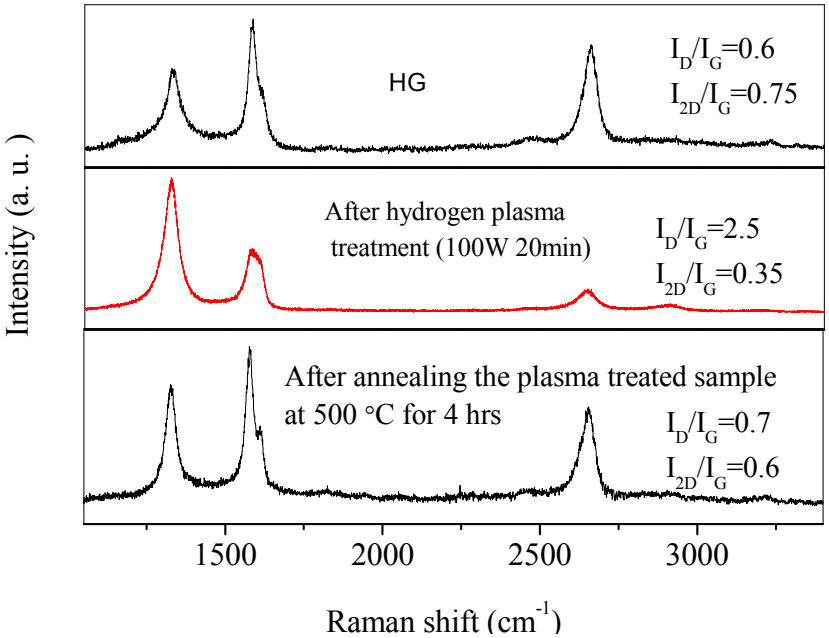

Figure 6. Raman spectra of pristine, plasma treated (100 W for 5 20 min) and annealed samples.

7.4.2 H_2 storage through Birch reduction

To chemically store hydrogen, we have carried out Birch reduction of EG, HG and RGO with lithium in liquid ammonia.[11-13] During the reaction, the amount of lithium (200 to 700 mg) and reaction time (1 hr to 2 hr) were varied. In Figure 7 we show infrared (IR) spectra of the pristine, as well as the hydrogenated samples. Hydrogenated samples clearly show aliphatic C-H stretching bands in the 2850-2950 cm^{-1} region. In Table 1, we show elemental analysis of the reduced samples. The maximum amount of hydrogen that can be incorporated in graphene is 7.7 wt %. Those reduced samples of EG (EGH), HG (HGH) and RGO (RGOH) obtained with a use of excess Li showed maximum hydrogen content of around 5 wt % (Table 1). And, these samples, containing ~ 5 wt % hydrogen were found to be stable and could be stored over long periods.

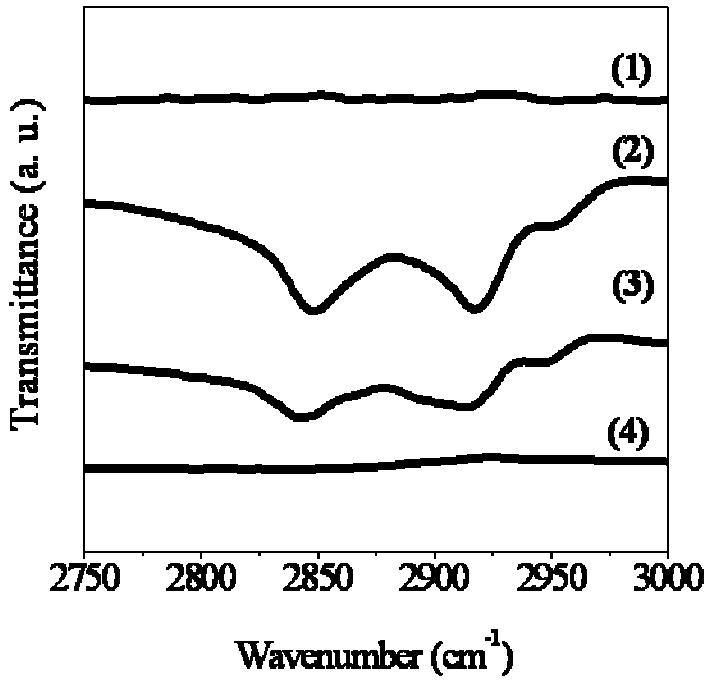

Figure 7. IR spectra of (1) EG, (2) EGH and EGH heated for 4 hrs (3) at 200 ºC and (4) at 500 ºC.

Table 1. C to H ratio of pristine and reduced samples inferred from elemental analysis.

Sample	C (Wt %)	H (Wt %)	CH (atomic ratio)
HG	99.5	0.5	
HG-H (Birch) (1 hr, Li = 200 mg, HG=70 mg)	98	2	C_8H_2
HG-H (Birch) (2 hr, Li = 200 mg, HG=70 mg)	97	3	C_8H_3
HG-H (Birch) (2 hr, Li = 700 mg, HG=70 mg)	95	5	C_8H_5
EG	99.75	0.25	
EG-H (Birch) (1 hr, Li = 200 mg, EG=70 mg)	95.5	4.5	$C_{16}H_9$
EG-H (Birch) (2 hr, Li = 200 mg, EG=70 mg)	95.5	4.5	$C_{16}H_9$
EG-H (Birch) (2 hr, Li = 700 mg, EG=70 mg)	95	5	C_8H_5
RGO	100	0	
RGO-H (Birch) (2 hr, Li = 700 mg, RGO=70 mg)	95	5	C_8H_5
RGO-H-350 ºC-10 hr	99	1	C_8H_1

We show AFM images of graphene (HG) before and after reduction in Figure 8.

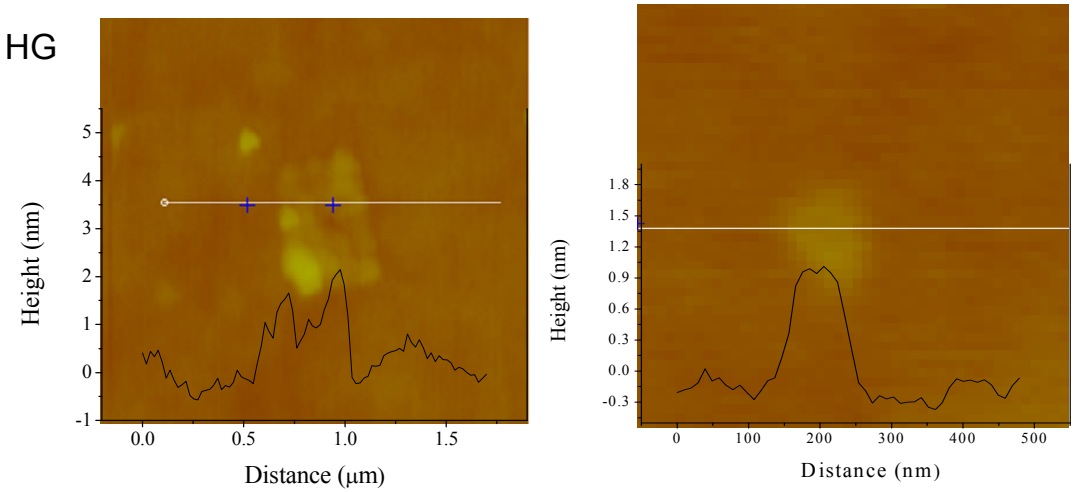

Figure 8a. AFM images of graphene (HG).

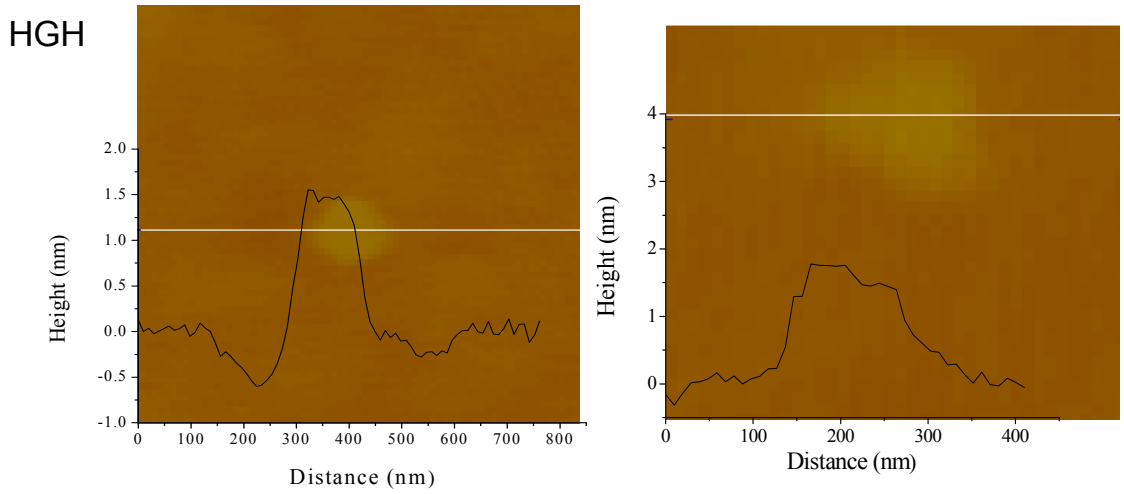

Figure 8b. AFM images of hydrogenated graphene (HGH).

Hydrogenated graphene shows similar features as the starting material with the number of layers remain unchanged. In Figures 9 and 10 we show, respectively, the Raman spectra of pristine as well as reduced EG and HG samples. On reduction, due to the C-H sp^3 bond formation and breaking of C=C sp^2 translational symmetry, intensity of D band increases and 2D band decrease. Increased defects in graphene lattice (due to sp^3 C-H bond formation)

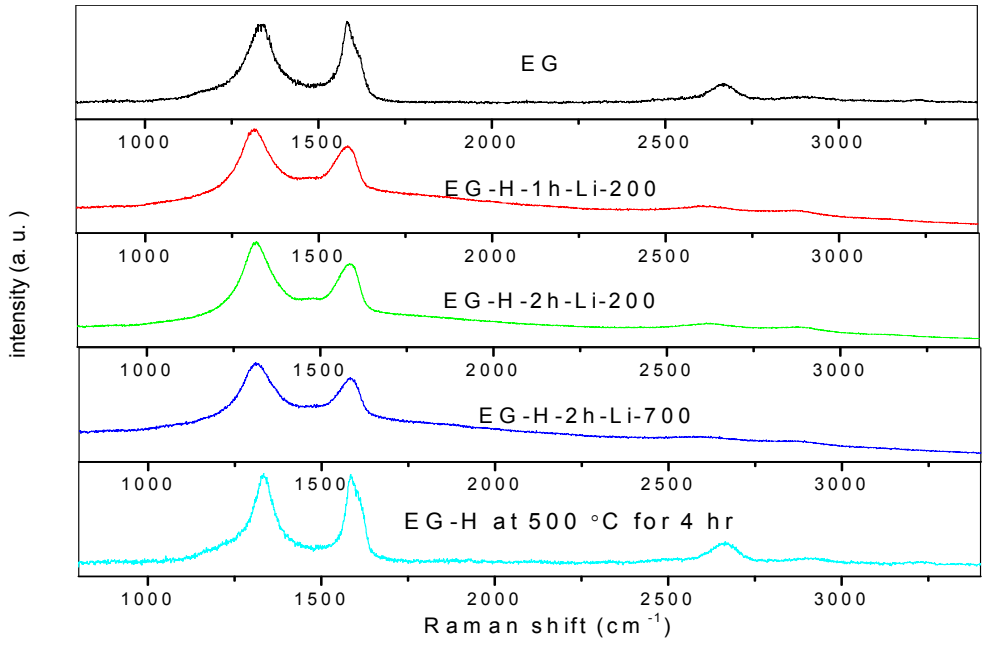

Figure 9. Raman spectra of EG and reduced EG samples.

causes evolution of D+G peak at 2909 cm^{-1}. Raman data of both pristine and hydrogenated samples are given in tables 2 and 3.

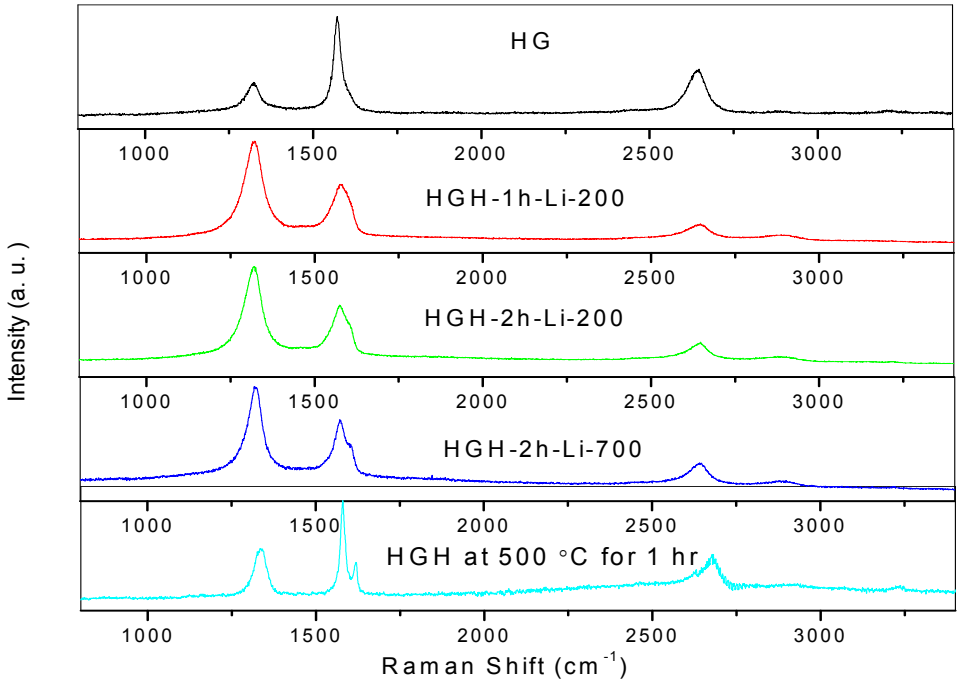

Figure 10. Raman spectra of HG and reduced HG samples.

Table 2. Raman data of pristine and hydrogenated EG samples.

Sample	D (cm^{-1})	G (cm^{-1})	2D (cm^{-1})	D+G (cm^{-1})	I_D/I_G	I_{2D}/I_G
EG	1334	1582	2668	2909	1	0.2
EG-1h (Li-200 mg)	1312	1582	2620	2894	1.8	0.25
EG-2h (Li-200mg)	1313	1584	2624	2890	1.8	0.3
EG-2h (Li-700 mg)	1310	1583	2607	2890	1.7	0.4
EG-H at 500 °C for 4 hr	1332	1583	2665	2908	1	0.1

Table 3. Raman data of pristine and hydrogenated HG samples.

Sample	D (cm^{-1})	G (cm^{-1})	D' (cm^{-1})	2D (cm^{-1})	D+G (cm^{-1})	I_D/I_G	I_{2D}/I_G
HG	1321	1571	1602	2640	-	0.3	0.45
HG-1h (Li-200 mg)	1318	1576		2638	2894	1.8	0.25
HG-2h (Li-200mg)	1316	1574	1603	2639	2890	1.8	0.3
HG-2h(Li-700 mg)	1319	1572	1603	2637	2890	1.7	0.4
HG-H at 500 °C for 1 hr	1333	1579	1617	2672	-	0.5	0.3

We show the UV spectrum of graphene (HG) before and after hydrogenation in Figure 11. On hydrogenation, the intensity of the 260 nm band decreases progressively with the hydrogen content and giving rise to a band around 235 nm.

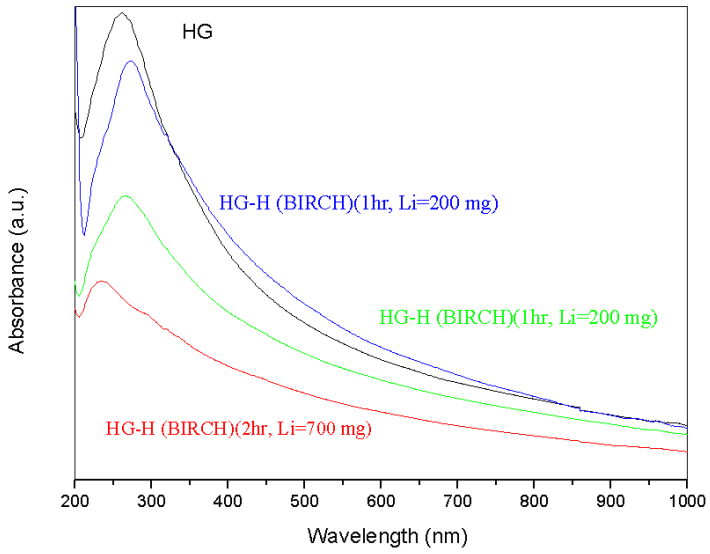

Figure 11. UV spectrum of HG before and after reduction.

The hydrogenated graphene containing ~ 5wt % hydrogen is stable and can be stored over long periods. We have examined its thermal stability in detail. In Figure 12 we show the change in weight percentage of hydrogen in EGH and HGH samples on heating to different temperatures (as obtained from elemental analysis). All the hydrogen gets released around 500 °C (Table 4). Gas chromatography shows that the evolution of hydrogen starts around 200 °C, and is complete at 500 °C (see inset of Figure 8). TGA of the hydrogenated samples shows weight loss starting around 200 °C, confirming gas chromatographic data. We have followed the loss of hydrogen on heating EGH and HGH by recording the IR spectra. C-H stretching bands in the IR spectrum gradually disappear on heating as can be seen from Figure 7.

Table 4. Change in weight percentage of hydrogen in the EGH, HGH and RGOH samples on heating at different temperatures.

Sample	C (Wt %)	H (Wt %)	CH (atomic ratio)
HG-H - 200 ^{o}C-4 hr	96	4.5	$C_8H_{4.5}$
HG-H-350 ^{o}C-4 hr	98.5	1.5	$C_8H_{1.5}$
HG-H-500 ^{o}C-1 hr	99.6	0.4	$C_8H_{0.4}$
EG- H-200 ^{o}C-4 hr	96	3.75	$C_8H_{3.75}$
EG-H-350 ^{o}C-4 hr	97	3	C_8H_3
EG-H-500 ^{o}C-4 hr	99	0.5	$C_8H_{0.5}$
RGO-H-350 ºC-10 hr	99	1	C_8H_1
RGO-H-500 ºC-1 hr	99.6	0.4	$C_8H_{0.4}$

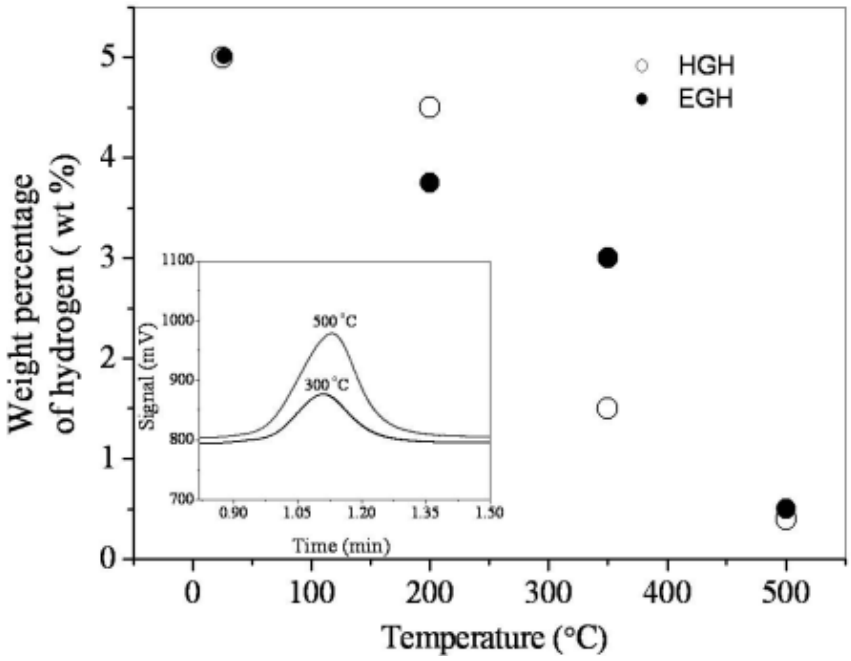

Figure 12. Change in the weight percentage of hydrogen of EGH and HGH with temperature. Inset shows the evolution of hydrogen as recorded by a gas chromatograph.

We also find that irradiation of the hydrogenated samples with UV radiation or with a KrF excimer laser results in dehydrogenation, as shown in the IR spectra (Figure 13). In the case of UV irradiation dehydrogenation occurs over a few hours, whereas the same result is obtained within 2 min using the laser. On dehydrogenation, the I_D/I_G ratio in the Raman spectrum reverts to the original value of graphene. The conductivity of the graphene samples substantially decreases on hydrogenation as expected[7] and increases again on dehydrogenation by thermal treatment or irradiation. In Figure 14 we show how the conductivity increases upon UV irradiation of the HGH sample.

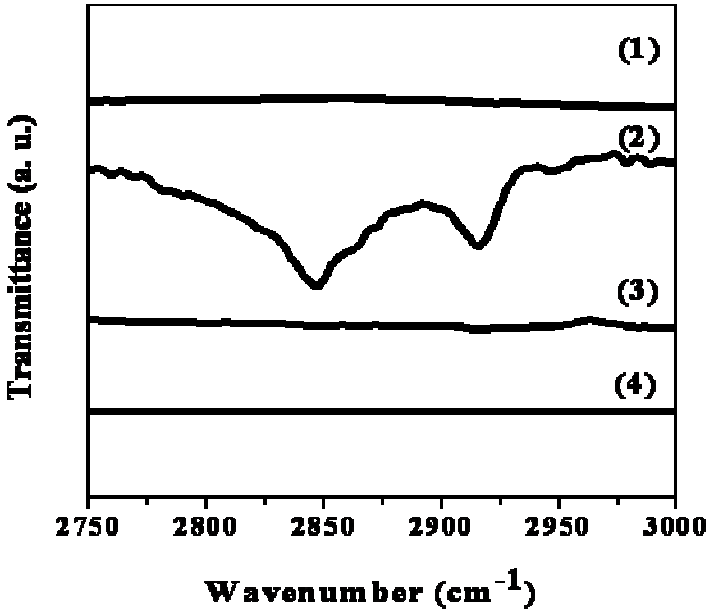

Figure 13. IR spectra of (1) HG, (2) HGH and HGH subjected to (3) UV and (4) laser radiation.

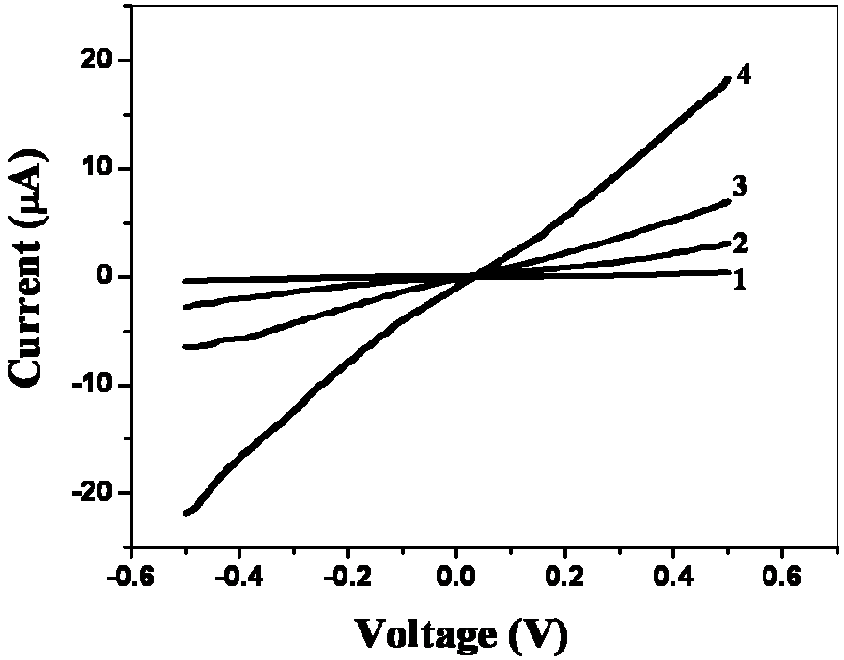

Figure 14. I-V characteristics of (1) as-prepared HGH and HGH subjected to UV irradiation for (2) 1 hr, (3) 2 hr and (4) 3 hr.

In order to understand the nature of hydrogenated graphene, Prof. Waghmare and co-workers carried out first-principles calculations based on density funcational theory within a generalized gradient approximation (GGA).[14] Local minima of energy landscape of H-graphene interaction are obtained through structural relaxation starting with different initial structures and using Hellman-Feynman forces and stresses, and local stability of the structure of local minima is assessed by obtaining frequencies of phonon modes. Two supercells with 18 and 4 carbon atoms were considered in simulation of interaction of hydrogen with different coverages.

Three different coverages of hydrogen: 25 % (C_4H_1), 50 % (C_4H_2) and 100 % (C_4H_4) and at least two configurations in each case: one with hydrogen atoms far (> 2 Å) from graphene (labeled *l*), and another with hydrogen atoms closer (< 1.2 Å labeled s) were considered. The latter typically results in a stable local minimum with the C-H bond length varying from 1.07 to 1.17 Å, while the former results in an unstable local minimum (saddle point) with the C-H bond length longer than 2.5 Å forming a transition state. In cases with coverages of 25 and 100 %, there is only one symmetry inequivalent configuration each, while there are two distinct configurations (S1 and S2) in the case of 50 % coverage, labeled by 12 and 13 indicating the atomic sites (see Figure 15) that hydrogen is closest to. Results showed that among the locally stable H-graphene states, 50 % of hydrogen coverage, corresponding to 4 wt % of hydrogen, has the lowest energy relative to the energy of graphene and isolated atomic hydrogen, consistent with experimental observations. Calculated phonons of S1 clearly showed two high frequency C-H stretching modes (for the two H atoms), confirming the observation of C-H bond formation. While the configurations with hydrogen atoms

farther from graphene have lower energies, they are locally unstable and form a transition state. These findings can be understood in terms of the competition between (a) the gain in

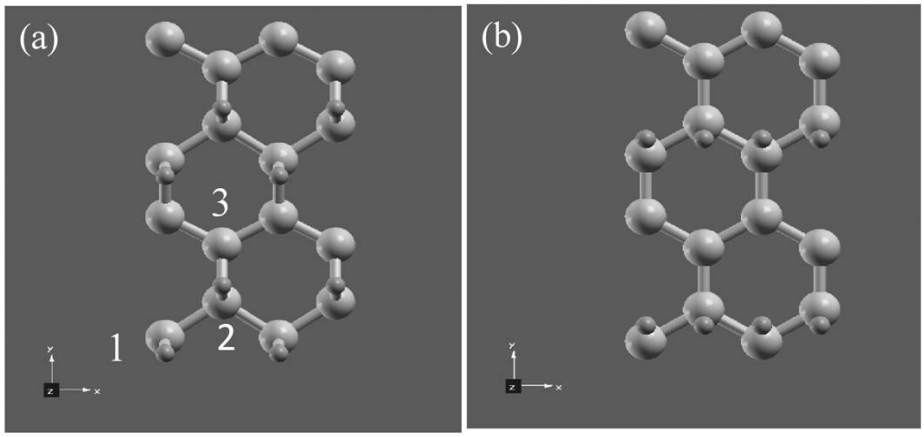

Figure 15. Hydrogen is chemically bonded to carbon in configuration S1 in (a), whereas it is not bonded to carbon in the transition state configuration S2 (b).

energy due to the formation of C-H bonds and (b) the energy cost associated with in-plane expansion of the C-C lattice. The stable configuration S1 is higher in energy than the transition state because it involves the stretching of the C-C bonds to about 1.52 Å. Hence, one needs to pump in a little energy in getting hydrogen chemically bound to graphene. The energy barrier for the release of chemically bonded hydrogen is very small, and involves significant relaxation and reconstruction of the lattice, which is considered to be important in H-graphene interaction based on a detailed first-principles study.

Magnetic properties of hydrogenated graphene

Hydrogenated graphene samples with hydrogen contents of 2 wt%, 3 wt% and 5 wt% (designated as HGH_1, HGH_2 and HGH_3 respectively) obtained by Birch reduction have been examined for the magnetic properties. From magnetization data it is evident that there is a gradual increase in the magnetic moment with increase in the hydrogen content. In Figure 16 we show the remanent magnetization (M_r), saturation magnetization (M_s) and magnetization at 3000 Oe (FC@10 K) of HG with different weight percentages of hydrogen. The values of these properties increase with hydrogen content. Increase in the magnetization values can be ascribed to the formation of tetrahedral carbons which can reduce the connectivity of the π - π sheets and hence the ring current diamagnetism. On dehydrogenation at 500 °C for 4 hours, the samples exhibit a decrease in the magnetic moment (Table 5). This observation clearly confirms that the increase in the magnetic properties arises from hydrogenation.

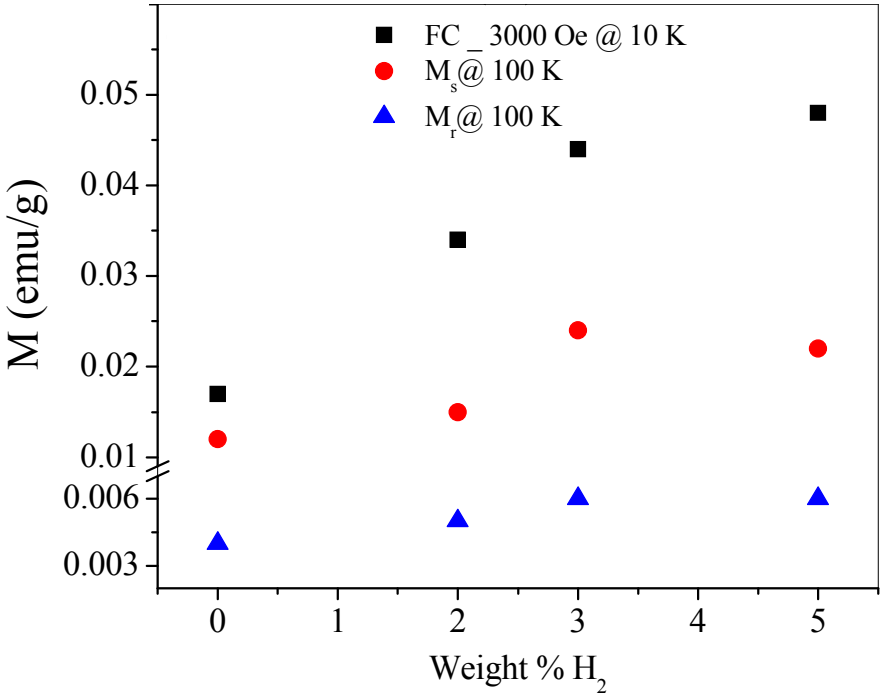

Figure 16. Comparison of the magnetic properties of the hydrogenated few-layer graphene (HGH_1, HGH_2 and HGH_3) with pristine sample (HG).

Table 5. Magnetic properties of the pristine, hydrogenated and dehydrogenated graphene samples.

Sample name	Wt (%) of hydrogen	M (emu/g) (FC @ 10 K)		Saturation magnetization (M_s)	
		3000 Oe	1 T	100 K	300 K
HG		0.017	0.025	0.012	0.01
HGH_1	2	0.034	0.07	0.015	0.012
HGH_2	3	0.044	0.092	0.024	0.02
HGH_3	5	0.048	0.099	0.022	0.016
HGH_2_DH	-	0.038	0.048	0.019	0.015

7.5 Conclusions

Birch reduction and hydrogen plasma treatment of few-layer graphenes give rise to hydrogenated samples containing up to 5 and 1.7 wt % of hydrogen respectively. Especially, chemical storage of hydrogen up to ~5 wt % employing Birch reduction is noteworthy and may have potential applications. Hydrogenation of graphene leads to an incease in the values of magnetic properties with the increase in hydrogen content. The hydrogenated samples containing sp^3 C-H bonds are stable at room temperature, but the hydrogen is progressively removed on heating, leading to complete removal at 500 °C. Laser or UV irradiation can also be employed to dissociate the C-H bonds to eliminate the hydrogen. While Birch reduction enabled us to incorporate ~5 wt % of hydrogen in few-layer graphenes, it may be possible to carry out hydrogenation more effectively by other methods. First-principles calculations reveal how dehydrogenation of reduced graphene is associated

with a small barrier and involves significant relaxation and reconstruction of the lattice. Graphene has the potential of being a useful H_2 storage material and H_2 uptake studies of improved graphene samples should be pursued.

7.6 References

[1] L. Schlapbach, A. Zuttel, *Nature* **2001**, *414*, 353.

[2] S. Pekker, J. P. Salvetat, E. Jakab, J. M. Bonard, L. Forr, *J. Phys. Chem. B* **2011**, *105*, 7938.

[3] A. Nikitin, H. Ogasawara, D. Mann, R. Denecke, Z. Zhang, H. Dai, K. Cho, A. Nilsson, *Phys. Rev. Lett.* **2005**, *95*, 225507.

[4] A. V. Talyzin, S. Luzan, I. V. Anoshkin, A. G. Nasibulin, H. Jiang, E. I. Kauppinen, V. M. Mikoushkin, V. V. Shnitov, D. E. Marchenko, D. Noreus, *ACS Nano* **2011**, *5*, 5132.

[5] H. C. Schniepp, J. L. Li, M. J. McAllister, H. Sai, M. Herrera-Alonso, D. H. Adamson, R. K. Prud'homme, R. Car, D. A. Saville, I. A. Aksay, *J. Phys. Chem. B* **2006**, *110*, 8535.

[6] S. Stankovich, D. A. Dikin, R. D. Piner, K. A. Kohlhaas, A. Kleinhammes, Y. Jia, Y. Wu, S. T. Nguyen, R. S. Ruoff, *Carbon* **2007**, *45*, 1558.

[7] D. C. Elias, R. R. Nair, T. M. G. Mohiuddin, S. V. Morozov, P. Blake, M. P. Halsall, A. C. Ferrari, D. W. Boukhvalov, M. I. Katsnelson, A. K. Geim, K. S. Novoselov, *Science* **2009**, *323*, 610.

[8] M. Jaiswal, C. H. Yi Xuan Lim, Q. Bao, C. T. Toh, K. P. Loh, B. OÌˆzyilmaz, *ACS Nano* **2011**, *5*, 888.

[9] L. Xie, L. Jiao, H. Dai, *J. Am. Chem. Soc.* **2010**, *132*, 14751.

[10] J. D. Jones, W. D. Hoffmann, A. V. Jesseph, C. J. Morris, G. F. Verbeck, J. M. Perez, *Appl. Phys. Lett.* **2010**, *97*, 233104.

[11] A. J. Birch, *J. Chem. Soc.* **1944**, 430.

[12] A. Govindaraj, *Current Science* **1993**, *65*, 868.

[13] A. Govindaraj, A. Rathna, J. Chandrasekhar, C. N. R. Rao, *Proc.Indian Acad. Sci.* **1993**, *105*, 303.

[14] G. Kresse, J. Hafner, *Phys. Rev. B* **1993**, *47*, 558.